Enrichment of hypermethylated DNA on chip for cancer diagnostics

RUBEN KOLKMAN

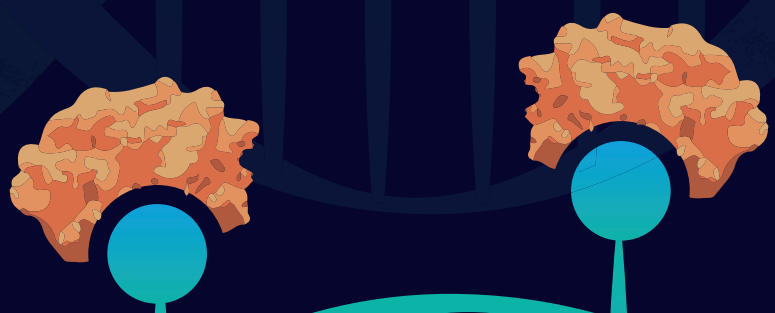

ENRICHMENT OF HYPERMETHYLATED DNA ON CHIP FOR CANCER DIAGNOSTICS

Ruben William Kolkman

ENRICHMENT OF HYPERMETHYLATED DNA ON CHIP FOR CANCER DIAGNOSTICS

DISSERTATION

to obtain
the degree of doctor at the Universiteit Twente,
on the authority of the rector magnificus,
prof. dr. ir. A. Veldkamp,
on account of the decision of the Doctorate Board
to be publicly defended
on Friday the 2nd of December 2022 at 14.45 hours

by

Ruben William Kolkman

born on the 27th of July, 1994
in Almelo, The Netherlands

This dissertation has been approved by:

Promotors
prof. dr. ir. J. Huskens
prof. dr. ir. L.I. Segerink

The research described in this thesis was performed within the laboratories of the Molecular NanoFabrication (MnF) group and the BIOS lab on a Chip group at the MESA+ Institute, the Techmed Centre for Biomedical Technology and Technical Medicine, Faculty of Science and Technology (TNW) and Faculty of Electrical Engineering, Mathematics and Computer Science (EEMCS) of The University of Twente. This research was supported by the Weijerhorst Foundation.

UNIVERSITY OF TWENTE. | MESA+ INSTITUTE | TECHMED CENTRE

BIOS Lab on a Chip group

MnF MOLECULAR NANO FABRICATION

Stichting De Weijerhorst
de stuwende kracht

Cover design: Barry Looije
Printed by: Ridderprint
ISBN: 978-90-365-5485-5
DOI: 10.3990/1.9789036554855

Graduation Committee:

Chairman:	prof. dr. J.N. Kok (University of Twente)
Promotors:	prof. dr. ir. J. Huskens (University of Twente)
	prof. dr. ir. L.I. Segerink (University of Twente)
Committee Members:	prof. dr. S.J.G. Lemay (University of Twente)
	prof. dr. D. Fernandez Rivas (University of Twente)
	prof. dr. K.W. Plaxco (University of California)
	prof. dr. ir. L. Brunsveld (Technical University of Eindhoven)
	prof. dr. R.D.M. Steenbergen (Amsterdam UMC)

Table of contents

Chapter 1

General introduction

In 2020 approximately 19 million new cancer cases were found and 9.9 million people died due to cancer.[1] Lung cancer is one of the deadliest cancer types, accountable for approximately 2 million deaths each year.[1] The origination of cancer can be attributed to many different aspects including virus infections, exposure to carcinogens and lifestyle of people. For example, it is known that an unhealthy diet, lack of physical activity, drinking alcohol and/or usage of tobacco increases the the risk for cancer development.

The earlier cancer is detected, the better the cancer survival rate and treatment conditions are.[2,3] In order to detect cancer at an early stage, screening programs are organized to screen a population without cancer symptoms (Figure 1.1).[4] In The Netherlands three different cancer screening programs are currently organized to screen for cervical cancer[5], breast cancer[6] and colon cancer.[7,8] These screening programs still suffer from the need of trained healthcare personnel, high costs, an invasive approach and/or limited attendance. Recently a self-test has been incorporated in the cervical cancer screening program, which aims to increase the number of attendees. Without cancer screening programs, cancer is typically diagnosed in a later stage, after the onset of cancer-related symptoms. This later stage makes the cancer treatment process more complicated, since it results in larger sized tumors with increased probability of metastases compared to cancer detection prior to cancer symptoms. People with cancer-related symptoms are subjected to a variety of diagnostic tools, such as imaging techniques and/or a tissue biopsy.[9] Those tools can be disadvantageous due to the possible need of a contrast agent, invasiveness and difficulty to encompass tumor heterogeneity. Also, the tumor needs to be sufficiently large to enable cancer detection. Ideally, cancer is detected prior to symptoms and in the preliminary phase of tumor development.

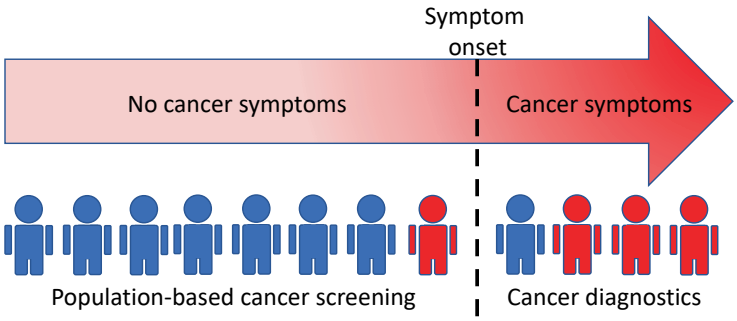

Figure 1.1. Scheme illustrating the difference between population-based cancer screening and cancer diagnostics. People with and without cancer are indicated in red and blue, respectively. Scheme based on the report by the WHO.[4]

Hypermethylated DNA (hmDNA) is one of the cancer biomarkers that can be detected in urine.[10,11] Upon the methylation, a methyl group (-CH_3) is covalently bound to a cytosine base while the other three bases adenosine, guanine and thymine remain unaffected (Figure 1.2). The methylation takes place at a CpG, which is a cytosine base followed by guanine base in the 5' – 3'direction. The hypermethylation of DNA is an epigenetic change which also occurs naturally in cells to regulate gene expression and is, therefore, not only cancer-related.[12] Nevertheless, altered methylation of genes, such as genes of promoter regions, can result in undesired changes in gene expression.[13] Specific cancer types, such as cervical, lung, and bladder cancer, can show the hypermethylation of specific genes.[10,11,14,15]

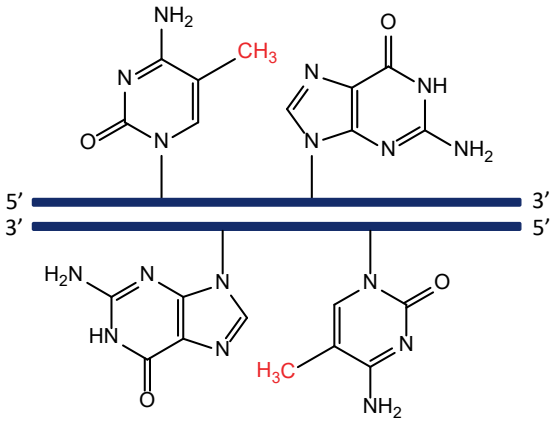

Figure 1.2. Methylated cytosines in a CpG complex. At both strands of DNA a cytosine base followed by a guanine base is displayed in the 5' – 3'direction. The blue lines represent the sugar-phosphate backbone of DNA. The covalent bound methyl group (-CH_3) to the cytosines is indicated in red.

One of the major challenges for hmDNA-based cancer detection in urine is the low concentration of hmDNA and the abundant presence of non-methylated DNA. The total DNA concentration in urine supernatant varies between 17 - 93 ng/mL,[16] whereas the hmDNA concentration can be as low as a few copies per ml of urine in early-stage cancers. Therefore, a step is required to preselect hmDNA from non-methylated DNA. hmDNA can be preselected by a hmDNA enrichment method where a surface is modified with proteins that binds hmDNA stronger than non-methylated DNA. An example of such a protein is methyl binding domain 2 (MBD2), which functions as a receptor toward methylated CpGs with a higher affinity compared to a non-methylated CpG.[17,18] This binding is due to the formation of multiple interactions pairs between a methylated CpG and MBD2 per hmDNA, defined as multivalent binding. Surface-bound DNA can be removed using an elution step. In this way, enrichment of hmDNA is an easy-to-perform method as only a binding and elution step is involved. However, usage in the clinics is limited at the moment due to the co-enrichment of non-methylated DNA.[19,20]

There is a need to overcome the limited hmDNA enrichment selectivity. Lowering the avidity of non-methylated DNA to the MBD2 surface is a requirement for the new hmDNA enrichment system. The avidity can be decreased by reducing the applied MBD2 surface receptor density which, thus, lowers the surface binding of non-methylated DNA. The surface binding of hmDNA will not directly be affected by the reduction of the MBD2 surface receptor density due to the stronger MBD2 methylated CpG binding strength. Furthermore, tuning the surface receptor density can result in superselective binding of multivalent targets.[21] Those systems possess the property that only a small increase in the surface receptor density is sufficient to switch from no to maximum target-surface coverages.

Aim and thesis outline

The aim of this is thesis is to develop a selective hmDNA enrichment method by adopting the principles of superselectivity and multivalent binding. The developed method should enable hmDNA-based cancer diagnostics in urine. The first part of this thesis focusses on the development of a hmDNA capture coating with MBD2 surface receptor density control. In the second part of the thesis the hmDNA enrichment selectivity of DNA mixtures were quantitatively assessed. In the third part a micropillared chip was developed to increase the electrochemical DNA detection sensitivity. In the last part a microfluidic device with a micropillar array was designed and used for hmDNA enrichment of DNA isolated from a cervical cancer cell line and the urine of a cervical cancer patient.

The work described in this thesis is part of the early cancer diagnostics project funded by the foundation the Weijerhorst which aims to develop a microfluidic chip for early-stage cancer detection. This project focus on three different research areas. First, cancer specific hmDNA biomarkers in urine will be determined. This research has been carried out at the Amsterdam UMC. Second, a method will be developed for selective hmDNA enrichment for DNA present in urine. Third, a biosensor will be developed to detect the presence of specific hmDNA using optical or electrochemical measures. This thesis describes the research in the second area.

Chapter 2 provides a perspective describing a new method for the improvement of the hmDNA enrichment selectivity. First the most suitable proteins present within the methyl binding domain protein family as a biorecognition elements for hmDNA enrichment are described. Next, the performance of hmDNA enrichment system used nowadays are discussed. The last part explains how multivalency can be used to enable superselective enrichment of hmDNA.

Chapter 3 reports a method to improve the hmDNA binding selectivity towards MBD2-modified surfaces. The MBD2 surface receptor density on gold surfaces is tuned by employing a thiol-based self-assembled monolayer (SAM). The effect of varying MBD2 surface receptor densities on the degree of DNA binding as function of the DNA methylation level has been assessed.

Chapter 4 demonstrates the hmDNA enrichment selectivity of the developed method in chapter 3. MBD2-modified surfaces were used to study the binding of DNA mixtures to and elution from MBD2 surfaces. A method has been developed to determine the hmDNA level in enriched DNA mixtures. The hmDNA enrichment selectivity from DNA mixture was assesses while varying the MBD2 surface receptor densities.

Chapter 5 describes the development of a micropillar-structured electrode for DNA sensing. Single stranded DNA probes immobilized on the electrode were used to bind to the target DNA. The binding of the target DNA was confirmed by a sandwich assay using a reporter DNA labeled with ferrocene. The electrochemical DNA sensing sensitivity was studied while varying the active surface of the micropillared electrode.

Chapter 6 introduces the development of a microfluidic chip to enable hmDNA enrichment. The chip consists of a hmDNA enrichment chamber with micropillars to increase the surface-to-volume ratio. DNA was isolated from a cervical cancer cell line and the urine of a cervical cancer patient. The methylation level for a cervical cancer specific hmDNA gene was assessed in the isolated DNA samples. Then, the microfluidic chip was used to enrich the isolated DNA samples with hmDNA followed by quantitative PCR (qPCR) detection of the cervical cancer specific hmDNA gene.

Chapter 7. Summarizes the work followed by recommendations for future research.

References

(1) Sung, H.; Ferlay, J.; Siegel, R. L.; Laversanne, M.; Soerjomataram, I.; Jemal, A.; Bray, F. Global Cancer Statistics 2020: GLOBOCAN Estimates of Incidence and Mortality Worldwide for 36 Cancers in 185 Countries. *CA. Cancer J. Clin.* **2021**, *71*, 209–249.

(2) Crosby, D.; Lyons, N.; Greenwood, E.; Harrison, S.; Hiom, S.; Moffat, J.; Quallo, T.; Samuel, E.; Walker, I. A Roadmap for the Early Detection and Diagnosis of Cancer. *Lancet Oncol.* **2020**, *21*, 1397–1399.

(3) Hanna, T. P.; King, W. D.; Thibodeau, S.; Jalink, M.; Paulin, G. A.; Harvey-Jones, E.; O'Sullivan, D. E.; Booth, C. M.; Sullivan, R.; Aggarwal, A. Mortality Due to Cancer Treatment Delay: Systematic Review and Meta-Analysis. *BMJ* **2020**, *371*, m4087.

(4) Copenhagen: WHO Regional Office for Europe. *A Short Guide to Cancer Screening. Increase Effectiveness, Maximize Benefits and Minimize Harm*; 2022.

(5) Aitken, C. A.; Van Agt, H. M. E.; Siebers, A. G.; Van Kemenade, F. J.; Niesters, H. G. M.; Melchers, W. J. G.; Vedder, J. E. M.; Schuurman, R.; Van den Brule, A. J. C.; Van der Linden, H. C.; Hinrichs, J. W. J.; Molijn, A.; Hoogduin, K. J.; Van Hemel, B. M.; de Kok, I. M. C. M. Introduction of Primary Screening Using High-Risk HPV DNA Detection in the Dutch Cervical Cancer Screening Programme: A Population-Based Cohort Study. *BMC Med.* **2019**, *17*, 228.

(6) Kalager, M.; Zelen, M.; Langmark, F.; Adami, H. Effect of Screening Mammography on Breast-Cancer Mortality in Norway. *N. Engl. J. Med.* **2010**, *363*, 1203–1210.

(7) Kortlever, T. L.; de Jonge, L.; Wisse, P. H. A.; Seriese, I.; Otto-Terlouw, P.; Van Leerdam, M. E.; Spaander, M. C. W.; Dekker, E.; Lansdorp-Vogelaar, I. The National FIT-Based Colorectal Cancer Screening Program in the Netherlands during the COVID-19 Pandemic. *Prev. Med. (Baltim).* **2021**, *151*, 106643.

(8) Breekveldt, E. C. H.; Lansdorp-Vogelaar, I.; Toes-Zoutendijk, E.; Spaander, M. C. W.; Van Vuuren, A. J.; Van Kemenade, F. J.; Ramakers, C. R. B.; Dekker, E.; Nagtegaal, I. D.; Krul, M. F.; Kok, N. F. M.; Kuhlmann, K. F. D.; Vink, G. R.; Van Leerdam, M. E.; Elferink, M. A. G.; Van Bergeijk, J.; Wiersma, T.; Van Grevenstein, W.; Frasa, M.; Van Gestel, L.; Meijer, G. Colorectal Cancer Incidence, Mortality, Tumour Characteristics, and Treatment before and after Introduction of the Faecal Immunochemical Testing-Based Screening Programme in the Netherlands: A Population-Based Study. *Lancet Gastroenterol. Hepatol.* **2022**, *7*, 60–68.

(9) World Health Organization. *Guide to Cancer - Guide to Cancer Early Diagnosis*; 2017.

(10) Bach, S.; Paulis, I.; Sluiter, N. R.; Tibbesma, M.; Martin, I.; Van de Wiel, M. A.; Tuynman, J. B.; Bahce, I.; Kazemier, G.; Steenbergen, R. D. M. Detection of Colorectal Cancer in Urine Using DNA Methylation Analysis. *Sci. Rep.* **2021**, *11*, 2363.

(11) Snoek, B. C.; Splunter, A. P. van; Bleeker, M. C. G.; Ruiten, M. C. van; Heideman, D. A. M.; Rurup, W. F.; Verlaat, W.; Schotman, H.; Gent, M. Van; Trommel, N. E. Van; Steenbergen, R. D. M. Cervical Cancer Detection by DNA Methylation Analysis in Urine. *Sci. Rep.* **2019**, *9*, 3088.

(12) Moore, L. D.; Le, T.; Fan, G. DNA Methylation and Its Basic Function. *Neuropsychopharmacology* **2013**, *38*, 23–38.

(13) Herman, J. G.; Baylin, S. B. Gene Silencing in Cancer in Association with Promoter Hypermethylation. *N. Engl. J. Med.* **2003**, *349*, 2042–2054.

(14) Bosschieter, J.; Lutz, C.; Segerink, L. I.; Vis, A. N.; Zwarthoff, E. C.; A van Moorselaar, R. J.; van Rhijn, B. W.; Heymans, M. W.; Jansma, E. P.; Steenbergen, R. D.; Nieuwenhuijzen, J. A. The Diagnostic Accuracy of Methylation Markers in Urine for the Detection of Bladder Cancer: A Systematic Review. *Epigenomics* **2018**, *10*, 673–687.

(15) Kandimalla, R.; van Tilborg, A. A.; Zwarthoff, E. C. DNA Methylation-Based Biomarkers in Bladder Cancer. *Nat. Rev. Urol.* **2013**, *10*, 327–335.

(16) van den Helder, R.; van Trommel, N. E.; van Splunter, A. P.; Lissenberg-Witte, B. I.; Bleeker, M. C. G.; Steenbergen, R. D. M. Methylation Analysis in Urine Fractions for Optimal CIN3 and Cervical Cancer Detection. *Papillomavirus Res.* **2020**, *9*, 100193.

(17) Hashimoto, H.; Liu, Y.; Upadhyay, A. K.; Chang, Y.; Howerton, S. B.; Vertino, P. M.; Zhang, X.; Cheng, X. Recognition and Potential Mechanisms for Replication and Erasure of Cytosine Hydroxymethylation. *Nucleic Acids Res.* **2012**, *40*, 4841–4849.

(18) Fraga, M. F. The Affinity of Different MBD Proteins for a Specific Methylated Locus Depends on Their Intrinsic Binding Properties. *Nucleic Acids Res.* **2003**, *31*, 1765–1774.

(19) Yegnasubramanian, S. Combination of Methylated-DNA Precipitation and Methylation-Sensitive Restriction Enzymes (COMPARE-MS) for the Rapid, Sensitive and Quantitative Detection of DNA Methylation. *Nucleic Acids Res.* **2006**, *34*, e19–e19.

(20) Warton, K.; Lin, V.; Navin, T.; Armstrong, N. J.; Kaplan, W.; Ying, K.; Gloss, B.; Mangs, H.; Nair, S. S.; Hacker, N. F.; Sutherland, R. L.; Clark, S. J.; Samimi, G. Methylation-Capture and Next-Generation Sequencing of Free Circulating DNA from Human Plasma. *BMC Genomics* **2014**, *15*, 476.

(21) Martinez-Veracoechea, F. J.; Frenkel, D. Designing Super Selectivity in Multivalent Nano-Particle Binding. *Proc. Natl. Acad. Sci.* **2011**, *108*, 10963–10968.

Chapter 2

Selective enrichment of hypermethylated DNA by a multivalent binding platform

The preselection of hypermethylated DNA (hmDNA) from liquid biopsy samples is key to enable early-stage cancer diagnostics. Due to limited selectivity of the existing preselection approaches, however, wide integration in the clinic is currently prohibited. Here, it is argued that an affinity method on a surface, such as used in affinity chromatography, can be significantly improved by employing the principles of multivalency and superselectivity. In the here proposed method, a methyl binding domain (MBD) protein immobilized at a surface is used as a receptor for (hyper)methylated DNA. By the organization of multiple MBDs on a surface, a multivalent binding platform is achieved. The MBD surface receptor density on that platform is key to increase the enrichment selectivity of hmDNA as a single MBD protein binds both methylated and non-methylated DNA with a small difference in affinity. When the receptor density is varied, multivalent analyte binding typically responds in a non-linear fashion, which phenomenon is called superselectivity. By careful tuning of the MBD density, it is envisaged that the selectivity for methylated over non-methylated DNA can be optimized. Strong applicability is foreseen in a medical setting by implementing such an enrichment step in an analytical process or a lab-on-a-chip device.

R.W. Kolkman, L.I. Segerink, J. Huskens. *Adv. Mater. Interfaces*, accepted.

2.1 Introduction

Cancer is a growing health concern worldwide.[1] Despite the increase in cancer survival rates over the last decades, cancer remains one of the deadliest diseases.[2,3] One of the key aspects of surviving cancer is to detect the disease as early as possible, thereby enlarging the window of opportunity of curing it.[4,5] A recent trend for early cancer diagnostics is the pre-symptomatic detection of cancer biomarkers in liquid biopsy samples and, therefore, improving the survival rate.[6,7]

Hypermethylated DNA (hmDNA) is one of the typical biomarkers found in liquid biopsy samples of cancer patients.[8,9] The presence of hmDNA in blood and urine is correlated to multiple types of cancer, including gastric, lung and ovarian cancer.[10–13] From a genetic point of view, DNA methylation takes place predominantly at promoter regions with a relative high amount of cytosine bases that are followed directly by a guanine (CpGs) in the 5'-to-3' direction, the so-called CpG-rich regions.[13] The methylation of a CpG is an epigenetic alternation in which a methyl group is covalently bonded to the cytosine base at the fifth carbon. By CpG methylation, gene expressions are controlled in cells. As a consequence, methylation can play a role in tumor development when tumor suppressor genes are methylated, thereby repressing the transcription and thus silencing these genes.[14] Hypermethylation refers to the situation that methylation of a promoter region occurs, which in a healthy situation does not occur.

Early disease detection as well as disease progress and the effectiveness of a therapy can be monitored by measuring the hmDNA concentration over time.[15] Yet, the concentration of hmDNA, especially in early-stage cancers, can be as low as a few DNA copies per liquid biopsy sample.[16–18] The current approach to measure hmDNA employs DNA isolation and bisulfite conversion, making it time-consuming and labor intensive. As a result, the method is not widely applicable in the clinic. Typically, hmDNA is detected in bisulfite-treated DNA samples by quantitative PCR (qPCR, of the region of interest; can be cancer dependent). Alternative hmDNA detection approaches that may be suitable for use in point-of-care applications, include electrochemistry,[19] CRISPR,[20] and isothermal amplification.[21]

The detection of specific hmDNA biomarkers by sequencing or biosensing approaches involves the ability to distinguish between hmDNA and non-methylated DNA.[22–24] Commonly a preselection step is applied, and three different approaches exist in order to differentiate between hmDNA and non-methylated "background" DNA.[25–27] The first approach uses methyl-sensitive restriction enzymes.[28–30] These enzymes are able to cleave DNA at a specific recognition sequence only when the CpG is (non-)methylated, depending on the enzyme used. For example, after digesting the DNA sample with a specific enzyme, all the non-methylated DNA is cleaved, while the methylated DNA remains intact. The second approach to differentiate between the two types of DNA is bisulfite conversion.[31,32] Using this chemical modification method, all non-methylated cytosines are converted into the base uracil, while all methylated cytosines remain unconverted. As a result, the base sequence of the non-methylated DNA changes,

allowing an easier differentiation using PCR. The third method uses affinity chromatography purification with an anti-5-methyl-cytosine antibody[33] or a methyl binding domain (MBD)[34,35] protein attached to the surface of beads employed in the method. This approach is based on enriching a DNA sample with hmDNA due to binding of the methylated DNA to the biorecognition element-modified surface. The used biorecognition element, or receptor, that is immobilized on the surface possesses a higher affinity for the hmDNA compared to non-methylated DNA thus enabling the separation. Each of the aforementioned preselection methods has its limitations regarding the selectivity, thus resulting in false positives and affecting negatively the ease of application in early-stage cancer diagnostics.[25–27,36–38] Specifically, the use of restriction enzymes can cause incomplete digestion[25,27,36]; bisulfite conversion results in DNA degradation[25–27]; and affinity purification suffers from the unwanted enrichment of non-methylated DNA.[25,37,38] For these reasons, there is a need for improving the preselection of hmDNA before implementation in the clinic can be considered.

Here, we will focus on a concept that provides the enrichment of hmDNA using an MBD protein bound to a capture surface by applying the principles of multivalent binding, and the superselective binding of hmDNA that results from it. Multivalency is a principle of binding that provides affinity, selectivity and organization.[39–42] The enhancement in binding strength of multivalent targets in comparison to monovalent ones is known as the multivalency effect or avidity.[43] When varying the receptor density on a surface, superselectivity can occur.[44] Superselectivity is the on/off binding behavior of multivalent targets that results from a non-linear dependence of the target coverage on the receptor density. Below a specific threshold receptor density, no binding takes place, while above this density the target binds with close to maximum surface coverage. Despite many of the fundamental aspects of multivalency and superselectivity have been addressed, few practical applications have resulted from it. Here, in the specific case of DNA binding to an MBD-covered surface, we envisage that the threshold density at which the transition from non-binding to binding occurs will depend on the number and density of CpG sites on the DNA and on whether these sites are methylated or not. Thus, one can rationalize conceptually that a careful tuning of the MBD density can result in hmDNA enrichment of DNA isolated from a liquid biopsy while non-methylated or less-methylated DNA is not enriched, thus, enabling selective hmDNA-based cancer diagnostics (Figure 2.1). Thus we aim to outline the strategy to develop a diagnostic tool that employs the principles of multivalency and superselectivity in hmDNA detection.

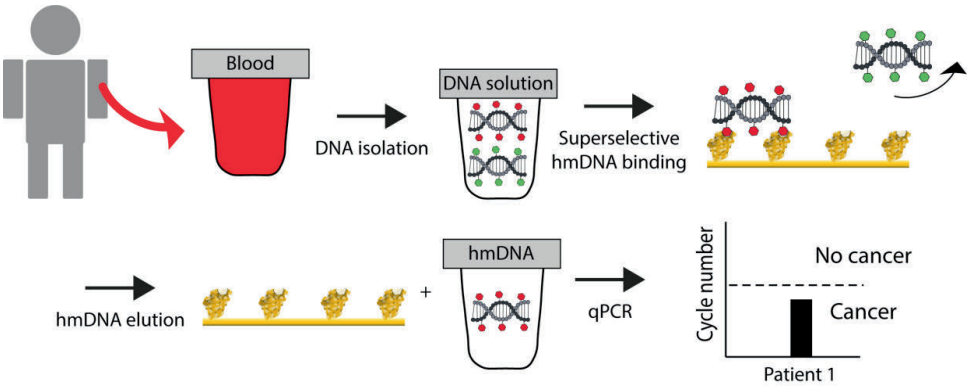

Figure 2.1. Conceptual illustration of the envisaged hmDNA enrichment process. DNA is isolated from a blood liquid biopsy containing both hmDNA and non-methylated DNA. C*pG and CpG are illustrated here by red and green hexagons, respectively, attached to the DNA at the top and bottom strand. Next, superselective enrichment of hmDNA on a capture surface with an optimal MBD surface receptor density. Only DNA with multiple C*pGs are able to bind to the surface due to a sufficient avidity. The hmDNA-enriched DNA sample is analyzed with qPCR to detect a cancer-specific hmDNA sequence.

In the concept proposed here, the enrichment of hmDNA from a solution can be achieved by immobilizing an MBD protein on a surface, possibly that of a column material or micro- and nanoparticles.[34,37,45] The MBD proteins on the surface function as receptors that can interact with the methylated CpGs (C*pG); the ligands from the DNA in solution. The binding site of MBD proteins interacts both with non-methylated CpG (CpG) and C*pG, but the affinity for C*pG is higher.[46–52] The multiple C*pG sites in hmDNA allow the formation of multiple non-covalent bonds to surface-immobilized MBD, resulting in an overall higher binding strength.

Here, we discuss how the general strategy of hmDNA enrichment using a capture surface coated with an MBD protein can be designed optimally by exploiting the principles of superselectivity and multivalent binding. We first discuss the binding performance and selectivities of the protein subtypes present within the MBD protein family toward methylated and non-methylated DNA. Thereafter we explain the principles of the enrichment strategy using an MBD protein, and we discuss the prerequisites to achieve highly selective multivalent binding of targets to a receptor-modified surface in various applications. Finally, we will conclude with an outlook on how the enrichment of hmDNA with superselectivity properties can be developed.

2.2 MBD protein as a receptor for hmDNA

The family of MBD proteins contains five members that have a higher binding affinity for methylated DNA compared to non-methylated DNA. These are methyl-CpG binding protein 2 (MeCP2)[53], MBD1[54], MBD2[55], MBD3[56] and MBD4.[57] Despite all are selective for a C*pG, the absolute binding affinities of the individual proteins within the MBD family for C*pG and CpG differ. The binding affinities of an MBD protein that is interacting with C*pG or CpG is important for the overall affinity with (non-)methylated DNA and for the selectivity of the enrichment of hmDNA.

The dissociation constants (K_d) of the C*pG-selective MBD proteins for both C*pG or CpG are compared in Table 2.1. The data reported in Table 2.1 shows that in particular MeCP2, MBD1 and MBD2 possess low K_d values for C*pG, but all proteins show, rather comparable, affinities for CpG. However, the direct comparison of the K_d values between different studies is complicated by the use of different DNA lengths and CpG positions, of slightly different reaction buffer compositions, and of different techniques to measure K_d. In the study by Fraga *et al.* it was concluded that the K_d values were strongly dependent on the DNA sequence used.[47]

In particular the ratio of the K_d values for CpG and C*pG, which is a measure for the selectivity, can be a proper measure to identify the most optimal receptor for the enrichment.[46–52] It can be expected that the factors complicating the comparison of K_d values between different proteins is largely eliminated by taking ratios, so by looking at the selectivities. As seen from Table 2.1, high selectivities (= $K_{d,CpG}/K_{d,C*pG}$) are achieved by MeCP2, MBD1 and MBD2, with values ranging from 50-295. Of these proteins, MBD1 seems to have the best selectivity.

From this analysis, decent individual selectivities are obtained for MeCP2, MBD1 and MBD2, which are much better than those of MBD3 and MBD4. Most likely, any of the first three can be used in achieving enrichment. Yet, as will become clear from the multivalency and superselectivity discussion below, the intrinsic selectivity (*i.e.*, the ratio of K_d values for individual CpG/C*pG sites) is not enough to predict the best selectivity in a multivalent binding event for (methylated) DNA that contains multiple C(*)pG sites. Qualitatively, the overall selectivity for binding hmDNA will be better when a good intrinsic selectivity is coupled to a relatively weak binding constant (high K_d), in particular for CpG, and high valency (number of interactions) leading to a "multiplication" of several individual selectivities. In that way, a large difference in overall K values for hmDNA and non-methylated DNA can be achieved in the biologically relevant concentration range. The next sections focus only on the use of the MBD2 protein, as this is the most used MBD protein nowadays in the literature for the enrichment of hmDNA.

Table 2.1. Reported K_d (nM) values of the MBD protein family upon interaction with DNA containing a C(*)pGs in various studies. In the table the used selectivity ($K_{d,CpG}/K_{d,C*pG}$) DNA length in base pairs (bp), number of C(*)pGs per sequences, location of C(*)pG in bp position from 5' to 3' direction, characterization technique and the studies are displayed. Data not determined or displayed in a study is shown as "ND".

MBD type	$K_{d,C*pG}$ (nM)	$K_{d,CpG}$ (nM)	Selectivity	DNA length (bp)	Number of C(*)pGs	Location of C(*)pG (bp)	Characterization technique	Reference
MeCP2	10	500	50	12	1	5	Fluorescence polarization	Hashimoto *et al.* [46]
	172	458	3	42	1	20	Capillary electrophoresis	Fraga *et al.*[47]
	27	ND	ND	24	1	12	Electrophoretic mobility shift assay	Buchmuller *et al.*[48]
	8	ND	ND	ND	ND	ND	Fluorescence anisotropy	Liu *et al.*[51]
MBD1	5	1400	280	12	1	5	Fluorescence polarization	Hashimoto *et al.*[46]
	244	72000	295	22	1	10	Surface plasmon resonance	Yu *et al.*[50]
MBD2	60	6500	108	12	1	5	Fluorescence polarization	Hashimoto *et al.*[46]
	3	188	63	42	1	20	Capillary electrophoresis	Fraga *et al.*[47]
	6	ND	ND	22	1	10	Fluorescence spectroscopy	Heimer *et al.*[49]
	12	ND	ND	ND	ND	ND	Fluorescence anisotropy	Liu *et al.*[51]
	29	ND	ND	17	1	8	Fluorescence polarization	Pan *et al.*[52]
MBD3	1300	6600	5	12	1	5	Fluorescence polarization	Hashimoto *et al.*[46]
	580	684	1	42	1	20	Capillary electrophoresis	Fraga *et al.*[47]
MBD4	220	1070	5	12	1	5	Fluorescence polarization	Hashimoto *et al.*[46]

2.3 Performance of existing hmDNA enrichment methods using MBD2

The enrichment of hmDNA is commonly performed by a surface modified with the MBD2 protein.[34,37,45,58] The general approach of enrichment consists of three consecutive steps. In the first step, MBD2 is immobilized onto the surface, such as a column material or nano/micro-size particles. In general, proteins can be immobilized by a wide variety of approaches,[59–62] but a detailed description of the protocols is outside the scope of this article. The second step is the actual binding of hmDNA to the MBD2-modified surface. The hmDNA binds to multiple MBD2 proteins when the spacing between C*pGs is between 3 - 20 base pairs.[63,64] This minimal distance is required to prevent steric hindrance. In the last step, the bound DNA is removed from the surface with an elution buffer to enable subsequent characterization. Table 2.2 provides an overview of various MBD2-based enrichment methods including DNA processing methods applied prior/post hmDNA enrichment.

A performance study of MBD2 used for hmDNA enrichment was performed by Nair *et al*.[65] Here, biotinylated MBD2 was immobilized on streptavidin-coated magnetic beads. Three different genes were used: a partly methylated DNA, fully methylated DNA, and fully non-methylated DNA originating from the cancerous LNCaP cell lines. As a control, the PrEC cell line was used, where all different genes were non-methylated. All non-methylated DNA was not significantly interacting with the MBD2-modified beads, while the partly or fully methylated DNA genes were. The authors were able to discriminate between the partly and fully methylated DNA using a salt washing step with a NaCl concentration ranging between 0.2 M and 2 M, as was validated by quantitative PCR (qPCR).

In a study by Warton *et al*., a method was developed to improve the methylated DNA enrichment by decreasing the amount of MBD2-functionalized magnetic beads upon enrichment of DNA.[38] They found a positive effect on the enrichment factor (the enriched amount of methylated DNA divided by the enriched amount of non-methylated DNA in a separate experiment) that was increased from a factor 7 to 30 by decreasing the amount of magnetic beads. An alternative is the incorporation of sperm DNA as blocking agent upon hmDNA enrichment.[66] The usage of the blocking agent improved the enrichment factor from 2.1 to 14.2.

The selectivity of hmDNA enrichment was studied in more detail by Yegnasubramanian *et al*. by using fragmented genomic DNA from white blood cells at input amounts ranging between 32 pg and 100 ng.[37] The genomic DNA was methylated using the M.SssI enzyme to create hmDNA. Here, magnetic particles covered with anti-histidine antibodies were modified with His-tagged MBD2 in the presence of 200 ng non-methylated plasmid DNA and used for the enrichment. After a 1 h incubation step with DNA, the magnetic beads were isolated with a magnetic rack. Subsequently, the beads were washed and followed by the elution of bound DNA using a temperature of 95 °C. Enrichment factors of 500-700-fold were found by qPCR at 4 and 100 ng hmDNA and non-methylated DNA input concentrations. Nevertheless, the authors showed that the

selectivity of an MBD2-based enrichment method is strongly dependent on the DNA input concentration (Figure 2.2). For example, enrichment factors of only 1 and 5 were achieved when using 11 ng non-methylated DNA and 0.03 or 0.1 ng of hmDNA, respectively. To improve the limited MBD2 enrichment selectivity, especially at low hmDNA and high non-methylated DNA input concentrations, they used methyl-sensitive restriction enzymes prior to the enrichment. This resulted in the detection of 32 pg hmDNA in a sample containing more than a 3000-fold higher concentration of non-methylated genomic DNA.

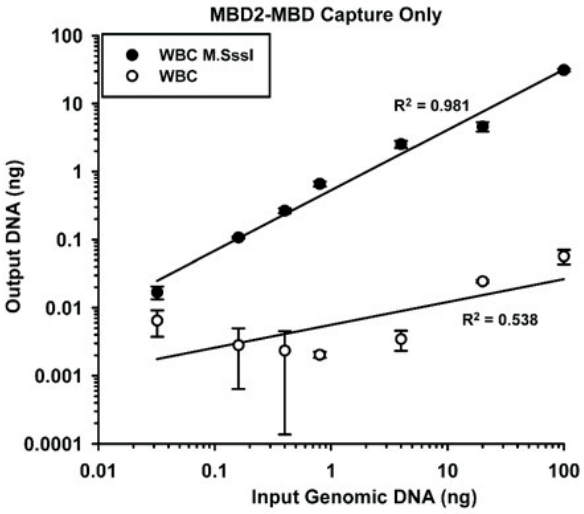

Figure 2.2. DNA input concentrations *versus* the amount of output DNA after hmDNA enrichment as quantified by qPCR. Fragmented genomic DNA from white blood cells was used in its non-methylated form (WBC, white filled circles) and in the hmDNA form (WBC M.SssI, black filled circles). hmDNA was formed by methylation of the non-methylated genomic DNA with the M.SssI enzyme. Reproduced from ref. 37 with permission from Oxford University Press.

All the standalone MBD2-based enrichment systems reported and discussed here did only report the fold of enrichment based on the quantification after enriching a solution with (hyper)methylated DNA or non-methylated DNA in separate experiments. Unfortunately, the selectivity of enriching DNA solutions containing both (hyper)methylated DNA and non-methylated DNA are currently unknown despite its importance for clinical implications. The enrichment selectivity determination of DNA mixtures is crucial as the concentration of hmDNA biomarkers in liquid biopsies can be orders of magnitude lower compared to that of non-methylated "background" DNA.[16–18] Furthermore, detailed understanding of the enrichment selectivity of DNA mixtures would provide information in which clinically relevant hmDNA concentration can be

differentiated from the non-methylated DNA. The MBD2-based enrichment systems were also not quantitatively tested with various DNA input concentrations in most of the studies.[38,65,66] Furthermore, the highly selective enrichment system developed by Yegnasubramanian *et al*.[37] is unfortunately rather complex, lengthy to perform, and needs methyl-sensitive restriction enzymes which are restricted in use due to the limited amount of available recognition sequences. Overall, the MBD2-based enrichment systems are only able to differentiate well between hmDNA and non-methylated DNA at high input concentrations but not at combined low and high input concentrations of hmDNA and non-methylated DNA, respectively. For that reason, the current hmDNA enrichment selectivity is too limited to function as a simple standalone system without any post-modification steps to enable wide integration in the clinic in early cancer diagnostics. To enable early-stage cancer diagnostics, the hmDNA enrichment selectivity should be increased. Additionally, the effect on the hmDNA enrichment selectivity using DNA mixtures with various hmDNA/non-methylated DNA ratios should be determined. Finally, the impact of different DNA input concentrations on the hmDNA enrichment should be verified.

Table 2.2. Applications of DNA samples enriched in hmDNA using MBD2-modified surfaces. Application, processing prior/post hmDNA enrichment, DNA origin, and references are displayed. Circulating free DNA and recombinase polymerase amplification are abbreviated as cfDNA and RPA, respectively.

Application	DNA processing steps (prior/post hmDNA enrichment)	DNA origin	References
CpG methylation profiling	Sonication of genomic DNA (prior) and whole genome amplification (post)	Prostate normal and cancer cells	Nair *et al.*[65]
Next-generation sequencing	-	cfDNA from plasma/serum	Warton *et al.*[38]
Calorimetric and/or electrochemical detection of genome methylation and methylation-specific genes	Restriction enzyme digest of genomic DNA (prior) and/or RPA (post)	Cancer/control cell lines and urine of prostate cancer patients	Wee *et al.*[66]
hmDNA-based prostate cancer detection	Methyl-sensitive restriction enzyme digest (prior)	Prostate cancer cell line and tissue	Yegnasubramanian *et al.* [37]

2.4 Multivalency as a tool for superselective biosensing

hmDNA contains multiple C*pGs, each of which functions as a ligand that can bind to the MBD2 receptors on the surface during enrichment. At increasing ligand and receptor densities, more non-covalent interaction pairs can be formed, which is a typical example of multivalent binding (Figure 2.3A).[43,67,68] Interaction pairs are formed when the geometrical locations between the ligand and receptor match.[68] Multivalent binding results into strong but reversible complex formation for which the overall binding strength, defined by the avidity constant (K_{av}), is significantly higher compared to a monovalent binding event.[69] Additionally, the K_{av} is increasing faster than the sum of the individual binding interactions. The avidity is strongly dependent on both the ligand and receptor densities, and more stable complexes are formed at higher densities.[70] An example is the binding of affitin receptors toward the pathogen *Staphylococcus aureus*.[71] The binding affinity was increased by the formation of a dendrimer containing multiple affitin receptors. As a result, an approximately 600-fold improvement in the K_d value down to ≈0.2 nM was achieved for the dendrimer-based system in comparison to the monovalent binding of affitin to *Staphylococcus aureus*. Another example is the trapping of viruses by multivalent interactions with DNA-based shells functionalized with antibodies.[72] The functionalized shell binds as sufficiently strong to the virus owing to multivalent interactions resulting into the suppression of virus binding to the cell surface.

Multivalent binding is composed of inter- and intramolecular interactions.[73] At interfaces, all ligands of an individual target bind to a receptor immobilized on a surface, for example, of a micro/nanoparticle, a cell, or a self-assembled monolayer. The advantages of surface binding is that a higher avidity constant and thus more stable complexes can be formed as a result of a higher effective molarity (*EM*).[74,75] *EM* describes the probability for intramolecular ring closure.[76] The overall binding or avidity constant, K_{av}, is dependent on the monovalent ligand-receptor binding strength (K_i), *EM* and the number of ligand-receptor interaction pairs (n), as described by equation 1.[43]

$$K_{av} = K_i(K_i EM)^{n-1} \quad (1)$$

Equation 1 can be read as follows. Monovalent binding (n=1) leads to a binding constant of K_i. For each additional interaction pair in a multivalent complex, the affinity increases with a factor $K_i EM$. This factor is therefore called the multivalent enhancement factor.

An example of multivalency in nature is the binding of a virus particle on a cell surface.[69] Efficient binding, possibly followed by endocytosis, of the virus particle is only possible in situations when the virus binds multivalently at the cell surface with sufficiently high *EM* and n. Therefore, virus binding can be prevented by the use of monovalent drug molecules that bind at the virus protein sites to decrease *EM* and n such that K_{av} becomes too weak for surface binding.

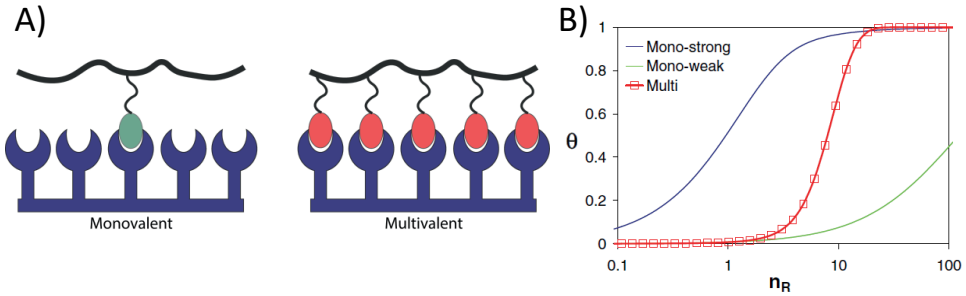

Figure 2.3. A) Illustration of the monovalent and multivalent interaction of a target to a receptor-modified surface. B) Overview of the degree of target binding as function of the receptor density for monovalent targets with low (green) and high (blue) ligand affinity for the receptor-modified surface and the multivalent target with low ligand affinity for the receptor (red).[44] n_R displays the surface receptor density and θ the target surface coverage. Adapted from ref. 44 by permission of National Academy of Sciences of the United states of America.

The enormous advantage of multivalent target binding on a surface is that it can be developed into a superselective binding system. Both the ligand and receptor densities are key to achieve superselective binding, as was described in a theoretical study in 2011 by the group of Frenkel.[44] In this study, an example was demonstrated for the degree of binding of nanoparticles on a surface as a function of the receptor density (Figure 2.3B). The surface binding was compared between monovalent targets on the one hand, which contained one ligand with either weak or strong affinity for the receptor on the surface, to a multivalent target with multiple low-affinity ligands. For both monovalent targets, the binding increased over a wide range of receptor densities at the same pace or slower than the increase in receptor density, which is characteristic for monovalent binding. In contrast, the multivalent target bound with a coverage that increased faster than the receptor density, which is the hallmark of superselective binding.

Superselectivity is used among others as a tool for targeting cells based on variations in their receptor densities to improve cancer cell-specific drug delivery.[77] Different ErbB2 receptor densities on cell surfaces were used to determine the effect on targeting by EC1 ligand-modified nanoparticle micelles. Three regimes of receptor densities were created with low, medium and high number of ErbB2 receptors per cell representing healthy, early and late stage cancer cells, respectively. A decrease of the K_d from 12.8 µM to 0.4 µM using a micelle modified with 40 ligands compared to a monovalent interaction was observed, as was validated using surface plasmon resonance spectroscopy. Additionally, cell uptake of the ligand-modified micelles depended on both the ligand and receptor density, as observed by flow cytometry. At healthy receptor densities, limited endocytosis took place for an 8-valent nanoparticle which was approximately twofold lower than for the 40-valent one. The endocytosis

remained limited for the 8-valent nanoparticles in early and high cancer stage cells but was significant for the 40-valent one, which is attributed to a larger *EM* and *n* which resulted in a K_{av} of the micelle that is sufficient for binding to the cancer cells.

A multivalent system is not directly a superselective system. Superselectivity is dependent on the multivalent enhancement factor K_iEM. In fact, if K_iEM is too high, less or no superselectivity is observed.[44,78] In such a case, the dependence of target binding at increasing receptor density is less strong. The preference of superselectivity for a low K_iEM is explained by noting that in such a "weak multivalent" system multiple ligand-receptor interaction pairs are mandatory to enable binding of the target to the surface. The location of ligands on a polymer that binds multivalently at a receptor-modified surface is crucial as well for the degree of superselectivity, as was described in a theoretical study by Tito *et al*.[79] The superselectivity was more pronounced when a polymer with locally assembled ligands was used at reduced ligand densities. The increase in superselectivity was attributed to reduced competition at the sensor surface upon binding, lesser blockage of the binding sites and increase in cooperativity.

The importance of superselectivity in discriminating between different targets on a receptor-modified surface was reported in experimental work by Dubacheva *et al*.[80] Their system was based on the interaction between a polymer modified with cyclodextrin ligands and a monolayer-modified surface containing a tunable receptor density of either ferrocene or adamantane. The two different receptors were used to study the effect of different binding strength, while the K_d values of ferrocene and adamantane are 200 µM and 10 µM, respectively. The higher affinity between the adamantane receptor and the target resulted in superselective binding at an approximately 16-fold lower receptor density to achieve maximum surface coverage compared to the usage of ferrocene receptors. Furthermore, maximal surface coverage of the target on the adamantane-coated surface could be achieved while binding of the target to the ferrocene-coated surfaces remained fully absent. This work has clearly shown that superselectivity enables to discriminate between the target and non-target by optimizing the receptor density.

This section has shown that it is critical to control the multivalent enhancement factor K_iEM to develop a superselective platform for the enrichment of (hyper)methylated DNA. The effect of the selective MBDs (MeCP2, MBD1 and MBD2) on the superselective enrichment of hmDNA should be investigated to decide which of these proteins provides the best superselectivity. The selectivity will, therefore, be a combination of both a good intrinsic selectivity and a low K_iEM. The possible *n* for both (hyper)methylated and non-methylated DNA depends on the DNA length. In liquid biopsies, such as blood and urine, the DNA is fragmented in comparison with cellular DNA, which can result in a decrease of the valency *n* for both types of DNA.[81,82] Due to lower *n* values of DNA from liquid biopsies, the K_{av} will be lower and, therefore, surface binding of DNA that lacks methylation will be reduced as well.

Conceptually the superselective device should be able to discriminate between hmDNA and non-methylated DNA binding (Figure 2.4). At low MBD densities, the

number of MBD interactions per DNA is too low for both hmDNA and non-methylated DNA to reach a K_{av} sufficient for surface binding. In the medium MBD density regime, multiple MBD interactions are formed with methylated DNA resulting in a sufficiently high K_{av} for surface binding. However, the number of MBD interactions is too little to enable surface binding of non-methylated DNA because of the lower K_i. On the other hand, if the MBD density becomes too large, too many MBD interactions can be formed with both hmDNA and non-methylated DNA. Consequently, K_{av} is sufficiently high to give surface binding for both types of DNA, resulting in a decrease of the selectivity of hmDNA enrichment.

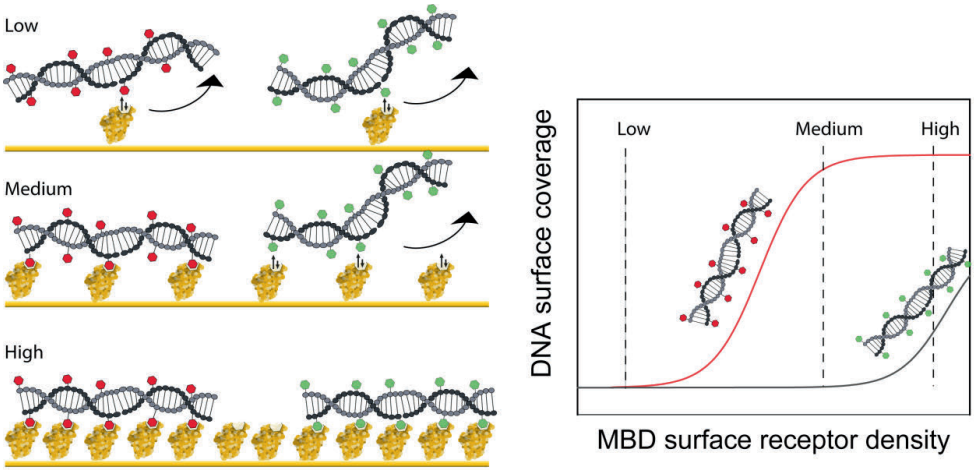

Figure 2.4. Conceptual illustration of the enrichment of (hyper)methylated DNA on a capture surface with a low, medium, or high MBD surface receptor density. The binding of DNA is dependent on whether the DNA is methylated or not and on the MBD surface receptor density. C*pGs and CpGs are indicated in red and green, respectively. At a low MBD surface receptor density (left, top), no DNA binding at all is takes place. At medium density (left, center), only (hyper)methylated DNA binding takes place. At high MBD2 density (left, bottom), binding of both (hyper)methylated DNA and non-methylated DNA is taking place. On the right, a DNA binding profile is displayed for (hyper)methylated DNA (red line) and non-methylated (black line) surface coverage at increasing MBD surface receptor density.

2.5. Conclusion and Perspectives

In summary, we have presented arguments that the limited selectivity of current hmDNA enrichment methods based on affinity chromatography can be improved by applying the principles of multivalency and superselectivity. Nowadays hmDNA enrichment methods predominantly use surface-bound MBD2 in which the MBD2 protein functions as a receptor. The limitation of MBD2 is that it possesses a decently,

but not exhaustively, higher (63- to 108-fold) binding affinity for C*pG compared to CpG, while similar binding affinities are observed for MeCP2 and MBD1 of the MBD protein family. Because of these relatively small differences in binding affinities, the hmDNA enrichment selectivities are limited. Reduced enrichment selectivities are especially profound upon the enrichment of DNA mixtures when the hmDNA concentration is (much) lower than that of non-methylated DNA. Liquid biopsies also contain hmDNA and non-methylated DNA, therefore, explaining the limited use of hmDNA enrichment in the clinics nowadays.

The here proposed method for increasing the selectivity of hmDNA enrichment employs the MBD surface receptor density as a control parameter, and it is affected by several crucial parameters. First, the density affects both the multivalency enhancement factor and the intrinsic selectivities of the receptors toward a C*pG and CpG. A high hmDNA selectivity will be favored by a low multivalency enhancement factor and a high intrinsic selectivity of the receptors. It should be determined which of the MBDs MeCP2, MBD1, and or MBD2 can fulfill the first parameter the best. Second, the number of CpGs within a sequence and its degree of methylation play an important role. To illustrate, the number of C*pGs in a DNA fragment can be as high as 1 C*pG per 10 base pairs, but this is sequence dependent.[17] Increasing CpG methylation results into a higher K_{av} with the MBD-modified surface. Therefore, lower MBD surface receptor densities can be used at higher degrees of CpG methylation. Future work should clarify what the role of increasing CpG methylation is on the binding at various MBD surface receptor densities. Third is the role of the DNA length in the enrichment of hmDNA. The effect of the DNA length is an important aspect of study, since various lengths of DNA are present in liquid biopsies. For example, the main DNA fragment sizes in blood and urine are ≈160 bp and ≈90 bp, respectively.[81,82] The longer the DNA, the more MBD-DNA interaction pairs can be formed, thus increasing K_{av}. It will be crucial to understand what the difference in the MBD surface receptor density will be for surface binding of, for example, 100 bp-long hmDNA compared to 200 bp-long non-methylated DNA. Furthermore, it should be investigated whether hmDNA can be enriched efficiently from a DNA sample. Likely this is especially important to enable hmDNA-based, early-stage cancer diagnostics where the hmDNA concentrations are typically very low (few copies per mL of sample). Overall, this study indicates that the enrichment of hmDNA can be improved significantly by optimizing the MBD surface receptor densities according to the principles of multivalency and superselectivity. The development of the superselective hmDNA enrichment system will be of interest for the clinics after the integration of the proposed method in a lab-on-a-chip device, ensuring fast and simplistic usage.

2.6 Acknowledgements

Nienke van Dongen is acknowledged for help with the schematic illustrations.

2.7 References

(1) Sung, H.; Ferlay, J.; Siegel, R. L.; Laversanne, M.; Soerjomataram, I.; Jemal, A.; Bray, F. Global Cancer Statistics 2020: GLOBOCAN Estimates of Incidence and Mortality Worldwide for 36 Cancers in 185 Countries. *CA. Cancer J. Clin.* **2021**, *71*, 209–249.

(2) Arnold, M.; Rutherford, M. J.; Bardot, A.; Ferlay, J.; Andersson, T. M. L.; Myklebust, T. Å.; Tervonen, H.; Thursfield, V.; Ransom, D.; Shack, L.; Woods, R. R.; Turner, D.; Leonfellner, S.; Ryan, S.; Saint-Jacques, N.; De, P.; McClure, C.; Ramanakumar, A. V.; Stuart-Panko, H.; Engholm, G.; Walsh, P. M.; Jackson, C.; Vernon, S.; Morgan, E.; Gavin, A.; Morrison, D. S.; Huws, D. W.; Porter, G.; Butler, J.; Bryant, H.; Currow, D. C.; Hiom, S.; Parkin, D. M.; Sasieni, P.; Lambert, P. C.; Møller, B.; Soerjomataram, I.; Bray, F. Progress in Cancer Survival, Mortality, and Incidence in Seven High-Income Countries 1995–2014 (ICBP SURVMARK-2): A Population-Based Study. *Lancet Oncol.* **2019**, *20*, 1493–1505.

(3) Siegel, R. L.; Miller, K. D.; Jemal, A. Cancer Statistics, 2020. *CA. Cancer J. Clin.* **2020**, *70*, 7–30.

(4) Crosby, D.; Lyons, N.; Greenwood, E.; Harrison, S.; Hiom, S.; Moffat, J.; Quallo, T.; Samuel, E.; Walker, I. A Roadmap for the Early Detection and Diagnosis of Cancer. *Lancet Oncol.* **2020**, *21*, 1397–1399.

(5) Hanna, T. P.; King, W. D.; Thibodeau, S.; Jalink, M.; Paulin, G. A.; Harvey-Jones, E.; O'Sullivan, D. E.; Booth, C. M.; Sullivan, R.; Aggarwal, A. Mortality Due to Cancer Treatment Delay: Systematic Review and Meta-Analysis. *BMJ* **2020**, *371*, m4087.

(6) Ignatiadis, M.; Sledge, G. W.; Jeffrey, S. S. Liquid Biopsy Enters the Clinic — Implementation Issues and Future Challenges. *Nat. Rev. Clin. Oncol.* **2021**, *18*, 297–312.

(7) Liu, B.; Ricarte Filho, J.; Mallisetty, A.; Villani, C.; Kottorou, A.; Rodgers, K.; Chen, C.; Ito, T.; Holmes, K.; Gastala, N.; Valyi-Nagy, K.; David, O.; Gaba, R. C.; Ascoli, C.; Pasquinelli, M.; Feldman, L. E.; Massad, M. G.; Wang, T.-H.; Jusue-Torres, I.; Benedetti, E.; Winn, R. A.; Brock, M. V.; Herman, J. G.; Hulbert, A. Detection of Promoter DNA Methylation in Urine and Plasma Aids the Detection of Non–Small Cell Lung Cancer. *Clin. Cancer Res.* **2020**, *26*, 4339–4348.

(8) De Rubis, G.; Rajeev Krishnan, S.; Bebawy, M. Liquid Biopsies in Cancer Diagnosis, Monitoring, and Prognosis. *Trends Pharmacol. Sci.* **2019**, *40*, 172–186.

(9) Feinberg, A. P.; Tycko, B. The History of Cancer Epigenetics. *Nat. Rev. Cancer* **2004**, *4*, 143–153.

(10) Van den Helder, R.; Wever, B. M. M.; Van Trommel, N. E.; Van Splunter, A. P.; Mom, C. H.; Kasius, J. C.; Bleeker, M. C. G.; Steenbergen, R. D. M. Non-Invasive Detection of Endometrial Cancer by DNA Methylation Analysis in Urine. *Clin. Epigenetics* **2020**, *12*, 165.

(11) Yokoi, K.; Yamashita, K.; Watanabe, M. Analysis of DNA Methylation Status in Bodily Fluids for Early Detection of Cancer. *Int. J. Mol. Sci.* **2017**, *18*, 735.

(12) Vrba, L.; Futscher, B. W. A Suite of DNA Methylation Markers That Can Detect Most Common Human Cancers. *Epigenetics* **2018**, *13*, 61–72.

(13) Zhang, J.; Yang, C.; Wu, C.; Cui, W.; Wang, L. DNA Methyltransferases in Cancer: Biology, Paradox, Aberrations, and Targeted Therapy. *Cancers (Basel)* **2020**, *12*, 2123.

(14) Herman, J. G.; Baylin, S. B. Gene Silencing in Cancer in Association with Promoter Hypermethylation. *N. Engl. J. Med.* **2003**, *349*, 2042–2054.

(15) Chen, X.; Zhang, J.; Ruan, W.; Huang, M.; Wang, C.; Wang, H.; Jiang, Z.; Wang, S.; Liu, Z.; Liu, C.; Tan, W.; Yang, J.; Chen, J.; Chen, Z.; Li, X.; Zhang, X.; Xu, P.; Chen, L.; Xie, R.; Zhou, Q.; Xu, S.; Irwin, D. L.; Fan, J. B.; Huang, J.; Lin, T. Urine DNA Methylation Assay Enables Early Detection and Recurrence Monitoring for Bladder Cancer. *J. Clin. Invest.* **2020**, *130*, 6278–6289.

(16) Zeng, J.; Nagrajan, H. K.; Yi, S. V. Fundamental Diversity of Human CpG Islands at Multiple Biological Levels. *Epigenetics* **2014**, *9*, 483–491.

(17) Illingworth, R.; Kerr, A.; DeSousa, D.; Jørgensen, H.; Ellis, P.; Stalker, J.; Jackson, D.; Clee, C.; Plumb, R.; Rogers, J.; Humphray, S.; Cox, T.; Langford, C.; Bird, A. A Novel CpG Island Set Identifies Tissue-Specific Methylation at Developmental Gene Loci. *PLoS Biol.* **2008**, *6*, e22.

(18) Corcoran, R. B.; Chabner, B. A. Application of Cell-Free DNA Analysis to Cancer Treatment. *N. Engl. J. Med.* **2018**, *379*, 1754–1765.

(19) Thapa, K.; Liu, W.; Wang, R. Nucleic Acid-Based Electrochemical Biosensor: Recent Advances in Probe Immobilization and Signal Amplification Strategies. *Wiley Interdiscip. Rev. Nanomed. Nanobiotechnol.* **2022**, *14*, e1765.

(20) Kaminski, M. M.; Abudayyeh, O. O.; Gootenberg, J. S.; Zhang, F.; Collins, J. J. CRISPR-Based Diagnostics. *Nat. Biomed. Eng.* **2021**, *5*, 643–656.

(21) Becherer, L.; Borst, N.; Bakheit, M.; Frischmann, S.; Zengerle, R.; von Stetten, F. Loop-Mediated Isothermal Amplification (LAMP) – Review and Classification of Methods for Sequence-Specific Detection. *Anal. Methods* **2020**, *12*, 717–746.

(22) Carrascosa, L. G.; Sina, A. A. I.; Palanisamy, R.; Sepulveda, B.; Otte, M. A.; Rauf, S.; Shiddiky, M. J. A.; Trau, M. Molecular Inversion Probe-Based SPR Biosensing for Specific, Label-Free and Real-Time Detection of Regional DNA Methylation. *Chem. Commun.* **2014**, *50*, 3585–3588.

(23) Syedmoradi, L.; Esmaeili, F.; Norton, M. L. Towards DNA Methylation Detection Using Biosensors. *Analyst* **2016**, *141*, 5922–5943.

(24) Feng, Q.; Wang, M.; Qin, L.; Wang, P. Dual-Signal Readout of DNA Methylation Status Based on the Assembly of a Supersandwich Electrochemical Biosensor without Enzymatic Reaction. *ACS Sensors* **2019**, *4*, 2615–2622.

(25) Olkhov-Mitsel, E.; Bapat, B. Strategies for Discovery and Validation of Methylated and Hydroxymethylated DNA Biomarkers. *Cancer Med.* **2012**, *1*, 237–260.

(26) Bhattacharjee, R.; Moriam, S.; Umer, M.; Nguyen, N.-T.; Shiddiky, M. J. A. DNA Methylation Detection: Recent Developments in Bisulfite Free Electrochemical and Optical Approaches. *Analyst* **2018**, *143*, 4802–4818.

(27) Locke, W. J.; Guanzon, D.; Ma, C.; Liew, Y. J.; Duesing, K. R.; Fung, K. Y. C.; Ross, J. P. DNA

Methylation Cancer Biomarkers: Translation to the Clinic. *Front. Genet.* **2019**, *10*, 1150.

(28) Hofner, M.; Krainer, J.; Pabinger, S.; Pulverer, W.; Nöhammer, C.; Weinhäusel, A. Multiplex Analyses Using Methylation Sensitive Restriction Enzyme qPCR. In *Epigenetics Methods*; Tollefsbol, T., Ed.; Elsevier, 2020; pp 181–212.

(29) McClelland, M.; Nelson, M. The Effect of Site Specific Methylation on Restriction Endonuclease Digestion. *Nucleic Acids Res.* **1985**, *13*, r201–r207.

(30) Nell, R. J.; Van Steenderen, D.; Menger, N. V; Weitering, T. J.; Versluis, M.; Van Der Velden, P. A. Quantification of DNA Methylation Independent of Sodium Bisulfite Conversion Using Methylation-sensitive Restriction Enzymes and Digital PCR. *Hum. Mutat.* **2020**, *41*, 2205–2216.

(31) Kojima, K.; Takahashi, N.; Yada, Y.; Koike, Y.; Matano, M.; Kono, Y.; Momoi, M. Y. White-Matter Damage in a Neonate with Disseminated Herpes Simplex Virus Infection. *Pediatr. Int.* **2012**, *54*, 409–412.

(32) Brena, R. M.; Huang, T. H.-M.; Plass, C. Quantitative Assessment of DNA Methylation: Potential Applications for Disease Diagnosis, Classification, and Prognosis in Clinical Settings. *J. Mol. Med.* **2006**, *84*, 365–377.

(33) Weber, M.; Davies, J. J.; Wittig, D.; Oakeley, E. J.; Haase, M.; Lam, W. L.; Schübeler, D. Chromosome-Wide and Promoter-Specific Analyses Identify Sites of Differential DNA Methylation in Normal and Transformed Human Cells. *Nat. Genet.* **2005**, *37*, 853–862.

(34) Rauch, T.; Pfeifer, G. P. Methylated-CpG Island Recovery Assay: A New Technique for the Rapid Detection of Methylated-CpG Islands in Cancer. *Lab. Investig.* **2005**, *85*, 1172–1180.

(35) Cross, S. H.; Charlton, J. A.; Nan, X.; Bird, A. P. Purification of CpG Islands Using a Methylated DNA Binding Column. *Nat. Genet.* **1994**, *6*, 236–244.

(36) Pajares, M. J.; Palanca-Ballester, C.; Urtasun, R.; Alemany-Cosme, E.; Lahoz, A.; Sandoval, J. Methods for Analysis of Specific DNA Methylation Status. *Methods* **2021**, *187*, 3–12.

(37) Yegnasubramanian, S; Lin, X.; Haffner, M. C.; DeMarzo, A. M.; Nelson, W. G. Combination of Methylated-DNA Precipitation and Methylation-Sensitive Restriction Enzymes (COMPARE-MS) for the Rapid, Sensitive and Quantitative Detection of DNA Methylation. *Nucleic Acids Res.* **2006**, *34*, e19.

(38) Warton, K.; Lin, V.; Navin, T.; Armstrong, N. J.; Kaplan, W.; Ying, K.; Gloss, B.; Mangs, H.; Nair, S. S.; Hacker, N. F.; Sutherland, R. L.; Clark, S. J.; Samimi, G. Methylation-Capture and Next-Generation Sequencing of Free Circulating DNA from Human Plasma. *BMC Genomics* **2014**, *15*, 476.

(39) Woythe, L.; Tito, N. B.; Albertazzi, L. A Quantitative View on Multivalent Nanomedicine Targeting. *Adv. Drug Deliv. Rev.* **2021**, *169*, 1–21.

(40) Yeldell, S. B.; Seitz, O. Nucleic Acid Constructs for the Interrogation of Multivalent Protein Interactions. *Chem. Soc. Rev.* **2020**, *49*, 6848–6865.

(41) Böhmer, V. I.; Szymanski, W.; Feringa, B. L.; Elsinga, P. H. Multivalent Probes in

Molecular Imaging: Reality or Future? *Trends Mol. Med.* **2021**, *27*, 379–393.

(42) Makhani, E. Y.; Zhang, A.; Haun, J. B. Quantifying and Controlling Bond Multivalency for Advanced Nanoparticle Targeting to Cells. *Nano Converg.* **2021**, *8*, 38.

(43) *Multivalency: Concepts, Research and Applications*; Huskens, J., Prins, L., Haag, R., Ravoo, B. J., Eds.; Wiley, 2018.

(44) Martinez-Veracoechea, F. J.; Frenkel, D. Designing Super Selectivity in Multivalent Nano-Particle Binding. *Proc. Natl. Acad. Sci.* **2011**, *108*, 10963–10968.

(45) Rauch, T. A.; Pfeifer, G. P. DNA Methylation Profiling Using the Methylated-CpG Island Recovery Assay (MIRA). *Methods* **2010**, *52*, 213–217.

(46) Hashimoto, H.; Liu, Y.; Upadhyay, A. K.; Chang, Y.; Howerton, S. B.; Vertino, P. M.; Zhang, X.; Cheng, X. Recognition and Potential Mechanisms for Replication and Erasure of Cytosine Hydroxymethylation. *Nucleic Acids Res.* **2012**, *40*, 4841–4849.

(47) Fraga, M. F.; Ballestar, E.; Montoya, G.; Taysavang, P.; Wade, P. A.; Esteller, M. The Affinity of Different MBD Proteins for a Specific Methylated Locus Depends on Their Intrinsic Binding Properties. *Nucleic Acids Res.* **2003**, *31*, 1765–1774.

(48) Buchmuller, B. C.; Kosel, B.; Summerer, D. Complete Profiling of Methyl-CpG-Binding Domains for Combinations of Cytosine Modifications at CpG Dinucleotides Reveals Differential Read-out in Normal and Rett-Associated States. *Sci. Rep.* **2020**, *10*, 4053.

(49) Heimer, B. W.; Tam, B. E.; Sikes, H. D. Characterization and Directed Evolution of a Methyl-Binding Domain Protein for High-Sensitivity DNA Methylation Analysis. *Protein Eng. Des. Sel.* **2015**, *28*, 543–551.

(50) Yu, Y.; Blair, S.; Gillespie, D.; Jensen, R.; Myszka, D.; Badran, A. H.; Ghosh, I.; Chagovetz, A. Direct DNA Methylation Profiling Using Methyl Binding Domain Proteins. *Anal. Chem.* **2010**, *82*, 5012–5019.

(51) Liu, M.; Movahed, S.; Dangi, S.; Pan, H.; Kaur, P.; Bilinovich, S. M.; Faison, E. M.; Leighton, G. O.; Wang, H.; Williams, D. C.; Riehn, R. DNA Looping by Two 5-Methylcytosine-Binding Proteins Quantified Using Nanofluidic Devices. *Epigenetics Chromatin* **2020**, *13*, 18.

(52) Pan, H.; Bilinovich, S. M.; Kaur, P.; Riehn, R.; Wang, H.; Williams, D. C. CpG and Methylation-Dependent DNA Binding and Dynamics of the Methylcytosine Binding Domain 2 Protein at the Single-Molecule Level. *Nucleic Acids Res.* **2017**, *45*, 9164–9177.

(53) Wakefield, R. I. D.; Smith, B. O.; Nan, X.; Free, A.; Soteriou, A.; Uhrin, D.; Bird, A. P.; Barlow, P. N. The Solution Structure of the Domain from MeCP2 That Binds to Methylated DNA. *J. Mol. Biol.* **1999**, *291*, 1055–1065.

(54) Ohki, I.; Shimotake, N.; Fujita, N.; Jee, J.-G.; Ikegami, T.; Nakao, M.; Shirakawa, M. Solution Structure of the Methyl-CpG Binding Domain of Human MBD1 in Complex with Methylated DNA. *Cell* **2001**, *105*, 487–497.

(55) Scarsdale, J. N.; Webb, H. D.; Ginder, G. D.; Williams, D. C. Solution Structure and Dynamic Analysis of Chicken MBD2 Methyl Binding Domain Bound to a Target-Methylated DNA Sequence. *Nucleic Acids Res.* **2011**, *39*, 6741–6752.

(56) Liu, K.; Lei, M.; Wu, Z.; Gan, B.; Cheng, H.; Li, Y.; Min, J. Structural Analyses Reveal That MBD3 Is a Methylated CG Binder. *FEBS J.* **2019**, *286*, 3240–3254.

(57) Walavalkar, N. M.; Cramer, J. M.; Buchwald, W. A.; Scarsdale, J. N.; Williams, D. C. Solution Structure and Intramolecular Exchange of Methyl-Cytosine Binding Domain Protein 4 (MBD4) on DNA Suggests a Mechanism to Scan for MCpG/TpG Mismatches. *Nucleic Acids Res.* **2014**, *42*, 11218–11232.

(58) Zou, H.; Harrington, J.; Rego, R. L.; Ahlquist, D. A. A Novel Method to Capture Methylated Human DNA from Stool: Implications for Colorectal Cancer Screening. *Clin. Chem.* **2007**, *53*, 1646–1651.

(59) Duan, X.; Mu, L.; Sawtelle, S. D.; Rajan, N. K.; Han, Z.; Wang, Y.; Qu, H.; Reed, M. A. Functionalized Polyelectrolytes Assembling on Nano-BioFETs for Biosensing Applications. *Adv. Funct. Mater.* **2015**, *25*, 2279–2286.

(60) Lahiri, J.; Isaacs, L.; Tien, J.; Whitesides, G. M. A Strategy for the Generation of Surfaces Presenting Ligands for Studies of Binding Based on an Active Ester as a Common Reactive Intermediate: A Surface Plasmon Resonance Study. *Anal. Chem.* **1999**, *71*, 777–790.

(61) Ostuni, E.; Grzybowski, B. A.; Mrksich, M.; Roberts, C. S.; Whitesides, G. M. Adsorption of Proteins to Hydrophobic Sites on Mixed Self-Assembled Monolayers. *Langmuir* **2003**, *19*, 1861–1872.

(62) Di Iorio, D.; Huskens, J. Surface Modification with Control over Ligand Density for the Study of Multivalent Biological Systems. *ChemistryOpen* **2020**, *9*, 53–66.

(63) Zou, D.; Zhang, D.; Liu, S.; Zhao, B.; Wang, H. Interplay of Binding Stoichiometry and Recognition Specificity for the Interaction of MBD2b Protein and Methylated DNA Revealed by Affinity Capillary Electrophoresis Coupled with Laser-Induced Fluorescence Analysis. *Anal. Chem.* **2014**, *86*, 1775–1782.

(64) Moreland, B.; Oman, K.; Curfman, J.; Yan, P.; Bundschuh, R. Methyl-CpG/MBD2 Interaction Requires Minimum Separation and Exhibits Minimal Sequence Specificity. *Biophys. J.* **2016**, *111*, 2551–2561.

(65) Nair, S. S.; Coolen, M. W.; Stirzaker, C.; Song, J. Z.; Statham, A. L.; Strbenac, D.; Robinson, M. D.; Clark, S. J. Comparison of Methyl-DNA Immunoprecipitation (MeDIP) and Methyl-CpG Binding Domain (MBD) Protein Capture for Genome-Wide DNA Methylation Analysis Reveal CpG Sequence Coverage Bias. *Epigenetics* **2011**, *6*, 34–44.

(66) Wee, E. J. H.; Ngo, T. H.; Trau, M. Colorimetric Detection of Both Total Genomic and Loci-Specific DNA Methylation from Limited DNA Inputs. *Clin. Epigenetics* **2015**, *7*, 65.

(67) Mammen, M.; Choi, S.-K.; Whitesides, G. M. Polyvalent Interactions in Biological Systems: Implications for Design and Use of Multivalent Ligands and Inhibitors. *Angew. Chemie Int. Ed.* **1998**, *37*, 2754–2794.

(68) Morzy, D.; Bastings, M. Significance of Receptor Mobility in Multivalent Binding on Lipid Membranes. *Angew. Chemie Int. Ed.* **2022**, *61*, e202114167.

(69) Fasting, C.; Schalley, C. A.; Weber, M.; Seitz, O.; Hecht, S.; Koksch, B.; Dernedde, J.; Graf,

C.; Knapp, E.-W.; Haag, R. Multivalency as a Chemical Organization and Action Principle. *Angew. Chemie Int. Ed.* **2012**, *51*, 10472–10498.

(70) Yeung, S. Y.; Mucha, A.; Deshmukh, R.; Boutrus, M.; Arnebrant, T.; Sellergren, B. Reversible Self-Assembled Monolayers (RSAMs): Adaptable Surfaces for Enhanced Multivalent Interactions and Ultrasensitive Virus Detection. *ACS Cent. Sci.* **2017**, *3*, 1198–1207.

(71) Vukojicic, P.; Béhar, G.; Tawara, M. H.; Fernandez-Villamarin, M.; Pecorari, F.; Fernandez-Megia, E.; Mouratou, B. Multivalent Affidendrons with High Affinity and Specificity toward Staphylococcus Aureus as Versatile Tools for Modulating Multicellular Behaviors. *ACS Appl. Mater. Interfaces* **2019**, *11*, 21391–21398.

(72) Sigl, C.; Willner, E. M.; Engelen, W.; Kretzmann, J. A.; Sachenbacher, K.; Liedl, A.; Kolbe, F.; Wilsch, F.; Aghvami, S. A.; Protzer, U.; Hagan, M. F.; Fraden, S.; Dietz, H. Programmable Icosahedral Shell System for Virus Trapping. *Nat. Mater.* **2021**, *20*, 1281–1289.

(73) Mulder, A.; Huskens, J.; Reinhoudt, D. N. Multivalency in Supramolecular Chemistry and Nanofabrication. *Org. Biomol. Chem.* **2004**, *2*, 3409-3424.

(74) Gomez-Casado, A.; Dam, H. H.; Yilmaz, M. D.; Florea, D.; Jonkheijm, P.; Huskens, J. Probing Multivalent Interactions in a Synthetic Host-Guest Complex by Dynamic Force Spectroscopy. *J. Am. Chem. Soc.* **2011**, *133*, 10849–10857.

(75) Perl, A.; Gomez-Casado, A.; Thompson, D.; Dam, H. H.; Jonkheijm, P.; Reinhoudt, D. N.; Huskens, J. Gradient-Driven Motion of Multivalent Ligand Molecules along a Surface Functionalized with Multiple Receptors. *Nat. Chem.* **2011**, *3*, 317–322.

(76) Huskens, J.; Mulder, A.; Auletta, T.; Nijhuis, C. A.; Ludden, M. J. W.; Reinhoudt, D. N. A Model for Describing the Thermodynamics of Multivalent Host-Guest Interactions at Interfaces. *J. Am. Chem. Soc.* **2004**, *126*, 6784–6797.

(77) Wang, J.; Min, J.; Eghtesadi, S. A.; Kane, R. S.; Chilkoti, A. Quantitative Study of the Interaction of Multivalent Ligand-Modified Nanoparticles with Breast Cancer Cells with Tunable Receptor Density. *ACS Nano* **2020**, *14*, 372–383.

(78) Magdalena Estirado, E.; Aleman Garcia, M. A.; Schill, J.; Brunsveld, L. Multivalent Ultrasensitive Interfacing of Supramolecular 1D Nanoplatforms. *J. Am. Chem. Soc.* **2019**, *141*, 18030–18037.

(79) Tito, N. B.; Frenkel, D. Optimizing the Selectivity of Surface-Adsorbing Multivalent Polymers. *Macromolecules* **2014**, *47*, 7496–7509.

(80) Dubacheva, G. V; Curk, T.; Auzély-Velty, R.; Frenkel, D.; Richter, R. P. Designing Multivalent Probes for Tunable Superselective Targeting. *Proc. Natl. Acad. Sci.* **2015**, *112*, 5579–5584.

(81) Burnham, P.; Dadhania, D.; Heyang, M.; Chen, F.; Westblade, L. F.; Suthanthiran, M.; Lee, J. R.; De Vlaminck, I. Urinary Cell-Free DNA Is a Versatile Analyte for Monitoring Infections of the Urinary Tract. *Nat. Commun.* **2018**, *9*, 2412.

(82) Burnham, P.; Kim, M. S.; Agbor-Enoh, S.; Luikart, H.; Valantine, H. A.; Khush, K. K.; De

Vlaminck, I. Single-Stranded DNA Library Preparation Uncovers the Origin and Diversity of Ultrashort Cell-Free DNA in Plasma. *Sci. Rep.* **2016**, *6*, 27859.

Chapter 3

Density control over MBD2 receptor-coated surfaces provides superselective binding of hypermethylated DNA

Using the biomarker hypermethylated DNA (hmDNA) for cancer detection requires a pretreatment to isolate or concentrate hmDNA from non-methylated DNA. Affinity chromatography using a methyl binding domain-2 (MBD2) protein can be used, but the relatively low enrichment selectivity of MBD2 limits its clinical applicability. Here, we developed a superselective, multivalent, MBD2-coated platform to improve the selectivity of hmDNA enrichment. The multivalent platform employs control over the MBD2 surface receptor density, which is shown to strongly affect the binding of DNA with varying degrees of methylation, improving both the selectivity and the affinity of DNAs with higher numbers of methylation sites. Histidine-10-tagged MBD2 was immobilized on gold surfaces with receptor density control by tuning the amount of nickel nitrilotriacetic acid-functionalized thiols in a thiol-based self-assembled monolayer. The required MBD2 surface receptor densities for DNA surface binding decreases for DNA with higher degrees of methylation. Both higher degrees of superselectivity and surface coverages were observed upon DNA binding at increasing methylation levels. Adopting the findings of this study into hmDNA enrichment of clinical samples has the potential to become more selective and sensitive than current MBD2-based methods and, therefore, to improve cancer diagnostics.

R.W. Kolkman, S. Michel-Souzy, D. Wasserberg, L.I. Segerink, J. Huskens. *ACS Appl. Mater. Interfaces*, **2022**, *14*, 40579-40589.

3.1 Introduction

Cancer is accountable for 9.9 million deaths worldwide in 2020, and it is thus one of the deadliest diseases in the world.[1] To decrease the number of cancer-related deaths, early detection of the disease is essential, since this improves the success rate of treatment.[2,3] Nationwide screening programs facilitate nowadays the pre-symptomatic detection of, for example, colorectal cancer[4] and cervical cancer[5] by determination of blood in stool and the presence of human papillomavirus in a cervical scrape, respectively. A positive outcome in the colorectal screening requires in general a colonoscopy for disease confirmation. Therefore, both pre-symptomatic detection methods are invasive and remain uncomfortable for the patient. As an alternative, cancer can also be detected by the analysis of liquid biopsies for the presence of cancer-specific biomarkers.[6,7] Liquid biopsies are predominantly non-invasive, can handle tumor heterogeneity and can be used to monitor progression of the disease.[8–10] However, the identification of suitable biomarkers and sufficiently sensitive detection to measure them in liquid biopsies remains a challenge.

One of the cancer biomarkers found in liquid biopsy samples is hypermethylated DNA (hmDNA).[11,12] hmDNA is circulating tumor DNA that is epigenetically changed by methylation.[11,12] The methylation results in the covalent addition of a methyl group to a cytosine base that is followed by a guanine base in the 5'-3' direction; the so called CpG region.[13] Methylation of CpGs occurs to regulate gene transcription, which also takes place in healthy cells.[14] However, methylation of specific genes, such as tumor suppressor genes, can cause different types of cancer including lung and bladder cancer.[13,15–17]

The usage of hmDNA as a biomarker for cancer detection is currently limited, because it is difficult to distinguish hmDNA from non-methylated DNA.[18–23] Current methods include the use of methylation-sensitive restriction enzymes,[24–26] bisulfite conversion,[27,28] and affinity purification.[29–31] However, the methods can result in DNA degradation upon bisulfite conversion, incomplete digestion when using a restriction enzyme digest, and selectivity issues during affinity purification.[18,19] The advantage of affinity purification is that it only involves a molecular recognition binding step followed by an elution step, thus requiring short assay times. Affinity purification of hmDNA is generally used to enrich a solution with hmDNA using beads of which the surfaces are modified with the methyl binding domain-2 (MBD2) protein.[20,30,32,33] The MBD2 protein is used as a receptor that interacts with a methylated CpG (C*pG, ligand) with a dissociation constant of 3 – 66 nM.[34–40] Furthermore, MBD2 has been demonstrated to have one of the best intrinsic binding selectivities among the proteins present within the MBD protein family,[34–40] with dissociation constant values ranging between 188 – 6500 nM for non-methylated CpG (CpG).[34,35] Despite this intrinsic binding selectivity of MBD2 for C*pG, the co-enrichment of non-methylated DNA upon

the isolation of hmDNA remains one of the greatest limitations of MBD-based affinity methods.[18,20,21,41]

Here we propose a strategy to improve the separation selectivity using affinity purification on chip by applying the principles of multivalency and superselectivity.[42–46] Upon the interaction of DNA with an MBD2-modified surface, multiple MBD2-C(*)pG interaction pairs can be formed between a DNA target and the surface.[47,48] The formation of multiple interaction pairs results in an increase of the avidity, which is attributed to the multivalency effect.[42,49] Surface binding of methylated or non-methylated DNA on an MBD2-modified surface is, therefore, only taking place when the avidity is sufficient for surface binding. As a direct result of the multivalent nature, the binding becomes superselective,[43,50,51] which indicates a sigmoidal, stronger-than-linear dependence of the avidity with MBD2 surface density,[43] and promises a strongly enhanced selectivity of binding of methylated *versus* non-methylated DNA.[50] Furthermore, a hallmark of superselectivity is the occurrence of a so-called threshold receptor density in the binding profile, *i.e.*, the receptor density at which the coverage of the multivalent binder increases from low to high.[43]

Here, we show the development of a method that employs the superselective binding of methylated DNA to achieve hmDNA enrichment at an MBD2-coated surface. In this work we focus on the binding of (methylated) DNA at MBD2-modified surfaces. The importance of controlling the MBD2 surface receptor density with respect to its binding selectivity toward methylated and non-methylated DNA is assessed. We employ a mixed thiol self-assembled monolayer (SAM) on a gold surface to achieve this density control. The degree of DNA binding on the MBD2-modified surfaces is assessed using up to 90-base pair (bp)-long DNA sequences, with between 0 and 5 C*pGs per sequence. We study the superselectivity of the binding of DNA as a function of CpG methylation to such MBD2-coated surfaces. Furthermore, we compare the maximum surface coverages of methylated DNA and non-methylated DNA and at which MBD2 densities these are reached. With the developed platform we will demonstrate how the hmDNA isolation selectivity can be improved by optimization of the MBD2 surface receptor density.

3.2 Results and discussion

3.2.1 Concept of superselective hmDNA enrichment at a receptor density-controlled platform

We aim to develop a superselective hmDNA enrichment platform by tuning the MBD2 surface receptor density (Figure 3.1). Upon binding of a DNA sequence with a specific number of C(*)pGs at the MBD2-modified surface, the avidity increases at higher

degrees of DNA methylation, thereby decreasing the threshold receptor density required for efficient DNA surface binding (Figure 3.1A). The MBD2 threshold density is defined as the minimal MBD2 density required for significant DNA binding. If the MBD2 density is too low, the possible number of interaction pairs between MBD2 and C(*)pG of DNA that can be formed is limited. In this situation the avidity is insufficient for the surface binding of both types of DNA. Increasing the MBD2 density results in an increase of the number of MBD2-C(*)pG interaction pairs and as a result, the avidity increases. The avidity increases faster for methylated DNA compared to non-methylated DNA because of the higher intrinsic affinity of MBD2 for each individual C*pG compared to CpG.[34–40] When the MBD2 density is increased further, both methylated and non-methylated DNA can bind strongly. As a direct consequence, we expect there is an optimal density range, at medium MBD2 surface receptor densities at which the MBD2 density is only sufficient for binding methylated DNA, while non-methylated DNA remains unbound (Figure 3.1B). In conclusion, control over the MBD2 surface receptor density is crucial for superselective hmDNA enrichment. Additionally, the MBD2 density also controls the total affinity of any bound DNA, and this control is important to fine-tune the efficacy of the surface as a capture layer.

Control over the MBD2 surface receptor density is enabled by employing a mixed SAM on a gold-coated surface of two ethylene glycol-alkanethiols, one with a hydroxyl and the other with an azide end group (Figure 3.1C). The hydroxyl thiol is the major component and is used to create an anti-fouling surface,[52–54] while the minor component, the azide thiol, is used to enable MBD2 immobilization. A linker molecule, bearing a dibenzocyclooctyne (DBCO) moiety on the one end and a nitrilotriacetic acid (NTA) functional group on the other end, was reacted at the azide groups of the SAM by employing the catalyst-free click chemistry reaction between the DBCO and azide functional groups.[55] The NTA functional groups were subsequently complexed with Ni^{2+} ions to form NiNTA moieties. Finally, the MBD2 protein fused with a histidine-10 (His_{10}) tag at the N-terminus (His_{10}MBD2) was immobilized at the surface *via* the NiNTA complexes. An individual NiNTA moiety has the possibility to interact with two histidines with a K_d of 14 µM.[56] Therefore, the number of NiNTA moieties interacting with the His_{10} tag is maximally 5. The MBD2 surface receptor density was varied by tuning the stoichiometric ratio between the hydroxyl and azide-functionalized thiols in the SAM, leading to controlled variation of the density of NiNTA groups as well as that of the MBD2s binding to these groups.

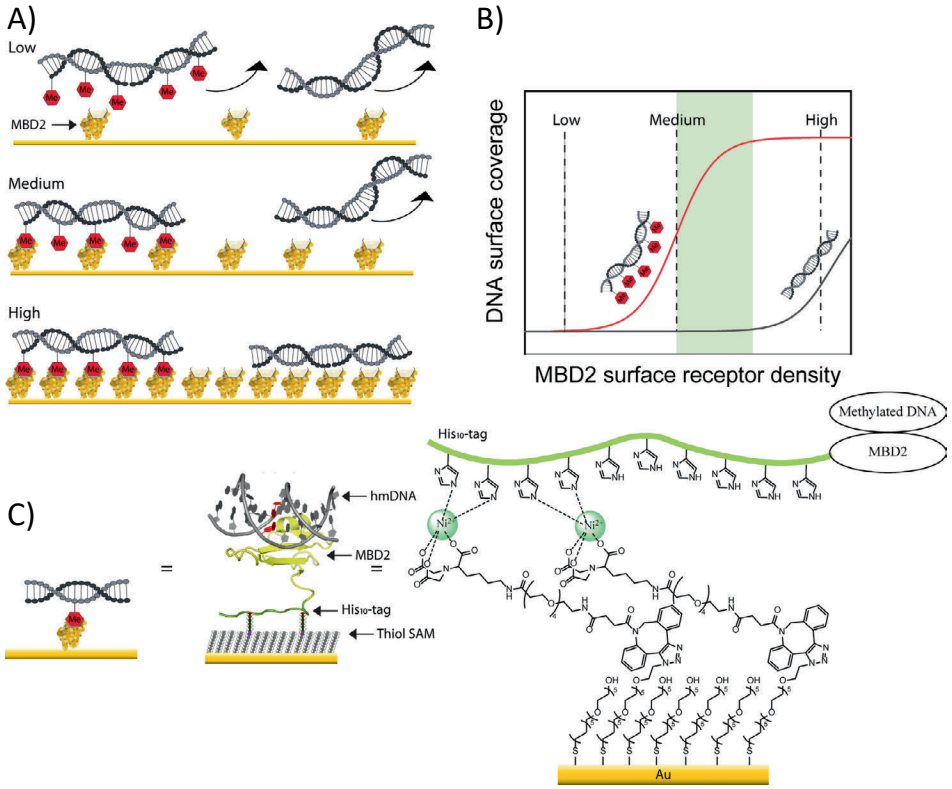

Figure 3.1. Design of a superselective surface coating for hmDNA enrichment. A) Schematic illustrations displaying the crucial role of the MBD2 surface receptor density for the superselective binding of methylated DNA at the surface. Low, medium, and high MBD2 surface receptor densities are illustrated and the subsequent degree of interaction with methylated DNA (DNA with red hexagons to represent C*pG) and non-methylated DNA. B) The DNA surface coverage on the MBD2-modified surface is displayed as a function of the MBD2 surface receptor density. The optimal MBD2 surface receptor density range to achieve optimal selectivity for enrichment of methylated DNA is indicated in green. C) Surface chemistry employed to control the degree of His_{10}MBD2 immobilization on a gold surface modified with a SAM of functionalized ethylene glycol-alkanethiols. Azide thiols are converted into NiNTA groups which interact with the His_{10} tag of MBD2. Each MBD2 protein interacts with an individual C(*)pG of the DNA. In the middle, the interaction between an immobilized His_{10}MBD2 protein (yellow) and a C*pG (red) in a DNA sequence (gray) is displayed, according to the MBD2 crystal structure.[57] On the right, the mixed ethylene glycol-alkanethiol-based SAM on a gold surface with azide and hydroxyl functional groups is shown. Azide-functionalized thiols are modified with a linker molecule bearing DBCO and NiNTA functional groups. The His_{10} tag of MBD2 is used to achieve immobilization of the protein on the surface.

3.2.2 Controlling the MBD2 surface receptor density

His_{10}MBD2 was produced using *E. coli* Rosetta (DE3) competent cells. The genetic information for the protein was based on the work of Bird *et al.* (Table S3.1).[58] The successful production and purification of His_{10}MBD2 were confirmed by sodium dodecyl sulfate-polyacrylamide gel electrophoresis (SDS-PAGE, Figure 3.2). The protein was isolated from lysed cells using NiNTA affinity column chromatography. The His_{10}MBD2 protein was eluted from the NiNTA column by employing an imidazole wash step. Thereafter, the His_{10}MBD2 protein was purified by size exclusion chromatography (SEC) and eluted in the immobilization buffer (IB). The final purity of the His_{10}MBD2 (molecular weight of ≈32 kDa) was confirmed by the presence of a single strong band at the expected molecular weight upon SDS-PAGE gel electrophoresis, thereby confirming the purity of the isolated His_{10}MBD2 sample.

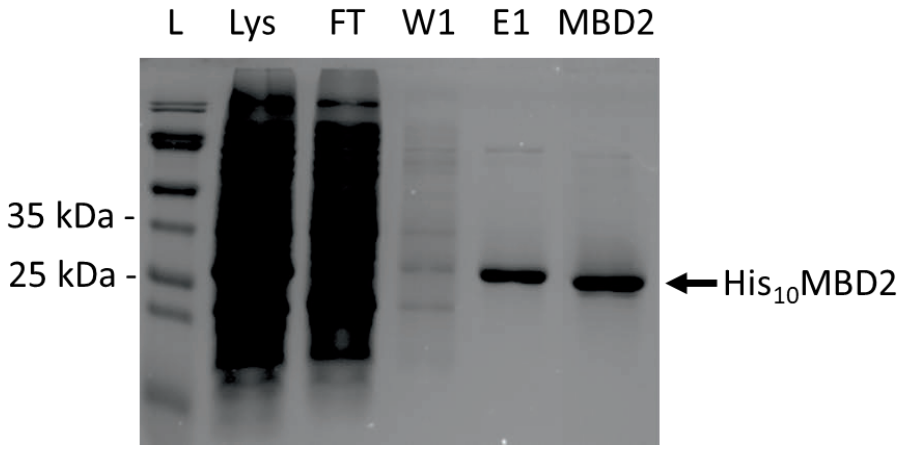

Figure 3.2. SDS-PAGE of the His_{10}MBD2 after isolation from *E. coli* Rosetta DE3 cells using NiNTA column chromatography and SEC. The gel was stained with Coomassie Blue prior to imaging. In the SDS-PAGE gel the ladder (L), cell lysate (Lys), flow through (FT), wash of the NiNTA column (W1), elution of the MBD2 with imidazole (E1), and the isolated His_{10}MBD2 after SEC (MBD2) are visible. The characteristic MBD2 band is visible at the expected molecular weight (≈32 kDa).

SAMs on gold substrates for quartz crystal microbalance (QCM) analysis were made by overnight immersion in mixtures of azide (minor) and hydroxyl-functionalized (major) ethylene glycol-alkanethiols in varying ratios. After mounting the sample inside a QCM chamber, all subsequent steps to bind MBD2 were monitored *in situ* by QCM (Figure 3.3). Figure 3.3A shows a typical example of MBD2 immobilization with 5% azide in the thiol mixture. After obtaining a stable baseline in buffer, a solution with the linker

molecule bearing the DBCO and NTA functional groups was flown over the SAM substrate. After 1.5 h a stable baseline was obtained, indicating completion of the reaction. Next, the NTA functional groups were complexed with Ni^{2+} by flushing a solution of $NiCl_2$ over the chip, followed by a washing step with water. Thereafter, the His_{10}MBD2 protein was immobilized on the surface. Upon the immobilization of MBD2, a typical binding curve was observed, with an initially rapid frequency decrease which leveled off quickly due to surface saturation. The total frequency shift (Δf) of irreversibly immobilized MBD2 is 13 Hz for 5% azide, which has been determined by comparing the baselines in IB prior to and after the addition of MBD2.

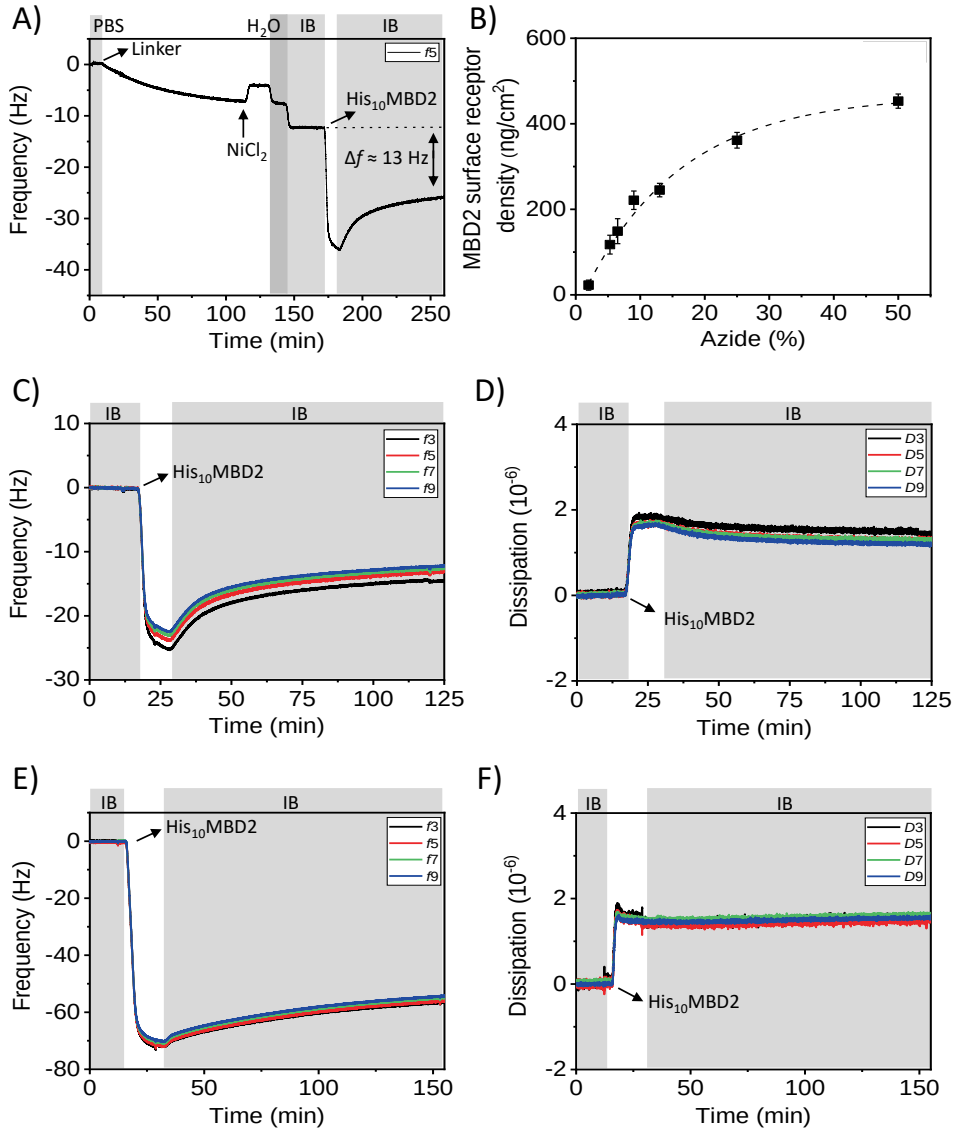

Figure 3.3. A) *In-situ* monitoring of the His_{10}MBD2 immobilization process by QCM. Prior to QCM measurement, a mixed SAM of hydroxyl and azide ethylene glycol-alkanethiols (95:5) was formed overnight. After obtaining a stable baseline, a solution with the DBCO-NTA linker molecule was flown over the SAM. Then, the NTA groups were complexed by $NiCl_2$, followed by the immobilization of His_{10}MBD2. Washing steps with PBS, Milli-Q (H_2O) and IB are indicated by the gray areas. B) MBD2 surface receptor density (determined after the 1.5 h washing step with IB) as a function of the percentage of azide-functionalized thiol in the underlying SAM determined with QCM. Δf_5 values of irreversibly immobilized MBD2 were converted to MBD2 surface receptor

densities using the Sauerbrey equation.[59] Each data point was obtained from at least two experiments. An exponential trendline was fitted to the data with $R^2 > 0.99$ to guide the eye. Error bars represent the standard deviation. C, E) Frequency and D, F) dissipation monitoring over time upon His_{10}MBD2 immobilization at overtones 3, 5, 7 and 9 using a SAM with C, D) 5% azide or E, F) 50% azide-functionalized thiols in the SAM.

The MBD2 surface receptor density is directly related to the percentage of azide in the underlying SAM (Figures 3.3B and S3.1-S3.7). We assume that the measured MBD2 frequency shifts are proportional to the MBD2 surface coverage. The QCM frequency shifts, Δf, of MBD2 at different azide fractions in the SAM then become a mass comparison measure according to the Sauerbrey equation.[59] This comparison seems valid as the trends for different overtones vary only marginally at both low and high MBD2 surface receptor densities, and the dissipation changes (ΔD) were $< 2 \times 10^{-6}$ (Figure 3.3C-F). The Δf of MBD2 can thus be used to express the MBD2 surface receptor density. Therefore, the Δf values are here converted to dry mass coverages (in ng/cm^2), assuming that 55% of the Δf values are due to hydration of the protein at the monolayer surface.[60] In comparison, a densely packed streptavidin layer typically shows a frequency shift of around 25 Hz.[61] Even though streptavidin and MBD2 have different molecular weights and their degrees of hydration (which affects QCM frequencies) may differ as well, we regard the here observed MBD2 frequency values ranging from 35 Hz (279 ng/cm^2) to 55 Hz (438 ng/cm^2) as indicative of dense packing because the frequency values level off in this range.

When using between 2% and 10% of azide in the SAM, the amount of irreversibly immobilized MBD2 increases linearly as a function of the amount of azide in the SAM. The coverage levels off above 10% azide in the SAM, and reaches a maximally packed MBD2 surface density at approximately 40% azide in the SAM. The relationship between the stoichiometric ratio of functional groups in the SAM and the degree of protein immobilization is in agreement with previously reported protein immobilization studies on thiol-based SAM systems.[62,63] Overall, we conclude that the MBD2 surface receptor density can be tuned by the stoichiometric ratio of hydroxyl and azide-functionalized ethylene glycol-alkanethiols in the SAM.

3.2.3 Binding methylated and non-methylated DNA to MBD2 surfaces

The binding response of DNA with varying degrees of CpG methylation on MBD2-modified surfaces was studied using a model DNA target sequence based on the *MAL* gene (Figure 3.4A).[64,65] In cancer cells, each of the 5 CpGs of the natural *MAL* gene is methylated.[64,65] The selected model DNA target is 40 or 90 bp long and contains up to

5 CpGs. To study the effect of different numbers of C(*)pG sites on binding to the MBD2 surfaces, we used the model DNA target with numbers of C(*)pGs ranging between 0 and 5 on the model DNA target. The DNA sequences used in this study are abbreviated as Mal*x*C(*)pG, where *x* represents the number of C(*)pGs in the model DNA target. The nucleotide sequences of the used model DNA targets can be found in Table S3.2. Varying the number of C(*)pG sites on the model DNA target was used, instead of using very different sequences, to minimize the effect of altering the binding kinetics upon the interaction of different DNA sequences with MBD2, as was reported by Fraga *et al*.[35] Mal2C(*)pG was used in two different versions: the C(*)pGs were located either close to or far away from each other with 22 or 66 bp separation between the C(*)pGs, respectively, and these were abbreviated as Mal2C(*)pG-far/close, respectively. For the Mal1C(*)pG, a length of only 40 bp was taken, but we assume this has little effect on the affinity since only monovalent binding is possible in this case. The location of the C(*)pGs in Mal4C(*)pG is slightly shifted compared to the other model DNA targets in order to evaluate the role of the C(*)pG location in a DNA sequence. For example, the second C(*)pG is located at the 32nd and 33rd nucleotide for Mal4C(*)pG and Mal5C(*)pG, respectively.

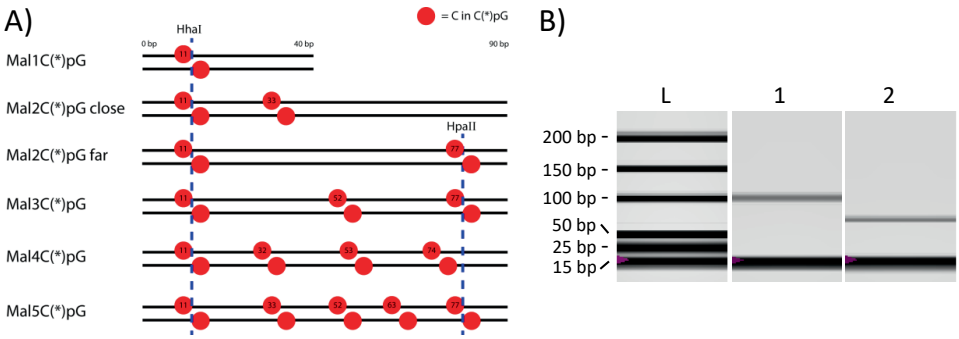

Figure 3.4. A) The model DNA targets, based on the Mal gene,[64,65] are 40 bp or 90 bp in length and consist of 1 (40 bp), 2, 3, 4, or 5 C(*)pGs (90 bp). Location of cytosines in C(*)pG is displayed here by the red circles with nucleotide numbers at the upper strand in the 5'-3' direction. The methylation-dependent restriction endonucleases HhaI and HpaII recognition sites are indicated by the blue dashed lines. B) Gel image generated by DNA electrophoresis of Mal3C(*)pG treated with HhaI and HpaII, showing the ladder (L) and HhaI and HpaII-digested Mal3C*pG (1) and Mal3CpG (2). The band at 15 bp in each lane is a marker.

The CpGs of all Mal*x*CpG constructs were methylated to C*pGs using the *M.SssI* enzyme in the presence of S-adenosylmethionine. As a typical example, successful methylation of the Mal3CpG sequence was confirmed by the blockage of digestion upon reacting the methylated sequence with the methylation-dependent restriction

endonucleases HhaI and HpaII, as was characterized by DNA electrophoresis (Figure 3.4A and B). HhaI and HpaII can digest DNA at their recognition sequences, 5'-GCGC-3' and 5'-CCGG-3', respectively, in the absence of CpG methylation. Both HhaI and HpaII have one recognition site on Mal3CpG, resulting in the reduction of the sequence length of 24 bp in the case of absence in CpG methylation. Electrophoresis showed retention of the full length for HhaI and HpaII-treated Mal3C*pG, while full digestion into the 66 bp product was observed for Mal3CpG. These results therefore confirm the successful methylation of the former sequence.

The binding of the model DNA targets at MBD2-modified surfaces with varying MBD2 surface receptor densities was monitored by QCM (Figure 3.5). A typical experiment is displayed in Figure 3.5A for the binding of Mal3C*pG and Mal5CpG at MBD2-coated surfaces with receptor densities corresponding to 98 ng/cm^{2}and 239 ng/cm^2, respectively (full adsorption processes are shown in Figures S3.12B and S3.8B). The negative control Mal5CpG was tested at a higher MBD2 density to promote its binding. Yet, no change in frequency was observed for Mal5CpG at the MBD2 surface, despite the higher receptor density and the higher number of CpG sites. This demonstrates the weak binding of non-methylated DNA at the MBD2 surface (at least up to MBD2 densities of 239 ng/cm^2) and confirms the anti-fouling properties of the MBD2-based capture layer. In contrast, during the first few minutes upon introducing the solution of Mal3C*pG, a sharp decrease of the frequency, signifying binding, was observed, followed by a rapid leveling off of the frequency change. Upon switching back to the binding buffer (BB), a significant part of the bound Mal3C*pG was washed away from the surface. The desorption of DNA can likely be attributed to a fraction of loosely bound DNA, while another fraction remained bound. We tentatively attribute this behavior to two distinct types of DNA binding occurring at the MBD2-modified surface: reversible and irreversible surface binding of DNA. The total amount of bound Mal3C*pG is reflected by the frequency shift after the binding step (Δf = 5.5 Hz), while the irreversibly bound Mal3C*pG is the amount of bound DNA determined after the washing step with BB (Δf = 1.5 Hz). We attribute the firmly bound fraction to DNA binding with a number of C*pG-MBD2 interactions that is large enough to achieve strong binding, while the weaker fraction uses a lower number of binding sites. Different numbers of interaction pairs can occur by local MBD2 density variations and/or a backfilling process. DNA binds first strongly with multiple interactions pairs to the mostly empty surface. Consequently, the number of free MBD2 sites lowers during the binding step, decreasing the possible number of interaction pairs that can be formed with newly arriving DNA that (back)fills the leftover spots on the surface, thus resulting in weaker DNA binding.

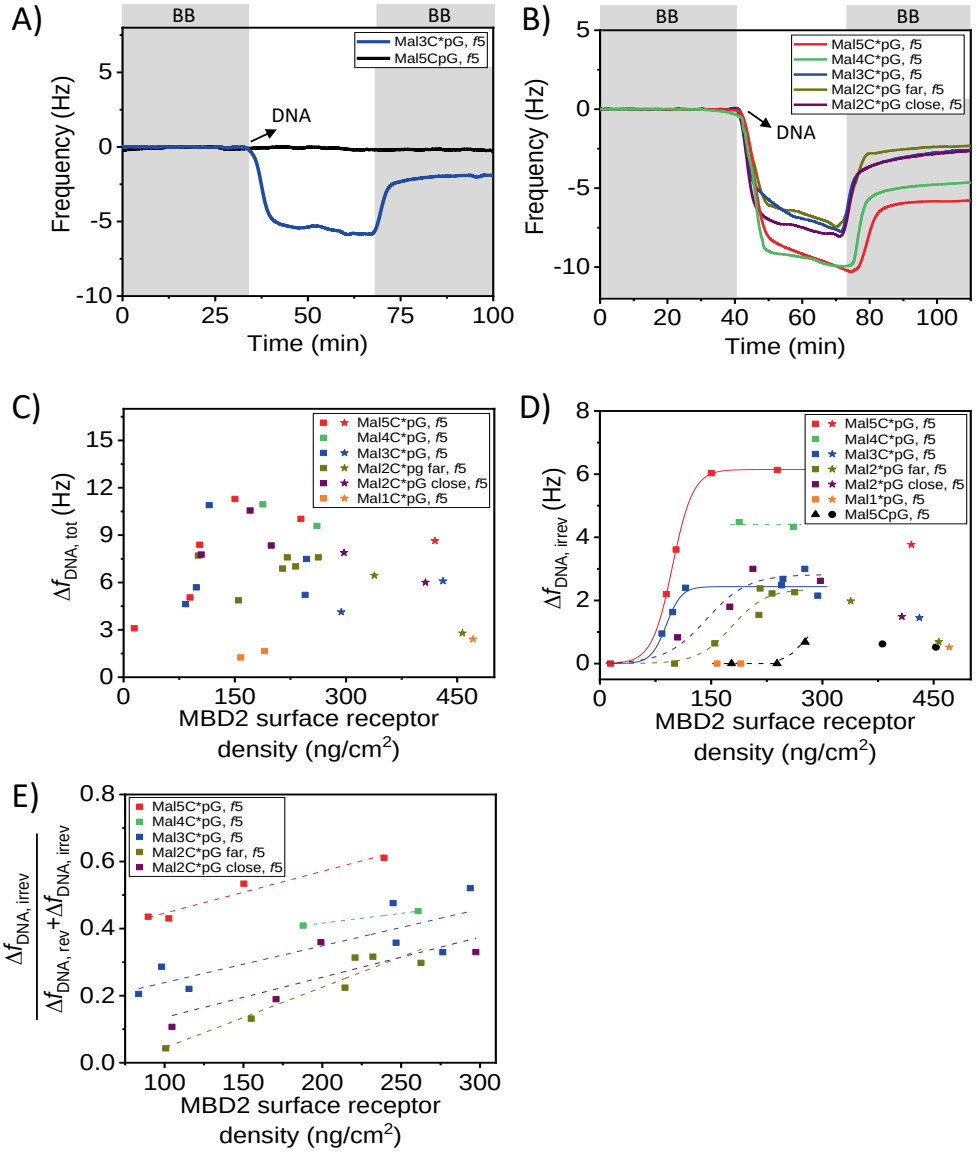

Figure 3.5. A) QCM time traces of the binding of 500 nM of Mal5CpG and of Mal3C*pG at MBD2-modified surfaces with receptor densities of 239 ng/cm^2 and 98 ng/cm^2, respectively. Washing steps with BB are indicated by the gray areas in the graph. B) DNA binding profiles of 500 nM Mal5C*pG (red), Mal4C*pG (green), Mal3C*pG (dark blue), and Mal2C*pG far (dark yellow) and close (purple) on MBD2-modified surfaces with a receptor density close to 263 ng/cm^2. Frequency changes for the C) total amount ($\Delta f_{DNA,\ tot}$) and D) irreversible fraction ($\Delta f_{DNA,\ irrev}$) of model DNA target with varying numbers of C(*)pG sites as a function of the MBD2 surface receptor density measured by QCM. The DNA concentration used was 500 nM for each DNA type. The numbers of

C*pGs per sequences are one (orange), two (dark yellow and purple, either far or close), three (dark blue), four (green), and five (red). DNA binding at MBD2 surface receptor densities of >300 ng/cm^2 and <300 ng/cm^2 (300 ng/cm^2 indicates dense protein packing, see text) is indicated by the star and square symbols for the various methylated DNA types, respectively. D) Mal5CpG lacking CpG methylation is indicated by the black colored triangles (Δf_{MBD2} <300 ng/cm^2) and spheres (Δf_{MBD2} >300 ng/cm^2). The data points of Mal5C*pG and Mal3C*pG were fitted by a logistic fit; dashed curves provide similar trends as guide to the eye. E) Irreversible fraction of DNA binding ($\Delta f_{DNA, irrev}/(\Delta f_{DNA, irrev} + \Delta f_{DNA, rev})$) as a function of the MBD2 surface receptor density given that $\Delta f_{DNA, rev} = \Delta f_{DNA, tot} - \Delta f_{DNA, irrev.}$ Linear trend lines were fitted through the data points as a guide to the eye.

The adsorption rate of DNA binding at the MBD2-modified surface was evaluated by comparing the DNA binding curves of Mal5C*pG, Mal4C*pG, Mal3C*pG, Mal2C*pG-close, and Mal2C*pG-far at an MBD2 surface receptor density of ≈263 ng/cm^2 as obtained from QCM experiments (Figure 3.5B). During the first minutes of DNA binding, the adsorption rates are comparable for the various types of DNA. This is expected as the mass transport rates of the various DNA types are identical due to the equal DNA lengths (90 bp). After the first minutes of DNA binding, the rate is reduced significantly for all DNA types. Full surface coverage has not been achieved during the 30 min DNA binding step as the DNA binding speed remains constant until switching to buffer. We take 30 min as a relevant time to start washing because we assume the binding sites are largely occupied, and the additionally binding DNA is mostly binding with a lower affinity and will be removed again during washing. Wash steps are continued until a stable plateau in frequency is reached, which signifies the retention of the irreversible DNA fraction.

The total amount of DNA binding as well as that of the irreversible fraction appeared to be dependent on the degree of DNA methylation and on the MBD2 surface receptor density (Figure 3.5C and D). MBD2 proteins were immobilized on SAM-modified surfaces at varying surface receptor densities followed by quantification of the DNA binding steps (Figures S3.8-S3.14). The degree of DNA binding was monitored for all the model DNA targets with 1 – 5 C*pGs and with 5 CpGs over the entire MBD2 surface receptor density range. The reversible fraction of DNA binding can be deduced by subtracting the irreversible frequency change from the total change; see Figure 3.5E.

As can be seen in both Figure 3.5C and D, the DNA surface coverage of Mal5C*pG, Mal3C*pG, and Mal2C*pG (close and far) decreases at high MBD2 surface receptor densities (roughly above 300 ng/cm^2). This decrease in DNA surface coverage is likely caused by steric hindrance between the MBD2 proteins at these high MBD2 densities. Steric hindrance is likely to result in a reduction of the accessible number of active sites

and, therefore, results in a decrease in avidity. Consequently, it cannot be concluded from the current data whether the maximum observed DNA surface coverage for Mal2C*pG (close and far), Mal1C*pG, and Mal5CpG is affected by steric hindrance between the MBD2 proteins and, therefore, has reached the upper plateau or not. We therefore restrict most of our analysis to MBD2 densities up to 300 ng/cm^2.

For the design of a selective DNA capture device, the irreversible fraction is the most relevant and may most accurately represent the fraction that binds with the highest possible valency as explained above. For Mal5C*pG and Mal3C*pG a clear sigmoidal trend was observed (Figure 3.5D) for the amount of (irreversible) DNA binding as a function of the MBD2 surface receptor density. At low MBD2 densities, the binding of both types of DNA is absent. The lack of binding is attributed to a too low avidity as the number of MBD2-C*pG interaction pairs that can be formed is limited. At increasing MBD2 surface receptor densities a sharp increase in the degree of binding is visible for both sequences. A further increase of the MBD2 surface receptor density results in reaching a maximum surface coverage of Mal5C*pG and Mal3C*pG. The increase of DNA binding from zero to the upper plateau takes place within a narrow range of MBD2 surface receptor densities. This observed DNA binding response is characteristic for superselective systems.[43,50,51] For both Mal5C*pG and Mal3C*pG, the threshold MBD2 densities correspond to ≈88 ng/cm^2. Though not tested as extensively, Mal4C*pG follows the same trend. At the threshold density observed for 3 and 5 C*pGs, no strong, irreversible DNA binding of the model DNA targets with two or fewer C*pGs per sequence occurs. All of these sequences require at least an MBD2 coverage of 159 ng/cm^2 before detectable DNA adsorption occurs. For Mal2C*pG-close and -far, the surface binding response is comparable, indicating minimal effect of the C*pG location on the binding efficiency of a sequence. However, the binding responses of both Mal2C*pG-close and far do differ notably from those of Mal5C*pG and Mal3C*pG. First, for both Mal2C*pG (close and far), the threshold MBD2 density increases to ≈159 ng/cm^2. Second, a lower degree of superselectivity (a less steep sigmoidal trend) is observed for both Mal2C*pG in comparison to Mal5C*pG and Mal3C*pG. Both the increase of the threshold MBD2 density and the lower degree of superselectivity are attributed to a reduction of the number of C*pGs per sequence, *i.e.*, the ligand valency, and the concomitantly lower avidities.[43] Furthermore, notable surface binding of Mal1C*pG and Mal5CpG requires MBD2 surface receptor densities >239 ng/cm^2, which is almost a 3-fold increase in the MBD2 surface receptor density compared to the MBD2 threshold for Mal5C*pG and Mal3C*pG. Overall, the MBD2 surface receptor density has been shown to control the superselective binding of methylated DNA and to tune the DNA surface binding according to its number of methylation sites.

Figure 3.5D also shows different upper plateau levels for DNAs with varying degrees of methylation. The frequencies of the upper plateau levels decrease according to valency from Mal5C*pG to Mal4C*pG to Mal3C*pG. The location of the C*pGs in the Mal4C*pG

sequence is different compared to the other types of DNA, but its binding follows the trend set by Mal5C*pG and Mal3C*pG. Therefore, we assume a minimal effect of the C*pG location on the DNA binding at MBD2-modified surfaces. The decreasing plateau trend can likely be attributed to a decrease in the overall affinity due to the decreasing number of interacting sites. On the other hand, the maximum total amounts of bound DNA at varying methylation levels are more comparable to each other below 300 ng/cm^2 of MBD2 (Figure 3.5C). We attribute this to the fact that the total bound DNA comprises both the reversible and irreversible DNA fractions and that more than one MBD2-C*pG interaction per DNA are already sufficient for significant transient DNA binding.

Despite the irreversible fraction being most relevant for our targeted application, analyzing trends by comparing the reversibly and irreversibly binding fractions is illustrative for studying the underlying binding mechanism. The ratio between the reversible and irreversible fractions of the total amounts of DNA that bind to the MBD2-modified surface (for MBD2 densities up to 300 ng/cm^2) is directly related to the degree of methylation of the DNA (Figure 3.5E). In all cases with two or more C*pGs, the fraction of irreversible binding increases with the MBD2 density. This behavior highlights the dependence on the receptor density, which is a hallmark of multivalent binding. The highest irreversible fractions are observed for Mal5C*pG, followed by Mal4C*pG, Mal3C*pG, and Mal2C*pG-close/far; for 1 C*pG and 5 CpGs, no binding was observed at these MBD2 densities. Thus, up to 61% of the total amount of bound Mal5C*pG binds irreversibly at the MBD2 platform. This trend is again attributed to the valency of the sequences and the resulting differences in avidity. It can be expected that the irreversible DNA fraction increases even to higher values upon the binding of DNA with higher methylation levels.

3.3 Conclusions and outlook

In this study we have demonstrated the development of a superselective multivalent platform that binds methylated DNA and employs the MBD2 surface receptor density as a way to control selectivity and affinity. The MBD2 surface receptor density was controlled by employing a thiol-based SAM and tuning the stoichiometric ratio between hydroxyl and azide-functionalized thiols in the SAM. The degree of (non-)methylated DNA binding was dependent on the MBD2 surface receptor density and the methylation status of the DNA. DNA containing 3 - 5 C*pGs per 90 base pairs displayed superselective binding behavior toward MBD2-modified surfaces. The degree of superselectivity was lower for sequences with fewer methylation sites. The degree of irreversible DNA binding to the MBD2 surface increases at higher degrees of DNA methylation and at higher MBD2 densities, showing the strength of the

multivalent control over the capture yield of the surface. Therefore, controlling MBD2 surface receptor density is essential for the superselective enrichment of methylated DNA.

Future work could assess the effects of DNA length and of the degree of methylation upon interaction with MBD2-modified surfaces. For example, the main fragment sizes of DNA isolated from blood and urine samples are approximately 160 bp and 90 bp, respectively.[66,67] Both a higher degree of methylation and a larger DNA fragment size can be expected to result in a higher avidity to an MBD2-coated surface as more C(*)pG-MBD2 interaction pairs can be formed. Likely, this affects the required MBD2 surface receptor density for (non-)methylated DNA surface binding. In addition, the effect of different DNA sequences upon hmDNA enrichment should be investigated, as Fraga *et al*. have shown that different binding kinetics occurs for various DNA sequences in their interaction with MBD2,[35] thus also affecting the avidity of (non-)methylated DNA toward MBD2 surfaces. Next, the developed superselective hmDNA binding platform should be tested with DNA isolated from cancer cell lines and human body fluids and improvements compared to currently applied methods should be assessed. Finally, the ability to elute surface bound DNA using a 2 M NaCl solution[68] should be evaluated to for instance sequence hmDNA enriched DNA samples for cancer diagnostics.

3.4 Acknowledgment

Dorothee Wasserberg and Sandra Michel-Souzy are thanked for the MBD2 production and purification and the fruitful discussions. Nienke van Dongen is acknowledged for help with the schematic illustrations.

3.5 Experimental section

3.5.1 Materials

30% Acrylamide/Bis solution 37.5:1, gravity flow columns, Experion DNA chips, Experion™ DNA 1K Reagents and Supplies as well as 4x Laemmli Sample Buffer were obtained from BioRad. Coomassie brilliant blue (Coomassie blue), NaCl, β-mercaptoethanol, dimethyl sulfoxide ≥99.7% (DMSO), EDTA, $MgCl_2$ ≥ 98.0% ($MgCl_2$), LB Broth, lysozyme from chicken egg white (≥90% lysozyme), phenylmethanesulfonyl fluoride (PMSF), ribonuclease A from bovine pancreas (RNase), deoxyribonuclease I from bovine pancreas (DNase), kanamycin sulfate from *Streptomyces kanamyceticus*, nickel(II) chloride hexahydrate ($NiCl_2$), N_α,N_α-bis(carboxymethyl)-L-lysine hydrate ≥ 97.0%, phosphate-buffered saline (PBS) tablets for 10 mM solution, H_2SO_4 95-97%, 0.2 µm membrane filter and sodium dodecyl sulfate ≥ 99% (SDS) were purchased from

Sigma Aldrich. Tris(hydroxymethyl)aminomethane (TRIS), isopropyl-β-D-thiogalactopyranoside ≥ 99% (IPTG), H_2O_2 33 % and ethanol absolute were bought from VWR. Imidazole 99% and Triton X-100 were obtained from ACROS Organics. Ni-NTA-agarose beads were purchased from Protino®. PD-10 Sephadex™ desalting columns were obtained from GE Health. DBCO-PEG_4-NHS ester was purchased from Click Chemistry Tools. All the DNA sequences were bought from Eurofins Genomics. Nuclease-free water, CpG methyltransferase (M.SssI), 1X NEBuffer™ 2, S-adenosylmethionine, Cutsmart buffer, HhaI, HpaII and high fidelity polymerase Q5 were purchased from New England Biolabs. $HSC_{11}(EG)_5$-OH and $HSC_{11}(EG)_5$-N_3 were bought from Prochimia. QCM gold-coated chips (QS-QSX301) were obtained from Quantum Design GmbH.

3.5.2 Methods

Cloning and transformation

The used bacterial strains and plasmids are displayed in Table 3.1 and 3.2 all the required molecular reagents to enable cloning and transformation were obtained from New England Biolabs. The His_{10}MBD2 gene was cloned in a pET-15b vector by Eurofins genomics. The His_{10}MBD2 gene (Table S3.1) was amplified by PCR using the primers displayed in Table 3.3 and high fidelity polymerase Q5 and cloned into pRSFDuet vector (Novagen) using the SLIC method[69] between NdeI-KpnI (MCS2) restriction sites as described before. The amplified DNA obtained from PCR was purified using a Macherey Nagel PCR clean-up kit. Then *E. coli* NovaBlue competent cells were transformed with the SLIC product. Plasmids were isolated and purified using the Qiagen miniprep kit. The plasmids were sequenced by Eurofins Genomics to confirm the sequence. Competent cells of *E. coli* Rosetta strain were transformed with the plasmid.

Table 3.1. Bacterial strains used in this study.

***E. coli* strain**	**Genotype/Characteristics**	**Origin**
Rosetta(DE3)	*F-ompT hsdSB(rB- mB-) gal dcm (DE3) pRARE (CamR)*	Novagen
NovaBlue	*endA1 hsdR17 (rK12– mK12+) supE44 thi-1 recA1 gyrA96 relA1 lac F'[proA+B+ lacIqZΔM15::Tn10] (TetR)*	Novagen

Table 3.2. Plasmid type used in this study.

Plasmids	Genotype/Characteristics	Origin
pET-15b	ApR, pT7	Novagen
pRSFDuet	Km^R, 2 MCS, P_{T7}, Ori RSF 1030	Novagen
pRSFDuet His_{10}MBD2	pRSFDuet carrying MBD2 gene with His_{10}-tag at N-terminus cloned into MCS 2	This study

Table 3.3. Primer sequence used to amplify the His_{10}MBD2 gene by PCR.

Primer	5' → 3'	Characteristics
His_{10}MBD2 fwd	AGAAGGAGATATACATATGCACCATCACCATCATCA CCATCATCACCACGATTGTCCTGCGTTG	For NdeI site in pDuet MCS2
His_{10}MBD2 rev	ACCAGACTCGAGGGTACCTTAAGCTTCATCACCGCT	For KpnI site in pDuet MCS2

His_{10}MBD2 production and purification

The *E. coli* bacteria were grown up to an optical density (OD) at 600 nm of 0.5 at 37°C in LB medium with 30 µg/ml of Kanamycin. The culture was cooled until it reached 17°C, followed by the expression of the His_{10}MBD2 protein after induction with 1 mM IPTG for 15 h at 17°C while stirring at 210 rpm. The culture was centrifuged (Allegra™ 25R) at 5000 rpm for 15 min at 4 °C to sediment the bacteria. The bacteria were lysed with sonication in a lysis buffer of 50 mM Tris-HCl pH 7.2, 300 mM NaCl, 30 mM imidazole, 0.1% β-mercaptoethanol, 1 mM EDTA, 20 mM $MgCl_2$, 1 mM PMSF, 0,5 mg/mL lysozyme, 20 µg/mL DNase, 20 µg/mL RNase A. Sonication (Fisherbrand™ 120) was performed on ice twice for 30 s with a waiting step in between of 2 min. The sonicated samples were centrifuged at 3100 rpm for 15 min at 4 °C, and the supernatant was then centrifuged at 40000 rpm for 60 min at 4°C (WX Ultra 90, Thermo Scientific). The supernatant was loaded on a NiNTA column and incubated for 30 min while shaking at 4°C . The column was washed with 25 mL washing buffer (50 mM Tris pH 7.2, 300 mM NaCl, 30 mM imidazole, 0.1% β-mercaptoethanol). His_{10}MBD2 was removed from the NiNTA column with an elution buffer (50 mM Tris pH 7.2, 300 mM NaCl, 650 mM imidazole, 0.1% β-mercaptoethanol). Directly afterward, the His_{10}MBD2 sample was purified with a PD10 column and eluted in the IB buffer (50 mM TRIS pH 7.2, 300 mM NaCl, 0.1% β-mercaptoethanol). The His_{10}MBD2 sample was aliquoted, snap-frozen and stored at -80°C until further use.

SDS-Page gel electrophoresis

Protein fractions were mixed with 4x Laemmli Sample Buffer + 0.1% β-mercaptoethanol at a 1:4 ratio and analyzed on 15% polyacrylamide gels with gel electrophoresis (BioRad) in a running buffer of 25 mM Tris, 192 mM glycine and 0.1% SDS. The separated proteins were stained using Coomassie brilliant blue solution consisting of 10% acetic acid, 40% ethanol, 50% Milli-Q water and 2 g/L Coomassie R250. The stained gel was then unstained with a solution of 10% acetic acid, 40% ethanol and 50% Milli-Q water, followed by imaging using FluorChem M hardware (Proteinsimple).

DNA methylation

DNA methylation was performed by mixing 4 µg of DNA with 8 units of *M.SssI* enzyme, S-adenosylmethionine at a concentration of 600 µM and 2.5 µL of NEBuffer™ 2. The reaction volume was increased to 25 µL with nuclease free water. The reaction was performed at 37 °C for 15 h in a T100 thermocycler (BioRad).

Methyl-sensitive restriction enzyme digest

10 ng of DNA was mixed with 1 µL of Cutsmart buffer, 5 units of HhaI and 5 units of HpaII. The total reaction volume was increased to 10 µL using nuclease free water. Digestion was performed for 15 h at 37 °C using a T100 thermocycler (Biorad). Afterward the enzymes were deactivated by a heat treatment of 85 °C for 20 min.

DNA electrophoresis

DNA samples were analyzed using DNA Experion chips and Experion™ DNA 1K Reagents and Supplies according to the instructions of the manufacturer on an automated electrophoresis system (Experion™, BioRad).

Synthesis of linker molecule

DBCO-PEG$_4$-NHS was dissolved in DMSO at 250 mM, directly aliquoted and stored at -18 °C until further use. N_α,N_α-bis(carboxymethyl)-L-lysine hydrate was dissolved in PBS pH 7.4 at 1 mM before the start of the reaction. The dissolved DBCO-OEG$_4$-NHS was added to the N_α,N_α-bis(carboxymethyl)-L-lysine hydrate solution at a final concentration of 0.1 mM. The reaction components were stirred overnight at 180 rpm to ensure completion of reaction.

SAM formation

Gold-coated QCM chips were cleaned in a piranha solution (H_2SO_4:H_2O_2 in ratio 3:1) for 10 s followed by immersion of the chips in Milli-Q water. Afterward, the chips were rinsed extensively with ethanol, Milli-Q water and ethanol, followed by drying using N_2. The gold chips were then oxidized using UV-ozone (BioForce, Nanosciences) for 30

min. A thiol solution was prepared using $HSC_{11}(EG)_5$-OH and $HSC_{11}(EG)_6$-N_3 at the desired ratio between the two components in ethanol with a total thiol concentration of 2 mM. The oxidized gold chips were completely immersed in the thiol solution overnight to form the SAM. After the SAM formation the QCM chips were rinsed extensively with ethanol, Milli-Q water and ethanol and dried in a stream of N_2.

Quartz crystal microbalance (QCM)

Gold-coated QCM chips modified with the SAM were mounted in the QCM Analyzer equipped with 4 individually addressable flow cells (Biolin Scientific). A flow rate of 30 µL/min was set during the experiments with a peristaltic pump (Biolin Scientific). All solutions were filtered with a 0.2 µm filter prior to use. Frequency and dissipation values used in this study are normalized for the used overtone. After each QCM experiment the system was cleaned with a 15 min washing step with 1% SDS solution continued by Milli-Q water for 15 min. Frequency shift of surface immobilized MBD2 is converted to MBD2 surface receptor densities using the Sauerbrey equation while assuming that 55% of the mass is due to water binding and using a Sauerbrey constant of 17.7 ng/(cm^2·Hz).

DNA binding to MBD2 surfaces

After SAM formation on the gold-coated QCM chip, the linker molecule was flushed over the surface for 1.5 h at a concentration of 0.1 mM in PBS pH 7.4 followed by the addition of 25 mM $NiCl_2$ in Milli-Q water for 10 min and a washing step with Milli-Q for 5 min and, subsequently, IB until the slope was constant. The washing step with Milli-Q was used to prevent the reduction of $NiCl_2$ by β-mercaptoethanol present in the IB. His_{10}MBD2 dissolved in IB at a concentration of 1 µM was added until stabilization of the signal. After MBD2 immobilization, a washing step with IB for 1.5 h was applied followed by flushing with BB until a stable signal was achieved. BB contains 50 mM TRIS, 350 mM NaCl, and 0.1% Triton X-100. Then 500 nM DNA dissolved in BB was added for 30 min followed by a washing step with BB. The MBD2 surface receptor density and degree of DNA binding were determined using the normalized frequency of the 5^{th} overtone (f_5).

3.6 Supporting information

Table S3.1. Gene sequence of His_{10}MBD2 based on the MBD2 amino acid sequence with UniProtKB/Swiss-Prot ID: Q9UBB5.1.[58]

	5’ - 3’
His_{10}MBD2 gene	ATGCACCATCACCATCATCACCATCATCACCACGATTGTCCTGCGTTGCC GCCCGGATGGAAAAAAGAGGAAGTTATTCGTAAATCTGGTCTGAGTGC GGGCAAGTCAGATGTATATTATTTCTCCCCTTCGGGTAAAAAGTTCCGT AGTAAACCTCAACTCGCGCGCTACCTTGGCAATACAGTGGATCTCAGTT CTTTCGATTTTCGCACTGGAAAGATGATGCCATCAAAGCTGCAAAAAAA TAAACAGCGCCTACGCAACGACCCACTTAACCAAAATAAAGGCAAACCA GATTTAAATACAACCTTACCCATTCGTCAGACTGCGTCTATTTTTAAACA ACCGGTCACCAAAGTAACCAATCATCCGAGTAACAAAGTTAAATCCGAC CCGCAACGCATGAACGAGCAACCGCGGCAGTTATTTTGGGAGAAGCGC TTGCAGGGCCTGTCGGCGTCCGATGTCACCGAACAGATCATTAAGACCA TGGAGTTGCCGAAAGGCCTGCAGGGCGTTGGTCCGGGTAGCAACGAC GAGACCCTGCTGTCAGCCGTGGCATCCGCGCTGCACACCAGCAGCGCA CCGATTACGGGTCAGGTGTCGGCTGCCGTGGAAAAAAACCCGGCCGTT TGGCTGAACACGTCGCAGCCGCTGTGCAAAGCCTTTATCGTCACGGACG AAGATATCCGAAAACAGGAAGAACGTGTGCAGCAGGTGCGTAAAAAA CTGGAAGAAGCTCTGATGGCCGACATACTGAGCAGAGCAGCAGACACG GAAGAAATGGATATCGAAATGGATAGCGGTGATGAAGCTTAA

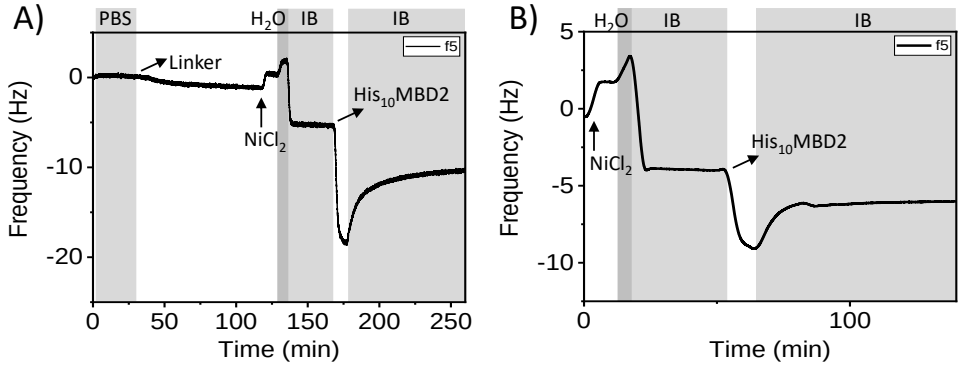

Figure S3.1. *In-situ* monitoring of the His_{10}MBD2 immobilization process by QCM. Prior to QCM measurement, a SAM with two ethylene glycol-alkanethiols was formed overnight with 2% azide functionalized thiols. The monitoring with QCM starts with reacting the DBCO-NTA linker molecule onto the SAM. The process is continued by activation of the NTA functional groups using $NiCl_2$ and the immobilization of His_{10}MBD2. The MBD2 surface receptor densities at the SAM containing 2% azide was: A) Δf = 3.9 Hz and B) Δf = 2.8 Hz. Washing steps with PBS, Milli-Q (H_2O) and IB are indicated by the grey areas.

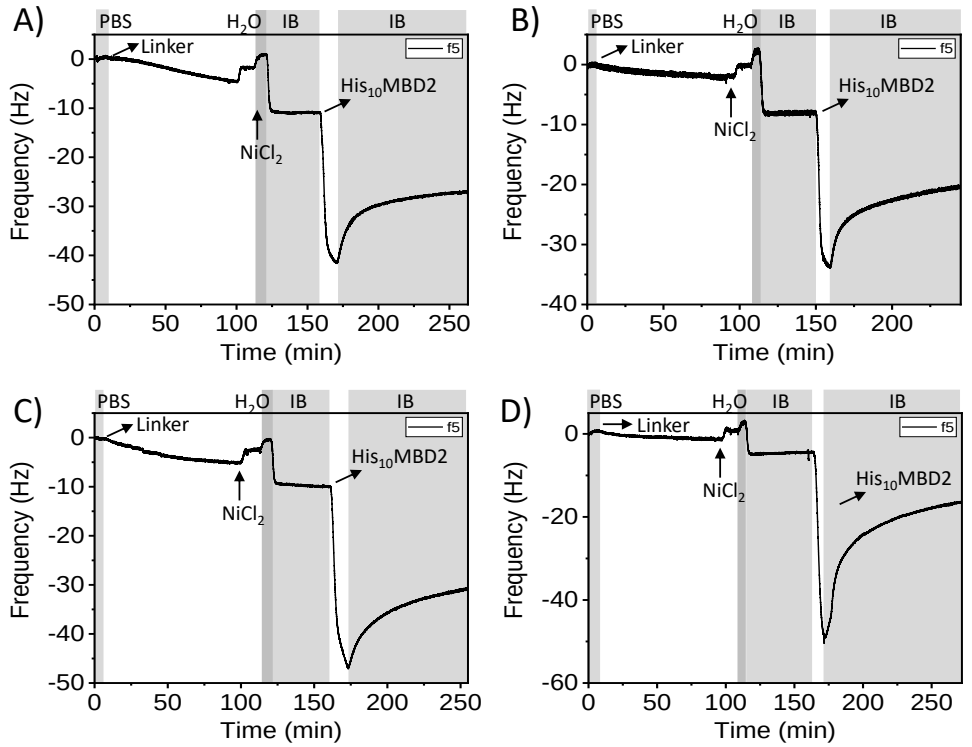

Figure S3.2. *In-situ* monitoring of the His_{10}MBD2 immobilization process by QCM. Prior to QCM measurement, a SAM with two ethylene glycol-alkanethiols was formed overnight with 5.3% azide functionalized thiols. The monitoring with QCM starts with reacting the DBCO-NTA linker molecule onto the SAM. The process is continued by activation of the NTA functional groups using $NiCl_2$ and the immobilization of His_{10}MBD2. The MBD2 surface receptor densities at the SAM containing 5.3% azide was: A) Δf = 16.0 Hz, B) Δf = 11.9 Hz, C) Δf = 17.99 Hz and D) Δf = 13.08 Hz. Washing steps with PBS, Milli-Q (H_2O) and IB are indicated by the grey areas.

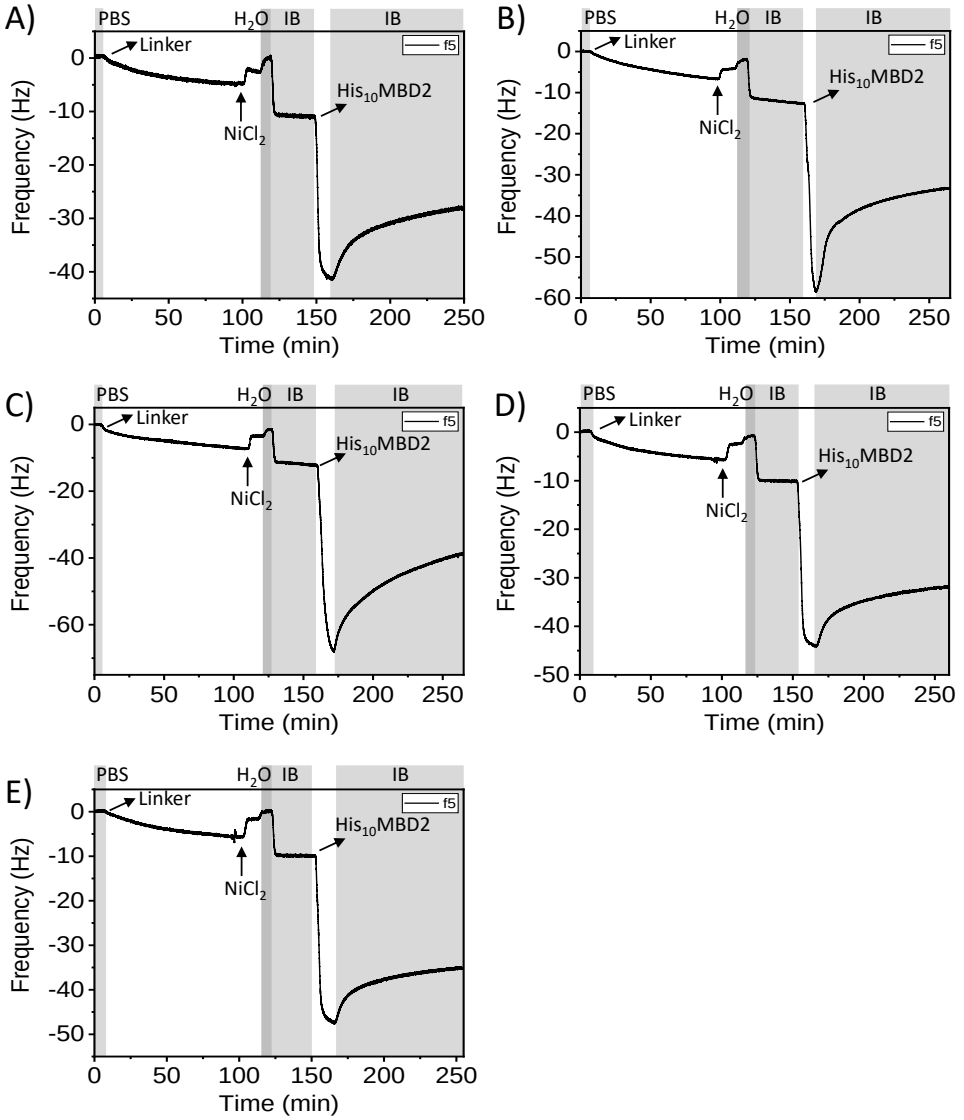

Figure S3.3. *In-situ* monitoring of the His_{10}MBD2 immobilization process by QCM. Prior to QCM measurement, a SAM with two ethylene glycol-alkanethiols was formed overnight with 6.5% azide functionalized thiols. The monitoring with QCM starts with reacting the DBCO-NTA linker molecule onto the SAM. The process is continued by activation of the NTA functional groups using $NiCl_2$ and the immobilization of His_{10}MBD2. The MBD2 surface receptor densities at the SAM containing 6.5% azide was: A) Δf = 14.4 Hz, B) Δf = 15.87 Hz, C) Δf = 20.5 Hz, D) Δf = 19.36 Hz and E) Δf = 23.58. Washing steps with PBS, Milli-Q (H_2O) and IB are indicated by the grey areas.

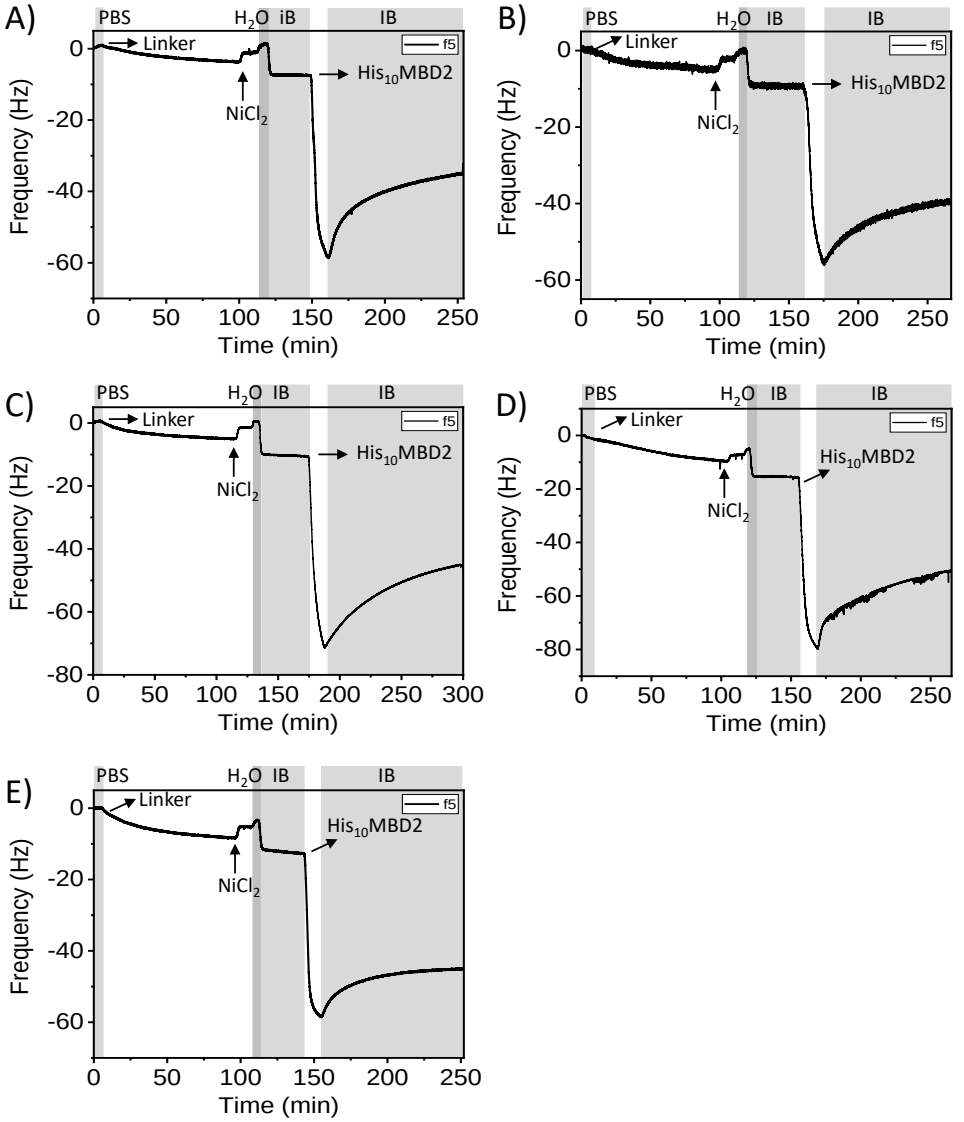

Figure S3.4. *In-situ* monitoring of the His_{10}MBD2 immobilization process by QCM. Prior to QCM measurement, a SAM with two ethylene glycol-alkanethiols was formed overnight with 9% azide functionalized thiols. The monitoring with QCM starts with reacting the DBCO-NTA linker molecule onto the SAM. The process is continued by activation of the NTA functional groups using $NiCl_2$ and the immobilization of His_{10}MBD2. The MBD2 surface receptor densities at the SAM containing 9% azide was: A) Δf = 23.72 Hz, B) Δf = 27.85 Hz, C) Δf = 30.98 Hz, D) Δf = 29.21 Hz and E) Δf = 27.12. Washing steps with PBS, Milli-Q (H_2O) and IB are indicated by the grey areas.

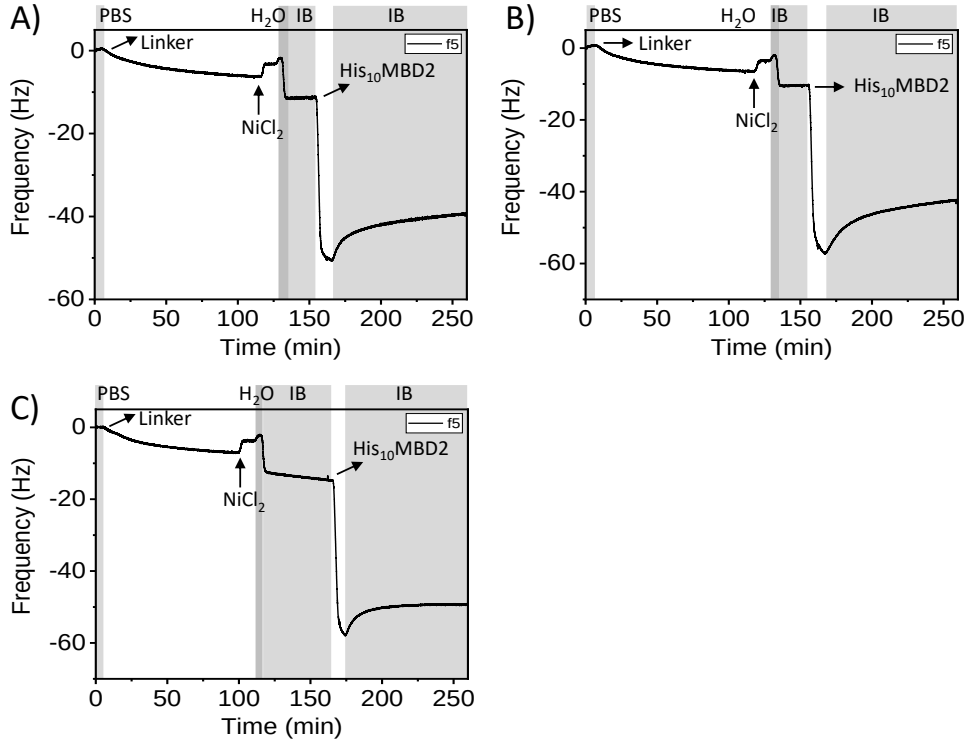

Figure S3.5. *In-situ* monitoring of the His_{10}MBD2 immobilization process by QCM. Prior to QCM measurement, a SAM with two ethylene glycol-alkanethiols was formed overnight with 13% azide functionalized thiols. The monitoring with QCM starts with reacting the DBCO-NTA linker molecule onto the SAM. The process is continued by activation of the NTA functional groups using $NiCl_2$ and the immobilization of His_{10}MBD2. The MBD2 surface receptor densities at the SAM containing 13% azide was: A) Δf = 29.14 Hz, B) Δf = 32.97 Hz, C) Δf = 30.15 Hz. Washing steps with PBS, Milli-Q (H_2O) and IB are indicated by the grey areas.

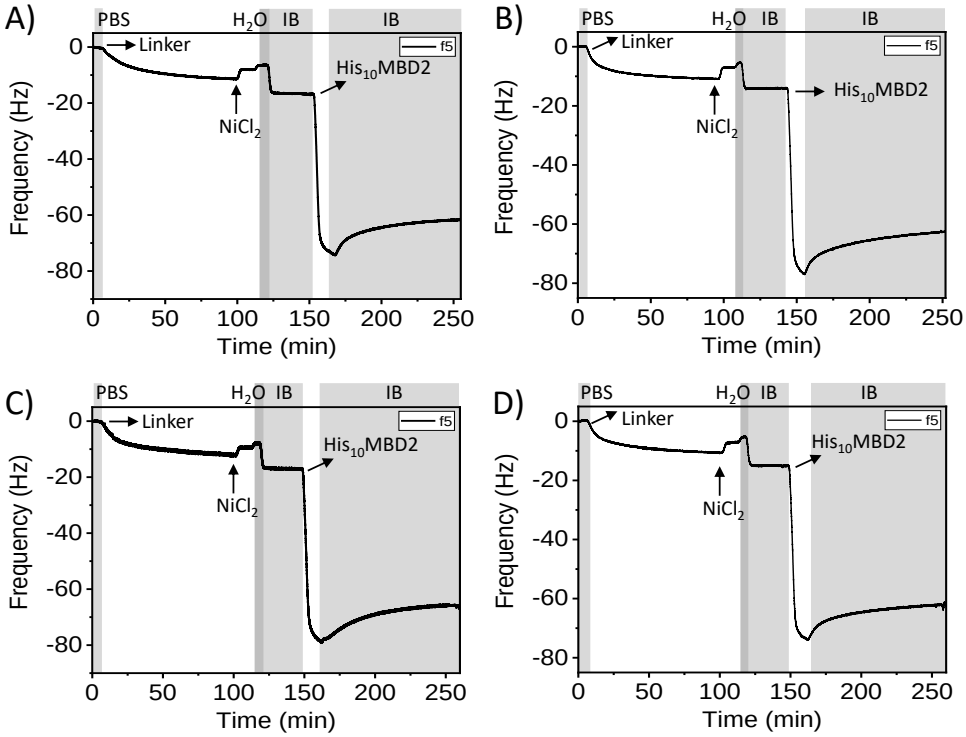

Figure S3.6. *In-situ* monitoring of the His_{10}MBD2 immobilization process by QCM. Prior to QCM measurement, a SAM with two ethylene glycol-alkanethiols was formed overnight with 25% azide functionalized thiols. The monitoring with QCM starts with reacting the DBCO-NTA linker molecule onto the SAM. The process is continued by activation of the NTA functional groups using $NiCl_2$ and the immobilization of His_{10}MBD2. The MBD2 surface receptor densities at the SAM containing 25% azide was: A) Δf = 42.47 Hz, B) Δf = 47.83 Hz, C) Δf = 46.44 Hz and D) Δf = 44.77 Hz. Washing steps with PBS, Milli-Q (H_2O) and IB are indicated by the grey areas.

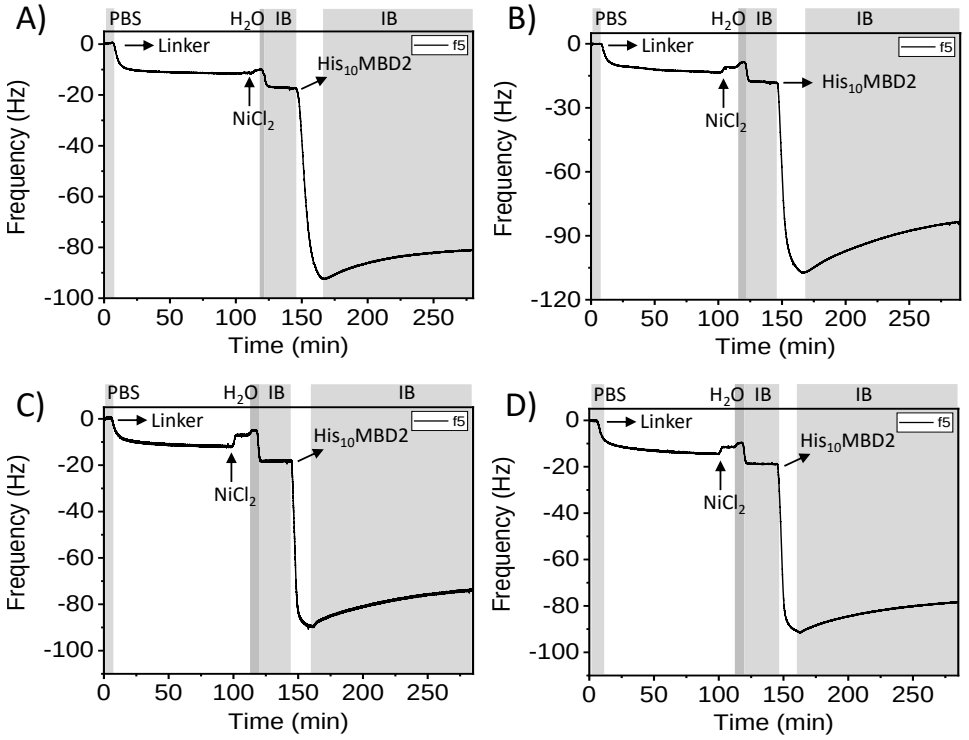

Figure S3.7. *In-situ* monitoring of the His_{10}MBD2 immobilization process by QCM. Prior to QCM measurement, a SAM with two ethylene glycol-alkanethiols was formed overnight with 50% azide functionalized thiols. The monitoring with QCM starts with reacting the DBCO-NTA linker molecule onto the SAM. The process is continued by activation of the NTA functional groups using $NiCl_2$ and the immobilization of His_{10}MBD2. The MBD2 surface receptor densities at the SAM containing 50% azide was: A) Δf = 59.14 Hz, B) Δf = 57.36 Hz, C) Δf = 54.09 Hz and D) Δf = 56.88 Hz. Washing steps with PBS, Milli-Q (H_2O) and IB are indicated by the grey areas.

Table S3.2. DNA sequences of the used model DNA targets in the 5’ – 3’direction. Location of the C(*)pGs are highlighted.

		5’ - 3’
Mal5C(*)pG	FWD	CAGGCAGATG**CG**CAGCACCAAGCAGAGAGGCC**CG**GTGCAGGA TCCCAGGCC**CG**AACCAGGCC**CG**GCTCAGTGGAGC**CG**GAAGGG GCAGGC
	REV	GCCTGCCCCTTC**CG**GCTCCACTGAGC**CG**GGCCTGGTT**CG**GGC CTGGGATCCTGCAC**CG**GGCCTCTCTGCTTGGTGCTG**CG**CATC TGCCTG
Ma4C(*)pG	FWD	CAGGCAGATG**CG**CAGCACCAAGCAGAGAGGC**CG**GGTGCAGGA TCCCAGGCCC**CG**ACCAGGCCAGGCTCAGTGG**CG**CTGGAAGGG GCAGGC
	REV	GCCTGCCCCTTCCAG**CG**CCACTGAGCCTGGCCTGGT**CG**GGGC CTGGGATCCTGCACC**CG**GCCTCTCTGCTTGGTGCTG**CG**CATC TGCCTG
Mal3C(*)pG	FWD	CAGGCAGATG**CG**CAGCACCAAGCAGAGAGGCCAGGTGCAGGA TCCCAGGCC**CG**AACCAGGCCTGGCTCAGTGGAGC**CG**GAAGGG GCAGGC
	REV	GCCTGCCCCTTC**CG**GCTCCACTGAGCCAGGCCTGGTT**CG**GGC CTGGGATCCTGCACCTGGCCTCTCTGCTTGGTGCTGCGCATC TGCCTG
Mal2C(*)pG far	FWD	CAGGCAGATG**CG**CAGCACCAAGCAGAGAGGCCAGGTGCAGGA TCCCAGGCCAGAACCAGGCCTGGCTCAGTGGAGC**CG**GAAGGG GCAGGC
	REV	GCCTGCCCCTTC**CG**GCTCCACTGAGCCAGGCCTGGTTCTGGC CTGGGATCCTGCACCTGGCCTCTCTGCTTGGTGCTG**CG**CATC TGCCTG
Mal2C(*)pG close	FWD	CAGGCAGATG**CG**CAGCACCAAGCAGAGAGGCC**CG**GTGCAGGA TCCCAGGCCAGAACCAGGCCTGGCTCAGTGGAGCAGGAAGGG GCAGGC
	REV	GCCTGCCCCTTCCTGCTCCACTGAGCCAGGCCTGGTTCTGGC CTGGGATCCTGCAC**CG**GGCCTCTCTGCTTGGTGCTG**CG**CATC TGCCTG
Mal1C(*)pG	FWD	CAGGCAGATG**CG**CAGCACCAAGCAGAGAGGCCAGGTGCAG
	REV	CTGCACCTGGCCTCTCTGCTTGGTGCTG**CG**CATCTGCCTG

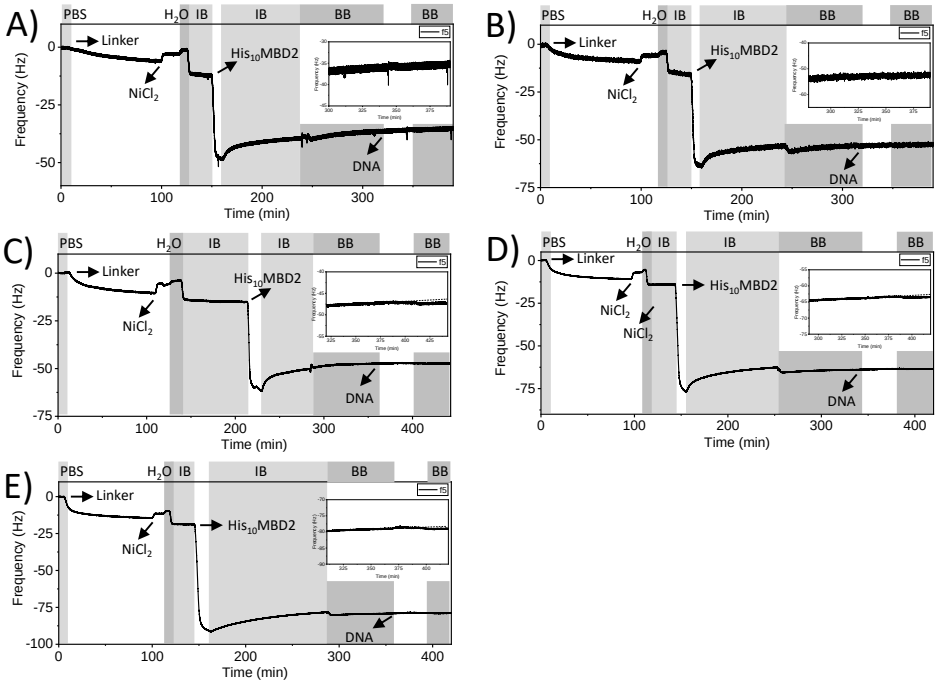

Figure S3.8. QCM time traces of the His_{10}MBD2 immobilization and subsequent DNA binding of Mal5CpG. Prior to the His_{10}MBD2 immobilization, the SAM was formed, followed by linker binding and activation of the NTA groups by $NiCl_2$. The binding of Mal5CpG was monitored on MBD2 surface receptor densities of: A) Δf = 22.3 Hz, B) Δf = 30.0 Hz, C) Δf = 34.7 Hz, D) Δf = 47.8 Hz and E) Δf = 56.9. Washing steps with PBS, Milli-Q (H_2O), IB and BB are indicated by the grey areas.

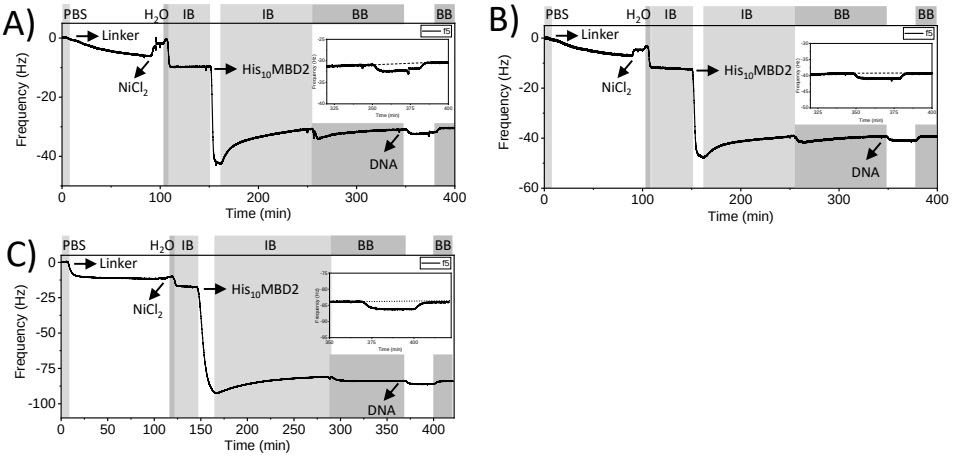

Figure S3.9. QCM time traces of the His_{10}MBD2 immobilization and subsequent DNA binding of Mal1C*pG. Prior to the His_{10}MBD2 immobilization, the SAM was formed, followed by linker binding and activation of the NTA groups by $NiCl_2$. The binding of Mal1C*pG was monitored on MBD2 surface receptor densities of: A) Δf = 19.9 Hz, B) Δf = 23.9 Hz and C) Δf = 59.1 Hz. Washing steps with PBS, Milli-Q (H_2O), IB and BB are indicated by the grey areas.

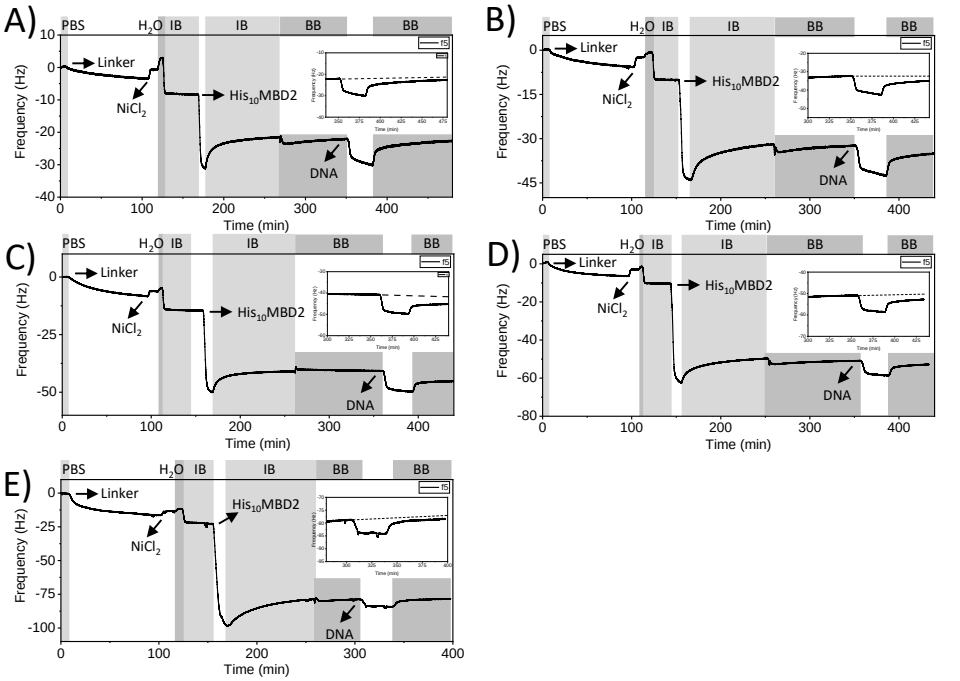

Figure S3.10. QCM time traces of the His_{10}MBD2 immobilization and subsequent DNA binding of Mal2C*pG close. Prior to the His_{10}MBD2 immobilization, the SAM was formed, followed by linker binding and activation of the NTA groups by $NiCl_2$. The binding of Mal2C*pG close was monitored on MBD2 surface receptor densities of: A) Δf = 13.2 Hz B) Δf = 22.0 Hz, C) Δf = 25.9 Hz, D) Δf = 37.3 Hz and E) Δf = 51.1 Hz. Washing steps with PBS, Milli-Q (H_2O), IB and BB are indicated by the grey areas.

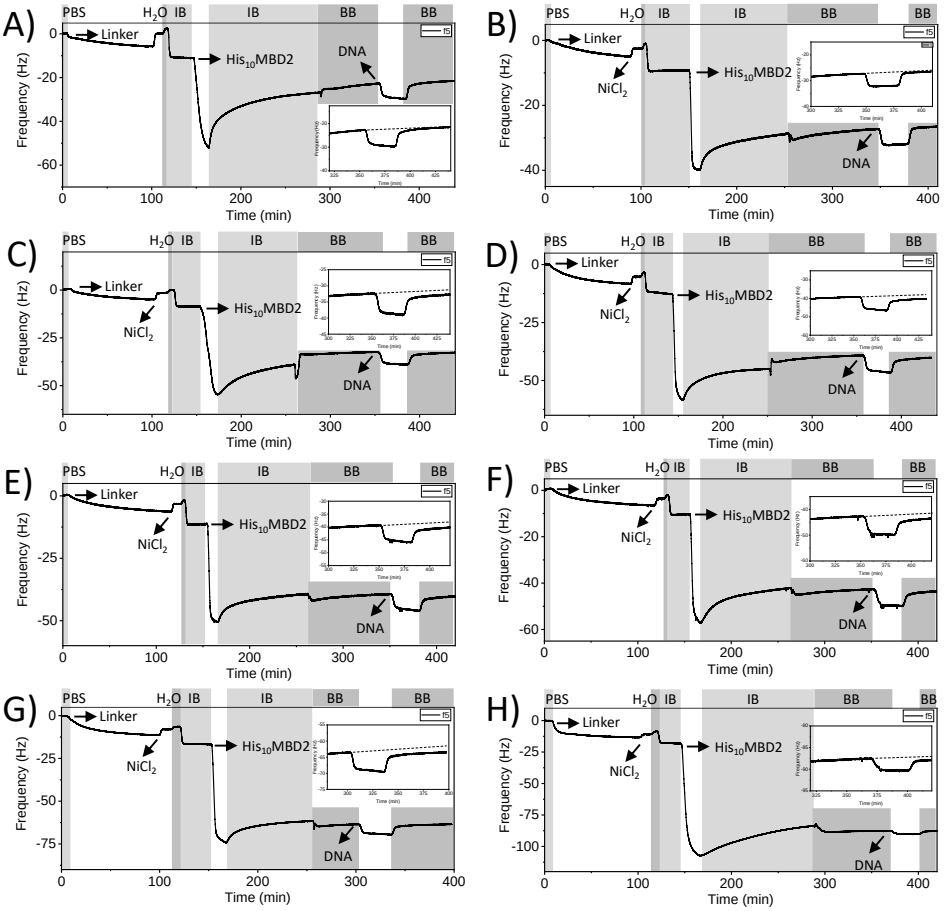

Figure S3.11. QCM times trace of the His_{10}MBD2 immobilization and subsequent DNA binding of Mal2C*pG far. Prior to the His_{10}MBD2 immobilization, the SAM was formed, followed by linker binding and activation of the NTA groups by $NiCl_2$. The binding of Mal2C*pG far was monitored on MBD2 surface receptor densities of: A) Δf = 12.6 Hz, B) Δf = 19.5 Hz, C) Δf = 26.9 Hz, D) Δf = 27.1 Hz, E) Δf = 29.1 Hz, F) Δf = 33.0 Hz, G) Δf = 42.5 Hz and H) Δf = 57.4 Hz. Washing steps with PBS, Milli-Q (H_2O), IB and BB are indicated by the grey areas.

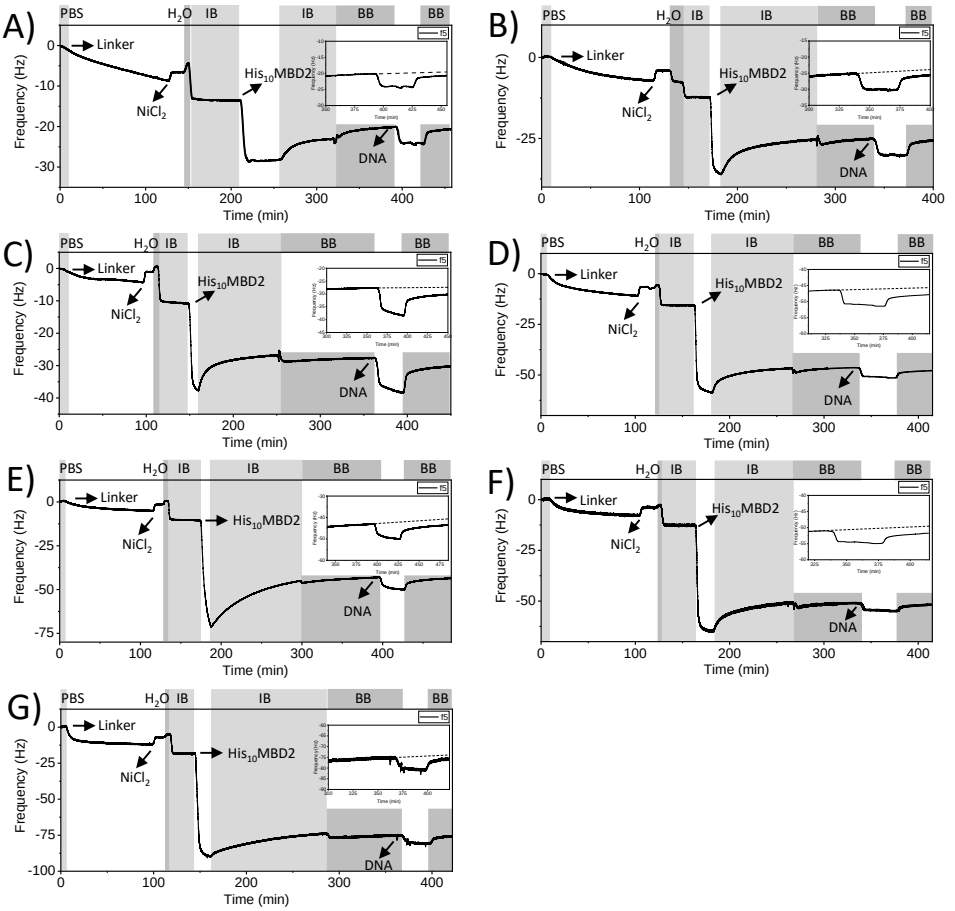

Figure S3.12. QCM time traces of the His_{10}MBD2 immobilization and subsequent DNA binding of Mal3C*pG. Prior to the His_{10}MBD2 immobilization, the SAM was formed, followed by linker binding and activation of the NTA groups by $NiCl_2$. The binding of Mal3C*pG far was monitored on MBD2 surface receptor densities of: A) Δf = 10.5 Hz, B) Δf = 12.3 Hz, C) Δf = 14.5 Hz, D) Δf = 30.8 Hz, E) Δf = 31.0 Hz, F) Δf = 36.9 Hz and G) Δf = 54.1 Hz. Washing steps with PBS, Milli-Q (H_2O), IB and BB are indicated by the grey areas.

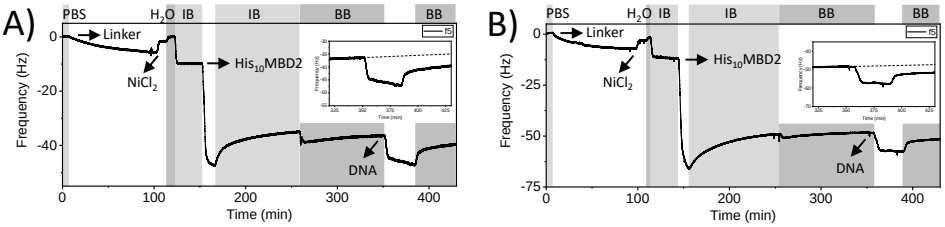

Figure S3.13. QCM times trace of the His_{10}MBD2 immobilization and subsequent DNA binding of Mal4C*pG. Prior to the His_{10}MBD2 immobilization, the SAM was formed, followed by linker binding and activation of the NTA groups by $NiCl_2$. The binding of Mal4C*pG far was monitored on MBD2 surface receptor densities of: A) Δf = 23.6 Hz and B) Δf = 32.7 Hz. Washing steps with PBS, Milli-Q (H_2O), IB and BB are indicated by the grey areas.

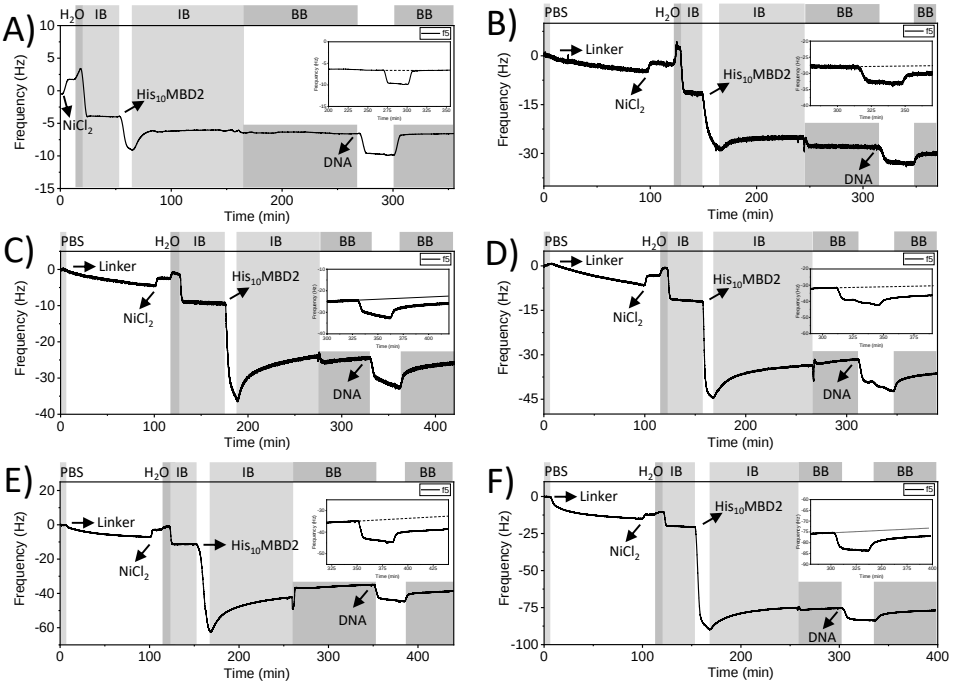

Figure S3.14. QCM times trace of the His_{10}MBD2 immobilization and subsequent DNA binding of Mal5C*pG. Prior to the His_{10}MBD2 immobilization, the SAM was formed, followed by linker binding and activation of the NTA groups by $NiCl_2$. The binding of Mal5C*pG was monitored on MBD2 surface receptor densities of: A) Δf = 1.8 Hz, B) Δf = 11.3 Hz, C) Δf = 12.9 Hz, D) Δf = 16.9 Hz, E) Δf = 30.0 Hz and F) Δf = 52.7 Hz. A) Does not displayer the linker molecule binding step. Washing steps with PBS, Milli-Q (H_2O), IB and BB are indicated by the grey areas.

3.7 References

(1) Sung, H.; Ferlay, J.; Siegel, R. L.; Laversanne, M.; Soerjomataram, I.; Jemal, A.; Bray, F. Global Cancer Statistics 2020: GLOBOCAN Estimates of Incidence and Mortality Worldwide for 36 Cancers in 185 Countries. *CA. Cancer J. Clin.* **2021**, *71*, 209–249.

(2) Crosby, D.; Lyons, N.; Greenwood, E.; Harrison, S.; Hiom, S.; Moffat, J.; Quallo, T.; Samuel, E.; Walker, I. A Roadmap for the Early Detection and Diagnosis of Cancer. *Lancet Oncol.* **2020**, *21*, 1397–1399.

(3) Hanna, T. P.; King, W. D.; Thibodeau, S.; Jalink, M.; Paulin, G. A.; Harvey-Jones, E.; O'Sullivan, D. E.; Booth, C. M.; Sullivan, R.; Aggarwal, A. Mortality Due to Cancer Treatment Delay: Systematic Review and Meta-Analysis. *BMJ* **2020**, *371*, m4087.

(4) Schreuders, E. H.; Ruco, A.; Rabeneck, L.; Schoen, R. E.; Sung, J. J. Y.; Young, G. P.; Kuipers, E. J. Colorectal Cancer Screening: A Global Overview of Existing Programmes. *Gut* **2015**, *64*, 1637–1649.

(5) Gok, M.; Heideman, D. A. M.; Van Kemenade, F. J.; Berkhof, J.; Rozendaal, L.; Spruyt, J. W. M.; Voorhorst, F.; Belien, J. A. M.; Babovic, M.; Snijders, P. J. F.; Meijer, C. J. L. M. HPV Testing on Self Collected Cervicovaginal Lavage Specimens as Screening Method for Women Who Do Not Attend Cervical Screening: Cohort Study. *BMJ* **2010**, *340*, c1040.

(6) Ignatiadis, M.; Sledge, G. W.; Jeffrey, S. S. Liquid Biopsy Enters the Clinic — Implementation Issues and Future Challenges. *Nat. Rev. Clin. Oncol.* **2021**, *18*, 297–312.

(7) Liu, B.; Ricarte Filho, J.; Mallisetty, A.; Villani, C.; Kottorou, A.; Rodgers, K.; Chen, C.; Ito, T.; Holmes, K.; Gastala, N.; Valyi-Nagy, K.; David, O.; Gaba, R. C.; Ascoli, C.; Pasquinelli, M.; Feldman, L. E.; Massad, M. G.; Wang, T.-H.; Jusue-Torres, I.; Benedetti, E.; Winn, R. A.; Brock, M. V.; Herman, J. G.; Hulbert, A. Detection of Promoter DNA Methylation in Urine and Plasma Aids the Detection of Non–Small Cell Lung Cancer. *Clin. Cancer Res.* **2020**, *26*, 4339–4348.

(8) Wan, J. C. M.; Massie, C.; Garcia-Corbacho, J.; Mouliere, F.; Brenton, J. D.; Caldas, C.; Pacey, S.; Baird, R.; Rosenfeld, N. Liquid Biopsies Come of Age: Towards Implementation of Circulating Tumour DNA. *Nat. Rev. Cancer* **2017**, *17*, 223–238.

(9) Cescon, D. W.; Bratman, S. V.; Chan, S. M.; Siu, L. L. Circulating Tumor DNA and Liquid Biopsy in Oncology. *Nat. Cancer* **2020**, *1*, 276–290.

(10) Corcoran, R. B.; Chabner, B. A. Application of Cell-Free DNA Analysis to Cancer Treatment. *N. Engl. J. Med.* **2018**, *379*, 1754–1765.

(11) De Rubis, G.; Rajeev Krishnan, S.; Bebawy, M. Liquid Biopsies in Cancer Diagnosis, Monitoring, and Prognosis. *Trends Pharmacol. Sci.* **2019**, *40*, 172–186.

(12) Feinberg, A. P.; Tycko, B. The History of Cancer Epigenetics. *Nat. Rev. Cancer* **2004**, *4*, 143–153.

(13) Zhang, J.; Yang, C.; Wu, C.; Cui, W.; Wang, L. DNA Methyltransferases in Cancer: Biology, Paradox, Aberrations, and Targeted Therapy. *Cancers (Basel)* **2020**, *12*, 2123.

(14) Bates, S. E. Epigenetic Therapies for Cancer. *N. Engl. J. Med.* **2020**, *383*, 650–663.

(15) Van den Helder, R.; Wever, B. M. M.; Van Trommel, N. E.; Van Splunter, A. P.; Mom, C. H.; Kasius, J. C.; Bleeker, M. C. G.; Steenbergen, R. D. M. Non-Invasive Detection of Endometrial Cancer by DNA Methylation Analysis in Urine. *Clin. Epigenetics* **2020**, *12*, 165.

(16) Yokoi, K.; Yamashita, K.; Watanabe, M. Analysis of DNA Methylation Status in Bodily Fluids for Early Detection of Cancer. *Int. J. Mol. Sci.* **2017**, *18*, 735.

(17) Vrba, L.; Futscher, B. W. A Suite of DNA Methylation Markers That Can Detect Most Common Human Cancers. *Epigenetics* **2018**, *13*, 61–72.

(18) Olkhov-Mitsel, E.; Bapat, B. Strategies for Discovery and Validation of Methylated and Hydroxymethylated DNA Biomarkers. *Cancer Med.* **2012**, *1*, 237–260.

(19) Locke, W. J.; Guanzon, D.; Ma, C.; Liew, Y. J.; Duesing, K. R.; Fung, K. Y. C.; Ross, J. P. DNA Methylation Cancer Biomarkers: Translation to the Clinic. *Front. Genet.* **2019**, *10*, 1150.

(20) Yegnasubramanian, S.; Lin, X.; Haffner, M. C.; DeMarzo, A. M.; Nelson, W. G. Combination of Methylated-DNA Precipitation and Methylation-Sensitive Restriction Enzymes (COMPARE-MS) for the Rapid, Sensitive and Quantitative Detection of DNA Methylation. *Nucleic Acids Res.* **2006**, *34*, e19.

(21) Warton, K.; Lin, V.; Navin, T.; Armstrong, N. J.; Kaplan, W.; Ying, K.; Gloss, B.; Mangs, H.; Nair, S. S.; Hacker, N. F.; Sutherland, R. L.; Clark, S. J.; Samimi, G. Methylation-Capture and Next-Generation Sequencing of Free Circulating DNA from Human Plasma. *BMC Genomics* **2014**, *15*, 476.

(22) Bhattacharjee, R.; Moriam, S.; Umer, M.; Nguyen, N.-T.; Shiddiky, M. J. A. DNA Methylation Detection: Recent Developments in Bisulfite Free Electrochemical and Optical Approaches. *Analyst* **2018**, *143*, 4802–4818.

(23) Pajares, M. J.; Palanca-Ballester, C.; Urtasun, R.; Alemany-Cosme, E.; Lahoz, A.; Sandoval, J. Methods for Analysis of Specific DNA Methylation Status. *Methods* **2021**, *187*, 3–12.

(24) Hofner, M.; Krainer, J.; Pabinger, S.; Pulverer, W.; Nöhammer, C.; Weinhäusel, A. Multiplex Analyses Using Methylation Sensitive Restriction Enzyme QPCR. In *Epigenetics Methods*; Tollefsbol, T., Ed.; Elsevier, 2020; pp 181–212.

(25) McClelland, M.; Nelson, M. The Effect of Site Specific Methylation on Restriction Endonuclease Digestion. *Nucleic Acids Res.* **1985**, *13*, r201–r207.

(26) Nell, R. J.; Steenderen, D.; Menger, N. V; Weitering, T. J.; Versluis, M.; Velden, P. A. Quantification of DNA Methylation Independent of Sodium Bisulfite Conversion Using Methylation-sensitive Restriction Enzymes and Digital PCR. *Hum. Mutat.* **2020**, *41*, 2205–2216.

(27) Kojima, K.; Takahashi, N.; Yada, Y.; Koike, Y.; Matano, M.; Kono, Y.; Momoi, M. Y. White-Matter Damage in a Neonate with Disseminated Herpes Simplex Virus Infection. *Pediatr. Int.* **2012**, *54*, 409–412.

(28) Brena, R. M.; Huang, T. H.-M.; Plass, C. Quantitative Assessment of DNA Methylation:

Potential Applications for Disease Diagnosis, Classification, and Prognosis in Clinical Settings. *J. Mol. Med.* **2006**, *84*, 365–377.

(29) Weber, M.; Davies, J. J.; Wittig, D.; Oakeley, E. J.; Haase, M.; Lam, W. L.; Schübeler, D. Chromosome-Wide and Promoter-Specific Analyses Identify Sites of Differential DNA Methylation in Normal and Transformed Human Cells. *Nat. Genet.* **2005**, *37*, 853–862.

(30) Rauch, T.; Pfeifer, G. P. Methylated-CpG Island Recovery Assay: A New Technique for the Rapid Detection of Methylated-CpG Islands in Cancer. *Lab. Investig.* **2005**, *85*, 1172–1180.

(31) Cross, S. H.; Charlton, J. A.; Nan, X.; Bird, A. P. Purification of CpG Islands Using a Methylated DNA Binding Column. *Nat. Genet.* **1994**, *6*, 236–244.

(32) Zou, H.; Harrington, J.; Rego, R. L.; Ahlquist, D. A. A Novel Method to Capture Methylated Human DNA from Stool: Implications for Colorectal Cancer Screening. *Clin. Chem.* **2007**, *53*, 1646–1651.

(33) Rauch, T. A.; Pfeifer, G. P. DNA Methylation Profiling Using the Methylated-CpG Island Recovery Assay (MIRA). *Methods* **2010**, *52*, 213–217.

(34) Hashimoto, H.; Liu, Y.; Upadhyay, A. K.; Chang, Y.; Howerton, S. B.; Vertino, P. M.; Zhang, X.; Cheng, X. Recognition and Potential Mechanisms for Replication and Erasure of Cytosine Hydroxymethylation. *Nucleic Acids Res.* **2012**, *40*, 4841–4849.

(35) Fraga, M. F.; Ballestar, E.; Montoya, G.; Taysavang, P.; Wade, P. A.; Esteller, M. The Affinity of Different MBD Proteins for a Specific Methylated Locus Depends on Their Intrinsic Binding Properties. *Nucleic Acids Res.* **2003**, *31*, 1765–1774.

(36) Buchmuller, B. C.; Kosel, B.; Summerer, D. Complete Profiling of Methyl-CpG-Binding Domains for Combinations of Cytosine Modifications at CpG Dinucleotides Reveals Differential Read-out in Normal and Rett-Associated States. *Sci. Rep.* **2020**, *10*, 4053.

(37) Heimer, B. W.; Tam, B. E.; Sikes, H. D. Characterization and Directed Evolution of a Methyl-Binding Domain Protein for High-Sensitivity DNA Methylation Analysis. *Protein Eng. Des. Sel.* **2015**, *28*, 543–551.

(38) Yu, Y.; Blair, S.; Gillespie, D.; Jensen, R.; Myszka, D.; Badran, A. H.; Ghosh, I.; Chagovetz, A. Direct DNA Methylation Profiling Using Methyl Binding Domain Proteins. *Anal. Chem.* **2010**, *82*, 5012–5019.

(39) Liu, M.; Movahed, S.; Dangi, S.; Pan, H.; Kaur, P.; Bilinovich, S. M.; Faison, E. M.; Leighton, G. O.; Wang, H.; Williams, D. C.; Riehn, R. DNA Looping by Two 5-Methylcytosine-Binding Proteins Quantified Using Nanofluidic Devices. *Epigenetics Chromatin* **2020**, *13*, 18.

(40) Pan, H.; Bilinovich, S. M.; Kaur, P.; Riehn, R.; Wang, H.; Williams, D. C. CpG and Methylation-Dependent DNA Binding and Dynamics of the Methylcytosine Binding Domain 2 Protein at the Single-Molecule Level. *Nucleic Acids Res.* **2017**, *45*, 9164–9177.

(41) Wee, E. J. H.; Ngo, T. H.; Trau, M. Colorimetric Detection of Both Total Genomic and Loci-Specific DNA Methylation from Limited DNA Inputs. *Clin. Epigenetics* **2015**, *7*, 65.

(42) *Multivalency: Concepts, Research and Applications*; Huskens, J., Prins, L., Haag, R.,

Ravoo, B. J., Eds.; Wiley, 2018.

(43) Martinez-Veracoechea, F. J.; Frenkel, D. Designing Super Selectivity in Multivalent Nano-Particle Binding. *Proc. Natl. Acad. Sci.* **2011**, *108*, 10963–10968.

(44) Fasting, C.; Schalley, C. A.; Weber, M.; Seitz, O.; Hecht, S.; Koksch, B.; Dernedde, J.; Graf, C.; Knapp, E.-W.; Haag, R. Multivalency as a Chemical Organization and Action Principle. *Angew. Chemie Int. Ed.* **2012**, *51*, 10472–10498.

(45) Magdalena Estirado, E.; Aleman Garcia, M. A.; Schill, J.; Brunsveld, L. Multivalent Ultrasensitive Interfacing of Supramolecular 1D Nanoplatforms. *J. Am. Chem. Soc.* **2019**, *141*, 18030–18037.

(46) Wang, J.; Min, J.; Eghtesadi, S. A.; Kane, R. S.; Chilkoti, A. Quantitative Study of the Interaction of Multivalent Ligand-Modified Nanoparticles with Breast Cancer Cells with Tunable Receptor Density. *ACS Nano* **2020**, *14*, 372–383.

(47) Zou, D.; Zhang, D.; Liu, S.; Zhao, B.; Wang, H. Interplay of Binding Stoichiometry and Recognition Specificity for the Interaction of MBD2b Protein and Methylated DNA Revealed by Affinity Capillary Electrophoresis Coupled with Laser-Induced Fluorescence Analysis. *Anal. Chem.* **2014**, *86*, 1775–1782.

(48) Moreland, B.; Oman, K.; Curfman, J.; Yan, P.; Bundschuh, R. Methyl-CpG/MBD2 Interaction Requires Minimum Separation and Exhibits Minimal Sequence Specificity. *Biophys. J.* **2016**, *111*, 2551–2561.

(49) Mammen, M.; Choi, S.-K.; Whitesides, G. M. Polyvalent Interactions in Biological Systems: Implications for Design and Use of Multivalent Ligands and Inhibitors. *Angew. Chemie Int. Ed.* **1998**, *37*, 2754–2794.

(50) Dubacheva, G. V; Curk, T.; Auzély-Velty, R.; Frenkel, D.; Richter, R. P. Designing Multivalent Probes for Tunable Superselective Targeting. *Proc. Natl. Acad. Sci.* **2015**, *112*, 5579–5584.

(51) Tito, N. B.; Frenkel, D. Optimizing the Selectivity of Surface-Adsorbing Multivalent Polymers. *Macromolecules* **2014**, *47*, 7496–7509.

(52) D'Agata, R.; Bellassai, N.; Jungbluth, V.; Spoto, G. Recent Advances in Antifouling Materials for Surface Plasmon Resonance Biosensing in Clinical Diagnostics and Food Safety. *Polymers (Basel)* **2021**, *13*, 1929.

(53) Vaisocherová, H.; Brynda, E.; Homola, J. Functionalizable Low-Fouling Coatings for Label-Free Biosensing in Complex Biological Media: Advances and Applications. *Anal. Bioanal. Chem.* **2015**, *407*, 3927–3953.

(54) Liu, M. C.; Oxnard, G. R.; Klein, E. A.; Swanton, C.; Seiden, M. V.; Liu, M. C.; Oxnard, G. R.; Klein, E. A.; Smith, D.; Richards, D.; Yeatman, T. J.; Cohn, A. L.; Lapham, R.; Clement, J.; Parker, A. S.; Tummala, M. K.; McIntyre, K.; Sekeres, M. A.; Bryce, A. H.; Siegel, R.; Wang, X.; Cosgrove, D. P.; Abu-Rustum, N. R.; Trent, J.; Thiel, D. D.; Becerra, C.; Agrawal, M.; Garbo, L. E.; Giguere, J. K.; Michels, R. M.; Harris, R. P.; Richey, S. L.; McCarthy, T. A.; Waterhouse, D. M.; Couch, F. J.; Wilks, S. T.; Krie, A. K.; Balaraman, R.; Restrepo, A.; Meshad, M. W.; Rieger-Christ, K.; Sullivan, T.; Lee, C. M.; Greenwald, D. R.; Oh, W.; Tsao, C.-K.; Fleshner, N.; Kennecke, H. F.; Khalil, M. F.; Spigel, D. R.; Manhas, A. P.; Ulrich, B.

K.; Kovoor, P. A.; Stokoe, C.; Courtright, J. G.; Yimer, H. A.; Larson, T. G.; Swanton, C.; Seiden, M. V.; Cummings, S. R.; Absalan, F.; Alexander, G.; Allen, B.; Amini, H.; Aravanis, A. M.; Bagaria, S.; Bazargan, L.; Beausang, J. F.; Berman, J.; Betts, C.; Blocker, A.; Bredno, J.; Calef, R.; Cann, G.; Carter, J.; Chang, C.; Chawla, H.; Chen, X.; Chien, T. C.; Civello, D.; Davydov, K.; Demas, V.; Desai, M.; Dong, Z.; Fayzullina, S.; Fields, A. P.; Filippova, D.; Freese, P.; Fung, E. T.; Gnerre, S.; Gross, S.; Halks-Miller, M.; Hall, M. P.; Hartman, A.-R.; Hou, C.; Hubbell, E.; Hunkapiller, N.; Jagadeesh, K.; Jamshidi, A.; Jiang, R.; Jung, B.; Kim, T.; Klausner, R. D.; Kurtzman, K. N.; Lee, M.; Lin, W.; Lipson, J.; Liu, H.; Liu, Q.; Lopatin, M.; Maddala, T.; Maher, M. C.; Melton, C.; Mich, A.; Nautiyal, S.; Newman, J.; Newman, J.; Nicula, V.; Nicolaou, C.; Nikolic, O.; Pan, W.; Patel, S.; Prins, S. A.; Rava, R.; Ronaghi, N.; Sakarya, O.; Satya, R. V.; Schellenberger, J.; Scott, E.; Sehnert, A. J.; Shaknovich, R.; Shanmugam, A.; Shashidhar, K. C.; Shen, L.; Shenoy, A.; Shojaee, S.; Singh, P.; Steffen, K. K.; Tang, S.; Toung, J. M.; Valouev, A.; Venn, O.; Williams, R. T.; Wu, T.; Xu, H. H.; Yakym, C.; Yang, X.; Yecies, J.; Yip, A. S.; Youngren, J.; Yue, J.; Zhang, J.; Zhang, L.; Zhang, L. (Quan); Zhang, N.; Curtis, C.; Berry, D. A. Sensitive and Specific Multi-Cancer Detection and Localization Using Methylation Signatures in Cell-Free DNA. *Ann. Oncol.* **2020**, *31*, 745–759.

(55) Kuzmin, A.; Poloukhtine, A.; Wolfert, M. A.; Popik, V. V. Surface Functionalization Using Catalyst-Free Azide−Alkyne Cycloaddition. *Bioconjug. Chem.* **2010**, *21*, 2076–2085.

(56) Lata, S.; Reichel, A.; Brock, R.; Tampé, R.; Piehler, J. High-Affinity Adaptors for Switchable Recognition of Histidine-Tagged Proteins. *J. Am. Chem. Soc.* **2005**, *127*, 10205–10215.

(57) Scarsdale, J. N.; Webb, H. D.; Ginder, G. D.; Williams, D. C. Solution Structure and Dynamic Analysis of Chicken MBD2 Methyl Binding Domain Bound to a Target-Methylated DNA Sequence. *Nucleic Acids Res.* **2011**, *39*, 6741–6752.

(58) Hendrich, B.; Bird, A. Identification and Characterization of a Family of Mammalian Methyl-CpG Binding Proteins. *Mol. Cell. Biol.* **1998**, *18*, 6538–6547.

(59) Sauerbrey, G. Verwendung von Schwingquarzen Zur Wägung Dünner Schichten Und Zur Mikrowägung. *Zeitschrift für Phys.* **1959**, *155*, 206–222.

(60) Larsson, C.; Rodahl, M.; Höök, F. Characterization of DNA Immobilization and Subsequent Hybridization on a 2D Arrangement of Streptavidin on a Biotin-Modified Lipid Bilayer Supported on SiO 2. *Anal. Chem.* **2003**, *75*, 5080–5087.

(61) Hamming, P. H. E.; Huskens, J. Streptavidin Coverage on Biotinylated Surfaces. *ACS Appl. Mater. Interfaces* **2021**, *13*, 58114–58123.

(62) Ostuni, E.; Grzybowski, B. A.; Mrksich, M.; Roberts, C. S.; Whitesides, G. M. Adsorption of Proteins to Hydrophobic Sites on Mixed Self-Assembled Monolayers. *Langmuir* **2003**, *19*, 1861–1872.

(63) Nelson, K. E.; Gamble, L.; Jung, L. S.; Boeckl, M. S.; Naeemi, E.; Golledge, S. L.; Sasaki, T.; Castner, D. G.; Campbell, C. T.; Stayton, P. S. Surface Characterization of Mixed Self-Assembled Monolayers Designed for Streptavidin Immobilization. *Langmuir* **2001**, *17*, 2807–2816.

(64) Overmeer, R. M.; Henken, F. E.; Bierkens, M.; Wilting, S. M.; Timmerman, I.; Meijer, C.

J.; Snijders, P. J.; Steenbergen, R. D. Repression of MAL Tumour Suppressor Activity by Promoter Methylation during Cervical Carcinogenesis. *J. Pathol.* **2009**, *219*, 327–336.

(65) Bosschieter, J.; Nieuwenhuijzen, J. A.; Hentschel, A.; Van Splunter, A. P.; Segerink, L. I.; Vis, A. N.; Wilting, S. M.; Lissenberg-Witte, B. I.; Van Moorselaar, R. J. A.; Steenbergen, R. D. M. A Two-Gene Methylation Signature for the Diagnosis of Bladder Cancer in Urine. *Epigenomics* **2019**, *11*, 337–347.

(66) Burnham, P.; Dadhania, D.; Heyang, M.; Chen, F.; Westblade, L. F.; Suthanthiran, M.; Lee, J. R.; De Vlaminck, I. Urinary Cell-Free DNA Is a Versatile Analyte for Monitoring Infections of the Urinary Tract. *Nat. Commun.* **2018**, *9*, 2412.

(67) Burnham, P.; Kim, M. S.; Agbor-Enoh, S.; Luikart, H.; Valantine, H. A.; Khush, K. K.; De Vlaminck, I. Single-Stranded DNA Library Preparation Uncovers the Origin and Diversity of Ultrashort Cell-Free DNA in Plasma. *Sci. Rep.* **2016**, *6*, 27859.

(68) Nair, S. S.; Coolen, M. W.; Stirzaker, C.; Song, J. Z.; Statham, A. L.; Strbenac, D.; Robinson, M. D.; Clark, S. J. Comparison of Methyl-DNA Immunoprecipitation (MeDIP) and Methyl-CpG Binding Domain (MBD) Protein Capture for Genome-Wide DNA Methylation Analysis Reveal CpG Sequence Coverage Bias. *Epigenetics* **2011**, *6*, 34–44.

(69) Jeong, J.; Yim, H.; Ryu, J.; Lee, H. S.; Lee, J.; Seen, D.; Kang, S. G. One-Step Sequence- and Ligation-Independent Cloning as a Rapid and Versatile Cloning Method for Functional Genomics Studies. *Appl. Environ. Microbiol.* **2012**, *78*, 5440–5443.

Chapter 4

Enrichment of hypermethylated DNA from DNA mixtures

Clinical use of the cancer biomarker hypermethylated DNA (hmDNA), which is detectable in liquid biopsies such as blood and urine, requires pre-concentration based on the degree of methylation. Here, we determined quantitatively the selectivity of hmDNA enrichment from DNA mixtures containing hmDNA and non-methylated DNA. hmDNA enrichment of DNA mixtures is applied to separate hmDNA from non-methylated DNA in a simple process with binding and elution steps. Upon hmDNA enrichment, hmDNA binds at the surface-immobilized methyl binding domain 2 (MBD2) protein receptors, and the applied MBD2 surface receptor density affects the binding selectivity for hmDNA. The DNA mixtures consisted of 90 bp-long DNA with a hmDNA content of 1%. Surface-bound DNA was effectively eluted from the MBD2-coated surface with an ammonium hydroxide solution to denature the MBD2 and thus dissociate its complex with (hm)DNA. The ratio of hmDNA and non-methylated DNA in the enriched DNA mixtures was determined by applying a digest with methyl-sensitive restriction enzyme to the enriched DNA mixtures, followed by quantitative polymerase chain reaction. This could be quantitatively determined in the range from 0.01% to 100%. The hmDNA level reached in the enriched DNA mixture was between approximately 7% and 30% depending on the applied MBD2 surface receptor density, compared to the 1% hmDNA level in the non-enriched DNA mixture. Our findings suggest that hmDNA can be enriched selectively in liquid biopsies, while controlling the applied MBD2 surface receptor densities.

R.W. Kolkman, L.I. Segerink, J. Huskens. *Manuscript in preparation*.

4.1 Introduction

Analysis of liquid biopsy samples does enable pre-symptomatic cancer detection and, therefore, has the ability to reduce cancer mortality.[1–4] Liquid biopsy-based cancer diagnostics also benefits from the minimal invasiveness and consequently minimal clinical risks for the patient, its ability to encompass tumor heterogeneity, and ability to monitor cancer progression over time.[5,6]

Cell-free DNA is present in liquid biopsies, such as blood and urine, because it is released into the circulation system by cells *via* apoptosis, necrosis and secretion.[7] Cell-free DNA in liquid biopsies originates from a wide variety of healthy cells, but, when a tumor occurs, also contains epigenetically or genetically altered DNA from these cancer cells.[7]

One of the cancer biomarkers is hypermethylated DNA (hmDNA).[8,9] DNA methylation involves the addition of a methyl group at the fifth carbon of cytosine followed by a guanine base in the 5' - 3' direction, defined as a CpG. The methylation of CpGs is a process used by healthy cells to regulate gene expression according to cell function over time.[10] In case of DNA hypermethylation, which can occur in tumor cells, the degree of CpG methylation is higher than normal, especially for so-called CpG islands, which contain high numbers of CpGs. Approximately 30,000 CpG islands are present in genomic DNA, which can be up to a few kilobasepairs in length containing numerous methylated CpGs.[11,12] On average, approximately 0.5% of the human genomic DNA is methylated.[11,12] The hypermethylation of specific genes is associated with varying types of cancer including bladder, breast, ovarian and lung cancer.[13–16]

Enabling cancer diagnostics based on the detection of hmDNA requires a step to differentiate between hmDNA and non/low-methylated DNA, especially at early cancer stages where the numbers of hmDNA copies in liquid biopsies are low.[5,11,12] Differentiation of hmDNA is in general achieved by either bisulfite conversion, by use of methyl-sensitive restriction enzymes, or by affinity chromatography.[17] Upon bisulfite conversion of DNA, unmethylated cytosines are chemically converted to the base uracil, while the methylated cytosines remain unaffected, allowing discrimination based on sequence. Applying a digest step with methyl-sensitive restriction enzymes results in DNA digestion dependent on CpG methylation. For example, the restriction enzymes cut the DNA at specific DNA recognition sequences of a few base pairs in length containing a CpG. The gold standard for affinity-based hmDNA enrichment employs a methyl binding domain 2 (MBD2) protein with affinity for methylated CpG (C*pG) as biorecognition element.[18,19] Affinity chromatography is favored due to its simplicity and short assay times as only a binding and an elution step are involved. The MBD2 protein possesses a 10 to 100-fold stronger dissociation constant (in the low

nanomolar regime) for C*pG in comparison to a non-methylated CpG (CpG), thereby enabling hmDNA enrichment.[20–26]

The selectivity of MBD2-based enrichment systems is conventionally displayed by the enrichment factor.[27,28] The enrichment factor is defined as the amount of isolated hmDNA divided by the amount of isolated non-methylated DNA obtained in two separate experiments.[27,28] Enrichment factors up to 700-fold were reported upon the use of 100 ng hmDNA and 100 ng non-methylated DNA in a study by Yegnasubramanian *et al*.[29] However, when using 0.1 ng hmDNA and 11 ng non-methylated DNA input,[29] which represent the typical ratio of hmDNA and non-methylated DNA found in the genome,[11,12] the enrichment factor was only 5. Notably, quantification of the selectivity of hmDNA enrichment from *mixtures* of DNA containing both hmDNA and non-methylated DNA is currently lacking for affinity-based enrichment. Quantification of selectivity from mixtures has only been performed in detail upon MBD2 enrichment followed by a restriction enzyme digest by Yegnasubramanian *et al.*,[29] but this method is too complex to employ it in a clinical setting as it involves a multistep process.

It is crucial to control and quantify the selectivity of MBD2-based hmDNA enrichment of DNA mixtures. First of all, knowing the enrichment selectivity provides information regarding the ratio of hmDNA and non-methylated DNA in the enriched DNA mixture. Second, knowing the enrichment selectivity helps to define the detection threshold upon the integration of an MBD2 enrichment step in a detection assay. For example, a high hmDNA enrichment selectivity has the potential to detect a specific cancer hmDNA gene at early stages when the hmDNA concentration is still extremely low. Recently we improved the hmDNA binding selectivity by the development of a multivalent hmDNA binding platform (Chapter 3). There, it was reported that control over the MBD2 surface receptor densities on the DNA binding platform is essential in order to improve the selectivity of hmDNA enrichment. This effect was ascribed to the multivalent[30,31] and superselective[32] binding properties of hmDNA at a density-controlled MBD2-modified surface. The recent improvement was not yet tested in the enrichment of hmDNA from DNA mixtures. Quantification of the hmDNA enrichment selectivity can be determined by polymerase chain reaction (PCR) amplification after subjecting the enriched DNA mixture to bisulfite conversion[33,34] or a methyl-sensitive restriction enzyme digest.[35–37] Then the amount of conversion or digestion is proportional to the ratio of hmDNA and non-methylated DNA in the enriched DNA mixture.

Here we show the quantitative determination of the selectivity of hmDNA enrichment from DNA mixtures using varying MBD2 surface receptor densities. DNA of 90 bp long was used in the methylated and non-methylated form in a 1:100 ratio to represent a model urine liquid biopsy sample.[11,12,38] The DNA mixture was first used to study the

degree of DNA binding to and elution from MBD2-coated surfaces to determine the elution efficiency. Varying MBD2 surface receptor densities were studied by using a thiol-based self-assembled monolayer (SAM, see Chapter 3). Then, the selectivity of the hmDNA enrichment was evaluated quantitively by determining the ratio of hmDNA and non-methylated DNA in the enriched DNA mixture. The enriched DNA mixture was first subjected to a methyl-sensitive restriction enzyme digest in order to distinguish between hmDNA and non-methylated DNA upon the analysis with quantitative PCR (qPCR). qPCR was first applied to a series of mixtures with pre-determined and varying ratios of hmDNA and non-methylated DNA in order to establish the relationship between the DNA ratio and the number of qPCR cycles. This calibration was then used to measure the ratio of hmDNA and non-methylated DNA in the enriched DNA mixtures. Finally, we determined the optimal MBD2 surface receptor density for selective hmDNA enrichment at which the highest hmDNA enrichment selectivity is achieved.

4.2 Results and discussion

4.2.1 Quantification method to assess the hmDNA enrichment selectivity from DNA mixtures

To assess the selectivity of hmDNA enrichment from DNA mixtures using MBD2-based affinity chromatography, a combination of a methyl-sensitive restriction enzyme digest and qPCR analysis is performed as schematically displayed in Figure 4.1A. First, hmDNA enrichment of the DNA mixture is performed using the MBD2-modified surface. The DNA mixture contains both hmDNA and non-methylated DNA. In the first step DNA binds to the MBD2-modified surface. After rinsing away the excess sample, the surface-bound DNA is removed from the surface in an elution step using a solution of ammonium hydroxide (pH 11.3). The pH of the eluent is above the isoelectric point of MBD2,[39] thereby causing the denaturation of MBD2. As a consequence, the non-covalent interactions between the MBD2 proteins and C(*)pGs are disrupted resulting in elution of the surface-bound DNA. To assess the ratio of hmDNA and non-methylated DNA in the enriched DNA mixture, the enriched DNA mixture is subjected to a digest with methyl-sensitive restriction enzymes, HpaII and HhaI. The non-methylated DNA is digested, while the hmDNA is protected from digestion due to CpG methylation. In the last step, the enriched and digested DNA mixtures are amplified by qPCR using a fixed DNA concentration. The number of cycles needed to reach the qPCR threshold (C_t value) is dependent on the ratio of hmDNA and non-methylated DNA in the enriched DNA sample. For example, if the amount of hmDNA in the DNA mixture is higher compared to the amount of non-methylated DNA, a relatively low amount of DNA is cut in the restriction enzyme digest step, which consequently results in a lower

C_t value. On the other hand, if the enriched DNA mixture contains more non-methylated DNA, the C_t value increases. This method thus enables the quantitative determination of the selectivity of the hmDNA enrichment process.

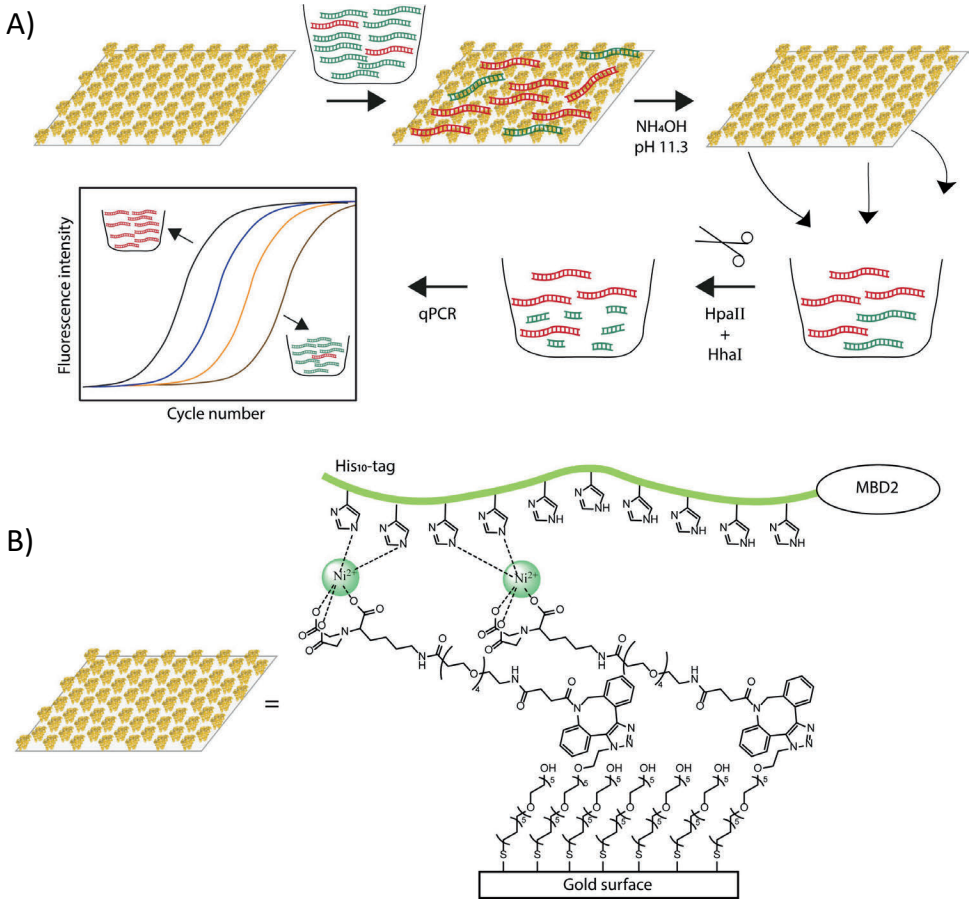

Figure 4.1. A) Schematic overview of the process to determine the ratio of hmDNA (red) and non-methylated DNA (green) in DNA mixtures upon hmDNA enrichment. hmDNA enrichment from a DNA mixture is performed on a gold surface modified with the MBD2 protein (yellow, see Chapter 3). Surface-bound DNA is removed by elution with aqueous ammonium hydroxide (pH 11.3). The hmDNA content in an enriched DNA mixture is determined by employing a digest with methyl-sensitive restriction enzymes (HpaII and HhaI) followed by qPCR analysis. B) Molecular structure of the employed surface chemistry to immobilize the MBD2 protein on the surface (see Chapter 3). The surface is modified with a SAM of ethylene glycol-alkanethiols functionalized with hydroxyl or azide-groups. To the azide thiol the linker molecule bearing DBCO and NiNTA functional groups is attached. The His_{10}-tag of the MBD2 interacts with the NiNTA functional groups on the surface enabling MBD2 surface immobilization. The

MBD2 surface receptor density is tuned by the stoichiometric ratio of hydroxyl and azide-functionalized thiols in the SAM.

The hmDNA enrichment was evaluated at a gold surface modified with control over the MBD2 surface receptor density by using an ethylene glycol-alkanethiol-based SAM (Figure 4.1B); see Chapter 3. The SAM consists of hydroxyl and azide-functionalized thiols. The hydroxyl-based thiols are used to create an anti-fouling surface,[40–43] while the azide ones are used to bind the MBD2. The ratio of these thiols controls the MBD2 density, which in turn was shown to affect the methylated DNA enrichment selectivity (Chapter 3). Prior to MBD2 immobilization, a linker molecule bearing a dibenzocyclooctyne (DBCO) and a nitrilotriacetic acid (NTA) functional group is bound to the azide-functionalized thiol. The linker molecule is covalently bound to the azide-functional groups by the catalyst-free click chemistry reaction between the DBCO and azide moieties.[44] Afterwards, the NTA moieties were transformed into nickel(II)NTA (NiNTA) by flushing nickel chloride ($NiCl_2$) over the surface. The surface-tethered NiNTA moieties were then used to enable the immobilization of the histidine 10-tagged MBD2 protein (His_{10}MBD2).[45]

To determine the selectivity of hmDNA enrichment a 90 bp-long sequence was used. The selected sequence originates from the *MAL* gene, which is found to be hypermethylated in cancer cells.[46,47] The DNA sequence length used is in agreement with the main fragment size of DNA in urine.[38] The DNA sequence used in this study is the model DNA target and contains 3 CpGs, which is used either in its methylated or its non-methylated form (Figure 4.2A and Table S4.1). The methylated and non-methylated forms of the model DNA target are abbreviated in this study as Mal3C*pG and Mal3CpG, respectively. Mal3C*pG is formed by the methylation of Mal3CpG in a reaction where Mal3CpG is mixed with the *M.SssI* enzyme in the presence of S-adenosylmethionine and a buffer overnight at 37 °C.[48–50] The model DNA target possesses both a recognition site for the methyl-sensitive restriction enzymes HhaI and HpaII at the first and third CpG in the 5'- 3' direction, which both become digested in the absence of CpG methylation. The primer binding place at Mal3C(*)pG is located before and after the recognition sites of HhaI and HpaII, respectively. In case of the digestion of Mal3CpG, primer binding is prevented upon qPCR, thus resulting in the absence of qPCR amplification. The DNA mixture used in this study consists of a 1:100 ratio of Mal3C*pG and Mal3CpG, representing typical methylation levels found in genomic DNA,[11,12] thus also representing DNA originating from a liquid biopsy.

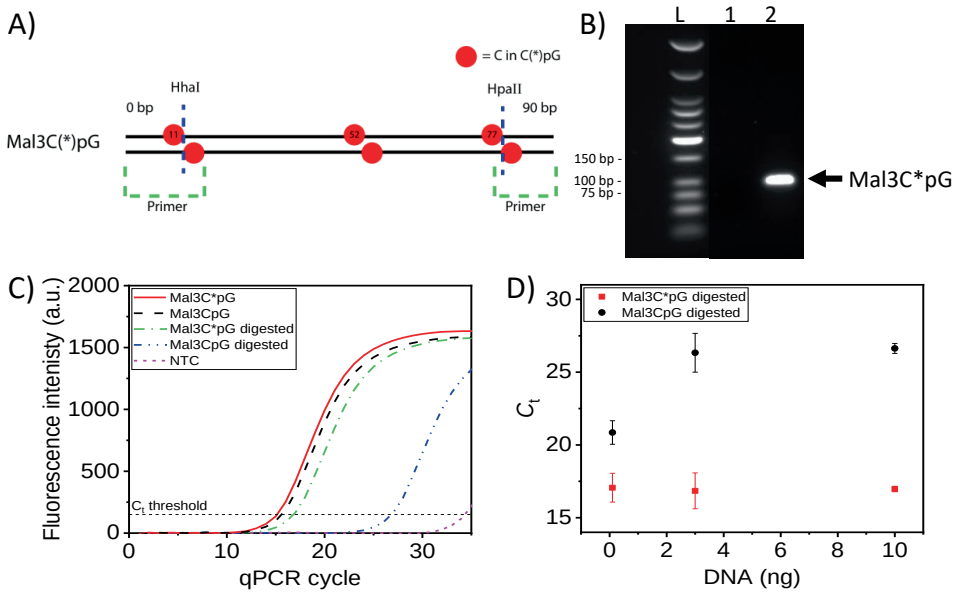

Figure 4.2. A) The 90 bp-long model DNA target Mal3C(*)pG with the location of cytosines in C(*)pGs displayed as red circles. The locations of the recognition sequence of methyl-sensitive restriction enzymes HhaI and HpaII on Mal3C(*)pG are indicated with the blue dashed lines. The primer binding regions are shown by the green dashed lines. B) Gel electrophoresis image of an amplified Mal3C*pG. To visualize the DNA, the SYBR safe DNA stain was used. In the gel image, the ladder (L), the control in absence of template (1) and amplified Mal3C*pG after reacting 10 ng Mal3C*pG with HhaI and HpaII (2) are shown. The Mal3C*pG band is visible at the expected DNA length of 90 bp. C) Validation of amplification of Mal3C(*)pG with qPCR, performed at a DNA concentration of 0.5 pg/µL. Mal3C(*)pG was treated with and without the methyl-sensitive restriction enzymes HhaI and HpaII using a DNA amount of 10 ng. The control in absence of template (NTC) is shown as well. The C_t threshold is indicated with the dashed horizontal line in the graph at a fluorescence intensity of 150 a.u. D) C_t value of Mal3C(*)pG at varying DNA amounts treated with HhaI and HpaII measured with qPCR. At the qPCR step, the DNA concentration was kept constant at 0.5 pg/µL. Error bars represent the standard deviation.

Mal3C*pG was successfully amplified by qPCR after HhaI and HpaII treatment as was confirmed by gel electrophoresis (Figure 4.2B). Upon amplification of Mal3C*pG the methylation status is lost, as non-methylated cytosines are used during the amplification. Only one band is visible in the gel for the Mal3C*pG treated with HhaI and HpaII, indicating the absence of any formed side products. The sequence length of the amplified DNA is approximately 90 bp, which matches the expected sequence

length based on the primer design (Table S4.2). Thus, these results confirm successful and specific amplification of Mal3C*pG after the restriction enzyme digest.

Despite CpG methylation, the Mal3C*pG sequence was not fully protected from the methyl-sensitive restriction digest of HhaI and HpaII as was observed with qPCR (Figure 4.2C). The C_t value is approximately 1.5 cycles higher for Mal3C*pG reacted with the restriction enzymes in comparison to non-enzyme-reacted Mal3C*pG. The C_t difference is likely due to both unspecific digestion of Mal3C*pG by HhaI and HpaII and incomplete methylation during the preparation of Mal3C*pG. Additionally, restriction enzyme-treated Mal3CpG does not result in complete prevention of Mal3CpG amplification. The C_t value is approximately 11 cycles higher for Mal3CpG reacted with the restriction enzymes in comparison to non-enzyme-reacted Mal3CpG. The difference in cycles (ΔC_t) between HhaI and HpaII-treated Mal3C*pG and Mal3CpG is dependent on the DNA concentration used during the digest step (Figure 4.2D). Below a DNA input concentration of 3 ng, the ΔC_t value decreases, indicative of a lower efficiency of the restriction enzyme digest. Hence, we worked with a DNA amount of 3 ng during digest of the DNA mixtures (see below). Yet, even at sufficiently high concentrations, the digest efficiency is not 100%, as indicated by the detectable C_t value in comparison to the non-template control (NTC, Figure 4.2C).

4.2.2 DNA binding to and elution from MBD2-coated surfaces

hmDNA enrichment of mixed DNA samples was performed in a capture device using a stepwise process (Figure 4.1A). A typical example of layer build-up and DNA binding monitored by quartz crystal microbalance (QCM) is shown in Figure 4.3A (see also Chapter 3). The capture surface was formed from a thiol-based SAM containing 9% azide-thiol on the gold surface. Then, the linker molecule was reacted to the surface. As a result of the covalent reaction, the QCM frequency is reduced. In the next step, the NTA moieties were transformed into NiNTA by flushing with a $NiCl_2$ solution. The MBD2 protein was successfully immobilized on the surface owing to the interaction between the His_{10}-tag of MBD2 with the NiNTA moieties on the surface. After the MBD2 immobilization, a washing step with immobilization buffer (IB) was applied to remove loosely bound MBD2. The amount of His_{10}MBD2 immobilization is determined by measuring the change in frequency (Δf). Δf was determined by subtracting the frequency of IB after MBD2 immobilization from the frequency while flushing with IB prior to MBD2 immobilization. The Δf observed equals to 23 Hz, which can be converted to an MBD2 surface receptor density of 183 ng/cm^2 using the Sauerbrey equation,[51] while assuming that 55% of the absorbed mass is due to bound water.[52] Additionally, the MBD2 surface receptor density is directly dependent on the fraction of azide-functionalized thiols in the SAM as was reported in Chapter 3. The MBD2-modified surface was subsequently used to monitor the enrichment process of the

1:100 DNA mixture. The DNA mixture, with a total DNA concentration of 500 nM (with 166 ng Mal3C*pG and 16.6 µg Mal3CpG), was flushed over the MBD2 surface for 60 min at a flow rate of 30 µL/min while recycling the DNA solution. The applied flow rate was kept constant throughout this work. Upon flowing the DNA mixture, a relatively small but significant decrease in frequency was observed over time, indicating binding of the DNA to the MBD2 surface. After the DNA binding step a washing step was applied to remove weakly attached DNA from the surface. The amount of DNA bound to the MBD2 surface was determined after the washing step with binding buffer (BB), and equaled to a Δ*f* of 1.6 Hz, which corresponds to 5.7 ng/cm^2 DNA using the Sauerbrey equation,[51] while assuming that 80% of the adsorbed mass is due to water associated to the DNA.[53,54]

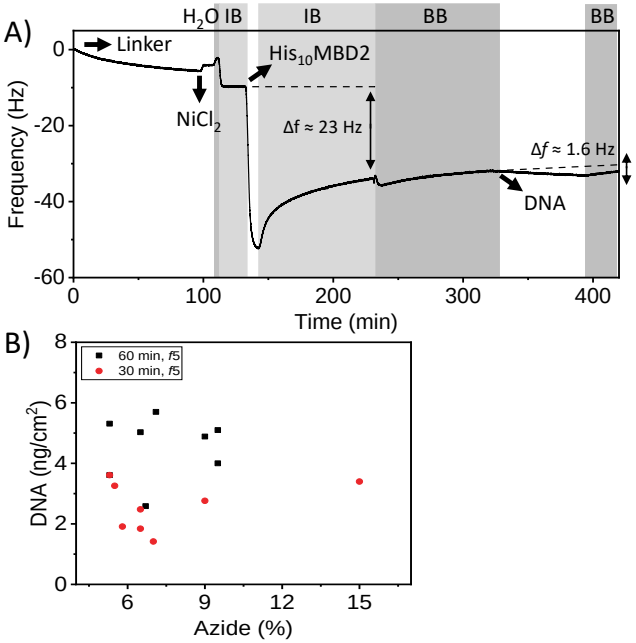

Figure 4.3. A) QCM monitoring of MBD2 layer formation and DNA binding from a DNA mixture. The QCM gold chip was modified with the SAM containing 9% azide-functionalized thiols prior to the QCM measurement. In consecutively performed steps, the DNA capture device is formed: binding of the linker molecule, activation of the NTA groups with $NiCl_2$ and His_{10}MBD2 immobilization. The DNA mixture consisted of a 1:100 ratio of Mal3C*pG and Mal3CpG. The total DNA concentration of the DNA mixture was 500 nM. Washing steps with PBS, Milli-Q water (H_2O), immobilization buffer (IB) and binding buffer (BB) are indicated by the gray areas. B) Amount of DNA binding as function of the azide percentage in the SAM upon the flowing of the 500 nM 1:100 DNA mixtures determined by QCM. The total DNA binding time was 30 min or 60 min.

The adsorption of DNA from the 1:100 DNA mixture was monitored *in situ* by QCM to determine the average amounts of DNA binding, upon a 30 min or 60 min DNA binding step, to MBD2 surfaces with different MBD2 densities. The same volume of the DNA mixture was used upon the DNA binding step of 30 min and 60 min, only the total recycling time was changed. The amount of DNA binding on MBD2 surfaces (with an area of ≈1 cm^2) was determined for azide percentages between 5.3 – 15% in the SAM. Thus, a higher azide percentage results in a higher MBD2 surface receptor density (see Chapter 3). The average mass of DNA that binds to the MBD2-modified surface for the DNA binding of 30 and 60 min amounts to 2.6±0.8 ng/cm^2 and 4.5±1.0 ng/cm^2, respectively (Figure 4.3B). Therefore, a longer DNA binding time results in more DNA binding to the MBD2 surface. The DNA binding time was not increased further in order to keep the DNA binding time practical. The amount of DNA binding was approximately constant and independent of the MBD2 density, albeit with a rather large variability over the measured MBD2 density range. Compared to the total amount of DNA available in the flowed sample (16.8 µg) and assuming that all DNA in the DNA mixtures comes in contact with the MBD2 surface, only a minor part of the DNA binds to the MBD2-coated QCM surface. Also, an approximately 3.5-fold lower DNA surface coverage is achieved in the DNA binding step compared to our previous work described in Chapter 3. There the binding of 500 nM Mal3C*pG to MBD2-coated QCM surfaces with a binding time of 30 min resulted in approximately 9 ng DNA binding. The Mal3C*pG concentration was thus there 500-fold times higher and in absence of Mal3CpG. Therefore, the lesser DNA binding observed here indicates some mass transport limitations at the DNA concentrations used here, even with a binding time of 60 min. Furthermore, the DNA binding of 90 bp-long non-methylated DNA at 500 nM for 30 min to MBD2 surfaces at the used azide percentages in the SAM was found negligible (Chapter 3). Therefore, most likely, the constant, but low, amounts of DNA adsorbing showed here indicates that the Mal3C*pG DNA is the major DNA type that binds.

Elution of surface-bound DNA is needed to allow quantification of the enrichment selectivity. Enrichment of hmDNA has been previously performed by others with magnetic beads modified with MBD2 followed by elution of surface-bound DNA with 2 M NaCl.[55,56] In our case, the elution of 90 bp-long DNA with only two C(*)pGs (Mal2C(*)pG, DNA sequence: see Table S4.1) bound to an MBD2 surface did not result in elution while flushing with 4 M NaCl at 30 µL/min for 20 min as no change in QCM frequency was observed (Figure 4.4A). As an alternative for the NaCl elution method, the use of a high-pH elution buffer was evaluated. First, 100 mM triethylamine (TEA) pH 11.5 was tested as elution buffer as the pH is above the isoelectric point of MBD2.[39] This resulted in successful elution of the surface-bound DNA as the frequency after elution returned to the frequency prior to the DNA binding step (Figure 4.4B). Nevertheless, it turned out that the DNA sample was not stable in TEA. As the elution

of surface-bound DNA with a high-pH buffer was effective, aqueous ammonium hydroxide (pH 11.3) was used to elute the surface-bound DNA. Upon subsequent assessment of the DNA concentration, the expected amount of enriched DNA was found after elution (see below), thus confirming that ammonium hydroxide does not lead to DNA degradation.

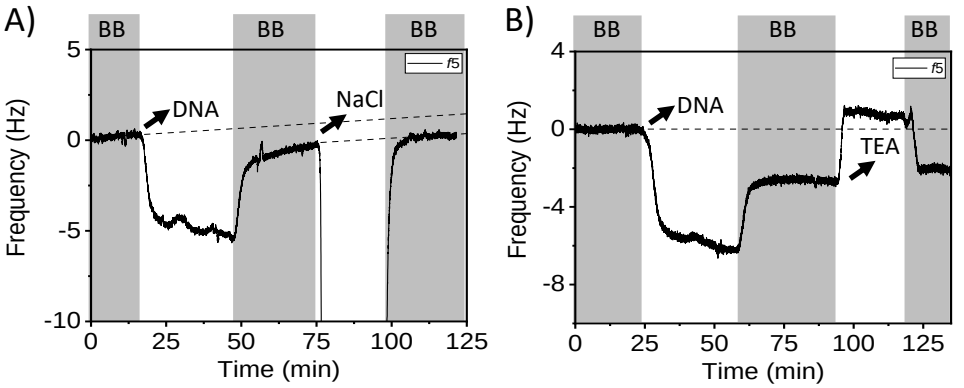

Figure 4.4. Monitoring of the elution of surface-captured DNA from MBD2-coated surfaces. SAM-modified gold surface with A) 18% and B) 7% azide-functionalized thiols were reacted with the linker molecule followed by the activation of the NTA groups with $NiCl_2$ and His_{10}MBD2 immobilization. A) 1 µM DNA mixture containing an equivalent amount of Mal2C*pG and Mal2CpG was flushed over the surface followed by flushing with 4 M NaCl for 20 min. B) 500 nM Mal3C*pG was flushed over the surface followed by elution with TEA pH 11.5 for 25 min. Washing steps with BB are indicated by the gray areas.

The concentrations of eluted DNA from the MBD2 surfaces were determined by using a fluorescent DNA-binding dye (AccuBlue).[57] The dye becomes fluorescent upon the binding to double-stranded DNA. The concentration determination step is applied to ensure equal total DNA input concentrations upon the qPCR determination of the Mal3C*pG/Mal3CpG ratio of enriched DNA mixtures. Otherwise, the qPCR C_t value would increase as the total DNA input concentration would be lowered, prohibiting the use of the C_t value for determination of the fraction of Mal3C*pG. The fluorescence response of the DNA binding dye as a function of the Mal3C(*)pG concentration depends on the DNA post-processing method. The fluorescence intensity of the dye is linearly dependent ($R^2 > 0.99$) on the DNA concentration, and the response is identical for Mal3C*pG and Mal3CpG when performing a control methylation reaction for Mal3CpG (Figure 4.5A). Upon the control reaction, Mal3CpG was mixed with the buffer in absence of both *M.SssI* enzyme and S-adenosylmethionine overnight at 37 °C. In case

Mal3CpG is used as received from the manufacturer, the fluorescence response is different compared to Mal3C*pG (Figure S4.1). Likely, the buffer affects the binding efficiency of the fluorescent DNA-binding dye. The slope of Mal3CpG is in that case 1.9-fold lower compared to Mal3C*pG. Therefore, Mal3CpG is used in this study after performing the control methylation reaction.

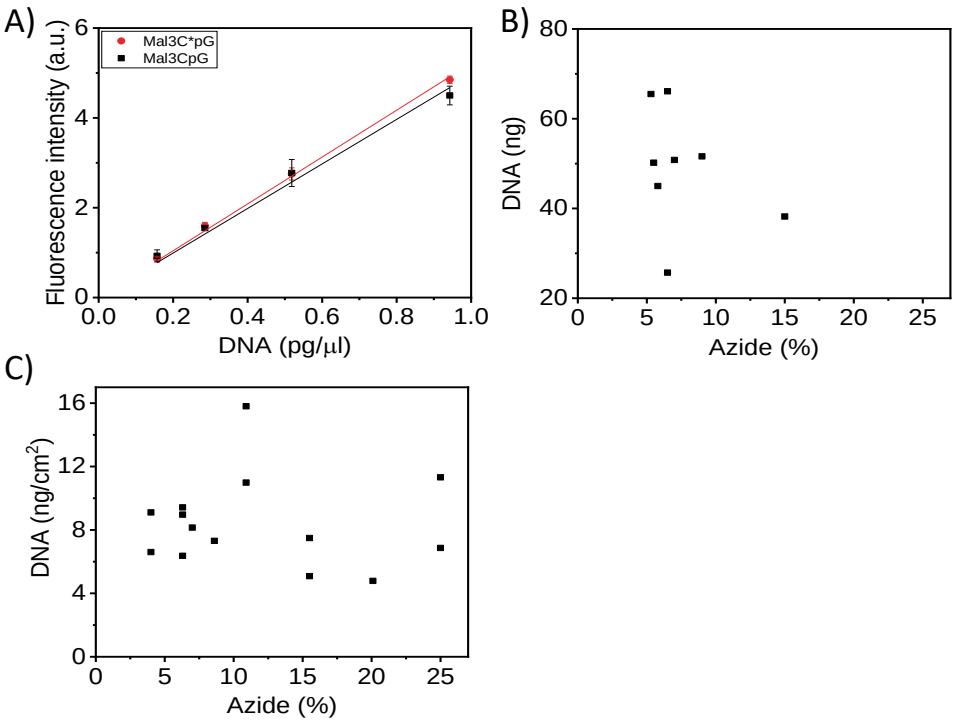

Figure 4.5. A) Calibration line of the Mal3C(*)pG concentration *versus* the intensity of the AccuBlue fluorescent dye that binds double-stranded DNA. The datapoints are fitted with a linear trendline with $R^2 > 0.99$ for Mal3C(*)pG. Error bars represent the standard deviation. B) and C) Amount of DNA eluted from the MBD2-modified surfaces as a function of the percentage of azide-functionalized thiols in the SAM. The 500 nM 1:100 DNA mixture was flushed for B) 30 min and C) 60 min over the surface. The amount of eluted DNA was determined with the AccuBlue dye. Surface-bound DNA was eluted from the B) QCM surface by flushing for 25 min with ammonium hydroxide and C) chip in the larger flow cell by immersion of the surface in 1 mL ammonium hydroxide for 25 min.

Subsequently, we processed the 1:100 mixed DNA samples after adsorption for 30 min to the MBD2 surface in the QCM flow cell followed by flushing with ammonium

hydroxide to elute surface-bound DNA for 25 min. Next, the eluted DNA sample was concentrated to a volume of 30 µL. The DNA concentration of the eluted DNA was determined using the AccuBlue dye as explained above. Between 25 ng and 66 ng DNA per substrate was eluted from the MBD2 surfaces (Figure 4.5B). Therefore, up to a 25-fold higher amount of DNA was eluted from the surface compared to the amount of bound DNA. A likely reason for the more than expected amount of eluted DNA is the elution of DNA that had been bound non-specifically to the tubing and/or the flow cell. We hypothesize that the MBD2 protein first binds non-specifically at the tubing and/or flow cell, thus creating extra DNA binding sites.

To prevent the elution of non-specifically bound DNA from the QCM flow cell set-up, the elution was performed outside the flow cell. Also, the surface area of a QCM gold chip is limited (≈1 cm^2), which limits the amount of DNA that can be captured on the surface. Therefore, the enrichment of the DNA mixtures was performed using 3.6 cm^2 gold-coated substrates in a custom-made Teflon flow cell. To study the effect of the MBD2 surface receptor density on the amount of bound DNA, SAMs with 4% - 25% of azide-functionalized thiols were used. The Teflon flow cell requires larger volumes of DNA solution for the DNA binding step compared to the QCM experiments due to the increase of the dead volume. A volume of 1.8 mL of the 500 nM DNA mixture (with 498 ng Mal3C*pG and 49.9 µg Mal3CpG) was flushed over the MBD2-coated surface for 60 min using a flow rate of 30 µL/min without recycling the DNA solution. This is a 3-fold increase in the total amount of DNA compared to the QCM experiments described above. After the DNA binding step, the surface was washed with BB. Then the chip was taken out of the Teflon flow cell set-up. Surface-bound DNA was eluted by immersion of the chip in 1 mL of ammonium hydroxide solution ensuring full immersion of the chip in the eluent. After elution of the bound DNA, the DNA concentration of the enriched DNA mixture was determined by the AccuBlue dye method (see above). The amounts of DNA eluted from the substrates is on average, 8.4±2.9 ng/cm^2 (Figure 4.5C). The amount of enriched DNA (corresponding to approximately 30 ng for the whole 3.6 cm^2 sample) is in decent agreement with the 4.5±1.0 ng/cm^2 of DNA bound at the MBD2 surfaces determined by QCM with a DNA binding time of 60 min. The higher eluted DNA amounts observed in the large flow cell applied for studying the elution are very likely due to the use of a different flow cell and the larger total amount of Mal3C(*)pG that was flushed over the surface compared to the QCM experiments. These results confirm that the elution of the DNA with aqueous ammonium hydroxide leads to essentially complete removal of the DNA from the surface.

4.2.3 Selectivity of hmDNA enrichment from DNA mixtures

The ratio of Mal3C*pG and Mal3CpG in a DNA mixture is determined by qPCR after treating the enriched DNA mixtures with the methyl-sensitive restriction enzymes HhaI

and HpaII. To create a calibration line, DNA mixtures with 1:0, 1:1, 1:10, 1:100, 1:1000, and 0:1 ratios of Mal3C*pG and Mal3CpG were characterized directly by qPCR, thus without enrichment on an MBD2 surface. The DNA samples were subjected to the restriction enzyme digest step and subsequently analyzed with qPCR at a constant total DNA input amount. A clear dependency between the C_t values and the fraction of Mal3C*pG in the DNA mixture was observed (Figure 4.6A). The lowest C_t values (16.8±1.2) were obtained for the samples containing only Mal3C*pG (1:0). On the other hand, the highest C_t values (26.3±1.3) were observed in case only Mal3CpG is present (0:1) due to that Mal3CpG is not protected against the restriction enzyme digest. The difference in C_t values (ΔC_t) between Mal3C*pG and Mal3CpG is equal to 9.5 cycles, which thus defines the working range for this analysis. This difference amounts to an approximately 700-fold concentration difference between Mal3C*pG and Mal3CpG attributed to the DNA digestion step, assuming that a 10-fold concentration increase corresponds to a ΔC_t of 3.3 cycles at 100% efficiency independent of the composition of the DNA mixture. Because the number of cycles for the 100% Mal3CpG sample is still below the threshold for accurate C_t detection (typically 35 cycles), the value indicates that approximately 0.1% of non-methylated DNA remains after the digestion step. For the mixed DNA samples 1:1 to 1:100, the C_t value is decreasing linearly when the amount of Mal3C*pG is increased in the DNA mixture. The decrease in the C_t value is due to the presence of more Mal3C*pG, thus resulting into more DNA remaining after the digestion of Mal3CpG by the restriction enzymes. The C_t of the digested 1:1000 mixture showed only a slightly higher C_t value compared to the 1:100 DNA mixture. The C_t of the 100% Mal3CpG sample indicates a boundary of the concentration range that can be measured accurately by this method. Overall, the method enables the determination of the enrichment selectivity using DNA mixtures with a 1:100 ratio of Mal3C*pG and Mal3CpG as input, which we used in the MBD2 capture devices.

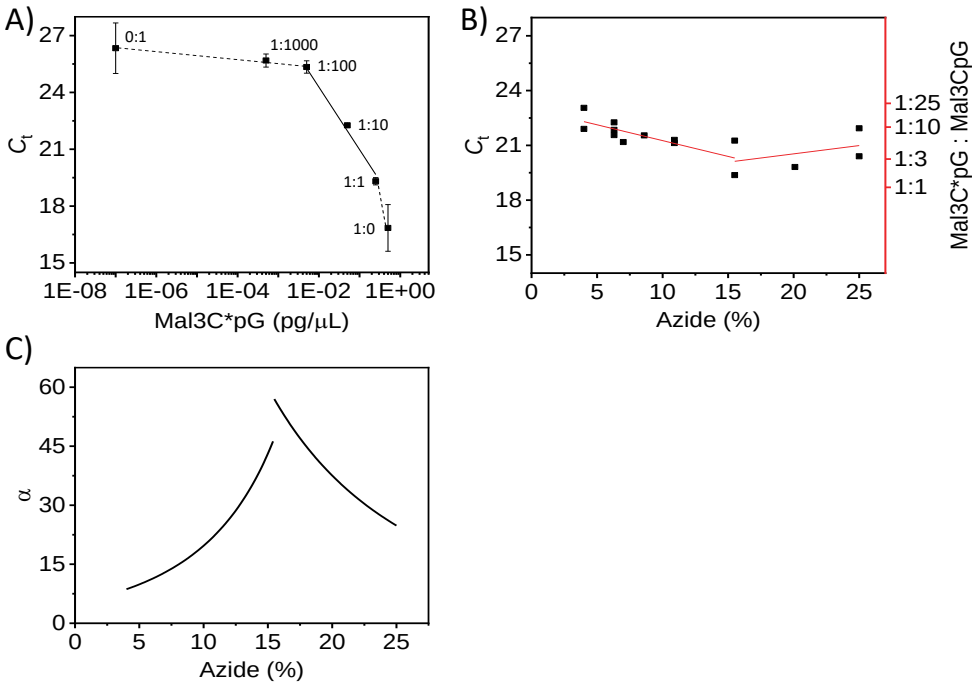

Figure 4.6. A) Calibration line of the qPCR C_t value as a function of the amount of Mal3C*pG for standardized DNA mixtures with Mal3CpG. The DNA samples were subjected to the methyl-sensitive restriction enzyme digest with HhaI and HpaII prior to qPCR analysis at a DNA amount of 3 ng. The total DNA concentration used for each DNA mixture/sample upon qPCR was 0.5 pg/µL. The linear trendline (R^2 > 0.97) between 1:1 and 1:100 is based on a slope of 3.3 C_t difference per 10-fold increase in the DNA concentration. Between 1:0 - 1:1 and 1:100 – 0:1 a dashed line is added as a guide to the eye. Error bars represent the standard deviation. B) C_t value of enriched DNA mixtures as a function of the fraction of azide-functionalized thiols in the SAM. The 1:100 DNA mixture was flushed over the surface for 60 min followed by elution of surface-bound DNA by immersing the chip in the ammonium hydroxide eluent. The DNA concentration of eluted samples was determined by the AccuBlue dye method. Restriction enzyme digest was performed at 3 ng DNA followed by qPCR using a DNA concentration of 0.5 pg/µL. The datapoints in the ranges of 4% - 15% and 15% - 25% azide was fitted with a linear trendline (red) and converted with the calibration plot in A) to determine the ratio of Mal3C*pG and Mal3CpG in the enriched DNA mixtures (right y-axis). C) hmDNA enrichment selectivity factor α as a function of the azide content in the SAM for the enriched 1:100 DNA mixture, as calculated from the two trendlines displayed in B) and eq. 1.

The DNA samples eluted from the MBD2 surfaces were then subjected to the methyl-sensitive restriction enzyme digest followed by qPCR analysis to determine the fraction of methylated DNA at varying MBD2 densities. The obtained C_t values were converted to determine the ratio of Mal3*CpG and Mal3CpG in the enriched DNA mixtures (Figure 4.6B). The fraction of methylated DNA in the enriched DNA is directly dependent on the applied MBD2 surface receptor density showing a distinct optimum at 15.5% of azide-functionalized thiols in the SAM. The average C_t value at 15.5% of azides corresponds to a ratio of 1:2.1, thus, indicating a Mal3C*pG fraction of approximately 30% in the enriched mixture. Therefore, the Mal3C*pG content increases with 30-fold in the enriched DNA mixture compared to 1% Mal3C*pG content in the non-enriched DNA mixture. Both at lower and higher azide contents than 15.5% the methylated DNA fraction in the enriched DNA mixtures decreases linearly as a function of the azide content. At 4% and 25% azide, the average C_t values correspond to ratios of 1:13.2 (7.0 % Mal3C*pG) and 1:4.7 (19.7% Mal3C*pG) of methylated DNA and non-methylated DNA in the enriched DNA mixture, respectively. The methylated DNA fraction in these cases is significantly lower compared to the methylated DNA fraction at 15% of azide. The decrease in the methylated DNA fraction at >15% of azide is expected as significant amounts of non-methylated DNA starts binding to the MBD2 surface at these densities (Chapter 3). Also, >15% of azide results in the formation of a close-packed MBD2 protein layer resulting in lowering of the number of active MBD2 sites (Chapter 3). At azide contents <15%, the MBD2 surface receptor density is decreasing. As a consequence, the overall binding affinity (avidity) of Mal3C(*)pG for the MBD2 surface is reduced. Reduction in avidity likely results into longer times required to reach comparable DNA surface coverages on the MBD2 surface. For example, it has already been shown in Figure 4.3B that an increase in the DNA binding time from 30 min to 60 min results in more DNA binding, independent of the used MBD2 surface receptor density. Longer equilibration times are likely to be especially profound for Mal3C*pG as the concentration of Mal3C*pG is a 100-fold lower in the DNA mixture compared to Mal3CpG. As a consequence, the MBD2 sites will become occupied more slowly over time by Mal3C*pG upon decrease of the (effective) MBD2 density, leaving more MBD2 sites available to interact with Mal3CpG. The binding of non-methylated DNA, with a binding time of 30 min at comparable DNA concentrations <15% of azide, was not observed in our previous work discussed in Chapter 3. Probably, the binding of non-methylated DNA was below the detection limit of the QCM with the studied DNA binding time of 30 min, while here a DNA binding time of 60 min was applied.

From the fraction of methylated DNA in the enriched DNA mixtures the hmDNA enrichment selectivity factor α was calculated by dividing the Mal3C*pG/Mal3CpG ratio after enrichment by that ratio before enrichment (Equation 1).

$$\alpha = \frac{Mal3C^{*}pG_{\mathrm{out}} / Mal3C^{*}pG_{\mathrm{in}}}{Mal3CpG_{\mathrm{out}} / Mal3CpG_{\mathrm{in}}} \quad (1)$$

where *Mal3C(*)pG*$_{out}$ and *Mal3C(*)pG*$_{in}$ indicate the amounts of Mal3C(*)pG in the enriched and input DNA mixtures, respectively. Highly selective hmDNA enrichment systems thus promote a high enrichment selectivity factor. The value of α for the SAM with 15% of azide is 57, which is the highest hmDNA enrichment selectivity achieved (Figure 4.6C). Lower hmDNA enrichment selectivities have been observed for surfaces with less or more than 15% azide in the SAM. Determination of the hmDNA enrichment selectivity confirms thus the importance of tuning the MBD2 surface receptor density to achieve efficient hmDNA enrichment.

4.3 Conclusion

In this work, the hmDNA enrichment selectivity of DNA mixtures with a methylated DNA content of 1% was determined as function of the MBD2 surface receptor density. A model DNA target of 90 bp in length with 3 Cp(*)Gs was chosen to determine the hmDNA enrichment selectivity. Tuning the fraction of azide-functionalized thiols in the SAM enables to control the MBD2 surface receptor density. The hmDNA level in enriched DNA mixtures was determined by reacting the enriched DNA mixtures with methyl-sensitive restriction enzymes followed by qPCR characterization. The hmDNA level was related to the qPCR C_t value and found quantifiable between 0.01% and 100% of hmDNA in the DNA mixture. The DNA that binds to the MBD2-modified surfaces upon hmDNA enrichment was successfully eluted by aqueous ammonia hydroxide pH 11.3. The hmDNA level in the enriched DNA mixture was dependent on the azide percentage in the SAM. The highest hmDNA enrichment selectivity was obtained using a SAM with 15% of azide, resulting in a hmDNA level of approximately 30% in the enriched DNA mixture. This is a 30-fold increase in the hmDNA level in comparison to the non-enriched DNA mixture. Furthermore, the use of less or more than 15% azide in the SAM resulted in a reduction of the hmDNA level down to 7.0% in the enriched DNA mixtures. Therefore, MBD2 surface receptor density control is essential for selective hmDNA enrichment of DNA mixtures.

Future research should assess the effects of DNA fragment size, the degree of methylation and the DNA binding time on the hmDNA enrichment selectivity. Furthermore, the flow cell used in this study can be further miniaturized into a microfluidic chip. Likely, further downscaling will result in a reduction of mass transport limitation, thus causing more DNA surface binding in a shorter period of time. It is also interesting to study whether such a microfluidic chip can be implemented in a clinically usable assay.

4.4 Acknowledgement

Marcel de Bruine is gratefully thanked for help with the design and production of the Teflon flow cell. Dorothee Wasserberg, Alessandro Carlino, and Lisette Knippenborg are acknowledged for their help with the qPCR experiments.

4.5 Experimental section

4.5.1 Materials

Gravity flow columns, Experion DNA chips, Microseal 'B' PCR Plate Sealing Film, SsoAdvanced Universal SYBR Green Supermix and ddPCR™ 96-well plates were obtained from BioRad. NaCl, β-mercaptoethanol, dimethyl sulfoxide ≥99.7% (DMSO), EDTA, $MgCl_2$ ≥ 98.0% ($MgCl_2$), LB Broth, lysozyme from chicken egg white (≥90% lysozyme), phenylmethanesulfonyl fluoride (PMSF), ribonuclease A from bovine pancreas (RNAse), deoxyribonuclease I from bovine pancreas (DNAse), kanamycin sulfate from *Streptomyces kanamyceticus*, nickel(II) chloride hexahydrate ($NiCl_2$), N_α,N_α-bis(carboxymethyl)-L-lysine hydrate ≥ 97.0%, phosphate-buffered saline (PBS) tablets for 10 mM solution, triethylamine, ammonium hydroxide solution 25%, H_2SO_4 95-97%, 0.2 µm membrane filter and sodium dodecyl sulfate ≥99% (SDS) were purchased from Sigma Aldrich. Tris(hydroxymethyl)aminomethane (Tris), isopropyl-β-D-thiogalactopyranoside ≥ 99% (IPTG), Tygon LMT-55 tubing, AccuBlue® next generation dsDNA quantification kits, H_2O_2 33 % and absolute ethanol were bought from VWR. Imidazole 99% and Triton X-100 were obtained from ACROS Organics. NiNTA-agarose beads were purchased from Protino®. PD-10 Sephadex™ desalting columns were obtained from GE Health. DBCO-PEG_4-NHS ester was purchased from Click Chemistry Tools. All the DNA sequences and primers were bought from Eurofins Genomics. Nuclease-free water, CpG methyltransferase (*M.SssI*), rCutsmart buffer™, S-adenosylmethionine, Quick-Load® Purple Low Molecular Weight DNA Ladder, Gel Loading Dye Purple (6X), HhaI and HpaII were purchased from New England Biolabs. $HSC_{11}(EG)_5$-OH and $HSC_{11}(EG)_5$-N_3 were bought from Prochimia. QCM gold-coated chips (QS-QSX301) were obtained from Quantum Design GmbH. NucleoSpin® Gel and PCR Clean-up was purchased from BIOKÉ. SYBR™ Safe DNA Gel Stain was obtained from Thermo Fisher. 96 well Microplate F-Bottom (black, fluotrac, high binding) was bought from Greiner BIO-ONE. 1-inch glass chips coated with 200 nm gold were obtained from Ssens.

4.5.2 Methods

DNA methylation

Methylation of DNA was performed by mixing 4 µg DNA with 8 units of *M.SssI* enzyme, S-adenosylmethionine at a concentration of 600 µM and 2.5 µL rCutsmart buffer™. The reaction volume was increased to 25 µL with nuclease-free water. The reaction was performed at 37 °C for 15 h in a T100 thermocycler (BioRad). The reaction was stopped by heating the mixture to 65 °C for 20 min.

DNA control methylation reaction

Mal3CpG was used in the non-methylated form after performing a control methylation reaction, unless indicated otherwise. A total of 4 µg Mal3CpG was mixed with 2.5 µL rCutsmart buffer™ and nuclease-free water in a total reaction volume of 25 µL. The mixture was heated to 37 °C for 15 h followed by 65 °C for 20 min using the thermocycler.

Methyl-sensitive restriction enzyme digest

DNA was mixed with 1 µL of rCutsmart™ buffer, 5 units HhaI and 5 units HpaII. The DNA amount used upon restriction enzyme digest was between 0.1 ng and 10 ng. The total reaction volume was increased to 10 µL using nuclease-free water. Digestion was performed for 15 h at 37 °C using the thermocycler. Afterwards the enzymes were deactivated by a heat treatment of 85 °C for 20 min.

qPCR

Mal3C(*)pG was amplified with CFX96 Touch qPCR Detection System (BioRad) using primers (Table S4.2) at a concentration of 300 nM, 5 µl SsoAdvanced Universal SYBR Green Supermix and nuclease free water. The qPCR assay volume was performed in a ddPCR™ 96-well plate using an assay volume of 10 µL. The starting concentration of Mal3C(*)pG upon amplification was 0.5 pg/µL. The 96-well plate was sealed using Microseal 'B' PCR Plate Sealing Film prior to qPCR. qPCR temperature steps were 98 °C for 1 min, 39 cycles of 98 °C for 10 s and 64 °C for 30 s, and 72 °C for 1 min. C_t values were determined at a fluorescence intensity threshold of 150 a.u.

Gel electrophoresis

qPCR-amplified DNA was characterized with gel electrophoresis using a 3% agarose gel stained with SYBR safe. DNA was mixed with Gel Loading Dye Purple prior to loading. On the gel, Quick-Load® Purple Low Molecular Weight DNA Ladder is included as reference. After gel electrophoresis the gel was visualized using Gel Doc™ EZ System (Bio-Rad).

His_{10}MBD2 production and purification

The *E. coli* bacteria were grown up to an optical density (OD) at 600 nm of 0.5 at 37 °C in LB medium with 30 µg/mL of Kanamycin according to the method described in Chapter 3. The culture was cooled down to 17 °C, followed by expression of the His_{10}MBD2 protein after induction with 1 mM of IPTG for 15 h at 17 °C while stirring at 210 rpm. The culture was centrifuged (Allegra™ 25R) at 5000 rpm for 15 min at 4 °C to sediment the bacteria. The bacteria were lysed with sonication in a lysis buffer of 50 mM Tris-HCl pH 7.2, 300 mM NaCl, 30 mM imidazole, 0.1% β-mercaptoethanol, 1 mM EDTA, 20 mM $MgCl_2$, 1 mM PMSF, 0,5 mg/mL lysozyme, 20 µg/mL DNAse, 20 µg/mL RNAse A. Sonication (Fisherbrand™ 120) was performed on ice twice for 30 s with a waiting step in between of 2 min. The sonicated samples were centrifuged at 3100 rpm for 15 min at 4 °C, and the supernatant was then centrifuged at 40000 rpm for 60 min at 4 °C (WX Ultra 90, Thermo Scientific). The supernatant was loaded on a NiNTA column and incubated for 30 min while shaking at 4°C. The column was washed with 25 mL washing buffer (50 mM Tris pH 7.2, 300 mM NaCl, 30 mM imidazole, 0.1% β-mercaptoethanol). His_{10}MBD2 was removed from the NiNTA column with an elution buffer (50 mM Tris pH 7.2, 300 mM NaCl, 650 mM imidazole, 0.1% β-mercaptoethanol). Directly afterwards, the His_{10}MBD2 sample was purified with a PD10 column and eluted in the IB buffer (50 mM TRIS pH 7.2, 300 mM NaCl, 0.1% β-mercaptoethanol). The His_{10}MBD2 sample was aliquoted, snap-frozen and stored at -80 °C until further use.

Synthesis of linker molecule

DBCO-PEG_4-NHS was dissolved in DMSO at 250 mM, directly aliquoted and stored at -18 °C until further use. N_α,N_α-bis(carboxymethyl)-L-lysine hydrate was dissolved in PBS pH 7.4 at 1 mM before the start of the reaction. The dissolved DBCO-OEG_4-NHS was added to the N_α,N_α-bis(carboxymethyl)-L-lysine hydrate solution up to a final concentration of 0.1 mM. The reaction components were stirred overnight at 180 rpm to ensure completion of the reaction.

SAM formation

Gold-coated chips were cleaned in a piranha solution (H_2SO_4:H_2O_2 in ratio 3:1) for 10 s followed by immersion of the chips in Milli-Q water. Afterwards, the chips were rinsed extensively with ethanol, Milli-Q water and ethanol, followed by drying using N_2. The gold chips were then oxidized using UV-ozone (BioForce, Nanosciences) for 30 min. A thiol solution was prepared using $HSC_{11}(EG)_5$-OH and $HSC_{11}(EG)_6$-N_3 at the desired ratio between the two components in ethanol with a total thiol concentration of 2 mM. The oxidized gold chips were completely immersed in the thiol solution overnight to form

the SAM. After the SAM formation the gold chips were rinsed extensively with ethanol, Milli-Q water and ethanol and dried in a stream of N_2.

Quartz crystal microbalance (QCM)

Gold-coated QCM chips modified with the SAM were placed in the QCM Analyzer equipped with four individually addressable flow cells (Biolin Scientific). A flow rate of 30 µL/min was set during the experiments with a peristaltic pump (Biolin Scientific). All solutions were filtered with a 0.2 µm filter prior to use. The frequency of the 5th overtone (f_5), which was normalized for the used overtone, was used in this study. After each QCM experiment the system was cleaned with a 15 min washing step with 1% SDS solution followed by Milli-Q water for 15 min.

Teflon flow cell

Gold-coated chips were mounted in a Teflon flow cell which was produced by 3D printing (Stratasys Objet 30 prime/pro). The channel height of the Teflon flow cell was 2 mm and the surface area of the chip in contact with the reagents equaled to 3.6 cm^2 when including the surface roughness of the gold layer.[58] Tygon tubing was connected to the flow cell at opposite sites functioning as in/outlet. Flow rates of 30 µL/min with a peristaltic pump were applied. All solutions were filtered with a 0.2 µm filter prior to use.

DNA binding to MBD2-coated surfaces

After SAM formation on the gold-coated chips, the linker molecule was flushed over the surface at a concentration of 0.1 mM in PBS pH 7.4 followed by the addition of 25 mM $NiCl_2$ in Milli-Q water, a washing step with Milli-Q and, subsequently, IB. His_{10}MBD2 dissolved in IB at a concentration of 1 µM was added. After MBD2 immobilization, a washing step with IB was applied followed by flushing with BB (50 mM TRIS, 350 mM NaCl and 0.1% Triton X-100). Then DNA dissolved in BB was added followed by a washing step with BB. Binding experiments were performed both in the QCM and the Teflon flow cell with some variation of the applied binding times (Table 4.1). Variations were applied as no waiting time is needed to obtain a stable signal upon use of the Teflon flow cell.

Table 4.1. Binding times of each component used for the binding of DNA to MBD2-coated surfaces in the QCM and Teflon flow cell set-up.

Component	QCM	Teflon flow cell
Linker molecule	1.5 h	1.5 h
$NiCl_2$	10 min	10 min
MQ	5 min	5 min
IB	until signal stability	5 min
MBD2	until signal stability	15 min
IB	1.5 h	1.5 h
BB	until signal stability	5 min
DNA	1 h	1 h
BB	until signal stability	1 h

Elution of DNA bound to MBD2-coated surfaces

DNA bound to an MBD2-coated surface was eluted by flushing the eluent over the surface or by taking the chip out of the QCM/Teflon flow cell followed by full immersion of the chip in the eluent. Three different eluents were used in this study: 4 M NaCl, 100 mM TEA pH 11.5, and 150 mM ammonium hydroxide pH 11.3. The total elution time was 25 min. The eluent was collected and concentrated on a NucleoSpin Gel & PCR Clean-up column in a volume of 30 µL.

DNA concentration determination

The Mal3C(*)pG concentration was determined using AccuBlue® Next generation dsDNA according to the instruction of the manufacturer. The assay volume in each well of the 96-well Microplate F-Bottom was 210 µL. The fluorescence intensity of the samples was measured using a plate reader (SpectraMax® iD3 Molecular Devices) using an excitation and emission wavelength of 468 nm and 507 nm, respectively.

4.6 Supporting information

Table S4.1. DNA sequence of Mal3C(*)pG and Mal2C(*)pG with the C(*)pG location marked.

		5’ - 3’
Mal3C(*)pG	FWD	CAGGCAGATG**CG**CAGCACCAAGCAGAGAGGCCAGGTGCAGGA TCCCAGGCC**CG**AACCAGGCCTGGCTCAGTGGAGC**CG**GAAGGG GCAGGC
	REV	GCCTGCCCCTTC**CG**GCTCCACTGAGCCAGGCCTGGTT**CG**GGC CTGGGATCCTGCACCTGGCCTCTCTGCTTGGTGCTG**CG**CATC TGCCTG
Mal2C(*)pG	FWD	CAGGCAGATG**CG**CAGCACCAAGCAGAGAGGCC**CG**GTGCAGGA TCCCAGGCCAGAACCAGGCCTGGCTCAGTGGAGCAGGAAGGG GCAGGC
	REV	GCCTGCCCCTTCCTGCTCCACTGAGCCAGGCCTGGTTCTGGC CTGGGATCCTGCAC**CG**GGCCTCTCTGCTTGGTGCTG**CG**CATC TGCCTG

Table S4.2. Primer sequence to amplify the 90 bp-long Mal3C(*)pG using qPCR.

	5’ - 3’
FWD	CAGGCAGATGCGC
REV	GCCTGCCCCTTCCG

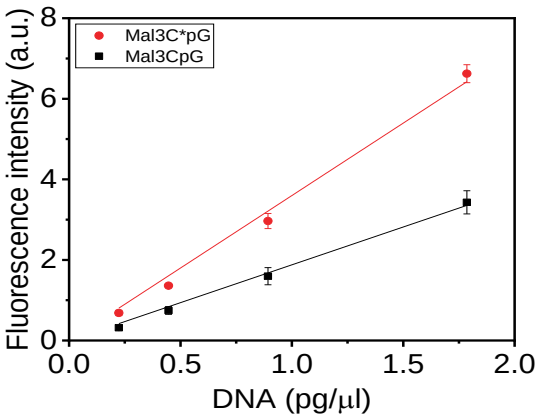

Figure S4.1. Calibration line of the Mal3C(*)pG concentration *versus* the intensity of the AccuBlue fluorescent dye that binds double stranded DNA. Mal3CpG is used as received from the manufacturer. The datapoints are fitted with a linear trendline with $R^2 > 0.99$ for Mal3C(*)pG. Error bars represent the standard deviation.

4.7 References

(1) Sung, H.; Ferlay, J.; Siegel, R. L.; Laversanne, M.; Soerjomataram, I.; Jemal, A.; Bray, F. Global Cancer Statistics 2020: GLOBOCAN Estimates of Incidence and Mortality Worldwide for 36 Cancers in 185 Countries. *CA. Cancer J. Clin.* **2021**, *71*, 209–249.

(2) Chen, X.; Gole, J.; Gore, A.; He, Q.; Lu, M.; Min, J.; Yuan, Z.; Yang, X.; Jiang, Y.; Zhang, T.; Suo, C.; Li, X.; Cheng, L.; Zhang, Z.; Niu, H.; Li, Z.; Xie, Z.; Shi, H.; Zhang, X.; Fan, M.; Wang, X.; Yang, Y.; Dang, J.; McConnell, C.; Zhang, J.; Wang, J.; Yu, S.; Ye, W.; Gao, Y.; Zhang, K.; Liu, R.; Jin, L. Non-Invasive Early Detection of Cancer Four Years before Conventional Diagnosis Using a Blood Test. *Nat. Commun.* **2020**, *11*, 3475.

(3) Normanno, N.; Cervantes, A.; Ciardiello, F.; De Luca, A.; Pinto, C. The Liquid Biopsy in the Management of Colorectal Cancer Patients: Current Applications and Future Scenarios. *Cancer Treat. Rev.* **2018**, *70*, 1–8.

(4) Pantel, K.; Alix-Panabières, C. Liquid Biopsy and Minimal Residual Disease — Latest Advances and Implications for Cure. *Nat. Rev. Clin. Oncol.* **2019**, *16*, 409–424.

(5) Corcoran, R. B.; Chabner, B. A. Application of Cell-Free DNA Analysis to Cancer Treatment. *N. Engl. J. Med.* **2018**, *379*, 1754–1765.

(6) Wan, J. C. M.; Massie, C.; Garcia-Corbacho, J.; Mouliere, F.; Brenton, J. D.; Caldas, C.; Pacey, S.; Baird, R.; Rosenfeld, N. Liquid Biopsies Come of Age: Towards Implementation of Circulating Tumour DNA. *Nat. Rev. Cancer* **2017**, *17*, 223–238.

(7) Schwarzenbach, H.; Hoon, D. S. B.; Pantel, K. Cell-Free Nucleic Acids as Biomarkers in Cancer Patients. *Nat. Rev. Cancer* **2011**, *11*, 426–437.

(8) Ehrlich, M. DNA Hypermethylation in Disease: Mechanisms and Clinical Relevance. *Epigenetics* **2019**, *14*, 1141–1163.

(9) Das, P. M.; Singal, R. DNA Methylation and Cancer. *J. Clin. Oncol.* **2004**, *22*, 4632–4642.

(10) Grady, W. M.; Yu, M.; Markowitz, S. D. Epigenetic Alterations in the Gastrointestinal Tract: Current and Emerging Use for Biomarkers of Cancer. *Gastroenterology* **2021**, *160*, 690–709.

(11) Zeng, J.; Nagrajan, H. K.; Yi, S. V. Fundamental Diversity of Human CpG Islands at Multiple Biological Levels. *Epigenetics* **2014**, *9*, 483–491.

(12) Illingworth, R.; Kerr, A.; DeSousa, D.; Jørgensen, H.; Ellis, P.; Stalker, J.; Jackson, D.; Clee, C.; Plumb, R.; Rogers, J.; Humphray, S.; Cox, T.; Langford, C.; Bird, A. A Novel CpG Island Set Identifies Tissue-Specific Methylation at Developmental Gene Loci. *PLoS Biol.* **2008**, *6*, e22.

(13) Van den Helder, R.; Wever, B. M. M.; Van Trommel, N. E.; Van Splunter, A. P.; Mom, C. H.; Kasius, J. C.; Bleeker, M. C. G.; Steenbergen, R. D. M. Non-Invasive Detection of Endometrial Cancer by DNA Methylation Analysis in Urine. *Clin. Epigenetics* **2020**, *12*, 165.

(14) Yokoi, K.; Yamashita, K.; Watanabe, M. Analysis of DNA Methylation Status in Bodily Fluids for Early Detection of Cancer. *Int. J. Mol. Sci.* **2017**, *18*, 735.

(15) Vrba, L.; Futscher, B. W. A Suite of DNA Methylation Markers That Can Detect Most Common Human Cancers. *Epigenetics* **2018**, *13*, 61–72.

(16) Zhang, J.; Yang, C.; Wu, C.; Cui, W.; Wang, L. DNA Methyltransferases in Cancer: Biology, Paradox, Aberrations, and Targeted Therapy. *Cancers (Basel)* **2020**, *12*, 2123.

(17) Locke, W. J.; Guanzon, D.; Ma, C.; Liew, Y. J.; Duesing, K. R.; Fung, K. Y. C.; Ross, J. P. DNA Methylation Cancer Biomarkers: Translation to the Clinic. *Front. Genet.* **2019**, *10*, 1150.

(18) Rauch, T.; Pfeifer, G. P. Methylated-CpG Island Recovery Assay: A New Technique for the Rapid Detection of Methylated-CpG Islands in Cancer. *Lab. Investig.* **2005**, *85*, 1172–1180.

(19) Cross, S. H.; Charlton, J. A.; Nan, X.; Bird, A. P. Purification of CpG Islands Using a Methylated DNA Binding Column. *Nat. Genet.* **1994**, *6*, 236–244.

(20) Hashimoto, H.; Liu, Y.; Upadhyay, A. K.; Chang, Y.; Howerton, S. B.; Vertino, P. M.; Zhang, X.; Cheng, X. Recognition and Potential Mechanisms for Replication and Erasure of Cytosine Hydroxymethylation. *Nucleic Acids Res.* **2012**, *40*, 4841–4849.

(21) Fraga, M. F.; Ballestar, E.; Montoya, G.; Taysavang, P.; Wade, P. A.; Esteller, M. The Affinity of Different MBD Proteins for a Specific Methylated Locus Depends on Their Intrinsic Binding Properties. *Nucleic Acids Res.* **2003**, *31*, 1765–1774.

(22) Buchmuller, B. C.; Kosel, B.; Summerer, D. Complete Profiling of Methyl-CpG-Binding Domains for Combinations of Cytosine Modifications at CpG Dinucleotides Reveals Differential Read-out in Normal and Rett-Associated States. *Sci. Rep.* **2020**, *10*, 4053.

(23) Heimer, B. W.; Tam, B. E.; Sikes, H. D. Characterization and Directed Evolution of a Methyl-Binding Domain Protein for High-Sensitivity DNA Methylation Analysis. *Protein Eng. Des. Sel.* **2015**, *28*, 543–551.

(24) Yu, Y.; Blair, S.; Gillespie, D.; Jensen, R.; Myszka, D.; Badran, A. H.; Ghosh, I.; Chagovetz, A. Direct DNA Methylation Profiling Using Methyl Binding Domain Proteins. *Anal. Chem.* **2010**, *82*, 5012–5019.

(25) Liu, M.; Movahed, S.; Dangi, S.; Pan, H.; Kaur, P.; Bilinovich, S. M.; Faison, E. M.; Leighton, G. O.; Wang, H.; Williams, D. C.; Riehn, R. DNA Looping by Two 5-Methylcytosine-Binding Proteins Quantified Using Nanofluidic Devices. *Epigenetics Chromatin* **2020**, *13*, 18.

(26) Pan, H.; Bilinovich, S. M.; Kaur, P.; Riehn, R.; Wang, H.; Williams, D. C. CpG and Methylation-Dependent DNA Binding and Dynamics of the Methylcytosine Binding Domain 2 Protein at the Single-Molecule Level. *Nucleic Acids Res.* **2017**, *45*, 9164–9177.

(27) Warton, K.; Lin, V.; Navin, T.; Armstrong, N. J.; Kaplan, W.; Ying, K.; Gloss, B.; Mangs, H.; Nair, S. S.; Hacker, N. F.; Sutherland, R. L.; Clark, S. J.; Samimi, G. Methylation-Capture and Next-Generation Sequencing of Free Circulating DNA from Human Plasma. *BMC Genomics* **2014**, *15*, 476.

(28) Wee, E. J. H.; Ngo, T. H.; Trau, M. Colorimetric Detection of Both Total Genomic and Loci-Specific DNA Methylation from Limited DNA Inputs. *Clin. Epigenetics* **2015**, *7*, 65.

(29) Yegnasubramanian, S.; Lin, X.; Haffner, M. C.; DeMarzo, A. M.; Nelson, W. G.

Combination of Methylated-DNA Precipitation and Methylation-Sensitive Restriction Enzymes (COMPARE-MS) for the Rapid, Sensitive and Quantitative Detection of DNA Methylation. *Nucleic Acids Res.* **2006**, *34*, e19.

(30) Mammen, M.; Choi, S.-K.; Whitesides, G. M. Polyvalent Interactions in Biological Systems: Implications for Design and Use of Multivalent Ligands and Inhibitors. *Angew. Chemie Int. Ed.* **1998**, *37*, 2754–2794.

(31) *Multivalency: Concepts, Research and Applications*; Huskens, J., Prins, L., Haag, R., Ravoo, B. J., Eds.; Wiley, 2018.

(32) Martinez-Veracoechea, F. J.; Frenkel, D. Designing Super Selectivity in Multivalent Nano-Particle Binding. *Proc. Natl. Acad. Sci.* **2011**, *108*, 10963–10968.

(33) Xiong, Z.; Laird, P. W. COBRA: A Sensitive and Quantitative DNA Methylation Assay. *Nucleic Acids Res.* **1997**, *25*, 2532–2534.

(34) Eads, C. A.; Danenberg, K. D.; Kawakami, K.; Saltz, L. B.; Blake, C.; Shibata, D.; Danenberg, P. V; Laird, P. W. MethyLight: A High-Throughput Assay to Measure DNA Methylation. *Nucleic Acids Res.* **2000**, *28*, e32.

(35) Nell, R. J.; Steenderen, D.; Menger, N. V.; Weitering, T. J.; Versluis, M.; Velden, P. A. Quantification of DNA Methylation Independent of Sodium Bisulfite Conversion Using Methylation-sensitive Restriction Enzymes and Digital PCR. *Hum. Mutat.* **2020**, *41*, 2205–2216.

(36) Hashimoto, K.; Kokubun, S.; Itoi, E.; Roach, H. I. Improved Quantification of DNA Methylation Using Methylation-Sensitive Restriction Enzymes and Real-Time PCR. *Epigenetics* **2007**, *2*, 86–91.

(37) Redshaw, N.; Huggett, J. F.; Taylor, M. S.; Foy, C. A.; Devonshire, A. S. Quantification of Epigenetic Biomarkers: An Evaluation of Established and Emerging Methods for DNA Methylation Analysis. *BMC Genomics* **2014**, *15*, 1174.

(38) Burnham, P.; Dadhania, D.; Heyang, M.; Chen, F.; Westblade, L. F.; Suthanthiran, M.; Lee, J. R.; De Vlaminck, I. Urinary Cell-Free DNA Is a Versatile Analyte for Monitoring Infections of the Urinary Tract. *Nat. Commun.* **2018**, *9*, 2412.

(39) Hendrich, B.; Bird, A. Identification and Characterization of a Family of Mammalian Methyl-CpG Binding Proteins. *Mol. Cell. Biol.* **1998**, *18*, 6538–6547.

(40) D'Agata, R.; Bellassai, N.; Jungbluth, V.; Spoto, G. Recent Advances in Antifouling Materials for Surface Plasmon Resonance Biosensing in Clinical Diagnostics and Food Safety. *Polymers (Basel)* **2021**, *13*, 1929.

(41) Vaisocherová, H.; Brynda, E.; Homola, J. Functionalizable Low-Fouling Coatings for Label-Free Biosensing in Complex Biological Media: Advances and Applications. *Anal. Bioanal. Chem.* **2015**, *407*, 3927–3953.

(42) Frutiger, A.; Tanno, A.; Hwu, S.; Tiefenauer, R. F.; Vörös, J.; Nakatsuka, N. Nonspecific Binding—Fundamental Concepts and Consequences for Biosensing Applications. *Chem. Rev.* **2021**, *121*, 8095–8160.

(43) Lin, P.-H.; Li, B.-R. Antifouling Strategies in Advanced Electrochemical Sensors and

Biosensors. *Analyst* **2020**, *145*, 1110–1120.

(44) Kuzmin, A.; Poloukhtine, A.; Wolfert, M. A.; Popik, V. V. Surface Functionalization Using Catalyst-Free Azide–Alkyne Cycloaddition. *Bioconjug. Chem.* **2010**, *21*, 2076–2085.

(45) Knecht, S.; Ricklin, D.; Eberle, A. N.; Ernst, B. Oligohis-Tags: Mechanisms of Binding to Ni^{2+}-NTA Surfaces. *J. Mol. Recognit.* **2009**, *22*, 270–279.

(46) Overmeer, R. M.; Henken, F. E.; Bierkens, M.; Wilting, S. M.; Timmerman, I.; Meijer, C. J.; Snijders, P. J.; Steenbergen, R. D. Repression of MAL Tumour Suppressor Activity by Promoter Methylation during Cervical Carcinogenesis. *J. Pathol.* **2009**, *219*, 327–336.

(47) Bosschieter, J.; Nieuwenhuijzen, J. A.; Hentschel, A.; Van Splunter, A. P.; Segerink, L. I.; Vis, A. N.; Wilting, S. M.; Lissenberg-Witte, B. I.; Van Moorselaar, R. J. A.; Steenbergen, R. D. M. A Two-Gene Methylation Signature for the Diagnosis of Bladder Cancer in Urine. *Epigenomics* **2019**, *11*, 337–347.

(48) Renbaum, P.; Abrahamove, D.; Fainsod, A.; Wilson, G. G.; Rottem, S.; Razin, A. Cloning, Characterization, and Expression in Escherichia Coli of the Gene Coding for the CpG DNA Methylase from Spiroplasma Sp. Strain MQ1(M Sssl). *Nucleic Acids Res.* **1990**, *18*, 1145–1152.

(49) Matsuo, K.; Silke, J.; Gramatikoff, K.; Schaffner, W. The CpG-Specific Methylase Sssl Has Topoisomerase Activity in the Presence of Mg^{2+}. *Nucleic Acids Res.* **1994**, *22*, 5354–5349.

(50) New England Biolabs. Recommended Protocol for Methylation of Genomic DNA https://international.neb.com/protocols/2018/09/12/recommended-protocol-for-methylation-of-genomic-dna (accessed 2022 -07 -06).

(51) Sauerbrey, G. Verwendung von Schwingquarzen Zur Wägung Dünner Schichten Und Zur Mikrowägung. *Z. Physik* **1959**, *155*, 206–222.

(52) Larsson, C.; Rodahl, M.; Höök, F. Characterization of DNA Immobilization and Subsequent Hybridization on a 2D Arrangement of Streptavidin on a Biotin-Modified Lipid Bilayer Supported on SiO2. *Anal. Chem.* **2003**, *75*, 5080–5087.

(53) Höök, F.; Ray, A.; Nordén, B.; Kasemo, B. Characterization of PNA and DNA Immobilization and Subsequent Hybridization with DNA Using Acoustic-Shear-Wave Attenuation Measurements. *Langmuir* **2001**, *17*, 8305–8312.

(54) Su, X.; Wu, Y.-J.; Knoll, W. Comparison of Surface Plasmon Resonance Spectroscopy and Quartz Crystal Microbalance Techniques for Studying DNA Assembly and Hybridization. *Biosens. Bioelectron.* **2005**, *21*, 719–726.

(55) Nair, S. S.; Coolen, M. W.; Stirzaker, C.; Song, J. Z.; Statham, A. L.; Strbenac, D.; Robinson, M. D.; Clark, S. J. Comparison of Methyl-DNA Immunoprecipitation (MeDIP) and Methyl-CpG Binding Domain (MBD) Protein Capture for Genome-Wide DNA Methylation Analysis Reveal CpG Sequence Coverage Bias. *Epigenetics* **2011**, *6*, 34–44.

(56) Chen, K.; Hu, J.; Moore, D. L.; Liu, R.; Kessans, S. A.; Breslin, K.; Lucet, I. S.; Keniry, A.; Leong, H. S.; Parish, C. L.; Hilton, D. J.; Lemmers, R. J. L. F.; van der Maarel, S. M.; Czabotar, P. E.; Dobson, R. C. J.; Ritchie, M. E.; Kay, G. F.; Murphy, J. M.; Blewitt, M. E.

Genome-Wide Binding and Mechanistic Analyses of Smchd1-Mediated Epigenetic Regulation. *Proc. Natl. Acad. Sci.* **2015**, *112*, E3535–E3544.

(57) Biotium. AccuBlue® NextGen dsDNA Quantitation Kit https://biotium.com/wp-content/uploads/2016/12/PI-31060.pdf (accessed 2022 -07 -06).

(58) Movilli, J.; Kolkman, R. W.; Rozzi, A.; Corradini, R.; Segerink, L. I.; Huskens, J. Increasing the Sensitivity of Electrochemical DNA Detection by a Micropillar-Structured Biosensing Surface. *Langmuir* **2020**, *36*, 4272–4279.

Chapter 5

Increasing the sensitivity of electrochemical DNA detection by a micropillar-structured biosensing surface

The available active surface area and the density of probes immobilized on this surface are responsible for achieving high specificity and sensitivity in electrochemical biosensors that detect biologically relevant molecules, including DNA. Here, we report the design of gold-coated, silicon micropillar-structured electrodes functionalized with modified poly-L-lysine (PLL) as adhesion layer to concomitantly assess gain in sensitivity by increase of the electrochemical area and control over the probe density. By systematically reducing the center-to-center distance between the pillars (pitch), denser micropillar arrays were formed at the electrode, resulting in a larger sensing area. Azido-modified peptide nucleic acid (PNA) probes were click-reacted onto the electrode interface exploiting PLL with appended oligo(ethylene glycol) (OEG) and dibenzocyclooctyne (DBCO) moieties (PLL-OEG-DBCO), for anti-fouling and probe binding properties, respectively. The selective electrochemical sandwich assay formation, composed of consecutive hybridization steps of the target complementary DNA (cDNA) and reporter DNA modified with the electroactive ferrocene functionality (rDNA-Fc), was monitored by quartz crystal microbalance. The DNA detection performance of micropillared electrodes with different pitch was evaluated by quantifying the cyclic voltammetric response of the surface-confined rDNA-Fc. By decrease of the pitch of the pillar array, the area of the electrode was enhanced by up to a factor 10.6. A comparison of the electrochemical data with the geometrical area of the pillared electrodes confirmed the validity of the increased sensitivity of the DNA detection by the design of the micropillar array.

This chapter has been published as:

J. Movilli[*], R.W. Kolkman[*], A. Rozzi, R. Corradini, L.I. Segerink, J. Huskens. *Langmuir,* **2020***, 36,* 4272–4279.

[*] = Equal first author contributions

5.1 Introduction

The invention of (bio)sensors represents a breakthrough for life sciences. The possibility to detect specific bioanalytes rapidly and quantitatively has propelled the economic and scientific effort towards the design and production of functional biorecognition devices.[1] Owing to their well-developed miniaturized fabrication processes, high signal-to-noise ratio, and real-time response, electrochemical biosensors are currently the gold standard for daily-life applications such as food/environmental control and point-of-care devices for the detection of biologically relevant molecules such as glucose,[2] phenol,[3] and drugs (*e.g.,* doxorubicin/gentamicin,[4] tobramycin[5]).

At the same time, the progress in genetics and genomics has led to the insight that biomolecules, such as proteins and DNA/RNA variants, can act as biomarkers providing valuable information for early diagnosis and monitoring of several types of tumors and genetic diseases.[6-8] Due to the small sample volume needed for analysis, the possibility of working with body fluids, and the relatively high sensitivity,[9] electrochemical DNA biosensors have gained in popularity as clinical assay devices for diseases that can be detected by DNA biomarkers,[10,11] such as Crohn's disease, multiple sclerosis, cystic fibrosis and cancer.[12-14] Nevertheless, the low concentrations of DNA biomarkers (up to 10^4 units/mL of plasma/serum)[15,16] has fuelled the development of signal amplification methods to achieve highly sensitive electrochemical detection.[17] Strategies have been reported based on enzyme amplification,[18-20] post-modification polymerization of conductive materials,[21,22] as well as the use of electroactive reporter probes.[23-25]

For surface-confined electrochemical DNA biosensors, the intrinsic sensitivity depends strongly on the surface architecture, which affects the display of probes at the interface together with the probe density (which have been defined as crucial parameters in DNA detection),[26-28] and the electrochemically active surface area of the biosensor.[5,29,30] The use of three-dimensional (3D) structures such as polymer brushes,[31] hydrogels,[32] nanodiscs,[33] gold nanoparticles,[34] nanoporous gold,[35] and nano-textured microelectrodes,[36] has significantly improved the electrochemical device performance and consequently the detection limit of target DNA analytes compared to flat substrates. Similarly, conductive macro- and nanopillar-structured substrates have been reported (though not applied in DNA sensing) to provide a higher surface area than planar electrodes.[37-40]

Schröper *et al.* have demonstrated that the electroactive surface area for nanopillar-based devices is often lower than predicted due to the strong dependence on the diffusivity of the electroactive species compared to a flat substrate.[41] On the other hand, microelectrodes and micropillar-structured substrates can steadily generate a higher signal,[42,43] thus representing an alternative for improving the sensitivity of the electrochemical biosensor. The groups of Compton and Del Campo showed with simulations the positive effect of reducing the center-to-center separation (pitch) of

gold-coated micropillars and increasing their aspect ratio on the electrochemical performance in a cyclic voltammetry (CV) setup in the case of electroactive species in solution.[44,45] An experimental demonstration showed a maximal signal enhancement for the peak current density of 1.6 and 6.2 times with respect to the projected surface area, using two different pillar geometries. In addition, Del Campo *et al*. showed the importance of achieving full wetting of the gold-coated micropillar-structured substrates to achieve full penetration of the pillar array by the solution and thus an optimal electrochemical sensitivity of the device.[44]

Poly-L-lysine (PLL) polymers grafted with poly(ethylene glycol) (PEG) units (PLL-PEG) have been shown to increase the lubrication properties of both hydrophobic (polydimethylsiloxane, PDMS) and metal oxide substrates, due to the hydrophilic nature of the PEG chains and the high content of trapped water.[46-48] In addition, modified PLL has been used to functionalize surfaces allowing fast and orthogonal biomolecule immobilization and to provide good anti-fouling properties.[49,50] In particular, PLL grafted with oligo(ethylene glycol) (OEG) and maleimide (Mal) moieties has been exploited by us to control the probe density of both engineered peptide nucleic acid (PNA) and DNA probes for DNA recognition.[27]

Here, we report the design and use of gold-coated, micropillar-structured electrodes, with control over the micropillar pitch to increase the sensitivity, and modified with functionalized PLL to anchor the probes for electrochemical DNA detection. The positively charged PLL, grafted with OEG and dibenzocyclooctyne (DBCO) groups (PLL-OEG-DBCO),[51] was self-assembled on the electrode surface to form a hydrophilic, orthogonally bio-functionalizable layer. An azido-PNA probe with a complementary sequence capable of detecting the *KRAS* gene[16] was used to illustrate potential applications for tumor DNA detection. The choice of PNA as a probe for DNA detection was driven by the higher affinity and selectivity for complementary DNA (cDNA) compared to DNA probes,[52] and their resistance to enzymes present in biological fluids.[53] In addition, the combination of modified PLL anchored with PNA probes has been proven to provide high hybridization efficiencies at elevated surface probe densities by the suppression of electrostatic repulsion occurring in DNA-probe devices.[27] The electrochemical detection of cDNA by a sandwich assay was performed using a reporter probe DNA, complementary to the free 5'-end of the target cDNA, bearing an electroactive ferrocene moiety (rDNA-Fc). The signal generated by CV was evaluated as a function of the micropillar pitch, in order to establish the relationship between the signal gain and the increased surface area, thus providing insight into the potential of the sensitivity gain reached by electrode microstructuring.

5.2 Results and discussion

5.2.1 Micropillar-based electrode design and probe functionalization

To investigate the sensitivity gain in electrochemical biosensors with higher surface areas created by 3D microstructuring, we employed flat (control) and micropillar-structured, gold-coated, silicon substrates with four different pitches (19, 14, 10 and 8 µm). These were used in combination with a proof-of-principle, sandwich assay-mediated recognition of the complementary DNA (cDNA, the model analyte) and rDNA-Fc to assess the electrochemical performance. Figure 5.1A shows the schematic overview of the micropillar biorecognition interface to detect DNA. Smaller pitches result in a larger density of pillars and concomitantly higher electroactive surface area available for subsequent functionalization and DNA binding. Consequently, more modified PLL is adsorbed, and a higher density of DBCO moieties per projected electrode area is displayed on the surface. The probe density on the electrode surface is set by the grafting density of DBCO groups attached to the PLL,[27,51] upon reacting the PNA-azide molecules to the DBCO groups by the strain-promoted azide-alkyne cycloaddition (SPAAC) click reaction (Figure 5.1B and C, Figures S5.1-S5.3).[54] The target cDNA (43 nt) and the reporter rDNA-Fc (23 nt) molecules (Table S5.1) are consecutively hybridized to the surface. Such a sandwich-like assay avoids the necessity of DNA post-modification for introducing the ferrocene redox moiety after the successful dual-hybridization event.[55] The main objective of this work was to observe the relationship between the response obtained from the electroactive rDNA-Fc specifically anchored at the interface and the surface area (enhanced by reducing the pillar pitch), thus demonstrating the signal amplification by micropillar-based electrodes in CV experiments.

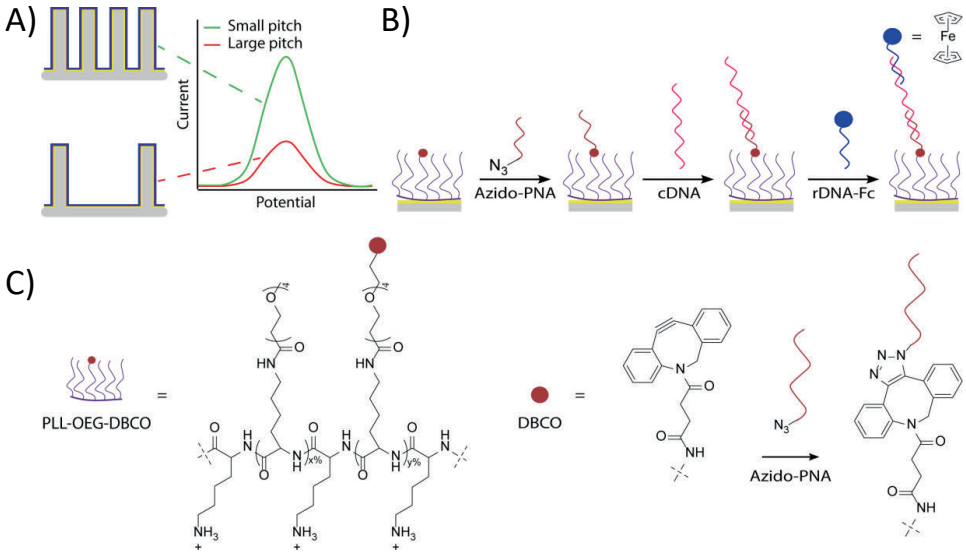

Figure 5.1. A) Schematic representation illustrating the concept of increased electrochemical surface area by reducing the pitch of the electrode design to gain electrochemical sensitivity. B) Overview of the chemical steps occurring at the PLL-OEG-DBCO-modified, gold-coated electrode interface, showing the sequential deposition of: the N_3-PNA probe, cDNA, and rDNA-Fc. C) Chemical structure of the PLL-OEG-DBCO used, together with the SPAAC reaction scheme between DBCO and azido-PNA (structures, sequences and characterization of the PNA and DNA molecules are shown in Figures S5.1-S5.3 and Table S5.1).

Silicon substrates with hexagonal micropillar arrays with a height of 36.7 µm and diameter of 4.0 µm were fabricated by photolithography and deep reactive ion etching (DRIE) according to the procedure reported by Elbersen *et al.*[56] (Figure S5.4). Figure 5.2A shows the micropillar array with a pitch of 8 µm, characterized by high-resolution scanning electron microscopy (HR-SEM; top view shown in Figure S5.5). The final electrode architecture was formed by sputtering a thin layer (≈200 nm) of gold on top of the substrate. Due to the sputter direction normal to the surface, the gold layer was thinner (≈50 nm on average) at the sides of the pillars. Nevertheless, a conformal and fully conductive layer was achieved (Figure 5.2B).

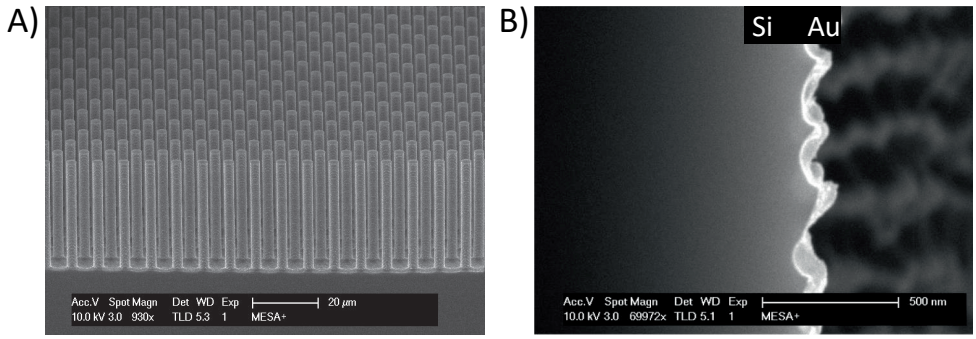

Figure 5.2. HR-SEM images showing: A) a tilted cross section of an 8 µm pitch micropillar-structured silicon substrate, with pillar height and diameter of 36.7 and 4 µm, respectively; B) zoom-in image of a cross-sectioned Si micropillar (taken at approximately halfway the pillar) showing the conformal gold coating (bright) inside the scallops.

The PLL polymer (15-30 kDa) grafted with OEG and DBCO functionalities (Figure 5.1C) was synthesized adapting a previously reported procedure.[27,51] OEG and DBCO groups were covalently grafted to the PLL side-chains in a one-step synthesis by N-hydroxysuccinimide (NHS) ester coupling (see Experimental section). The mol fractions of appended groups in the PLL-OEG-DBCO were determined by ^{1}H-NMR, which yielded percentages of 27.6 for the OEG and 3.0 for the DBCO moieties (Figure S5.6). The total grafting density of functionalized lysine side chains was kept below 35-40% to ensure strong adsorption to the surface.[57,58] The azido-PNA probe was synthesized as previously reported.[59]

As a proof of concept, the surface functionalization processes of modified-PLL deposition, azido-PNA immobilization, and consecutive cDNA and rDNA-Fc hybridization steps were followed on a flat substrate by quartz crystal microbalance with dissipation (QCM-D) monitoring (Figure 5.3). Upon mounting a UV-ozone-activated gold chip in the QCM chamber, both the PLL-OEG-DBCO adsorption and the azido-PNA steps showed a decrease of the resonance frequency (blue line, 5th overtone), which remained stable after washing with phosphate-buffered saline (PBS) (see Figure 5.3A). Consecutive injections of cDNA (43 nt) and rDNA-Fc (23 nt) solutions produced frequency shifts (Δf) of ≈16 Hz and ≈12 Hz (average of two measures), respectively, demonstrating the recognition ability of the DNA-bioresponsive interface and the feasibility of the sandwich assay. These frequency shifts correspond, using the Sauerbrey equation,[60] to cDNA and rDNA-Fc densities of 2.5×10^{12} and 3.4×10^{12} molecules/cm^2, assuming that 80% of the mass is due to adsorbed water.[61] The length difference between the DNA molecules and their hybridization can cause hydration changes and consequently an overestimation of the hybridization efficiency. By taking into account the different numbers of nucleotides between cDNA and rDNA-Fc, the hybridization efficiency was approximately 140% (not corrected for differences in

hydration, as well as the mass and hydration of the Fc moiety), which is within the error for QCM monitoring, as already reported by the Knoll and Höök groups.[62,63]

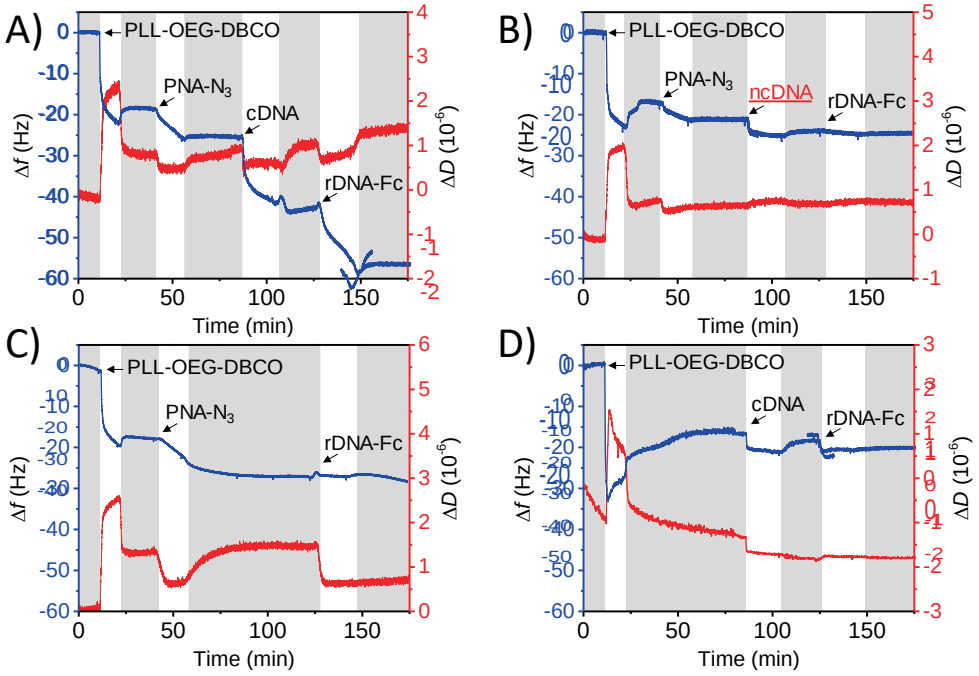

Figure 5.3. QCM-D time traces of: A) the stepwise adsorption process comprising PLL-OEG-DBCO deposition, anchoring of azido-PNA, and the detection of the cDNA and rDNA-Fc; B) control using ncDNA instead of cDNA; C) control without cDNA; d) control without azido-PNA. In all experiments, the concentrations were 0.5 mg/mL for the modified-PLL solutions and 0.5 µM for the azido-PNA, cDNA, rDNA-Fc and ncDNA solutions. PBS (pH 7.4) washing steps (gray bars) were performed before and after every adsorption step. The 5th overtone was used for both Δf and ΔD.

The selectivity of the PNA-modified surface was investigated by controls, using a non-complementary DNA sequence (ncDNA, 43 nt; Figure 5.3B) and by leaving out either the cDNA (Figure 5.3C) or the PNA probe anchoring steps (Figure 5.3D) in the sandwich assay. All controls showed a near or full absence of signal for the DNA and/or rDNA-Fc steps, after the rinsing step. Noteworthy, despite a Δf of approximately 2 Hz for the ncDNA (Figure 5.3B) and 0.5 Hz for the cDNA (in the absence of the azido-PNA step, Figure 5.3D, corresponding to a 3.1% of the total cDNA binding in the detection in Figure 5.3A), fouling was largely absent. In conclusion, a selective response of rDNA-Fc was obtained only in the case of PNA probe anchoring and the double hybridization sequence in the sandwich assay.

In addition, to demonstrate a good wettability of the micropillar-structured substrates by means of modified PLL, contact angle goniometry was performed on three model substrates, two with a micropillar array having pitches of 19 µm and 8 µm and a flat substrate. The low values reported in Table S5.2 indicate good wetting, in agreement with the presence of the adsorbed PLL-OEG-DBCO and the increased hydrophilicity in the micropillar area even after 24 h. Overall, these results indicate the feasibility of probe anchoring and the performance of the sandwich assay in a micropillar array without wetting problems.

5.2.2 Performance of micropillar electrodes in electrochemical DNA detection

The micropillar-structured electrodes used in this work consist of two parts, namely the pillared section, where the micropillars are positioned, and a flat area surrounding the pillar array, as schematically displayed in Figure 5.4. The projected areas of the flat and pillared sections (PA_f and PA_p) are 0.19 cm^2 and 0.25 cm^2, respectively (thus, the total projected surface area PA_{tot} = 0.44 cm^2). Upon the introduction of the micropillars in the electrode design, a theoretical surface area enhancement factor (*SE*) (= A_{tot}/PA_{tot}, where A_{tot} is the total geometric electrode area) is defined. When taking into account only the micropillared section of the electrode, the geometric surface area of that section (A_p) is expected to increase with a factor $1+\frac{2}{3}\sqrt{3}\cdot\pi\cdot d_p\cdot h_p/p^2$ (*i.e.*, the theoretical surface enhancement factor for the pillared section, SE_p, see Table S5.3), where d_p is the pillar diameter, h_p is the pillar height, and *p* is the pitch of the hexagonal micropillar array (see Electrochemical analysis section in the SI and Figure S5.7).

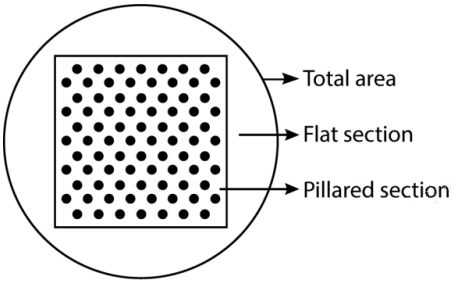

Figure 5.4. Schematic top-view representation of the whole projected micropillar-structured electrode area (PA_{tot} = 0.44 cm^2), showing the micropillar (pillared section, PA_p = 0.25 cm^2) and the surrounding flat (flat section, PA_f = 0.19 cm^2) area.

The increase of the surface area by the micropillars was experimentally assessed using CV. The electrochemically active area of two gold-coated micropillar-structured substrates (19 and 8 µm pitch) and of a flat sample was determined using a 0.1 M solution of H_2SO_4.[41] Qualitatively, the areas of both the oxidation and reduction peaks

were significantly higher for the micropillar-structured substrates compared to the flat one (Figure S5.8). By integrating the reduction peaks, the total electroactive surface areas ($A_{tot,exp}$) were 0.57 cm^2 for the flat electrode and 1.26 cm^2 and 3.68 cm^2 for the micropillar-structured ones (with pitches of 19 µm and 8 µm, respectively, Table S5.4). For the flat sample, the observed area is 1.29 times higher than the geometric area, which is attributed to substrate roughness introduced by the gold sputtering process. For the pillared samples, however, the experimental areas were approximately a factor 1.5 higher than the expected geometric surface areas. This higher increase for the pillared samples is attributed to the combined roughness effects caused by scallop formation, the roughness of the Si surface (both introduced by the DRIE etching process), and the Au sputtering process. For this reason, two different roughness factors were defined, one for the flat section (s_f = 1.29, Electrochemical analysis section in the SI) and one for the pillared section (s_p = 1.48; see Figure S5.9). The $A_{tot,exp}$ values were found to be in good agreement with the geometric surface area calculations after including the roughness factors, with a maximum error <8%. The experimental surface enhancement factors for the total area (flat + pillared sections) were then calculated by the ratio of the experimental surface area of a micropillared electrode and that of the flat one, amounting to 2.21 and 6.46 for the 19 and 8 µm pitch, respectively. When viewing the area increase effect of the pillared section only, surface enhancement factors of 3.14 and 10.6 were found, showing a clear contribution of the pillars and a decreasing pitch on the expected electrochemical signal amplification (see Electrochemical analysis in the SI).

The relationship between the electrode surface area and the DNA sensitivity was quantified by CV experiments using the DNA sandwich detection scheme (Figure 5.1B). Micropillar-structured electrodes with pitches of 19, 14, 10, 8 µm and a flat substrate, pre-incubated with PLL-OEG-DBCO and azido-PNA probe solutions, were covered with a cDNA solution followed by rDNA-Fc deposition to perform the CV measurements after the sandwich assay hybridization (Figure S5.10). The dependence of the total charge involved in the redox process (Q) due to the surface-anchored electroactive Fc moiety, which is related to the peak area in the CV, was evaluated as a function of the scan rate, and the results are presented in Figure S5.11. The constant values of Q *vs* scan rate indicate that the electron transfer processes occurred at the interface as expected for surface-confined species. Control experiments performed by exploiting ncDNA (Figure S5.12A) or by omitting one step of the sandwich assay (azido-PNA anchoring or cDNA hybridization, Figure S5.12B and C) showed the absence of physisorbed electroactive material, which is attributed to the retained anti-fouling properties of the self-assembled modified PLL at the electrode interface, and thus confirms the specificity of the sandwich assay.

The DNA sensitivity enhancement was assessed by evaluating the dependence of Q (from Figure S5.11) on the pitch p of the micropillar-structured electrodes. Figure 5.5 shows a linear increase of Q *versus* $1/p^2$, confirming the effect of the pillar architecture on the detected signal. In this graph, the intercept with the y-axis indicates the flat sample. The linearity of the fit demonstrates not only the absence of diffusion effects

but also the uniformity of the detected rDNA-Fc and cDNA. Consequently, assuming both hybridization steps to be 100% efficient, the surface coverage Γ could be derived from the slope (see the Electrochemical analysis section in SI), providing a value of $(9.0\pm0.2)\times10^{-12}$ mol/cm^2, or $(5.4\pm0.1)\times10^{12}$ rDNA-Fc moieties/cm^2, which matches well to the results obtained from QCM as described above. When using the semi-empirical method described in our previous work,[27] using PLL-appended maleimide reactive groups to bind PNA probes applied to a flat substrate, a density of 3.7×10^{12} molecules/cm^2 was expected, which compares well with the value observed here. Thus, these results validate the modified-PLL approach to control the density of probe molecules at both flat and micropillar-structured substrates.

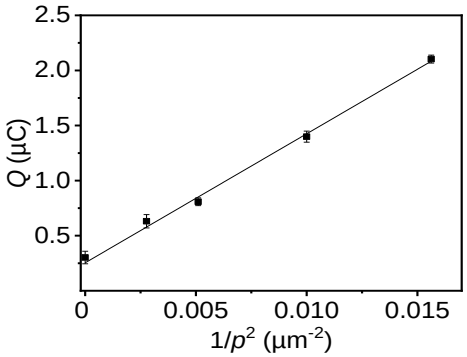

Figure 5.5. Dependence of the total charge *Q* involved in the surface-confined redox process of the Fc-covered electrodes (0.1 M $NaClO_4$ electrolyte) resulting from the sandwich assay, as a function of $1/p^2$ (where *p* is the pitch). Datapoints correspond to the average values of *Q* for the flat and 19 µm, 14 µm, 10 µm, and 8 µm pitch samples, derived from the experiments shown in Figure S5.10. The concentrations of the species used for the DNA binding scheme were 1.0 mg/ml for modified PLL, 0.5 µM for azido-PNA, cDNA and rDNA-Fc in PBS (pH 7.4). The equation of the linear fitting is y=117.10x (±3.80) + 0.25 (± 0.04). The error bars indicate the standard deviation.

A comparison of the two extremes in Figure 5.5, corresponding to the flat and the 8 µm pitch micropillar-structured substrates, shows that the signal enhancement due to the occurrence of the pillar array was approximately a factor of 7.0. The reported value agrees with the experimental surface enhancement factors found by the sulfuric acid measurements, confirming that the increase of the electroactive surface area is the key factor in improving the performance of surface-based electrochemical DNA sensors. When comparing only the pillared section of the micropillar array sample to the flat sample, an enhancement factor of 10.6 was deduced. Overall, these data confirm that the 3D electrode interface design, in correlation with the probe density control, can rationally define the gain in sensitivity for electrochemical DNA detection, showing how the combinations of substrate and biosensing layer can determine the outcome of the recognition device.

5.3 Conclusion and outlook

In summary, we have presented the potential gain in sensitivity for the electrochemical DNA detection by the application azido-PNA probes clicked to a PLL-OEG-DBCO adhesion layer adsorbed on micropillar-structured substrates at various pitches. Compared to flat substrates, the densely structured micropillar arrays allowed up to one order of magnitude larger electrochemical active surface areas that can accommodate comparatively more PNA probes and consequently more target DNA to be detected by the final sandwich assay. The total amount of redox charges from the hybridized reporter rDNA-Fc probe scaled linearly with the electrochemically active surface area, defined by the pitch, indicating the surface-confined electron transfer and similar probe densities between substrates. Overall, this proof-of-concept micropillar-structured electrode design, combined with the surface functionalization approach of modified PLL, increased the total sensitivity by more than one order of magnitude.

Micropillar-structured electrodes improve the electrochemical detection of, among others, DNA molecules in buffer and clinical samples exploiting the third dimension by enhancing the detection area and, thus, the sensitivity. The proposed design gives room for further customizing the physical (substrate) and chemical (adhesion layer) characteristics of the biorecognition surface. Consequently, the geometrical parameters and the probe density can be varied to maximize the sensitivity. By eliminating the flat section of the current electrode, a fully covered micropillar electrode might further improve the amplification factor. Moreover, different etching recipes could produce taller pillars. As an example, the hypothetical use of 125 µm long pillars, as exploited by Del Campo, together with halving both the pitch and pillar diameter, would have generated a 70 times higher electrochemical signal compared to a flat substrate. Other contributions can be obtained from the surface roughness and the probe density, by enhancement of the grafting density of appended groups at the PLL, which could result in a final signal enhancement factor of 2-3 orders of magnitude. The occurrence of diffusion limitations, as well as electrostatic and steric repulsion of the incoming DNA, needs to be investigated. However, these effects might be reduced by integrating such 3D architectures in microfluidic devices. All in all, the advantages of probing more sensing surface, the possible extension to other detection systems, together with the orthogonal control of the biorecognition interface at the molecular level, define the potential directions for producing label-free signal amplification at electrochemical, optical, and gravimetric biosensing devices.

5.4 Acknowledgments

Jacopo Movilli is acknowledged for the PLL synthesis. Andrea Rozzy and Roberto Corradini are gratefully thanked for providing the PNA probe.

5.5 Experimental section

5.5.1 Materials

Poly-L-lysine hydrobromide (MW = 15-30 kDa by viscosity), $NaClO_4$, deuterated water and tablets for 10 mM PBS solution (pH 7.4), were obtained from Sigma-Aldrich. H_2SO_4 (95%) was purchased from VWR Chemical and HCl was obtained from SelectiPur. Methyl-OEG_4-NHS ester was obtained from ThermoFisher Scientific, while DBCO-OEG_4-NHS was obtained from Click Chemistry Tools. The membrane for dialysis (Spectra/Por, 6-8 kDa cutoff, diameter 6.4 mm) were purchased from Spectrum Labs, Greece. cDNA (complementary to KRAS sequence: 43 nt, 5'-ATG ACTGAATATAAACTTGTGGTAGTTGGAGCTGGTGGCGTAG-3') and ncDNA (42 nt, 5'-CTACGCCACCTCAACCTA CGCCACCTCCACCTACGCCACCTC-3') were purchased from Eurofins Genomics and used as received. The ferrocene-labelled DNA (23 nt; MW 7487 g/mol; 5'-ACCACAAGTTTATATTCAGTCAT-Fc-3') was aquired from Biomers.net GmbH. Gold QCM chips (with a fundamental frequency of 5 MHz) were purchased from Biolin Scientific. Silicon p^{++} wafers (<100> oriented, one-side polished, 525±25 µm substrate thickness, 0.01-0.025 Ωcm resistivity) were obtained from Okmetic Finland, while the positive Olin 907-17 photoresist was obtained from Arch Chemicals. The PNA probe was synthesized using a previously described procedure.[59]

5.5.2 Methods

Synthesis and Quantification of PLL-OEG-DBCO grafted percentages

The synthesis of PLL-OEG-DBCO and the quantification of the molfractions of OEG and DBCO grafted to the PLL backbone were done adapting previously reported procedures.[27,51,57] Briefly, 10 mg/ml of PLL HBr were dissolved in PBS 7.4, and stoichiometric amounts of Methyl-OEG_4-NHS and DBCO-OEG_4-NHS (both dissolved in DMSO at concentration of 250 mM) were added under vigorous stirring. After 4 h, the solution was dialyzed with a dialysis membrane (molecular cut-off 6 to 8 kDa) against decreasing concentrations of PBS in Milli-Q water, until a full 24 h cycle in Milli-Q water. The final solution was freeze-dried overnight. The obtained product was analyzed by NMR and stored at -20°C in Milli-Q water. Quantification of the molfractions has been reported in the Supporting Information.

^{1}H NMR of PLL-OEG-DBCO (400 MHz D2O) δ [ppm] = 1.26–1.56 (lysine γ-CH_2), 1.61-1.82 (lysine β, δ-CH_2), 2.48 (ethylene glycol CH_2 from both OEG and DBCO coupled, -CH_2-C(=O)-NH), 2.96 (free lysine, H_2N-CH_2), 3.14 (ethylene glycol CH_2 of coupled lysine from both OEG and DBCO, C(=O)-NH-CH_2-), 3.35 (OEG methoxy, -O-CH_3), 3.59-3.77 (ethylene glycol from both OEG and DBCO, CH_2-O-), 4.27 (lysine backbone, NH-CH-C(O)-), 7.22-7.69 (DBCO from coupled DBCO, CArH).

Micropillar-structured substrate fabrication

Micropillar-structured electrodes were fabricated according to a reported procedure.[56] In summary, a positive photoresist (Olin 907-17) was deposited on a p^{++} silicon substrate followed by photolithography to create a circular patterned photoresist (5 × 5 mm) with spacing between the circles varying between 8 and 19 µm (Figure S5.4 step A). Micropillar-structured substrates were formed via DRIE (SPTS Pegasus, etching rate of ~ 10 µm/min, 20 °C) until the desired micropillar height was achieved (Figure S5.4 step B). The created substrates were then cleaned in O_2/CF_4 plasma (Tepla 360) for 30 min and in a solution of HCl, H_2O_2, and H_2O (1:1:5 ratio, 70°C) for 15 min to strip the fluorocarbon residues and photoresist from the substrates. Prior to the gold sputtering the silicon modified substrates were cleaned for 10 min in HNO_3 and 30 s in HF to remove the silicon dioxide layer. Immediately after the HF step, a gold layer was sputtered (TCOathy) conformally over the entire substrate at 10^{-2} mbar and 50 W for 1800 s (Figure S5.4 step C).

Quartz Crystal Microbalance (QCM)

Gold-coated (50 nm, QSX301) QCM-D chips from LOT-Quantum were cleaned for 5 min in basic piranha solution (H_2O: NH_4OH: H_2O_2 in ratio 5:1:1) at 70 °C for 5 min and then washed extensively with Milli-Q water and EtOH. After drying under nitrogen flow, and oxidized with UV-ozone (Bioforce chamber, Nanosciences) for 15 min, the chips were mounted in the chambers and a flow rate of 80 µl/min was used for all the steps. QCM-D measurements were performed using a Q-Sense E4 4-channel quartz crystal microbalance with a peristaltic pump (Biolin Scientific), monitoring the 5^{th} fundamental overtone. All experiments were performed in PBS buffer solution (10 mM, pH 7.4) at 22 °C. The Δf for cDNA and rDNA-Fc are averaged from two measurements.

Scanning Electron Microscopy

Micropillar-structured substrate were visualized using HR-SEM (FEI Sirion HR-SEM) at an acceleration voltage of 10 kV. The cross-section image was taken after cutting the micropillar-structured electrode with a diamond cut pen and sonication in ethanol for 30 min.

Cyclic Voltammetry experiments

Gold-coated CV chips (flat and micropillar-structured substrates) were cleaned for 30 s in piranha solution, washed extensively with water and EtOH, and dried with nitrogen. The experiments for the determination of the active surface area were performed using 0.1 M H_2SO_4 solution as electrolyte, at a scan rate of 100 mV/s.[41] The reduction peak area was used to determine the active electrochemical surface area via the theoretical charge density value of 448 µC/cm^2 for gold surfaces.[41] The theoretical surface area of the substrate used as working electrode is 0.44 cm^2 due to the O-ring, used to have conformal contact between the electrochemical cell and the substrate.

In case of the electrochemical DNA detection by sandwich assay for both flat and micropillar-structured substrates, the gold chips were immersed in a solution

consisting of PLL-OEG(27.6)-DBCO(3.0) (1 mg/ml, PBS pH 7.4) for 60 min, after activation by UV-ozone for 15 min. Then, PBS (pH 7.4) solutions containing azide-PNA (0.5 µM), cDNA (0.5 µM) and rDNA (0.5 µM) were consecutively deposited on top of the functionalized PLL-OEG-DBCO substrate, respectively for 4 h, and 1 h for each step of hybridization, under gentle shaking. After each deposition, a rinsing step with Milli-Q followed by a drying step with N_2 was performed. Alternatively, a solution of ncDNA (0.5 µM in PBS 7.4, for 1 h) was used for the selectivity experiment. All the CV experiment were measured varying the scan rate between 10 and 200 mV/s in freshly 0.1 M $NaClO_4$ as electrolyte (degassed for 5 min).

Electrochemical measurements were performed in a three-electrode setup (custom-built glass electrochemical cell) with a platinum disk as counter electrode, a red rod reference electrode (Ag/AgCl, saturated KCl solution, Radiometer Analytical), and the gold substrates as working electrode (theoretical surface area of 0.44 cm^2). Data analysis was done using CHI760D software (CH Instruments, Inc. Austin, USA) and the methodology reported in the Electrochemical Analysis section in the SI. The CV experiments were repeated twice.

5.6 Supporting information

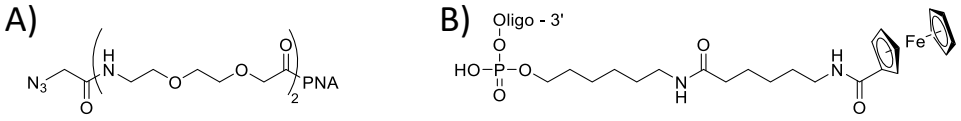

Figure S5.1. Chemical structures of A) PNA and B) DNA linkers to respectively anchor azide and ferrocene moieties. The [2-(2-aminoethoxy)ethoxy]acetyl (AEEA) PNA linker, with 2-azidoacetyl functional group, was already reported in a previous work.[59] A new batch of this PNA was produced and characterized (see Figure S5.2 and S5.3 for batch characterization).

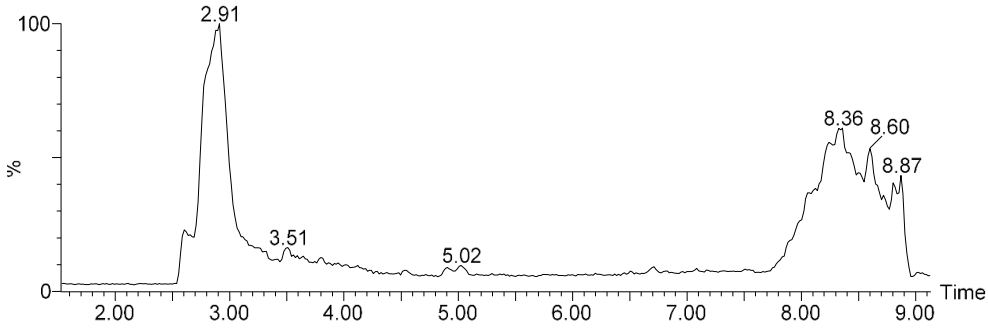

Figure S5.2. Chromatogram of probe the batch of PNA-N_3, used for the present work; peak at 2.91 min corresponds to the target PNA. For comparison of other batches, see ref. 59.

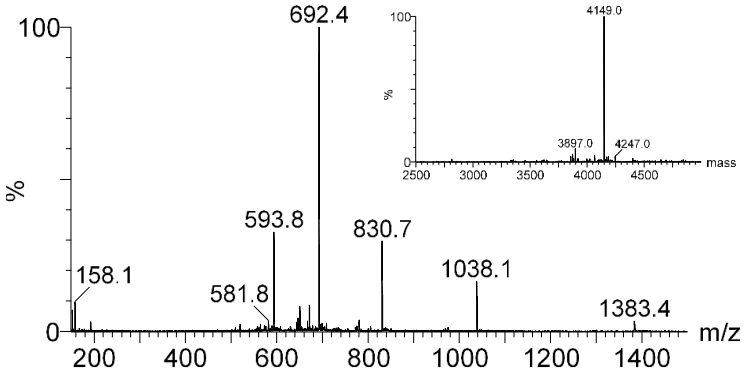

Figure S5.3. Mass spectrum of PNA-N_3, multicharged ions: 1384 $[MH_3]^{3+}$, 1038 $[MH_4]^{4+}$ 831 $[MH_5]^{5+}$, 692 $[MH_6]^{6+}$, 594 $[MH_7]^{7+}$. The inset shows the reconstructed molecular mass: calculated MW 4147.1, *m/z found* 4149.0.

Table S5.1. Sequences of DNA and PNA molecules used in this work. PNA-N_3 was chosen with a sequence that have been shown to be a relevant tract of the *KRAS* gene subject to point mutations present in several tumors.[16,64]

Oligo	Sequence 5'→ 3'(number of nucleotides)	Role
PNA-N_3	N_3-CTA CGC CAC CAG CT-Gly-NH_2 (14); ε (260 nm): 127900 $M^{-1}cm^{-1}$	PNA probe WT *KRAS*
cDNA	ATG ACT GAA TAT AAA CTT GTG GTA GTT GGA GCT GGT GGC GTA G (43)	Target, complementary to PNA-N_3
ncDNA	CTA CGC CAC CTC AAC CTA CGC CAC CTC CAC CTA CGC CAC CTC (42)	Non complementary to PNA-N_3
rDNA-Fc	ACC ACA AGT TTA TAT TCA GTC AT-Fc (23)	Reporter, complementary to the 5'end of cDNA

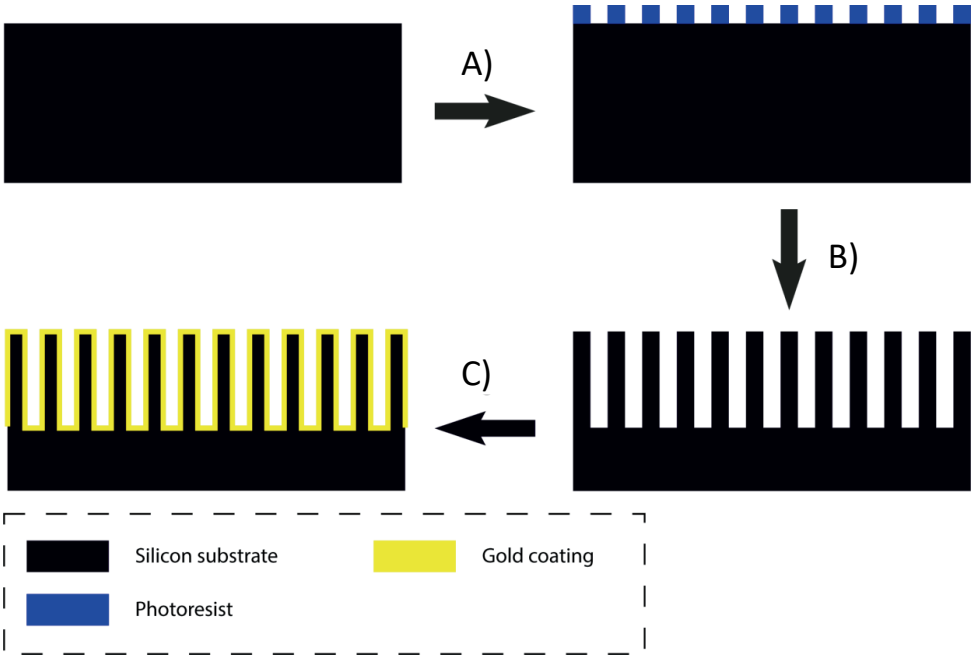

Figure S5.4. Schematic illustration of the fabrication process of micropillar-structured substrates. A) Deposition of photoresist on silicon wafer followed by patterning of the photoresist by photolithography. B) Deep reactive ion etching to create the micropillar-structured substrate. C) Coating of the micropillar-structured substrate with gold by sputtering.

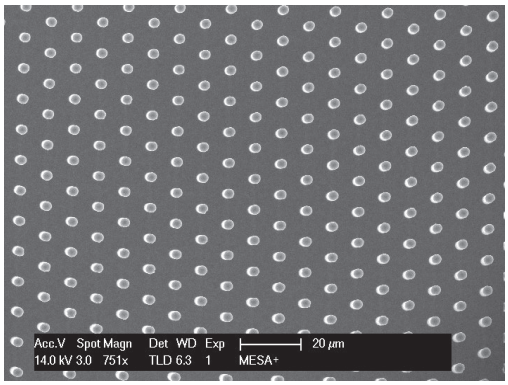

Figure S5.5. Top-view SEM image of a micropillar array (10 µm pitch), showing the hexagonal design of the micropillar section.

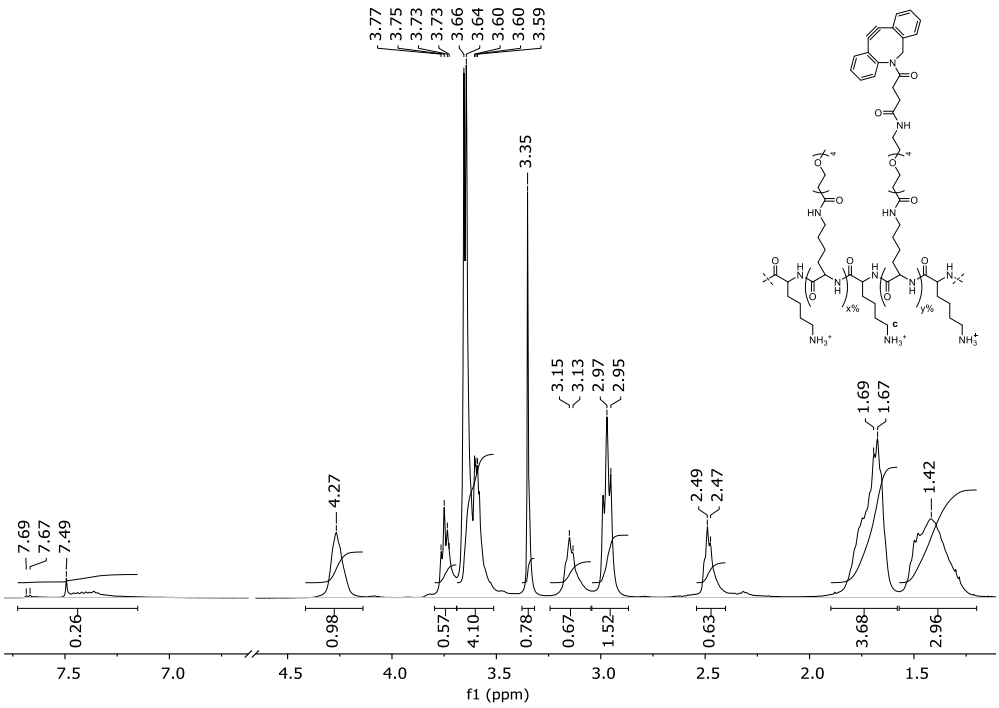

Figure S5.6. ^{1}H-NMR spectra of PLL-OEG-DBCO after purification by dialysis. Quantification of the grafted OEG and DBCO percentages, 27.6% and 3.0%, respectively, has been performed according to a previously published procedure (see below).[27,51]

PLL-OEG(27.6%)-DBCO(3%)

Quantification of OEG and DBCO grafted densities were obtained according to our previously reported procedure,[4,5] using the integral ratios of the characteristic signals in the ^{1}H-NMR spectra (see Figure S5.6). Integrals were normalized to the peak at 4.27 ppm (lysine backbone), and the ones at 2.96 ppm (free lysine), 3.14 ppm (functionalized lysine of both DBCO and OEG side groups, and 7.22-7.69 ppm (DBCO) were used for the calculations.

All the integrals used correspond to two protons, except the DBCO one, which corresponds to eight. Consequently, it was normalized by dividing for a factor of four. The sum of the integrals of free and functionalized lysine correspond to the total amount of lysine at the PLL backbone. Therefore:

$$PLL\ functionalization\ (\%) = \frac{integral\ of\ functional\ Lys}{integrals\ of\ free\ Lys + functional\ Lys} \quad (1)$$

$$DBCO\ functionalization\ (\%) = \frac{(DBCO\ integral)/4}{integrals\ of\ free\ Lys + functional\ Lys} \quad (2)$$

$$OEG_{\ functionalization}\ (\%) = PLL_{\ functionalization} - DBCO_{\ functionalization} \quad (3)$$

Table S5.2. Water contact angle values of gold-coated flat (∞ pitch) and micropillar-structured Si substrates (19 µm and 8 µm pitch) before and after UV-ozone activation, and after immersion in a 1 mg/ml PLL-OEG-DBCO solution in PBS at pH 7.4 (control substrates in PBS without PLL). Next, the substrates were immersed in PBS (pH 7.4) for 24 h and the contact angle values monitored again. Standard deviations (in brackets) were calculated measuring three different spots of the same substrate.

Pitch size (µm)	Before activation	After activation	After 1 h of PLL-OEG-DBCO	After 24 h in PBS 7.4
Flat	59.9° (±1.3°)	<15°	31.6° (±1.5°)	32.7° (±1.9°)
Flat (control)	/	<15°	<20° (only PBS)	38.6° (±2.2°)
19	96.2 (±2.3°)	<15°	34.4° (±2.8°)	36.1° (±3.2°)
19 (control)	/	<15°	<20° (only PBS)	45.2 (±4.1°)
8	104.3 (±1.8°)	<15°	35.9° (±2.0°)	37.4° (±2.3°)
8 (control)	/	<15°	<20° (only PBS)	46.2 (±2.6°)

Electrochemical analysis

Active surface area determination

The projected areas of the total (PA_{tot}, 0.44 cm^2), flat (PA_f, 0.19 cm^2) and pillared (PA_p, 0.25 cm^2) sections for electrochemical substrates are shown in Figure 5.4. Assuming absence of surface imperfections, the total geometric surface area (A_{tot}), is given by eq. 4:

$$A_{tot} = A_f + A_p \qquad \text{eq.4}$$

Where A_f and A_p are the geometric areas of the flat and pillared sections of a micropillar-structured substrate, respectively. In particular, for the flat section:

$$A_f = PA_f \qquad \text{eq.5}$$

while for the pillared section:

$$A_p = PA_p(1 + \frac{2}{3}\sqrt{3} \cdot \pi \frac{d_p \cdot h_p}{p^2}) \qquad \text{eq. 6}$$

where d_p is the pillar diameter (4 µm), h_p the pillar height (36.7 µm), and p the pitch (µm). The factor $1+\frac{2}{3}\sqrt{3} \cdot \pi \cdot d_p \cdot h_p / p^2$ is the factor SE_p by which the surface area of a unit cell containing a single pillar in a hexagonal design increases from flat to pillar (see Figure S5.7). Without a micropillar in this unit cell, the area is $½\sqrt{3} \cdot p^2$. When a micropillar is placed in the unit cell, the area is increased with the sides of the pillar, amounting to $\pi \cdot d_p \cdot h_p$, leading to a total area of $½\sqrt{3} \cdot p^2 + \pi \cdot d_p \cdot h_p$. Taking the ratio between these areas leads to the aforementioned surface enhancement factor in the pillar area, SE_p.

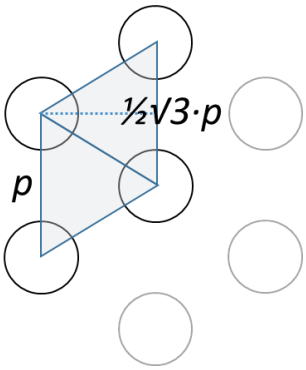

Figure S5.7. Section of the hexagonal micropillar array with the two triangles jointly covering one micropillar.

For simplicity, we ignored effects of the non-perfect fit of the hexagonal pillar lattice in the square pillar area (error on the total number of pillars is <0.002 %), and the

sidewall surrounding the pillar section, introduced by etching the pillars into the substrate (estimated to be < 1%). Therefore, the total theoretical surface enhancement factor (SE_{tot}) by the incorporation of micropillars is given by A_{tot}/PA_{tot}.

Contributions from roughness factors (sputtered gold and DRIE etching process) can be responsible for the differences in values between the calculated geometric and experimentally (CV) determined surface areas. Therefore, two roughness factors were defined, one for the flat area (s_f = 1.29), ascribed to the sputtering of gold, and one for the pillared section (s_p = 1.48), attributed to the DRIE etching process and the gold sputtering. In detail, s_f was calculated by the ratio between the experimentally determined surface area ($A_{tot,exp}$ = 0.57 cm^2) and the geometric surface area (A_{tot} = 0.44 cm^2) of a flat gold surface, while s_p was calculated from the slope of the linear fit from the relationship between the experimental determined surface areas and the geometrical ones for the pillared section using various pitch sizes. For this linear fit, the experimentally (CV) determined areas for the pillared section (Figure S5.8), obtained by subtracting the flat area (by taking the corresponding fraction of the experimental surface area of the flat sample) from the total area, were plotted versus the geometric area of the same pillared part (A_p) as shown in Figure S5.9. The calculated geometric surface areas including both roughness factors, were then calculated by multiplying the terms A_f and A_p respectively with s_f and s_p. Consequently, the calculated surface enhancement factors, relative to the experimental flat area, were determined.

Table S5.3. Geometrical areas and theoretical surface enhancement factors for the total area (A_{tot} and SE) and pillared section (A_p and SEp) without surface roughness using eqs. 4-6.

Pitch size (µm)	A_{tot}	A_p	SE	SE_p
Flat ($p = \infty$)	0.44	0.25	1	1
19	0.81	0.62	1.83	2.48
8	2.52	2.33	5.71	9.32

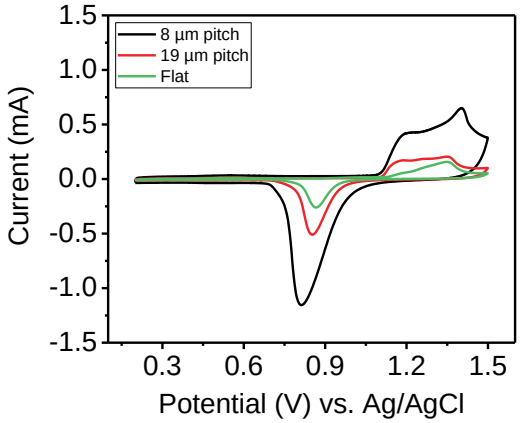

Figure S5.8. Cyclic voltammograms of gold-coated p^{++} type silicon micropillar-structured substrates with pitch 8 µm and 19 µm (black and red lines, respectively) and flat one (green line). Experiments were performed in 0.1 M H_2SO_4 with a scan rate of 100 mV/s.

Table S5.4. Experimental areas for flat and micropillar-structured (19 and 8 µm pitch) electrodes using 0.1 M H_2SO_4 solution at CV experiments with a scan rate of 100 mV/s.

Pitch size (µm)	$A_{tot,exp}$ (cm^2)
Flat ($p = \infty$)	0.57
19	1.26
8	3.68

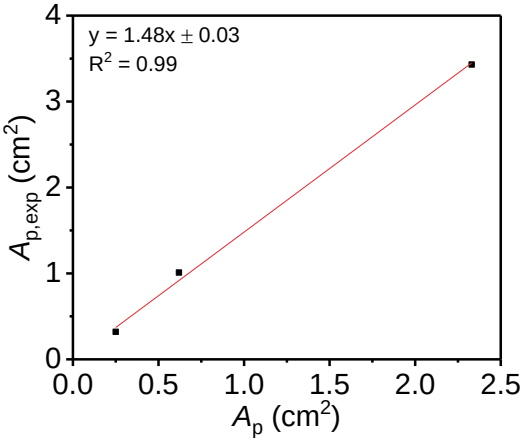

Figure S5.9. Experimental (CV in 0.1 M aq. H_2SO_4)[41] surface area of the pillar section ($A_{p,exp}$) of flat and micropillar-structured substrates as a function of the geometric surface area of the pillar section without surface roughness (A_p). The surface roughness factor in the pillared section (s_p = 1.48) was determined from the slope of a linear fit through the origin.

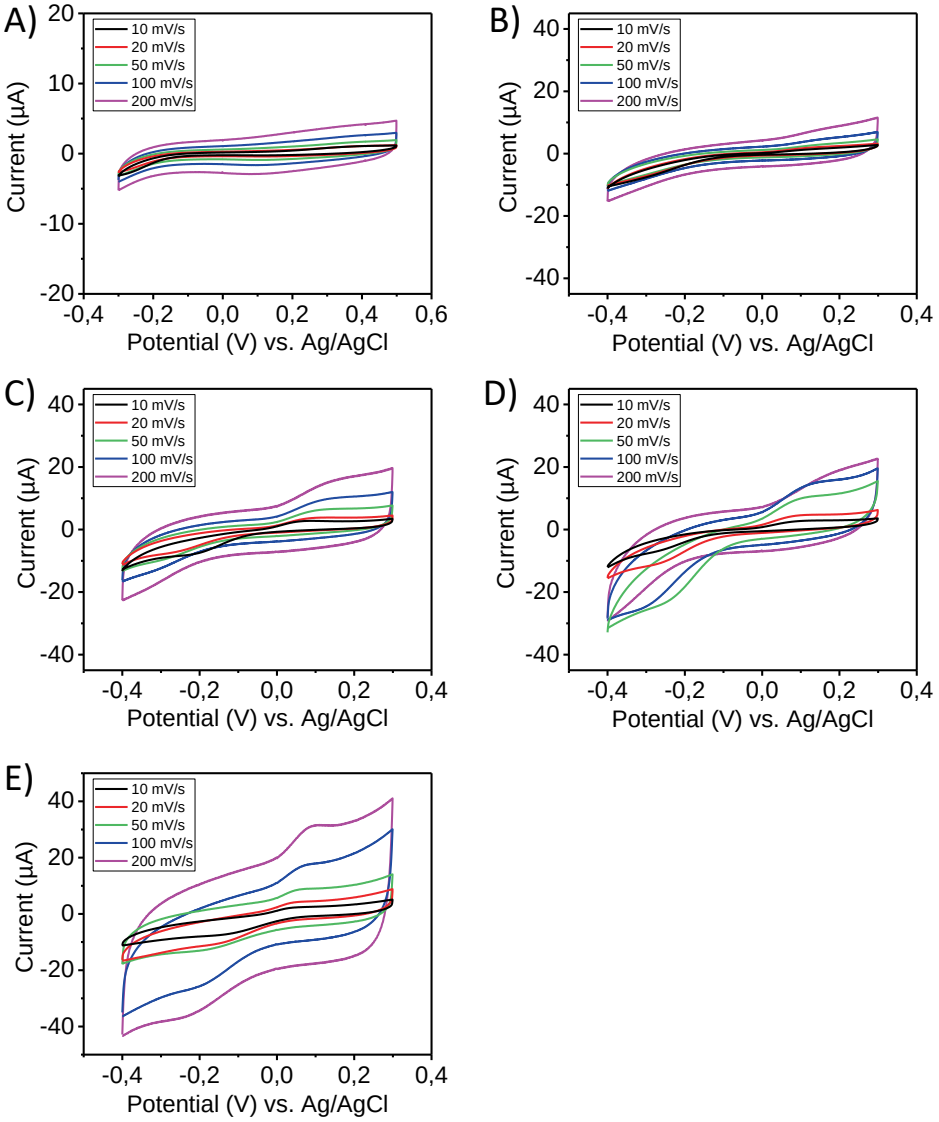

Figure S5.10. Cyclic voltammograms of PLL-OEG(27.6)-DBCO(3.0)-functionalized Au coated substrates after anchoring of PNA-N_3 and the consecutive double hybridization of cDNA and rDNA-Fc for the sandwich assay for A) flat substrate and micropillar-structured ones with increasing pitch of B) 19 µm, C) 14 µm, D) 10 µm and E) 8 µm size. Freshly prepared 0.1 M $NaClO_4$ solution was degassed for 5 min and used as electrolyte for the all CV experiments. All the solutions were prepared in PBS (pH 7.4) at concentration of 1 mg/ml and 1 µM, respectively for PLL-OEG-DBCO and PNA, while 0.5 µM for both cDNA and rDNA-Fc in the same buffer.

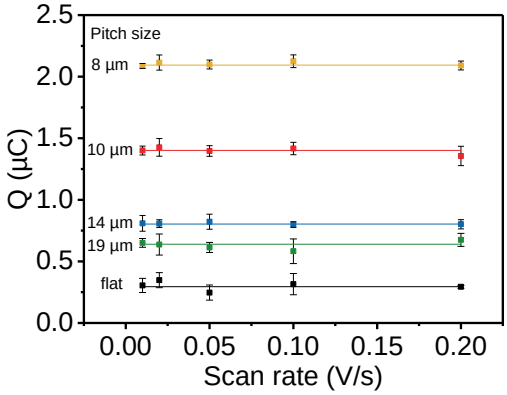

Figure S5.11. Dependence of the amount of charges involved in the redox process (*Q*) versus scan rate (0.01 – 0.2 V/s), derived from the average values from experiments in Figure S5.10. The substrates used were flat (black), 19 µm (green), 14 µm (blue), 10 µm (red) and 8 µm (ochre) pitch. Prior to the CV experiments, freshly prepared 0.1 M $NaClO_4$ solution was degassed for 5 min and used as the electrolyte. The concentrations of PLL-OEG-DBCO and PNA were 1.0 mg/ml and 0.5 µM respectively, while 1 µM for both cDNA and rDNA-Fc in PBS (pH 7.4). Datapoints corresponds to two measurements. The error bars indicate the standard deviation.

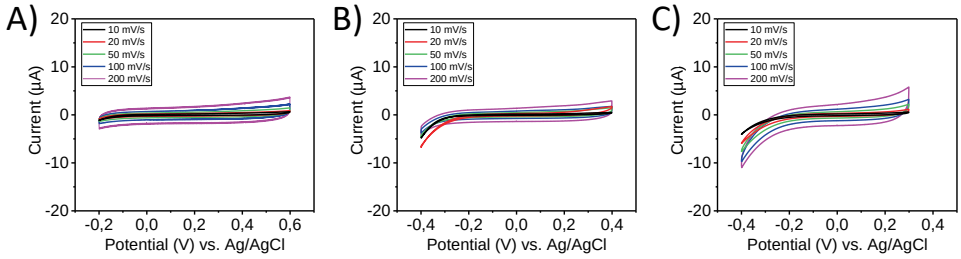

Figure S5.12. Voltammograms of the control experiments at gold flat surface functionalized with PLL-OEG(27.6)-DBCO(3.0). A) Selectivity experiment performed after the immobilization of PNA-azide and using ncDNA in the sandwich assay. Evaluation of the specific electrochemical response of the biosensing layer and the sandwich assay when B) the PNA probe anchoring or C) the cDNA hybridization step are missing. Before each CV experiments, freshly prepared 0.1 M $NaClO_4$ electrolyte solution was degassed for 5 min. The concentrations of the components used were 1.0 mg/ml for modified PLL, 0.5 µM for PNA-azide, cDNA and rDNA-Fc. All the deposition steps were done in PBS (pH 7.4).

Quantification of the area under the reduction peak at cyclic voltammograms

To obtain the points of the amount of charges involved in the redox process (*Q*) in Figure S5.11, the cyclic voltammograms in Figure S5.10 were treated according to the following procedure: the first derivative was applied to the anodic segment of interest to find the peak potential (E_p). A range of ± 0.25 V was defined from the E_p to set the baseline between these potentials and the peak area, related to (*Q*), was recorded. All the passages were performed by means of the CHI760D software (CH Instruments, Inc. Austin, USA).

Probe density determination by CV

The average surface coverage of rDNA-Fc molecules for the flat and micropillar-structured substrates was calculated adapting the following equation:[23]

$$\Gamma = Q/nFA \tag{7}$$

where Γ is the surface coverage (mol/cm^2), *Q* is the area of the reductive signal (in C), *F* is the Faraday constant (96485.34 C/mol), *n* is the number of electrons involved in the redox process (1 for ferrocene), and *A* the total active surface area of the working electrode. To show the effect of the pitch variation, eq 8 was derived to obtain calculated values of *Q*, Q_{calc}, to obtain the dependence of *Q* on the pitch:

$$Q_{calc} = nF\Gamma(SE_pPA_p + SE_fPA_f) \tag{8}$$

Here, SE_p is dependent on *p* as described above (eq. 4), and the second term is a constant which is shown as the abscissa. Γ is thus obtained from the slope of the fitting in Figure 5.5. Results expressed in molecules/cm^2 have been calculated by multiplying Γ by the Avogadro's number (N_A).

5.7 References

(1) Kawamura, A.; Miyata, T. Biosensors. In *Biomaterials Nanoarchitectonics*; Ebara, M., Ed.; Elsevier, 2016; 157-176.

(2) Wang, J. Electrochemical Glucose Biosensors. *Chem. Rev.* **2008**, *108*, 57–69.

(3) Liu, F.; Piao, Y.; Choi, J. S.; Seo, T. S. Three-Dimensional Graphene Micropillar Based Electrochemical Sensor for Phenol Detection. *Biosens. Bioelectron.* **2013**, *50*, 387–392.

(4) Arroyo-Currás, N.; Somerson, J.; Vieira, P. A.; Ploense, K. L.; Kippin, T. E.; Plaxco, K. W. Real-Time Measurement of Small Molecules Directly in Awake, Ambulatory Animals. *Proc. Natl. Acad. Sci.* **2017**, *114*, 645–650.

(5) Arroyo-Currás, N.; Scida, K.; Ploense, K. L.; Kippin, T. E.; Plaxco, K. W. High Surface Area Electrodes Generated via Electrochemical Roughening Improve the Signaling of Electrochemical Aptamer-Based Biosensors. *Anal. Chem.* **2017**, *89*, 12185–12191.

(6) Rifai, N.; Gillette, M. A.; Carr, S. A. Protein Biomarker Discovery and Validation: the Long

and Uncertain Path to Clinical Utility. *Nat. Biotechnol.* **2006**, *24*, 971–983.

(7) Dawson, S.; Tsui, D.; Murtaza, M.; Biggs, H.; Rueda, O. M.; Chin, S.; Dunning, M. J.; Gale, D.; Forshew, T.; Mahler-Araujo, B.; Rajan, S.; Humphray, S.; Becq, J.; Halsall, D.; Wallis, M.; Bentley, D.; Caldas, C.; Rosenfeld, N. Analysis of Circulating Tumor DNA to Monitor Metastatic Breast Cancer. *N. Engl. J. Med.* **2013**, *368*, 1199–1209.

(8) Yong, E. Cancer Biomarkers: Written in Blood. *Nature* **2014**, *511*, 524–526.

(9) Grieshaber, D.; MacKenzie, R.; Vörös, J.; Reimhult, E. Electrochemical Biosensors - Sensor Principles and Architectures. *Sensors* **2008**, *8*, 1400–1458.

(10) Drummond, T. G.; Hill, M. G.; Barton, J. K. Electrochemical DNA Sensors. *Nat. Biotechnol.* **2003**, *21*, 1192–1199.

(11) Ricci, F.; Plaxco, K. W. E-DNA Sensors for Convenient, Label-Free Electrochemical Detection of Hybridization. *Microchim. Acta* **2008**, *163*, 149–155.

(12) Das, J.; Ivanov, I.; Montermini, L.; Rak, J.; Sargent, E. H.; Kelley, S. O. An Electrochemical Clamp Assay for Direct, Rapid Analysis of Circulating Nucleic Acids in Serum. *Nat. Chem.* **2015**, *7*, 569–575.

(13) Grody, W. W.; Cutting, G. R.; Klinger, K. W.; Richards, C. S.; Watson, M. S.; Desnick, R. J. Laboratory Standards and Guidelines for Population-Based Cystic Fibrosis Carrier Screening. *Genet. Med.* **2001**, *3*, 149–154.

(14) Maurano, M.: Humbert, R.; Rynes, E.; Thurman, R.; Haugen, E.; Wang, H.; Reynolds, A.; Sandstrom, R.; Qu, H.; Brody, J.; Shafer, A.; Neri, F.; Lee, K.; Kutyavin, T.; Stehling-Sun, S.; Johnson, A.; Canfield, T.; Giste, E.; Diegel, M.; Bates, D. Hansen, R.; Neph, S.; Sabo, P.; Heimfeld, S.; Raubitschek, A.; Ziegler, S.; Cotsapas, C.; Sotoodehnia, N.; Glass, I.; Sunyaev, S.; Kaul, R.; Stamatoyannopoulos, J. A. Systematic Localization of Common Disease-Associated Variation in Regulatory DNA. *Science* **2012**, *337*, 1190–1195.

(15) Bellassai, N.; Spoto, G. Biosensors for Liquid Biopsy: Circulating Nucleic Acids to Diagnose and Treat Cancer. *Anal. Bioanal. Chem.* **2016**, *408*, 7255–7264.

(16) Thierry, A.; Mouliere, F.; El Messaoudi, S.; Mollevi, C.; Lopez-Crapex, E.; Rolet, F.; Gillet, B.; Gongora, C.; Dechelotte, P.; Robert, B.; Del Rio, M.; Lamy, P.; Bibeau, F.; Nouaille, M.; Loriot, V.; Jarrousse, A.; Molina, F.; Mathonnet, M.; Pezet, D.; Ychou, M. Clinical Validation of the Detection of KRAS and BRAF Mutations from Circulating Tumor DNA. *Nat. Med.* **2014**, *20*, 430–435.

(17) Nguyen, A. H.; Sim, S. J. Nanoplasmonic Biosensor: Detection and Amplification of Dual Bio-Signatures of Circulating Tumor DNA. *Biosens. Bioelectron.* **2015**, *67*, 443–449.

(18) Campbell, C. N.; Gal, D.; Cristler, N.; Banditrat, C.; Heller, A. Enzyme-Amplified Amperometric Sandwich Test for RNA and DNA. *Anal. Chem.* **2002**, *74*, 158–162.

(19) Patolsky, F.; Lichtenstein, A.; Willner, I. Electronic Transduction of DNA Sensing Processes on Surfaces: Amplification of DNA Detection and Analysis of Single-Base Mismatches by Tagged Liposomes. *J. Am. Chem. Soc.* **2001**, *123*, 5194–5205.

(20) Wang, J.; Kawde, A. N.; Musameh, M.; Rivas, G. Dual Enzyme Electrochemical Coding for Detecting DNA Hybridization. *Analyst* **2002**, *127*, 1279–1282.

(21) Yang, I. V.; Thorp, H. H. Modification of Indium Tin Oxide Electrodes with Repeat Polynucleotides: Electrochemical Detection of Trinucleotide Repeat Expansion. *Anal. Chem.* **2001**, *73*, 5316–5322.

(22) Hu, Q.; Kong, J.; Han, D.; Niu, L.; Zhang, X. Electrochemical DNA Biosensing via Electrochemically Controlled Reversible Addition-Fragmentation Chain Transfer Polymerization. *ACS Sens.* **2019**, *4*, 235–241.

(23) Pheeney, C. G.; Barton, J. K. DNA Electrochemistry with Tethered Methylene Blue. *Langmuir* **2012**, *28*, 7063–7070.

(24) Ahmed, M. U.; Nahar, S.; Safavieh, M.; Zourob, M. Real-Time Electrochemical Detection of Pathogen DNA Using Electrostatic Interaction of a Redox Probe. *Analyst*. **2013**, *138*, 907-915.

(25) Hu, Q.; Deng, X.; Yu, X.; Kong, J.; Zhang, X. One-Step Conjugation of Aminoferrocene to Phosphate Groups as Electroactive Probes for Electrochemical Detection of Sequence-Specific DNA. *Biosens. Bioelectron.* **2015**, *65*, 71–77.

(26) Biagiotti, V.; Porchetta, A.; Desiderati, S.; Plaxco, K. W.; Palleschi, G.; Ricci, F. Probe Accessibility Effects on the Performance of Electrochemical Biosensors Employing DNA Monolayers. *Anal. Bioanal. Chem.* **2012**, *402*, 413–421.

(27) Movilli, J.; Rozzi, A.; Ricciardi, R.; Corradini, R.; Huskens, J. Control of Probe Density at DNA Biosensor Surfaces Using Poly(L-Lysine) with Appended Reactive Groups. *Bioconjug. Chem.* **2018**, *29*, 4110–4118.

(28) Yu, Z. G.; Lai, R. Y. Effect of Signaling Probe Conformation on Sensor Performance of a Displacement-Based Electrochemical DNA Sensor. *Anal. Chem.* **2013**, *85*, 3340–3346.

(29) Suni, I. I. Impedance Methods for Electrochemical Sensors Using Nanomaterials. *Trends Anal. Chem.* **2008**, *27*, 604–611.

(30) Wang, X.; Smirnov, S. Label-Free DNA Sensor Based on Surface Charge Modulated Ionic Conductance. *ACS Nano* **2009**, *3*, 1004–1010.

(31) Henry, O. Y. F.; Kirwan, S.; Debela, A. M.; O'Sullivan, C. K. Electrochemical Genosensor Based on Three-Dimensional DNA Polymer Brushes Monolayers. *Electrochem. commun.* **2011**, *13*, 1155–1158.

(32) Kowalczyk, A.; Fau, M.; Karbarz, M.; Donten, M.; Stojek, Z.; Nowicka, A. M. Hydrogel with Chains Functionalized with Carboxyl Groups as Universal 3D Platform in DNA Biosensors. *Biosens. Bioelectron.* **2014**, *54*, 222–228.

(33) Kugel, V.; Ji, H. Nanopillars for Sensing. *J. Nanosci. Nanotechnol.* **2014**, *14*, 6469–6477.

(34) Saeed, A. A.; Sánchez, J. L. A.; O'Sullivan, C. K.; Abbas, M. N. DNA Biosensors Based on Gold Nanoparticles-Modified Graphene Oxide for the Detection of Breast Cancer Biomarkers for Early Diagnosis. *Bioelectrochemistry* **2017**, *118*, 91–99.

(35) Daggumati, P.; Matharu, Z.; Seker, E. Effect of Nanoporous Gold Thin Film Morphology on Electrochemical DNA Sensing. *Anal. Chem.* **2015**, *87*, 8149–8156.

(36) Soleymani, L.; Fang, Z.; Lam, B.; Bin, X.; Vasilyeva, E.; Ross, A. J.; Sargent, E. H.; Kelley, S.

O. Hierarchical Nanotextured Microelectrodes Overcome the Molecular Transport Barrier to Achieve Rapid, Direct Bacterial Detection. *ACS Nano* **2011**, *5*, 3360–3366.

(37) Prehn, R.; Cortina-Puig, M.; Muñoz, F. X. A Non-Enzymatic Glucose Sensor Based on the Use of Gold Micropillar Array Electrodes. *J. Electrochem. Soc.* **2012**, *159*, F134–F139.

(38) Anandan, V.; Rao, Y. L.; Zhang, G. Nanopillar Array Structures for Enhancing Biosensing Performance. *Int. J. Nanomedicine* **2006**, *1*, 73–79.

(39) Yang, M. H.; Kim, D. S.; Yoon, J. H.; Hong, S. B.; Jeong, S. W.; Yoo, D. E.; Lee, T. J.; Lee, S. J.; Lee, K. G.; Choi, B. G. Nanopillar Films with Polyoxometalate-Doped Polyaniline for Electrochemical Detection of Hydrogen Peroxide. *Analyst* **2016**, *141*, 1319–1324.

(40) Penmatsa, V.; Kim, T.; Beidaghi, M.; Kawarada, H.; Gu, L.; Wang, Z.; Wang, C. Three-Dimensional Graphene Nanosheet Encrusted Carbon Micropillar Arrays for Electrochemical Sensing. *Nanoscale* **2012**, *4*, 3673–3678.

(41) Schröper, F.; Brüggemann, D.; Mourzina, Y.; Wolfrum, B.; Offenhäusser, A.; Mayer, D. Analyzing the Electroactive Surface of Gold Nanopillars by Electrochemical Methods for Electrode Miniaturization. *Electrochim. Acta* **2008**, *53*, 6265–6272.

(42) Davies, T. J.; Ward-Jones, S.; Banks, C. E.; Del Campo, J.; Mas, R.; Muñoz, F. X.; Compton, R. G. The Cyclic and Linear Sweep Voltammetry of Regular Arrays of Microdisc Electrodes: Fitting of Experimental Data. *J. Electroanal. Chem.* **2005**, *585*, 51–62.

(43) Numthuam, S.; Kakegawa, T.; Anada, T.; Khademhosseini, A.; Suzuki, H.; Fukuda, J. Synergistic Effects of Micro/Nano Modifications on Electrodes for Microfluidic Electrochemical ELISA. *Sensors Actuators B Chem.* **2011**, *156*, 637–644.

(44) Sánchez-Molas, D.; Esquivel, J. P.; Sabaté, N.; Muñoz, F. X.; del Campo, F. J. High Aspect-Ratio, Fully Conducting Gold Micropillar Array Electrodes: Silicon Micromachining and Electrochemical Characterization. *J. Phys. Chem. C* **2012**, *116*, 18831–18846.

(45) Prehn, R.; Abad, L.; Sánchez-Molas, D.; Duch, M.; Sabaté, N.; del Campo, F. J.; Muñoz, F. X.; Compton, R. G. Microfabrication and Characterization of Cylinder Micropillar Array Electrodes. *J. Electroanal. Chem.* **2011**, *662*, 361–370.

(46) Lee, S.; Spencer, N. D. Adsorption Properties of Poly(L-Lysine)-Graft-Poly(Ethylene Glycol) (PLL-*g*-PEG) at a Hydrophobic Interface: Influence of Tribological Stress, pH, Salt Concentration, and Polymer Molecular Weight. *Langmuir* **2008**, *24*, 9479–9488.

(47) Lee, S.; Mu, M.; Ratoi-salagean, M.; Vo, J.; Paul, S. M. De; Spikes, H. A.; Textor, M.; Spencer, N. D. Boundary Lubrication of Oxide Surfaces by Poly(L-Lysine)-*g*-Poly(Ethylene Glycol) (PLL-*g*-PEG) in Aqueous Media. *Tribol Lett*. **2003**, *15*, 231–239.

(48) Müller, M.; Lee, S.; Spikes, H. A.; Spencer, N. D. The Influence of Molecular Architecture on the Macroscopic Lubrication Properties of the Brush-like Co-Polyelectrolyte Poly(L-Lysine)-*g*-Poly(Ethylene Glycol) (PLL-*g*-PEG) Adsorbed on Oxide Surfaces. *Tribol. Lett.* **2003**, *15*, 395–405.

(49) Huang, N.; Vörös, J.; De Paul, S. M.; Textor, M.; Spencer, N. D. Biotin-Derivatized Poly(L-Lysine)-*g*-Poly(Ethylene Glycol): A Novel Polymeric Interface for Bioaffinity Sensing. *Langmuir* **2002**, *18*, 220–230.

(50) Pasche, S.; De Paul, S. M.; Vörös, J.; Spencer, N. D.; Textor, M. Poly(L-Lysine)-Graft-Poly(Ethylene Glycol) Assembled Monolayers on Niobium Oxide Surfaces: A Quantitative Study of the Influence of Polymer Interfacial Architecture on Resistance to Protein Adsorption by ToF-SIMS and in Situ OWLS. *Langmuir* **2003**, *19*, 9216–9225.

(51) Di Iorio, D.; Marti, A.; Koeman, S.; Huskens, J. Clickable Poly-L-Lysine for the Formation of Biorecognition Surfaces. *RSC Adv*. **2019**, *9*, 35608–35613.

(52) Chakrabarti, M. C.; Schwarz, F. P. Thermal Stability of PNA/DNA and DNA/DNA Duplexes by Differential Scanning Calorimetry. *Nucleic Acids Res.* **1999**, *27*, 4801–4806.

(53) Demidov, V. V.; Potaman, V. N.; Frank-Kamenetskil, M. D.; Egholm, M.; Buchard, O.; Sönnichsen, S. H.; Nlelsen, P. E. Stability of Peptide Nucleic Acids in Human Serum and Cellular Extracts. *Biochem. Pharmacol.* **1994**, *48*, 1310–1313.

(54) Kuzmin, A.; Poloukhtine, A.; Wolfert, M. A.; Popik, V. V. Surface Functionalization Using Catalyst-Free Azide-Alkyne Cycloaddition. *Bioconjugate Chem.* **2010**, *21*, 2076–2085.

(55) Umek, R.; Lin, S.; Vielmetter, J.; Terbrueggen, R.; Irvine, B.; Yu, C.; Kayyem, J.; Yowanto, H.; Blackburn, G.; Farkas, D.; Chen, Y. Electronic Detection of Nucleic Acids: A Versatile Platform for Molecular Diagnostics. *J. Mol. Diagnostics* **2001**, *3*, 74–84.

(56) Elbersen, R.; Tiggelaar, R. M.; Milbrat, A.; Mul, G.; Gardeniers, H.; Huskens, J. Controlled Doping Methods for Radial p/n Junctions in Silicon. *Adv. Energy Mater.* **2015**, *5*, 1–8.

(57) Duan, X.; Mu, L.; Sawtelle, S. D.; Rajan, N. K.; Han, Z.; Wang, Y.; Qu, H.; Reed, M. A. Functionalized Polyelectrolytes Assembling on Nano-BioFETs for Biosensing Applications. *Adv. Funct. Mater.* **2015**, *25*, 2279–2286.

(58) Han, Z.; Wang, Y.; Duan, X. Biofunctional Polyelectrolytes Assembling on Biosensors – A Versatile Surface Coating Method for Protein Detections. *Anal. Chim. Acta* **2017**, *964*, 170–177.

(59) Veerbeek, J.; Steen, R.; Vijselaar, W.; Rurup, W. F.; Korom, S.; Rozzi, A.; Corradini, R.; Segerink, L.; Huskens, J. Selective Functionalization with PNA of Silicon Nanowires on Silicon Oxide Substrates. *Langmuir* **2018**, *34*, 11395–11404.

(60) Sauerbrey, G. Verwendung von Schwingquarzen Zur Wägung Dünner Schichten Und Zur Mikrowägung. *Zeitschrift für Phys.* **1959**, *155*, 206–222.

(61) Höök, F.; Ray, a.; Nordén, B.; Kasemo, B. Characterization of PNA and DNA Immobilization and Subsequent Hybridization with DNA Using Acoustic-Shear-Wave Attenuation Measurements. *Langmuir* **2001**, *17*, 8305–8312.

(62) Su, X.; Wu, Y. J.; Knoll, W. Comparison of Surface Plasmon Resonance Spectroscopy and Quartz Crystal Microbalance Techniques for Studying DNA Assembly and Hybridization. *Biosens. Bioelectron.* **2005**, *21*, 719–726.

(63) Larsson, C.; Rodahl, M.; Höök, F. Characterization of DNA Immobilization and Subsequent Hybridization on a 2D Arrangement of Streptavidin on a Biotin-Modified Lipid Bilayer Supported on SiO_2. *Anal. Chem.* **2003**, *75*, 5080–5087.

(64) Bettegowda, C.; Sausen, M.; Leary, R. J.; Kinde, I.; Wang, Y.; Agrawal, N.; Bartlett, B. R.; Wang, H.; Luber, B.; Alani, R. M.; Antonarakis, E. S.; Azad, N. S.; Bardelli, A.; Brem, H.;

Cameron, J. L.; Lee, C. C.; Fecher, L. A.; Gallia, G. L.; Gibbs, P.; Le, D.; Giuntoli, R. L.; Goggins, M.; Hogarty, M. D.; Holdhoff, M.; Hong, S.-M.; Jiao, Y.; Juhl, H. H.; Kim, J. J.; Siravegna, G.; Laheru, D. A.; Lauricella, C.; Lim, M.; Lipson, E. J.; Marie, S. K. N.; Netto, G. J.; Oliner, K. S.; Olivi, A.; Olsson, L.; Riggins, G. J.; Sartore-Bianchi, A.; Schmidt, K.; Shih, L.-M.; Oba-Shinjo, S. M.; Siena, S.; Theodorescu, D.; Tie, J.; Harkins, T. T.; Veronese, S.; Wang, T.-L.; Weingart, J. D.; Wolfgang, C. L.; Wood, L. D.; Xing, D.; Hruban, R. H.; Wu, J.; Allen, P. J.; Schmidt, C. M.; Choti, M. A.; Velculescu, V. E.; Kinzler, K. W.; Vogelstein, B.; Papadopoulos, N.; Diaz, L. Detection of Circulating Tumor DNA in Early- and Late-Stage Human Malignancies. *Sci. Transl. Med.* **2014**, *6*, 224ra24.

Chapter 6

Enrichment of hypermethylated DNA from cells and urine on chip to detect cervical cancer

Preselection of cancer-specific hypermethylated DNA (hmDNA) from a background of total DNA is important for the development of liquid biopsy diagnostics but remains challenging. Here, a microfluidic chip was developed for the selective enrichment of hmDNA from DNA isolated from cultured cervical cancer cells and from the urine of a cervical cancer patient. The microfluidic chip consists of a hmDNA enrichment chamber with a micropillar array, which was produced by photolithography and deep reactive ion etching. Methyl binding domain 2 (MBD2) protein was immobilized on the micropillar-structured substrate to function as a capture coating for hmDNA. Surface-bound DNA was eluted from the MBD2-coated surface by using an ammonium hydroxide solution. The micropillar array increases the surface area 8.1-fold compared to a non-pillared device, and possesses a hmDNA enrichment capacity of 4.6 ng. In order to validate the performance of the hmDNA enrichment device, DNA was isolated from a cervical cancer cell line, primary keratinocytes serving as control, the urine of a cervical cancer patient and a healthy volunteer. Assessing the methylation level of the *MAL* gene, which is known to be a biomarker for cervical cancer, by quantitative methylation-specific polymerase chain reaction on the isolated DNA samples confirmed the presence of hypermethylation of the *MAL* gene in the cervical cancer cell line and urine of a cervical cancer patient. The hypermethylated *MAL* gene from the cancer cell line was completely bound to the chip and selectively enriched in the eluent as was confirmed by quantitative polymerase chain reaction (qPCR). An amount of 150 ng of DNA isolated from the urine of the cervical patient was sufficient for hmDNA enrichment and subsequent detection of the hypermethylated *MAL* gene with qPCR.

R.W. Kolkman, B.M.M. Wever, A.P. Van Splunter, J.G. Bomer, R.D.M. Steenbergen, L.I. Segerink, J. Huskens. *Manuscript in preparation*.

6.1 Introduction

In a liquid biopsy such as blood and urine various cancer biomarkers can be measured[1–3] which are secreted into body fluids by cancer cells throughout the body.[4,5] An example of this is the detection of cell-free DNA (cfDNA) shed by the tumor, known as circulating tumor DNA. The use of urine is upcoming and advantageous over, for example, blood analysis as urine can be collected non-invasively and repeatedly by an individual without the need for trained healthcare workers. Hypermethylated DNA (hmDNA) is one of the cancer biomarkers that can be detected in urine.[6,7] hmDNA is epigenetically changed DNA where a methyl group is covalently bound to cytosine bases in CpG complexes. The hypermethylation of gene promoter regions can result in undesired changes in the gene expression and is, therefore, related to cancer.[8] The detection of DNA methylation of specific gene regions in urinary cfDNA is associated to several cancers, like cervical,[9] bladder,[10] colon,[11] endometrial,[12] and lung cancer.[13]

Detection of hmDNA in urine requires a preselection step which distinguishes hmDNA from non-methylated DNA. Prior to this preselection step is DNA isolated from urine to separate DNA from other urine components such as salts, proteins and hormones, to simplify sample handling and hmDNA detection. The common method for preselection of hmDNA is bisulfite conversion.[14,15] With bisulfite conversion all the non-methylated cytosines are converted to the base uracil while methylated cytosines are protected against this conversion. The change in the DNA sequence can then be measured with a polymerase chain reaction (PCR). However, the main limitations of the bisulfite conversion method are significant DNA fragmentation and incomplete DNA conversion.[16,17] As a consequence, typically hundreds of ng DNA are used to convert DNA isolated from urine with the bisulfite method followed by the detection of specific hmDNA cancer genes.[18,19]

Recent improvements make the preselection of hmDNA by an enrichment method a suitable alternative to bisulfite conversion (see Chapters 3 and 4). hmDNA enrichment is typically performed using a methyl binding domain 2 (MBD2) protein attached to a surface.[20,21] MBD2 bioreceptors interact with low nanomolar binding affinities with methylated CpGs, while less strong binding affinities (100-1000 nM) are reported between MBD2 and non-methylated CpG.[22–28] MBD2-based enrichment of hmDNA has been studied, but clinical applications are limited due to the co-enrichment of non-methylated DNA.[29–31] hmDNA enrichment can be favorable as the assay times are typically short since only a binding and an elution step is performed and the enrichment conditions are mild, which prevents DNA fragmentation. Previously we have shown that the hmDNA enrichment selectivity can be improved by controlling the applied MBD2 surface receptor density (Chapter 3) which resulted in a 30-fold increase in the hmDNA content in the enriched DNA mixture (Chapter 4). Nevertheless, we have so far only tested our hmDNA enrichment method using synthetic DNA but not with

DNA samples isolated from cell lines and urine samples. Furthermore, the used flow cell for hmDNA enrichment was constrained by limited hmDNA enrichment efficiencies in combination with the need of larger sample volumes.

The use of microfluidics is favored owing to the high surface-to-volume ratios, which decrease the diffusion distance of analytes to the surface[32,33] and thus increases the probability of hmDNA surface binding to the MBD2-coated surface. Microfluidic systems are also reducing contaminations as they are typically closed systems, and require minimal sample handling. Therefore, microfluidic devices are applied in many different applications such as DNA extraction,[34] point of care diagnostics[35,36] and wearable biosensors.[37] The surface-to-volume ratios in microfluidics can be increased further by using microstructures.[38–40] A typical example is the integration of a micropillar array in the microfluidic device,[41–46] the use of which results in reduction of mass transport limitation due to µm spacing between the micropillars. Furthermore, a micropillar array results in an enhanced surface area and thus in a higher DNA binding capacity.[47,48] The surface-to-volume ratio will especially be important upon hmDNA enrichment in early-stage cancer diagnostics, where the hmDNA concentration can be in the attomolar regime.

Here, we report the development of a micropillar-structured microfluidic hmDNA enrichment device that enables hmDNA-based cervical cancer detection in cultured cervical cancer cells and in a urine sample of a woman diagnosed with cervical cancer using quantitative polymerase chain reaction (qPCR). We first examined the hmDNA enrichment capacity of the device. We then performed hmDNA enrichment studies on fragmented DNA isolated from a cervical cancer cell line and use fragmented DNA isolated from primary keratinocytes as a control. The hmDNA enrichment selectivity of cell line DNA was evaluated by detecting the presence of a specific hmDNA cancer gene with qPCR. At last, the hmDNA enrichment device was used to enrich hmDNA from cfDNA isolated from the urine of a cervical cancer patient, while using the urine of a healthy volunteer as a control, followed by hmDNA cancer gene detection with qPCR.

6.2 Results and discussion

6.2.1 Microfluidic hmDNA enrichment device

A microfluidic chip with a micropillar array was developed to enrich hmDNA from DNA isolated from cell lines or urine supernatant samples (Figure 6.1). The hmDNA-enriched sample is used to enable hmDNA-based cancer detection with qPCR (Figure 6.1A). On the left and right side of the chip, the inlet and outlet are present. Enrichment of hmDNA is performed in the hmDNA capture chamber of the microfluidic chip. This chamber consists of a micropillar array to enlarge the binding capacity and to shorten

the diffusion distance of DNA to the MBD2 surface, thus to reduce mass transport limitations and increase the hmDNA enrichment efficiency. The enrichment chamber is rectangularly shaped with dimensions of 5.0 mm × 2.5 mm and a channel height of approximately 30 µm. Micropillars with a diameter of approximately 4 µm are positioned with a center-to-center separation of 8 µm from each other in this chamber. Thus, roughly 110,000 micropillars are positioned in the enrichment chamber. hmDNA enrichment is performed by coating the surface of the microfluidic chip with the hmDNA capture coating consisting of surface-immobilized MBD2 proteins, as described in Chapters 3 and 4. The hmDNA enrichment is performed in a two-step process. The first step is the DNA binding step where the DNA mixture, containing DNA with varying degrees of methylation, is flushed through the microfluidic chip. The binding affinity of DNA that binds to the MBD2-modified surface is amongst others dependent on the degree of DNA methylation. In the second step, surface-bound DNA is eluted from the MBD2-coated surface by flushing with aqueous ammonium hydroxide (pH 11.3). The eluent is a denaturation agent for the MBD2 proteins, causing the disruption of the non-covalent interactions between hmDNA and the MBD2 proteins (Chapter 4). The hmDNA enrichment on the chip is followed by analysis of the enriched DNA sample outside the chip with qPCR to detect a specific hmDNA cancer gene.

A closed microfluidic chip was formed by clamping a glass slide with a 1.5 µm thick PDMS layer on top of the gold-coated micropillars (Figure 6.1B). Gold-coated micropillars were used to immobilize the MBD2 on the surface (Figure 6.1C). This immobilization is a multistep process (Chapter 3). First, a thiol-based self-assembled monolayer (SAM) was formed on the gold-coated micropillars with hydroxyl and azide-functionalized thiols. The hydroxyl-functionalized thiols were used to prevent non-specific binding to the chip, while the azides were used to enable MBD2 surface immobilization. To the azide-terminated thiols a linker molecule, with on one side a dibenzocyclooctyne (DBCO) functional group and on the other side a nitrilotriacetic acid (NTA) group, was reacted. Subsequently, the NTA functional groups were brought in contact with a $NiCl_2$ solution to form NiNTA moieties. At last, the NiNTA moieties were used to interact with the histidine 10 (His_{10})-tagged MBD2 protein to enable surface immobilization of MBD2. In this study, SAMs with 15% azide-functionalized thiols were used, which was shown before to result in the highest hmDNA enrichment selectivity (Chapter 4).

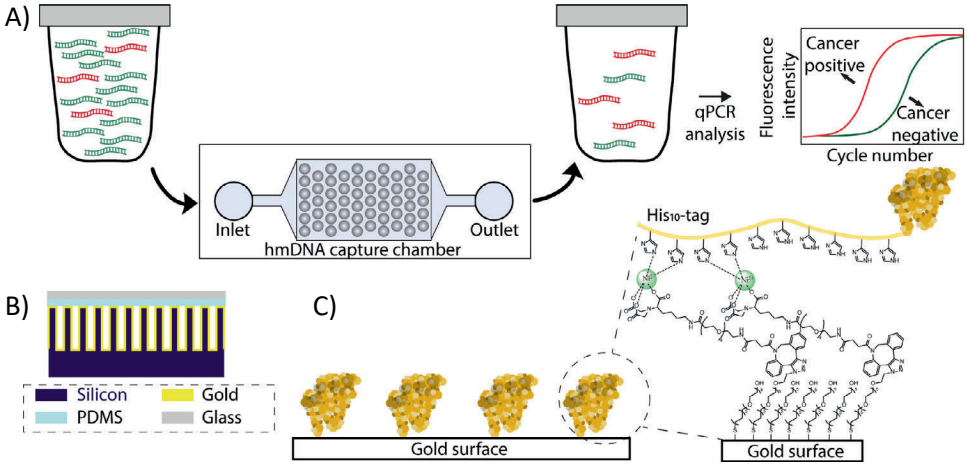

Figure 6.1 A) The enrichment of hmDNA (red) from a DNA mixture is performed in the microfluidic chip containing the hmDNA capture chamber with a micropillar array. The DNA mixture consists of hmDNA and non-methylated DNA (green). The enriched DNA sample is characterized with qPCR to detect the presence of a specific hmDNA cancer gene. B) Schematic image of the cross section of the hmDNA capture chamber with micropillars. The micropillars are coated with a gold layer and clamped to a glass chip with a 1.5 µm thick PDMS layer. C) Surface architecture of the hmDNA capture coating consisting of surface-immobilized MBD2 proteins (yellow objects). A thiol-based SAM was formed on the gold surface with azide and hydroxyl-terminated groups (see Chapter 3). The azide-functionalized thiols were used to bind a linker molecule with a DBCO and NiNTA functional groups. The His_{10}-tag fused to the MBD2 protein binds to the NiNTA functional groups.

Micropillar-structured substrates were made from silicon by photolithography and deep reactive ion etching (DRIE, Bosch process),[49] and these were coated with a gold layer according to our previously reported work.[48] The micropillars were etched into the silicon substrate, therefore, the top of the micropillars is at an equal height compared to non-etched silicon allowing easy closing of the device on top of the pillars. After gold layer deposition, the substrate was imaged by scanning electron microscopy (SEM, Figure 6.2). The micropillars are cylindrically shaped with a height of 27 µm and a diameter of 4.1 µm (Figure 6.2A). The micropillars show a negative tapering to 3.3 µm diameter at the bottom of the micropillars and scallops are present (Figure 6.2B and C), which are typically observed in DRIE-processed silicon substrates.[49–51] In Figure 6.2D the inlet/outlet with bifurcated channels followed by the micropillar array is visible. Bifurcated channels are used to spread the solution over the entire micropillar array in the microfluidic chip.

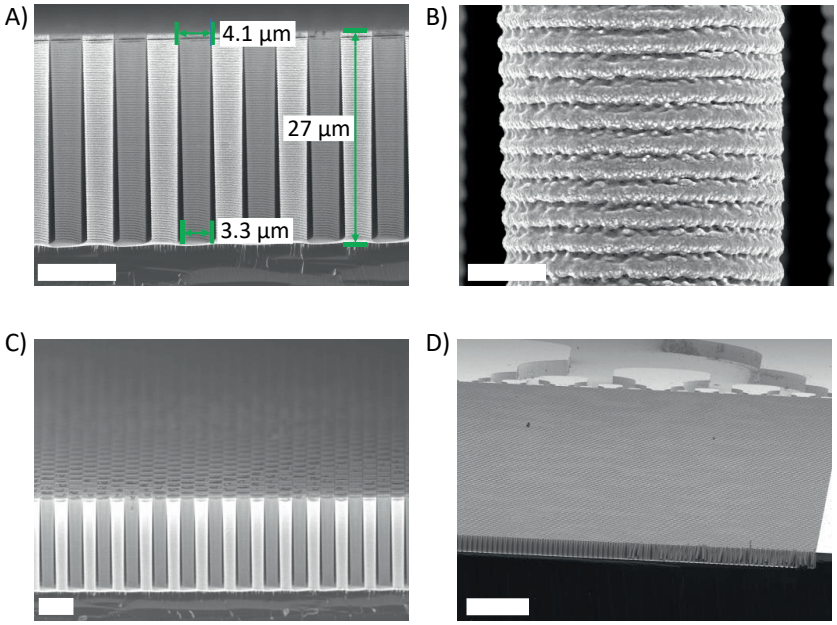

Figure 6.2. SEM images of the gold-coated, micropillar-structured silicon substrate. Micropillars were formed in a silicon substrate by the DRIE Bosch process and coated with a gold layer by sputtering. A gold-coated micropillar-structured substrate was cross-sectioned manually prior to SEM analysis. A) Dimensions of the micropillars (scalebar: 10 µm), B) part of an individual micropillar with scallops (scalebar: 1 µm), C) slightly tilted micropillar array (scalebar: 10 µm) and D) part of the inlet/outlet with bifurcated channels and micropillar array (scalebar: 100 µm).

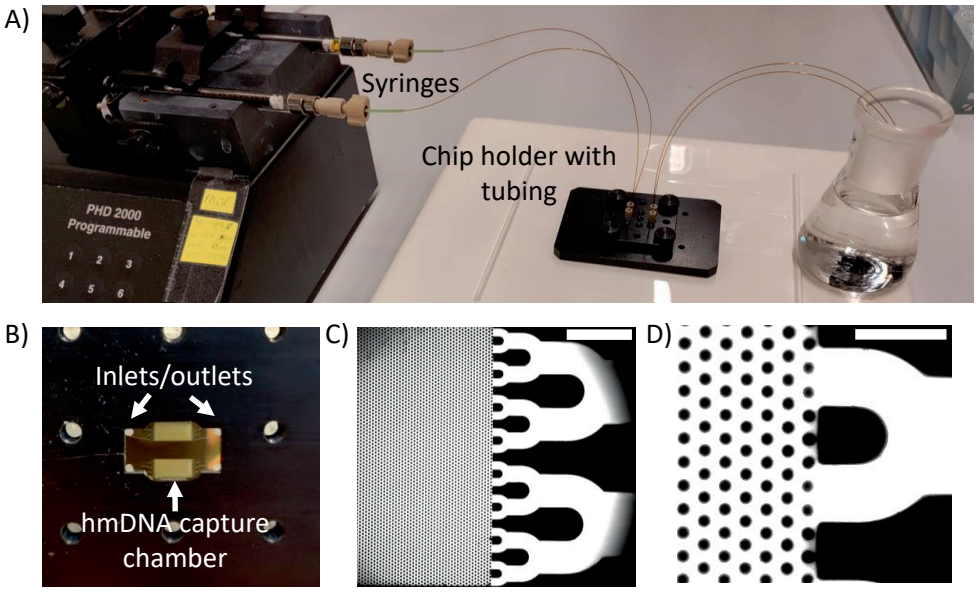

Figure 6.3. A) Photograph of the hmDNA enrichment flow-cell set-up. The set-up consists of the hmDNA enrichment device in the chip holder. Tubing is attached to the microfluidic chip using the chip holder. Fluid flow is applied through the microfluidic chip using the syringes attached to the syringe pump. B) Photograph of the bottom of the hmDNA enrichment device in the chip holder containing a window to monitor the fluid flow. On each chip two individually addressable and separated hmDNA capture chambers are present with their own inlet and outlet. C) Overview (scalebar 150 µm) and D) zoomed-in (scalebar 30 µm) fluorescence microscopy image of the micropillared section and inlet/outlet part of the microfluidic hmDNA enrichment device filled with 150 µM fluorescein.

The micropillar-structured substrate was sealed with a PDMS-coated glass slide and clamped in a chip holder to form the microfluidic device (Figure 6.3A). The glass slide was coated with a 1.5 µm thick PDMS layer to prevent leakage of the microfluidic hmDNA enrichment device. Each hmDNA enrichment chip contains two individually addressable hmDNA capture chambers (Figure 6.3B). On both sides of the micropillar chip an inlet/outlet is located. The flow cell holder contains a window, which is used to monitor the fluid flow in the enrichment device through the glass slide. The microfluidic device was first flushed with water using forward flow at a flow rate of 20 µL/min for 15 min. After filling the microfluidic device, the flow was switched to reverse flow and the flow rate was decreased to 2 µL/min. The flow rate was kept constant for all the subsequently applied flow steps with the device in this work. To visualize filling of the microfluidic device an aqueous solution of fluorescein was flushed through the

chip and monitored by fluorescence microscopy (Figure 6.3C and D). Within 2 min of flushing with the fluorescein solution, the fluorescence signal was observed in both the hmDNA capture chamber containing the micropillar array and the bifurcated inlet/outlet, thereby confirming uniform filling of the chip.

To study the performance of the hmDNA enrichment device, the hmDNA enrichment capacity was determined and compared to a similar microfluidic device without a micropillar array. The theoretical surface areas of the hmDNA capture chambers are 1.38 cm^2 and 0.17 cm^2 for the devices with and without micropillar array, respectively, accounting also for surface roughness[48] due to the scallops and sputtered gold. Before hmDNA enrichment, the hmDNA capture coating was formed. The gold-coated substrate was first modified with the thiol-based SAM containing 15% azide-functionalized thiols. The SAM was formed by immersion of the substrate in a thiol solution overnight. Then, the device was sealed with the PDMS-coated glass and clamped in the chip holder. Thereafter, flow was applied to the devices to bind the linker molecule onto the SAM, followed by activation of the NTA complexes into NiNTA by flushing with a $NiCl_2$ solution and the surface immobilization of the His_{10}MBD2 proteins. The hmDNA enrichment capacity was determined using a 90 bp-long synthetic DNA containing three methylated CpGs (C*pGs, Mal3C*pG, sequence, see Table S6.1). A solution of Mal3C*pG (28 ng/µL, 500 nM) dissolved in binding buffer (BB) was flushed through the chip for 60 min to ensure a high degree of hmDNA binding at the MBD2-modified surface. Thus, in total 3360 ng of Mal3C*pG was flushed through the chip, as the flow rate was kept constant at 2 µL/min. After the DNA binding step, a 15 min washing step with BB was applied to remove weakly bound Mal3C*pG from the MBD2-coated surface. Subsequently, the aqueous ammonium hydroxide eluent was flushed through the chip with forward flow for 25 min while collecting the eluent. The volume of eluted Mal3C*pG samples is thus 50 µL, which was kept constant throughout this study. The number of cycles needed to reach the qPCR threshold (C_t value) is related to the Mal3C*pG concentration (Figure 6.4A) and, therefore, the C_t value can be used to assess the Mal3C*pG concentration in the eluted Mal3C*pG samples (Figure 6.4B). The qPCR amplification efficiency was 94.5% based on the slope of the calibration curve, indicating a good qPCR performance. An 11.5-fold higher Mal3C*pG concentration was found in the eluted Mal3C*pG sample from the microfluidic device with the micropillar array (4.60±0.99 ng) compared to the one without micropillar array (0.40±0.02 ng). The increase in the eluted Mal3C*pG concentration is directly attributed to the increase in the microfluidic chip surface area and is in good agreement compared to the increase in the surface area (8.1-fold). The direct correlation between bound DNA amount and chip surface area indicates absence or a limited effect of mass transport limitation, which is likely due to the relatively high hmDNA concentration used here. Overall, these results show the successful

development of the hmDNA enrichment device and the gain in binding capacity by the use of the micropillar array.

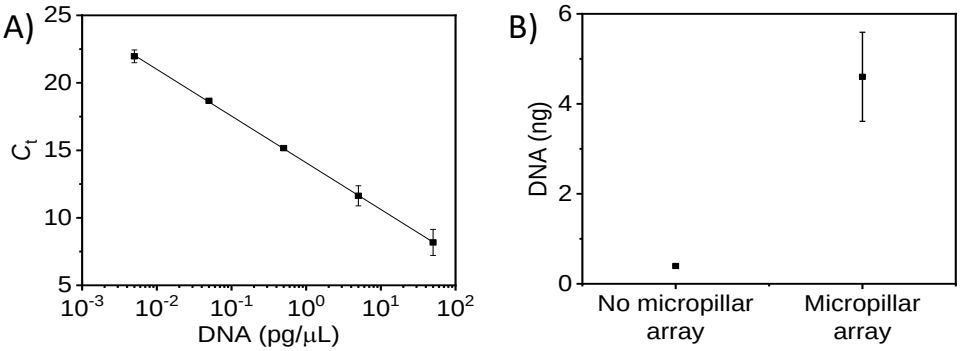

Figure 6.4. Determining the capacity of the hmDNA enrichment device. A) Calibration of Mal3C*pG with qPCR using varying Mal3C*pG input concentrations (n = 2). The datapoints were fitted with a linear fit (R^2 > 0.99). qPCR was performed using Sso Advanced Universal SYBR Green Supermix and corresponding primers (Table S6.2). B) Amount of Mal3C*pG eluted from the MBD2 surface using the hmDNA enrichment devices with and without micropillar array (n = 2). Mal3C*pG was flushed through the device at 500 nM in BB for 60 min at a flow rate of 2 µL/min. The enrichment device was functionalized with the thiol-based SAM containing 15% of azide thiol. The hmDNA capture coating was then formed in several steps in the microfluidic device: binding of the linker molecule, activation of the NTA groups with $NiCl_2$, and His_{10}MBD2 immobilization. After the hmDNA binding step a washing step with BB was applied for 15 min followed by elution of surface-bound hmDNA using aqueous ammonium hydroxide. The eluent was collected and characterized by qPCR. The error bars indicate the standard deviation.

6.2.2 hmDNA-based cervical cancer detection in DNA isolated from cells and urine samples

As a benchmark, DNA isolated from cells and urine supernatant samples were analyzed with quantitative methylation-specific PCR (qMSP) to determine the methylation level.[52,53] DNA was isolated from the EK11 and SiHa cells, which originate from primary human foreskin keratinocytes and human cervical cancer cell line, respectively.[52] Urinary cfDNA was isolated from the urine supernatant of a cervical cancer patient and of a healthy volunteer. The urine supernatant, instead of unfractioned urine, was used as a source for DNA to reduce the isolation of unfragmented genomic DNA originating from bladder cells that are present in the urine. DNA isolated from the urine

supernatant is highly fragmented with a mean fragment size of 90 bp.[54] However, DNA isolated from cells contain high molecular weight (mainly intact) genomic DNA. To make the fragment size of isolated cell DNA comparable to that of the urine DNA, the cell DNA was sheared to a main fragment size of 150 bp using ultrasonication (Figure S6.1).

The *MAL* gene is known to be hypermethylated in cervical cancer and can be detected in urine as a marker for cervical cancer.[52] As a benchmark, qMSP was performed on the isolated DNA samples targeting a CpG-rich region of the *MAL* gene after bisulfite conversion, as based on the work of Steenbergen *et al.* (Table S6.3).[55,56] In case the *MAL* gene is unmethylated, the primer and probes used with qMSP cannot anneal. Therefore, the absence of signal upon qMSP indicates the absence of *MAL* methylation. The Actin Beta (*ACTB*) gene was also targeted in the bisulfite-converted DNA samples with qMSP to function as an internal reference gene.[53] The targeted *ACTB* gene has no CpGs and is, therefore, not susceptible to bisulfite conversion.[53] The methylation levels are determined by performing the comparative C_t method using the C_t ratio of *MAL* and *ACTB*.[57] The methylation levels of the DNA samples are expressed by the $\log_2$ C_t ratio, were methylation levels of -13.3 indicate absence of methylation of the *MAL* gene targeted with the primers/probe with respect to the reference gene *ACTB*.[58] Methylation of the *MAL* gene was absent in DNA from the EK11 cells and the urine of a healthy volunteer (Figure 6.5). On the other hand, high *MAL* methylation levels were found in the SiHA cell DNA. Also, in the DNA isolated from the urine of a cervical cancer patient high *MAL* methylation levels were found, indicating that a significant part of the *MAL* copies present in the urine DNA are hypermethylated. Overall, both the cell DNA and urine DNA validated with qMSP are suitable to determine the selectivity of the hmDNA enrichment device when targeting the *MAL* gene with qPCR for cervical cancer detection.

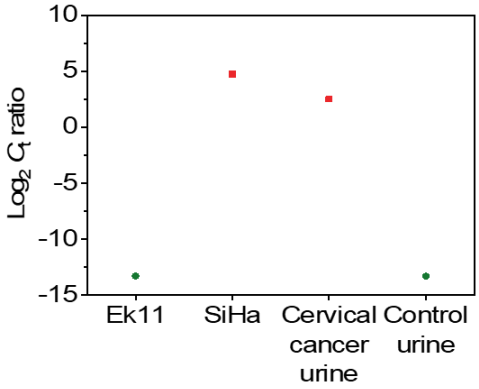

Figure 6.5. *MAL* methylation level in DNA isolated from EK11 and SiHa cells (n = 3) and urine supernatant samples of a cervical cancer patient and healthy control (n = 1). DNA isolated from EK11 and SiHa cells were sheared using ultrasonication prior to use. An amount of 250 ng DNA was subjected to bisulfite conversion. A total of 50 ng bisulfite-converted DNA was used for the qMSP analysis. The *MAL* methylation levels were calculated with the comparative C_t method using the C_t of *ACTB* and expressed as the $\log_2 C_t$ ratio.

DNA isolated from both the EK11 and SiHa cells and DNA from urine samples of a cervical cancer patient and a healthy control were amplified with qPCR targeting the *MAL* gene to enable detection of *MAL* in hmDNA-enriched DNA samples. Primers were designed for qPCR to target a 106 bp length of *MAL* gene (Table S6.4). Different primers were used for qPCR compared to qMSP as qPCR is used to detect the *MAL* gene in enriched DNA samples, which are, thus, not converted in the bisulfite treatment. The PCR products were characterized with DNA electrophoresis (Figure 6.6A and B). The band of the amplified *MAL* targets is close to the expected length of 106 bp independent of the DNA origin (cells or urine DNA). Moreover, no side products were formed upon *MAL* amplification in the various tested DNA samples as no other DNA bands were observed in the gel images. Therefore, the *MAL* gene was successfully amplified in the DNA samples from the cell lines and urine samples.

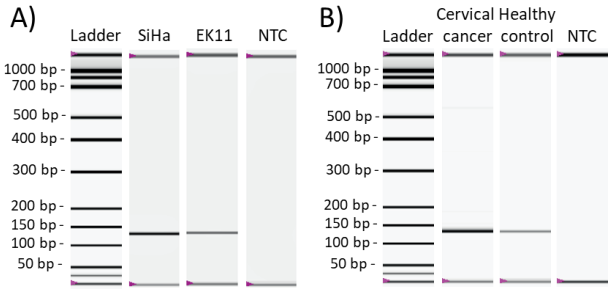

Figure 6.6. Gel images generated by DNA electrophoresis after qPCR amplification of the *MAL* gene from DNA isolated from A) cells and B) urine supernatant. *MAL* was amplified in the isolated DNA originating from: A) SiHa cells and EK11 cells; B) urinary cfDNA from cervical cancer patient and from a healthy control. DNA isolated from EK11 and SiHa cells were sheared using ultrasonication prior to use. Each gel image shows a ladder, a no-template control (NTC) and a lower and upper marker in each lane.

Subsequently, we explored whether the DNA isolated from the cancer and non-cancer cells SiHa and EK11 could be enriched in hmDNA selectively by the use of the micropillared capture device. Prior to hmDNA enrichment, the micropillared device was coated with MBD2 proteins using a SAM with 15% of azide thiol. After surface immobilization of MBD2 as described above, the DNA binding step was performed. In total 300 ng cell DNA dissolved in BB with a total volume of 120 µL was flushed through the chip for 60 min. Therefore, approximately 87,000 *MAL* copies can potentially be enriched when assuming that the full genomic DNA is present in the DNA sample isolated from the SiHa cells. Throughout the DNA binding step, the flow-through was collected to determine the C_t value of *MAL* to evaluate which fraction of the *MAL* copies does not bind to the MBD2-modified surface. After the DNA binding step the washing and elution steps were applied. Three samples were collected during the hmDNA enrichment: DNA input solution, DNA flow-through, and the hmDNA-enriched DNA sample upon elution. Subsequently, the collected samples were characterized with qPCR to determine the *MAL* C_t value in each collected sample.

The C_t value of the *MAL* gene in the unenriched SiHa DNA sample (input) was equal to 28.8±0.5 cycles (Figure 6.7A). The *MAL* gene could not be detected in the flow-through of enriched SiHa DNA below the qPCR upper limit (35 cycles), indicating the absence of *MAL* copies in the flow-through. The absence of *MAL* in the flow-through indicates that all *MAL* copies were bound to the MBD2 surface while flushing the DNA solution through the micropillar device. Absence of *MAL* in the flow-through is expected as the *MAL* methylation level is high in the SiHa DNA sample, thus resulting into a high avidity and binding efficiency of *MAL* to the MBD2 surface. As a result, the C_t value of *MAL* in

the enriched SiHA DNA sample was 1.5 cycles lower in comparison to the *MAL* C_t value in the input sample, indicating a higher *MAL* concentration. The ΔC_t of 1.5 was converted to determine the concentration difference when assuming that the qPCR efficiency of *MAL* is 100%, independent of the methylation status and sample origin. The total amount of *MAL* found in the enriched SiHa DNA fraction was approximately equal (117.9%) of the total amount of *MAL* present in the DNA input solution sample (Table 6.1). The increase in *MAL* concentration is attributed to the 2.4-fold smaller volume of the enriched solution (50 µL) compared to the input solution (120 µL) and is therefore, in proper agreement with the concentration increase measured by qPCR. The detection of all *MAL* in the enriched sample confirms that the *MAL* is hypermethylated and supports the observed absence of *MAL* in the flow-through. As a consequence, it is likely that no DNA is removed from the surface upon washing the surface with BB after the DNA binding step.

For the EK11 cell DNA, the *MAL* C_t value equals to 31.6±0.7 cycles in the input sample. The C_t values observed in the flow-through and enriched fraction of EK11 were 0.4 cycles and 1.7 cycles higher in comparison to the input solution, respectively (Figure 6.7A, Table 6.1). The main fraction (75.8%) of the non-methylated *MAL* was thus found in the flow-through while only 12.8% was detected in the enriched fraction. The remainder of the *MAL* (11.4%) is likely washed away from the MBD2 surface after the DNA binding step. Despite the absence of *MAL* methylation in EK11 still a minor fraction of *MAL* is detected in the enriched DNA from the EK11 cell line. This co-enrichment of non-methylated DNA is attributed to the (partial) background methylation of the CpGs which were not targeted by the primers and probe during qMSP.[52,56] Furthermore, an individual C*pG present in the primers and probe binding area is also likely not detected after bisulfite conversion with qMSP, as this results only in a single bp mismatch upon annealing. As was discussed in Chapter 3, the presence of two C*pGs in DNA with a length of 90 bp is already sufficient to ensure surface binding at the used MBD2 surface receptor density here. Additionally, the fragment size of sonicated DNA is widely distributed (80 – 600 bp). Thus, multiple interactions pairs can be formed by the (non-)methylated CpGs in *MAL* with MBD2 proteins on the surface. As both C*pG and CpG interact with MBD2, though a C*pG interacts with a higher affinity to MBD2, the avidity is thus likely high enough for partial binding of *MAL*, especially with some degree of background methylation.

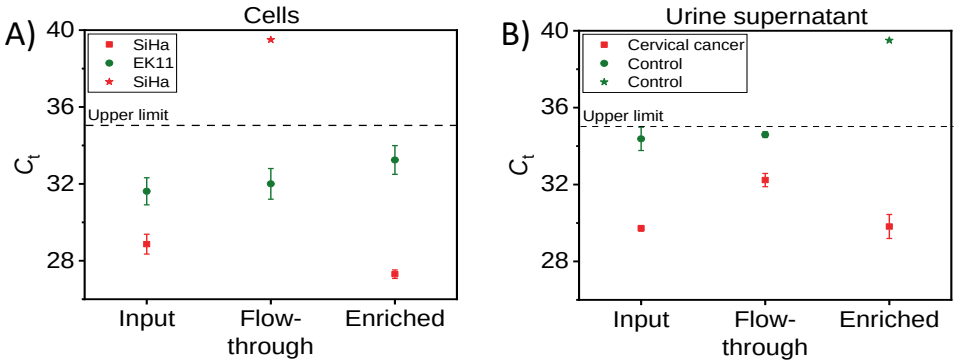

Figure 6.7. DNA isolated from A) cells and B) urine supernatant was enriched for hmDNA. The *MAL* C_t values in the input, flow-through and enriched samples were determined by qPCR. hmDNA enrichment was performed in the hmDNA enrichment device with a micropillar array (n = 2). The hmDNA capture coating with MBD2 was formed in the device as described above. A) 300 ng DNA isolated from EK11 and SiHa cells and B) 150 ng DNA isolated from urine supernatant dissolved in 120 µL BB was flushed for 60 min through the device. After the DNA binding step the system was flushed for 15 min with BB followed by a 25 min elution step using aqueous ammonium hydroxide. For all the steps in the enrichment device a flow rate of 2 µL/min was used. DNA isolated from EK11 and SiHa cells were sheared using ultrasonication prior to use. The error bars indicate the standard deviation. The error bars indicate the standard deviation.

To evaluate the efficiency of the hmDNA enrichment device for enrichment of hmDNA from urine, we tested DNA isolated from urine supernatant of a cervical cancer patient and of a healthy control. Urine DNA was enriched for hmDNA by flushing 150 ng DNA through the chip for 1 h at a flow rate of 2 µL/min. The C_t value of enriched urine DNA of the cervical cancer patient was 29.8±0.6 cycles, and thus encompasses 38.9% of the total copies of *MAL* present in the input sample (Figure 6.7B, Table 6.1). In the flow-through less *MAL* was detected (2.5 higher C_t value), which is only 17.7% of the input. A significant remainder of *MAL* (43.4%) is thus detected neither in the enriched nor in the flow-through sample. Likely, *MAL* is removed from the MBD2 surface after the DNA binding step upon washing with BB as the methylation of *MAL* (and other genes) is more heterogeneous in urine compared to cell line DNA. We attribute this to the fact that DNA in urine originates both from healthy and cancer cells. Typically, DNA with a lower degree of methylation will be removed more easily from the MBD2 surface upon the washing step with BB (see Chapter 3). As discussed above, upon the hmDNA enrichment of cell line DNA approximately all (methylated) *MAL* copies were detected in either the enriched or flow-through sample. The differences are thus attributed to the heterogeneity in methylation of the *MAL* gene in the urine sample. Furthermore,

the main fragment size of isolated DNA in urine is close to 90 bp with a maximum length of 300 bp,[54] while the sonicated DNA is on average 150 bp in length with an upper limit of 600 bp (Figure S6.1). Likely, the longer cell DNA is able to bind with a higher avidity to the MBD2 surface compared to the shorter urine DNA. This higher avidity is attributed to more MBD2 C*pG interaction pairs formed from longer DNA sequences. As a consequence, cell DNA will thus be less easily removed from the MBD2 surface upon washing, and more *MAL* ends up in the enriched sample.

As a control experiment, DNA isolated from urine of a healthy control was also enriched for hmDNA (Figure 6.7B, Table 6.1). As expected, the reverse effect was observed upon enrichment compared to DNA isolated from the urine of a cervical cancer patient. The *MAL* C_t value could not be detected in the enriched DNA sample below the qPCR threshold. On the other hand, the flow-through contained the major part of *MAL* as the C_t value is only 0.6 higher compared to the input. The total *MAL* amount in the flow-through was equal to 66.2% from the input sample. The remaining amount of *MAL* is likely washed away from the surface after the DNA binding step. Furthermore, it can be noticed that the C_t value of *MAL* differs in the input samples between DNA isolated from urine of a cervical cancer patient and the healthy volunteer, which might be due to variations between individuals.[59]

Table 6.1. *MAL* C_t values in the input, flow-through, and enriched samples of DNA isolated from cells (SiHA and EK11) and from urine supernatant (cervical cancer patient and healthy volunteer). ΔC_t values were calculated by subtracting the C_t values of the input sample from the enriched or flow-through sample. ΔC_t values were used to determine the fractions of input *MAL* present in each sample, while correcting the enriched samples for the 2.4-fold concentration increase. The percentage of *MAL* was calculated by assuming a 100% qPCR efficiency. C_t values that could not be determined with qPCR, and consequently the percentage of *MAL*, is shown here as "ND".

Sample origin	Sample type	C_t	ΔC_t	Amount of DNA (%)
SiHa cells	Input	28.8	-	-
	Flow-through	ND	ND	ND
	Enriched	27.3	-1.5	117.9
EK11 cells	Input	31.6	-	-
	Flow-through	32	0.4	75.8
	Enriched	33.3	1.7	12.8
Cervical cancer urine	Input	29.7	-	-
	Flow-through	32.2	2.5	17.7
	Enriched	29.8	0.1	38.9
Control urine	Input	34.3	-	-
	Flow-through	34.9	0.6	66.2
	Enriched	ND	ND	ND

6.3 Conclusion and outlook

In this work, we developed a microfluidic hmDNA enrichment chip for hmDNA-based cervical cancer detection in urine. The chip contains a hmDNA enrichment chamber with an array of micropillars. The chip was coated with a gold layer and modified with a thiol-based SAM with NiNTA moieties enabling surface immobilization of His_{10}-tagged MBD2 proteins. The hmDNA enrichment capacity of the chip was determined to be 4.6 ng. DNA was isolated from cervical cancer and control cells and from urine samples of a cervical cancer patient and a healthy volunteer to validate the hmDNA enrichment performance of the chip. The *MAL* gene was confirmed to be hypermethylated in

cervical cancer cells and urine DNA. hmDNA enrichment of cell DNA showed a high hmDNA enrichment selectivity and efficiency of the chip. The *MAL* gene was detected only in hmDNA enriched DNA from the urine of a cervical cancer patient, thus enabling cervical cancer diagnostics. Overall, these results demonstrate the high selectivity and clinical utility of the developed hmDNA enrichment chip. Future research includes enlarging the sample size of this study to determine the clinical usefulness. Then, testing whether the developed chip can also be used to enrich urine DNA with other hmDNA cancer biomarkers to facilitate for example lung and bladder cancer diagnostics and determining the minimal required isolated DNA sample amount upon hmDNA enrichment. Furthermore, it should be tested whether the chip enables early-stage cancer diagnostics. Finally, the chip will be further optimized by reducing the elution volume and combining both the hmDNA enrichment and detection on the same chip to enable point-of-care hmDNA-based cancer detection.

6.4 Acknowledgement

Birgit Wever, Annina van Splunter and Renske Steenbergen are thanked for providing the DNA isolated from cells and urine, qMSP analysis and the fruitful discussions. Johan Bomer is acknowledged for the production of the micropillared lab-on-a-chip device.

6.5 Experimental section

6.5.1 Materials

Gravity flow columns, Experion DNA chips, Microseal 'B' PCR Plate Sealing Film, SsoAdvanced Universal SYBR Green Supermix, ddPCR™ 96-well plates, Experion™ DNA 1K Reagents and Supplies were obtained from BioRad. NaCl, β-mercaptoethanol, dimethyl sulfoxide ≥99.7% (DMSO), EDTA, $MgCl_2$ ≥ 98.0% ($MgCl_2$), LB Broth, lysozyme from chicken egg white (≥90% lysozyme), phenylmethanesulfonyl fluoride (PMSF), ribonuclease A from bovine pancreas (RNAse), deoxyribonuclease I from bovine pancreas (DNAse), kanamycin sulfate from *Streptomyces kanamyceticus*, nickel(II) chloride hexahydrate ($NiCl_2$), N_α,N_α-bis(carboxymethyl)-L-lysine hydrate ≥ 97.0%, sodium carbonate, phosphate-buffered saline (PBS) tablets for 10 mM solution, H_2SO_4 95-97%, 0.2 µm membrane filter, ammonium hydroxide solution 25%, fluorescein, triethylamine and sodium dodecyl sulfate ≥ 99% (SDS) were purchased from Sigma Aldrich. Tris(hydroxymethyl)aminomethane (Tris), isopropyl-β-D-thiogalactopyranoside ≥ 99% (IPTG), HNO_3, H_2O_2 33 % and absolute ethanol were bought from VWR. Imidazole 99% and Triton X-100 were obtained from ACROS Organics. Ni-NTA-agarose beads were purchased from Protino®. PD-10 Sephadex™

desalting columns were obtained from GE Health. DBCO-PEG_4-NHS ester was purchased from Click Chemistry Tools. All the DNA sequences, primers and probes were bought from Eurofins Genomics and Eurogentec. gBlocks™ Gene Fragments were obtained from Integrated DNA Technologies. QIAamp DNA mini kit and EpiTect MethyLight Master Mix were bought from Qiagen while Quick-DNA urine kit and EZ DNA Methylation kit were obtained from Zymo Research. Nuclease-free water, CpG methyltransferase (M.SssI), rCutsmart buffer™ and S-adenosylmethionine were purchased from New England Biolabs. $HSC_{11}(EG)_5$-OH and $HSC_{11}(EG)_5$-N_3 were bought from Prochimia. NucleoSpin® Gel and PCR Clean-up was purchased from BIOKÉ. Silicon wafers were obtained from Okmetic Finland, while MEMpax glass wafer was purchased from Schott. Positive Olin 907-17 photoresist was obtained from Arch Chemicals and the dry film photoresist foil MX5020 was obtained from DuPont. Fused silica tubing with an outer and inner diameter of 360 µm and 100 µm was obtained from Inacom BV.

6.5.2 Methods

PDMS-coated chips

MEMpax glass wafers were cleaned in piranha (H_2SO_4:H_2O_2 in ratio 3:1) and covered with a PDMS layer by spin coating. The wafer was then heated to 60 °C for 10 min followed by dicing (DAD3220, Disco) into separate chips.

Micropillar-structured chips

A silicon wafer was cleaned in 99% HNO_3 for 5 min, 1% HF for 1 min and 99% HNO_3 for 1 min. A positive photoresist was deposited on the silicon wafer followed by a photolithography step. Micropillar-structured substrates were formed by DRIE (Oxford PlasmaPro 100 Estrelas). The created substrates were then cleaned in O_2/CF_4 plasma (Tepla 360) for 60 min and in a piranha solution heated to 105 °C for 1 h to strip the fluorocarbon residues and photoresist from the substrates. A dry film photoresist foil was placed on the wafer followed by photolithography and powder-blasting. The foil was removed by immersion of the wafer in a 2% sodium carbonate solution heated to 50 °C for 1 h followed by washing with demineralized water. Prior to the gold sputtering, the modified silicon substrates were cleaned for 30 s in HF to remove the silicon dioxide layer and 5 min in HNO_3. Immediately after the HF step, a tantalum layer (3 min 200 W) and gold layer (30 min 50 W) was sputtered (TCOathy) at 10^{-2} mbar. Finally, the wafer was diced into separate chips.

Microfluidic chips

Gold-coated micropillar-structured chips were covered with a glass chip modified with the 1.5 µm PDMS layer and mounted in an in-house made chip holder. Fused silica

tubing was connected to the chip holder and syringes using microfluidic connectors. Flow rates of 2 µL/min with a syringe pump (Harvard PHD 2000) were applied. All solutions were filtered with a 0.2 µm filter prior to use. Filling of the microfluidic chip was confirmed by flushing with fluorescein and using a fluorescence microscope (Leica DMI5000 M).

His_{10}MBD2 production and purification

The *E. coli* bacteria were grown up to an optical density (OD) of 0.5 at 600 nm at 37 °C in LB medium with 30 µg/m of Kanamycin according to the procedure described in Chapter 3. The culture was cooled down to 17 °C, followed by expression of the His_{10}MBD2 protein after induction with 1 mM of IPTG for 15 h at 17 °C while stirring at 210 rpm. The culture was centrifuged (Allegra™ 25R) at 5000 rpm for 15 min at 4 °C to sediment the bacteria. The bacteria were lysed with sonication in a lysis buffer of 50 mM Tris-HCl pH 7.2, 300 mM NaCl, 30 mM imidazole, 0.1% β-mercaptoethanol, 1 mM EDTA, 20 mM $MgCl_2$, 1 mM PMSF, 0.5 mg/mL lysozyme, 20 µg/mL DNAse, 20 µg/mL RNAse A. Sonication (Fisherbrand™ 120) was performed on ice twice for 30 s with a waiting step in between of 2 min. The sonicated samples were centrifuged at 3100 rpm for 15 min at 4 °C, and the supernatant was then centrifuged at 40000 rpm for 60 min at 4°C (WX Ultra 90, Thermo Scientific). The supernatant was loaded on a NiNTA column and incubated for 30 min while shaking at 4°C . The column was washed with 25 mL washing buffer (50 mM Tris pH 7.2, 300 mM NaCl, 30 mM imidazole, 0.1% β-mercaptoethanol). His_{10}MBD2 was removed from the NiNTA column with an elution buffer (50 mM Tris pH 7.2, 300 mM NaCl, 650 mM imidazole, 0.1% β-mercaptoethanol). Directly afterwards, the His_{10}MBD2 sample was purified with a PD10 column and eluted in the IB buffer (50 mM TRIS pH 7.2, 300 mM NaCl, 0.1% β-mercaptoethanol). The His_{10}MBD2 sample was aliquoted, snap-frozen and stored at -80°C until further use.

Mal3CpG methylation

Methylation of Mal3CpG was performed by mixing 4 µg Mal3CpG with 8 units of *M.SssI* enzyme, S-adenosylmethionine at a concentration of 600 µM and 2.5 µL rCutsmart buffer™. The reaction volume was increased to 25 µL with nuclease-free water. The reaction was performed at 37 °C for 15 h in a T100 thermocycler (BioRad). The reaction was stopped by heating the mixture to 65 °C for 20 min.

Synthesis of linker molecule

DBCO-PEG_4-NHS was dissolved in DMSO at 250 mM, directly aliquoted and stored at -18 °C until further use. N_α,N_α-bis(carboxymethyl)-L-lysine hydrate was dissolved in PBS pH 7.4 at 1 mM before the start of the reaction. The dissolved DBCO-OEG_4-NHS was added to the N_α,N_α-bis(carboxymethyl)-L-lysine hydrate solution at a final

concentration of 0.1 mM. The reaction components were stirred overnight at 180 rpm to ensure completion of the reaction.

SAM formation

Gold-coated micropillar-structured chips were cleaned in a piranha solution for 10 s followed by immersion of the chips in Milli-Q water. Afterwards, the chips were rinsed extensively with ethanol, Milli-Q water and ethanol, followed by drying using N_2. The gold chips were then oxidized using UV-ozone (BioForce, Nanosciences) for 30 min. A thiol solution was prepared using 85% $HSC_{11}(EG)_5$-OH and 15% $HSC_{11}(EG)_6$-N_3 in ethanol with a total thiol concentration of 2 mM. The oxidized gold chips were completely immersed in the thiol solution overnight to form the SAM. After the SAM formation the gold chips were rinsed extensively with ethanol, Milli-Q water and ethanol and dried in a stream of N_2.

hmDNA enrichment

The linker molecule was flushed through the SAM-modified microfluidic chips for 1.5 h, at a concentration of 0.1 mM in PBS pH 7.4 followed by the addition of 25 mM $NiCl_2$ in Milli-Q water for 10 min and a washing step with Milli-Q for 5 min. His_{10}MBD2 dissolved in IB at a concentration of 1 µM was added for 15 min. After MBD2 immobilization, a washing step with IB was applied for 15 min. Then DNA dissolved in BB (50 mM Tris, 350 mM NaCl and 0.1% Triton X-100) was added for 1 h followed by a washing step with BB for 15 min. Surface-bound DNA was eluted by flushing with 150 mM ammonium hydroxide pH 11.3 solution. The eluent was collected and purified on a NucleoSpin Gel & PCR Clean-up column in a volume of 30 µL.

qPCR

DNA was amplified with CFX96 Touch qPCR Detection System (BioRad) using primers (Tables S6.2 and S6.4) at a concentration of 300 nm, 5 µL SsoAdvanced Universal SYBR Green Supermix and nuclease-free water. The qPCR assay volume was performed in a ddPCR™ 96-well plate using an assay volume of 10 µL. The 96-well plate was sealed using Microseal 'B' PCR Plate Sealing Film prior to qPCR analysis. qPCR temperature steps for Mal3C*pG amplification were 98 °C for 1 min, 39 cycles of 98 °C for 10 s and 64 °C for 30 s and 72 °C for 1 min. For the amplification of the *MAL* gene in DNA isolated from cell lines and urine, temperature steps of 98 °C for 3 min and 35 cycles of 98 °C for 15 s and 63.9 °C for 30 s were used. C_t values were determined at a fluorescence intensity threshold of 200 a.u.

DNA electrophoresis

DNA samples were analyzed using DNA Experion chips and Experion™ DNA 1K Reagents and Supplies according to the instruction of the manufactures on an automated electrophoresis system (Experion™, BioRad).

Cell cultures

Primary human foreskin keratinocytes (EK-11) and the cervical cancer cell line (SiHa) were cultured as described previously.[60]

Clinical samples

Urine samples were randomly selected from a previously published cohort.[9] Briefly, the urine samples of women with histologically confirmed cervical cancer were collected preceding primary cancer treatment within the SOLUTION 1 study. Urine samples of healthy female volunteers served as controls and were collected within the Urine Controls (URIC) biobank. Controls had no oncological history within 5 years prior to collection. The Medical Ethical Committee of the VU University Medical Centre (Amsterdam, The Netherlands) approved the use of samples collected from women diagnosed with cervical cancer (no. 2016.213) and healthy female controls (no. 2018.657). All women were 18 years or older and written informed consent was obtained from each participant.

Urine collection and processing

Urine was collected from home and processed as described previously.[9] Collection tubes contained ethylenediamine tetraacetic acid (EDTA) as a preservative agent (final concentration 40 mM) to maintain DNA quality.[61] The urine supernatant was acquired by centrifugation at 3000g for 15 min. Urine samples were stored at -20 °C until DNA extraction.

DNA isolation and bisulfite conversion

DNA of EK-11 and SiHa was isolated using the QIAamp DNA mini kit. Isolated genomic DNA was fragmented on a Covaris S220 Focused-Ultrasonicator (Covaris Inc., Woburn, MA) to a target size of 150 bp. The size distribution of the sheared DNA was measured on a Tapestation (Agilent Technologies, Santa Clara, CA). Urinary cfDNA was isolated from 15 mL urine supernatant using the Quick DNA urine kit. DNA concentrations were measured using a NanoDrop 1000 (Thermo Fisher Scientific). Purified DNA (250 ng) was subjected to sodium bisulfite treatment using the EZ DNA Methylation kit. All procedures were performed according to manufacturer's instructions.

DNA methylation analysis

DNA methylation analysis was performed by qMSP, as previously described.[56] In short, *MAL* methylation levels were measured by a multiplex qMSP targeting the hypermethylated promoter region of the *MAL* gene and a reference gene (*ACTB*). The qMSP analysis was run on a ViiA7 real-time PCR system (Applied Biosystems) using 50 ng modified (cf)DNA mixed with EpiTect MethyLight Master Mix, primers, and Taqman probes (Table S6.3). *ACTB* was taken along as reference gene for quality assessment

and input normalization. Samples with a *ACTB* C_t value ≥ 32 from methylation analysis were excluded to ensure sufficient input and quality. Double-stranded gBlocks™ Gene Fragments containing the amplicon sequences of *MAL* and *ACTB* were used as technical quality control. Methylation levels were computed by normalizing the methylation level of *MAL* according to the reference gene *ACTB* using the comparative C_t method ($2^{-\Delta C_t} \times 100$) to obtain C_t ratios, and log transformed.

6.6 Supporting information

Table S6.1. DNA sequence of Mal3C*pG. Location of the C(*)pGs are highlighted.

	5′ - 3′
FWD	CAGGCAGATG**CG**CAGCACCAAGCAGAGAGGCCAGGTGCAGGATCCCAGGCC**CG**AACCAGGCCTGGCTCAGTGGAGC**CG**GAAGGGGCAGGC
REV	GCCTGCCCCTTC**CG**GCTCCACTGAGCCAGGCCTGGTT**CG**GGCCTGGGATCCTGCACCTGGCCTCTCTGCTTGGTGCTG**CG**CATCTGCCTG

Table S6.2. Primer sequence to amplify the 90 bp-long hmDNA with 3 C*pGs using qPCR.

	5′ - 3′
FWD	CAGGCAGATGCGC
REV	GCCTGCCCCTTCCG

Table S6.3. Primer and probe sequences with fluorescent label for qMSP targeting the *MAL* gene of bisulfite-converted DNA isolated from the EK11 and SiHa cell lines and from urine samples of a cervical cancer patient and a healthy volunteer.

		5′ - 3′	
ACTB	FWD	TGGTGATGGAGGAGGTTTAGTAAGT	
	REV	AACCAATAAAACCTACTCCTCCCTTAA	
MAL	FWD	CGCGTAGTATTAAGTAGAGAGGTTCG	
	REV	ATCTACAATAAAAAATAAAACCGACCG	
ACTB	Probe	ACCACCACCCAACACACAATAACAAACACA	**CY5**
MAL	Probe	CCACTAAACCGACGCTAATTCGACGCT	**FAM**

Table S6.4. qPCR primer sequence to amplify DNA isolated from the EK11 and SiHa cell lines and urine samples of a cervical cancer patient and a healthy volunteer.

	5′ - 3′
FWD	CAGCTGGGAGCAACCTC
REV	CTTCCGCGTCCACTGAG

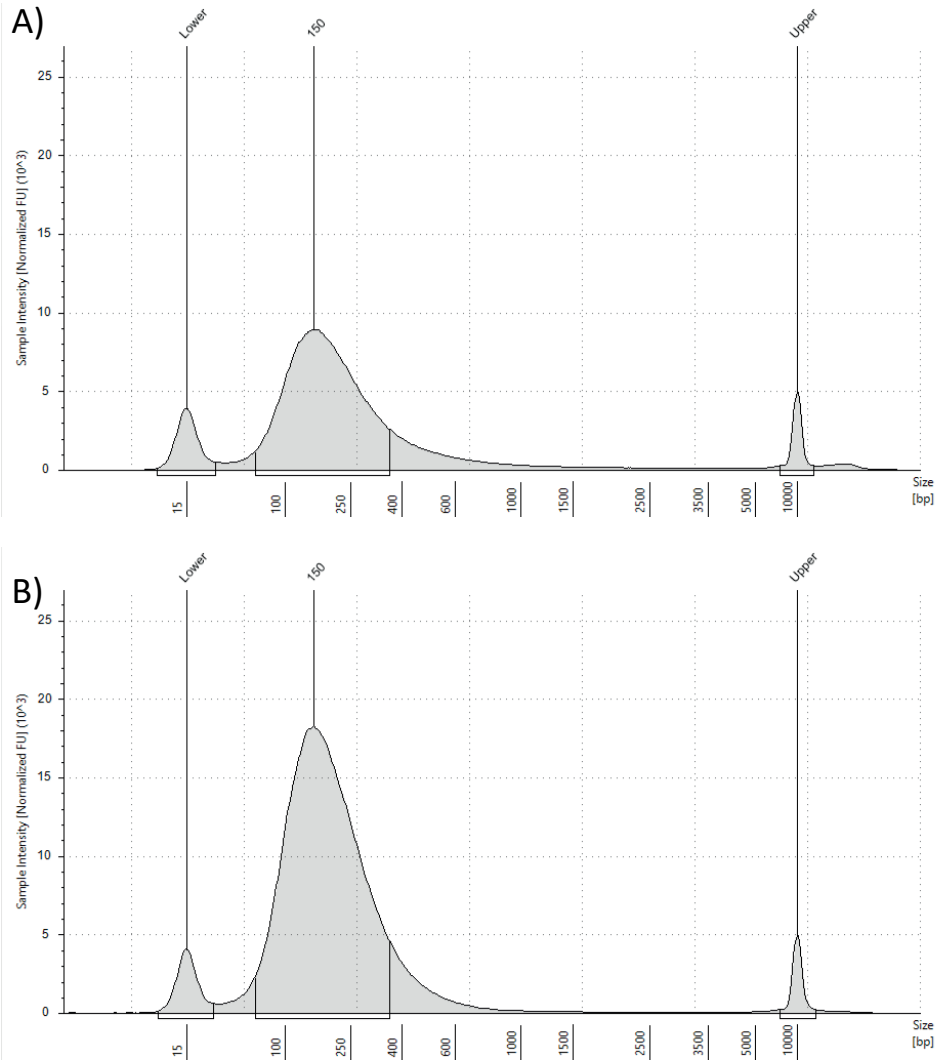

Figure S6.1. Covaris sheared DNA isolated from the A) EK11 and B) SiHa cell line characterized with the Tapestation automated electrophoresis system. The bands at 15 bp and 10.000 bp are the lower and upper markers, respectively.

6.7 References

(1) Bettegowda, C.; Sausen, M.; Leary, R. J.; Kinde, I.; Wang, Y.; Agrawal, N.; Bartlett, B. R.; Wang, H.; Luber, B.; Alani, R. M.; Antonarakis, E. S.; Azad, N. S.; Bardelli, A.; Brem, H.; Cameron, J. L.; Lee, C. C.; Fecher, L. A.; Gallia, G. L.; Gibbs, P.; Le, D.; Giuntoli, R. L.; Goggins, M.; Hogarty, M. D.; Holdhoff, M.; Hong, S.-M.; Jiao, Y.; Juhl, H. H.; Kim, J. J.; Siravegna, G.; Laheru, D. A.; Lauricella, C.; Lim, M.; Lipson, E. J.; Marie, S. K. N.; Netto, G. J.; Oliner, K. S.; Olivi, A.; Olsson, L.; Riggins, G. J.; Sartore-Bianchi, A.; Schmidt, K.; Shih, L.-M.; Oba-Shinjo, S. M.; Siena, S.; Theodorescu, D.; Tie, J.; Harkins, T. T.; Veronese, S.; Wang, T.-L.; Weingart, J. D.; Wolfgang, C. L.; Wood, L. D.; Xing, D.; Hruban, R. H.; Wu, J.; Allen, P. J.; Schmidt, C. M.; Choti, M. A.; Velculescu, V. E.; Kinzler, K. W.; Vogelstein, B.; Papadopoulos, N.; Diaz, L. A. Detection of Circulating Tumor DNA in Early- and Late-Stage Human Malignancies. *Sci. Transl. Med.* **2014**, *6*, 224ra24.

(2) Haber, D. A.; Velculescu, V. E. Blood-Based Analyses of Cancer: Circulating Tumor Cells and Circulating Tumor DNA. *Cancer Discov.* **2014**, *4*, 650–661.

(3) Oshi, M.; Murthy, V.; Takahashi, H.; Huyser, M.; Okano, M.; Tokumaru, Y.; Rashid, O. M.; Matsuyama, R.; Endo, I.; Takabe, K. Urine as a Source of Liquid Biopsy for Cancer. *Cancers (Basel)* **2021**, *13*, 2652.

(4) Schwarzenbach, H.; Hoon, D. S. B.; Pantel, K. Cell-Free Nucleic Acids as Biomarkers in Cancer Patients. *Nat. Rev. Cancer* **2011**, *11*, 426–437.

(5) Wan, J. C. M.; Massie, C.; Garcia-Corbacho, J.; Mouliere, F.; Brenton, J. D.; Caldas, C.; Pacey, S.; Baird, R.; Rosenfeld, N. Liquid Biopsies Come of Age: Towards Implementation of Circulating Tumour DNA. *Nat. Rev. Cancer* **2017**, *17*, 223–238.

(6) Salvi, S.; Martignano, F.; Molinari, C.; Gurioli, G.; Calistri, D.; De Giorgi, U.; Conteduca, V.; Casadio, V. The Potential Use of Urine Cell Free DNA as a Marker for Cancer. *Expert Rev. Mol. Diagn.* **2016**, *16*, 1283–1290.

(7) Bryzgunova, O. E.; Laktionov, P. P. Extracellular Nucleic Acids in Urine: Sources, Structure, Diagnostic Potential. *Acta Naturae* **2015**, *7*, 48–54.

(8) Luo, H.; Wei, W.; Ye, Z.; Zheng, J.; Xu, R. Liquid Biopsy of Methylation Biomarkers in Cell-Free DNA. *Trends Mol. Med.* **2021**, *27*, 482–500.

(9) Van den Helder, R.; Steenbergen, R. D. M.; Van Splunter, A. P.; Mom, C. H.; Tjiong, M. Y.; Martin, I.; Rosier-van Dunné, F. M. F.; Van der Avoort, I. A. M.; Bleeker, M. C. G.; Van Trommel, N. E. HPV and DNA Methylation Testing in Urine for Cervical Intraepithelial Neoplasia and Cervical Cancer Detection. *Clin. Cancer Res.* **2022**, *28*, 2061–2068.

(10) Kandimalla, R.; Van Tilborg, A. A.; Zwarthoff, E. C. DNA Methylation-Based Biomarkers in Bladder Cancer. *Nat. Rev. Urol.* **2013**, *10*, 327–335.

(11) Bach, S.; Paulis, I.; Sluiter, N. R.; Tibbesma, M.; Martin, I.; Van de Wiel, M. A.; Tuynman, J. B.; Bahce, I.; Kazemier, G.; Steenbergen, R. D. M. Detection of Colorectal Cancer in Urine Using DNA Methylation Analysis. *Sci. Rep.* **2021**, *11*, 2363.

(12) Van den Helder, R.; Wever, B. M. M.; Van Trommel, N. E.; Van Splunter, A. P.; Mom, C. H.; Kasius, J. C.; Bleeker, M. C. G.; Steenbergen, R. D. M. Non-Invasive Detection of

Endometrial Cancer by DNA Methylation Analysis in Urine. *Clin. Epigenetics* **2020**, *12*, 165.

(13) Liu, B.; Ricarte Filho, J.; Mallisetty, A.; Villani, C.; Kottorou, A.; Rodgers, K.; Chen, C.; Ito, T.; Holmes, K.; Gastala, N.; Valyi-Nagy, K.; David, O.; Gaba, R. C.; Ascoli, C.; Pasquinelli, M.; Feldman, L. E.; Massad, M. G.; Wang, T.-H.; Jusue-Torres, I.; Benedetti, E.; Winn, R. A.; Brock, M. V.; Herman, J. G.; Hulbert, A. Detection of Promoter DNA Methylation in Urine and Plasma Aids the Detection of Non–Small Cell Lung Cancer. *Clin. Cancer Res.* **2020**, *26*, 4339–4348.

(14) Kojima, K.; Takahashi, N.; Yada, Y.; Koike, Y.; Matano, M.; Kono, Y.; Momoi, M. Y. White-Matter Damage in a Neonate with Disseminated Herpes Simplex Virus Infection. *Pediatr. Int.* **2012**, *54*, 409–412.

(15) Brena, R. M.; Huang, T. H.-M.; Plass, C. Quantitative Assessment of DNA Methylation: Potential Applications for Disease Diagnosis, Classification, and Prognosis in Clinical Settings. *J. Mol. Med.* **2006**, *84*, 365–377.

(16) Bhattacharjee, R.; Moriam, S.; Umer, M.; Nguyen, N.-T.; Shiddiky, M. J. A. DNA Methylation Detection: Recent Developments in Bisulfite Free Electrochemical and Optical Approaches. *Analyst* **2018**, *143*, 4802–4818.

(17) Warnecke, P. M.; Stirzaker, C.; Song, J.; Grunau, C.; Melki, J. R.; Clark, S. J. Identification and Resolution of Artifacts in Bisulfite Sequencing. *Methods* **2002**, *27*, 101–107.

(18) Bach, S.; Paulis, I.; Sluiter, N. R.; Tibbesma, M.; Martin, I.; van de Wiel, M. A.; Tuynman, J. B.; Bahce, I.; Kazemier, G.; Steenbergen, R. D. M. Detection of Colorectal Cancer in Urine Using DNA Methylation Analysis. *Sci. Rep.* **2021**, *11*, 2363.

(19) Wever, B. M. M.; Bach, S.; Tibbesma, M.; ter Braak, T. J.; Wajon, D.; Dickhoff, C.; Lissenberg-Witte, B. I.; Hulbert, A.; Kazemier, G.; Bahce, I.; Steenbergen, R. D. M. Detection of Non-Metastatic Non-Small-Cell Lung Cancer in Urine by Methylation-Specific PCR Analysis: A Feasibility Study. *Lung Cancer* **2022**, *170*, 156–164.

(20) Rauch, T.; Pfeifer, G. P. Methylated-CpG Island Recovery Assay: A New Technique for the Rapid Detection of Methylated-CpG Islands in Cancer. *Lab. Investig.* **2005**, *85*, 1172–1180.

(21) Cross, S. H.; Charlton, J. A.; Nan, X.; Bird, A. P. Purification of CpG Islands Using a Methylated DNA Binding Column. *Nat. Genet.* **1994**, *6*, 236–244.

(22) Hashimoto, H.; Liu, Y.; Upadhyay, A. K.; Chang, Y.; Howerton, S. B.; Vertino, P. M.; Zhang, X.; Cheng, X. Recognition and Potential Mechanisms for Replication and Erasure of Cytosine Hydroxymethylation. *Nucleic Acids Res.* **2012**, *40*, 4841–4849.

(23) Fraga, M. F. The Affinity of Different MBD Proteins for a Specific Methylated Locus Depends on Their Intrinsic Binding Properties. *Nucleic Acids Res.* **2003**, *31*, 1765–1774.

(24) Buchmuller, B. C.; Kosel, B.; Summerer, D. Complete Profiling of Methyl-CpG-Binding Domains for Combinations of Cytosine Modifications at CpG Dinucleotides Reveals Differential Read-out in Normal and Rett-Associated States. *Sci. Rep.* **2020**, *10*, 4053.

(25) Heimer, B. W.; Tam, B. E.; Sikes, H. D. Characterization and Directed Evolution of a

Methyl-Binding Domain Protein for High-Sensitivity DNA Methylation Analysis. *Protein Eng. Des. Sel.* **2015**, *28*, 543–551.

(26) Yu, Y.; Blair, S.; Gillespie, D.; Jensen, R.; Myszka, D.; Badran, A. H.; Ghosh, I.; Chagovetz, A. Direct DNA Methylation Profiling Using Methyl Binding Domain Proteins. *Anal. Chem.* **2010**, *82*, 5012–5019.

(27) Liu, M.; Movahed, S.; Dangi, S.; Pan, H.; Kaur, P.; Bilinovich, S. M.; Faison, E. M.; Leighton, G. O.; Wang, H.; Williams, D. C.; Riehn, R. DNA Looping by Two 5-Methylcytosine-Binding Proteins Quantified Using Nanofluidic Devices. *Epigenetics Chromatin* **2020**, *13*, 18.

(28) Pan, H.; Bilinovich, S. M.; Kaur, P.; Riehn, R.; Wang, H.; Williams, D. C. CpG and Methylation-Dependent DNA Binding and Dynamics of the Methylcytosine Binding Domain 2 Protein at the Single-Molecule Level. *Nucleic Acids Res.* **2017**, *45*, 9164–9177.

(29) Yegnasubramanian, S.; Lin, X.; Haffner, M. C.; DeMarzo, A. M.; Nelson, W. G. Combination of Methylated-DNA Precipitation and Methylation-Sensitive Restriction Enzymes (COMPARE-MS) for the Rapid, Sensitive and Quantitative Detection of DNA Methylation. *Nucleic Acids Res.* **2006**, *34*, e19.

(30) Warton, K.; Lin, V.; Navin, T.; Armstrong, N. J.; Kaplan, W.; Ying, K.; Gloss, B.; Mangs, H.; Nair, S. S.; Hacker, N. F.; Sutherland, R. L.; Clark, S. J.; Samimi, G. Methylation-Capture and Next-Generation Sequencing of Free Circulating DNA from Human Plasma. *BMC Genomics* **2014**, *15*, 476.

(31) Olkhov-Mitsel, E.; Bapat, B. Strategies for Discovery and Validation of Methylated and Hydroxymethylated DNA Biomarkers. *Cancer Med.* **2012**, *1*, 237–260.

(32) Convery, N.; Gadegaard, N. 30 Years of Microfluidics. *Micro Nano Eng.* **2019**, *2*, 76–91.

(33) Xie, Y.; Dai, L.; Yang, Y. Microfluidic Technology and Its Application in the Point-of-Care Testing Field. *Biosens. Bioelectron. X* **2022**, *10*, 100109.

(34) Cunha, M. L.; da Silva, S. S.; Stracke, M. C.; Zanette, D. L.; Aoki, M. N.; Blanes, L. Sample Preparation for Lab-on-a-Chip Systems in Molecular Diagnosis: A Review. *Anal. Chem.* **2022**, *94*, 41–58.

(35) Syedmoradi, L.; Daneshpour, M.; Alvandipour, M.; Gomez, F. A.; Hajghassem, H.; Omidfar, K. Point of Care Testing: The Impact of Nanotechnology. *Biosens. Bioelectron.* **2017**, *87*, 373–387.

(36) Gervais, L.; de Rooij, N.; Delamarche, E. Microfluidic Chips for Point-of-Care Immunodiagnostics. *Adv. Mater.* **2011**, *23*, H151–H176.

(37) Kim, J.; Campbell, A. S.; de Ávila, B. E.-F.; Wang, J. Wearable Biosensors for Healthcare Monitoring. *Nat. Biotechnol.* **2019**, *37*, 389–406.

(38) Dong, J.; Zhang, R. Y.; Sun, N.; Hu, J.; Smalley, M. D.; Zhou, A.; Hua, Y.; Rothermich, W.; Chen, M.; Chen, J.; Ye, J.; Teng, P.; Qi, D.; Toretsky, J. A.; Tomlinson, J. S.; Li, M.; Weiss, P. S.; Jonas, S. J.; Federman, N.; Wu, L.; Zhao, M.; Tseng, H.; Zhu, Y. Coupling Nanostructured Microchips with Covalent Chemistry Enables Purification of Sarcoma-Derived Extracellular Vesicles for Downstream Functional Studies. *Adv. Funct. Mater.*

2020, *30*, 2003237.

(39) Yu, X.; Xia, Y.; Tang, Y.; Zhang, W.-L.; Yeh, Y.-T.; Lu, H.; Zheng, S.-Y. A Nanostructured Microfluidic Immunoassay Platform for Highly Sensitive Infectious Pathogen Detection. *Small* **2017**, *13*, 1700425.

(40) Tsougeni, K.; Tserepi, A.; Constantoudis, V.; Gogolides, E.; Petrou, P. S.; Kakabakos, S. E. Plasma Nanotextured PMMA Surfaces for Protein Arrays: Increased Protein Binding and Enhanced Detection Sensitivity. *Langmuir* **2010**, *26*, 13883–13891.

(41) Cady, N. C.; Stelick, S.; Batt, C. A. Nucleic Acid Purification Using Microfabricated Silicon Structures. *Biosens. Bioelectron.* **2003**, *19*, 59–66.

(42) Christel, L. A.; Petersen, K.; McMillan, W.; Northrup, M. A. Rapid, Automated Nucleic Acid Probe Assays Using Silicon Microstructures for Nucleic Acid Concentration. *J. Biomech. Eng.* **1999**, *121*, 22–27.

(43) Benítez, J. J.; Topolancik, J.; Tian, H. C.; Wallin, C. B.; Latulippe, D. R.; Szeto, K.; Murphy, P. J.; Cipriany, B. R.; Levy, S. L.; Soloway, P. D.; Craighead, H. G. Microfluidic Extraction, Stretching and Analysis of Human Chromosomal DNA from Single Cells. *Lab Chip* **2012**, *12*, 4848–4854.

(44) Hass, K. N.; Bao, M.; He, Q.; Liu, L.; He, J.; Park, M.; Qin, P.; Du, K. Integrated Micropillar Polydimethylsiloxane Accurate CRISPR Detection System for Viral DNA Sensing. *ACS Omega* **2020**, *5*, 27433–27441.

(45) Sheng, W.; Chen, T.; Kamath, R.; Xiong, X.; Tan, W.; Fan, Z. H. Aptamer-Enabled Efficient Isolation of Cancer Cells from Whole Blood Using a Microfluidic Device. *Anal. Chem.* **2012**, *84*, 4199–4206.

(46) Zhou, M.; Gao, D.; Yang, Z.; Zhou, C.; Tan, Y.; Wang, W.; Jiang, Y. Streaming-Enhanced, Chip-Based Biosensor with Acoustically Active, Biomarker-Functionalized Micropillars: A Case Study of Thrombin Detection. *Talanta* **2021**, *222*, 121480.

(47) Petralia, S.; Sciuto, E. L.; Conoci, S. A Novel Miniaturized Biofilter Based on Silicon Micropillars for Nucleic Acid Extraction. *Analyst* **2017**, *142*, 140–146.

(48) Movilli, J.; Kolkman, R. W.; Rozzi, A.; Corradini, R.; Segerink, L. I.; Huskens, J. Increasing the Sensitivity of Electrochemical DNA Detection by a Micropillar-Structured Biosensing Surface. *Langmuir* **2020**, *36*, 4272–4279.

(49) Wu, B.; Kumar, A.; Pamarthy, S. High Aspect Ratio Silicon Etch: A Review. *J. Appl. Phys.* **2010**, *108*, 051101.

(50) Miller, K.; Li, M.; Walsh, K. M.; Fu, X. A. The Effects of DRIE Operational Parameters on Vertically Aligned Micropillar Arrays. *J. Micromechanics Microengineering* **2013**, *23*, 035039.

(51) Kuo-Shen Chen; Ayon, A. A.; Xin Zhang; Spearing, S. M. Effect of Process Parameters on the Surface Morphology and Mechanical Performance of Silicon Structures after Deep Reactive Ion Etching (DRIE). *J. Microelectromechanical Syst.* **2002**, *11*, 264–275.

(52) Overmeer, R. M.; Henken, F. E.; Bierkens, M.; Wilting, S. M.; Timmerman, I.; Meijer, C. J.; Snijders, P. J.; Steenbergen, R. D. Repression of MAL Tumour Suppressor Activity by

Promoter Methylation during Cervical Carcinogenesis. *J. Pathol.* **2009**, *219*, 327–336.

(53) Harden, S. V; Guo, Z.; Epstein, J. I.; Sidransky, D. Quantitative GSTP1 Methylation Clearly Distinguishes Benign Prostatic Tissue and Limited Prostate Adenocarcinoma. *J. Urol.* **2003**, *169*, 1138–1142.

(54) Burnham, P.; Dadhania, D.; Heyang, M.; Chen, F.; Westblade, L. F.; Suthanthiran, M.; Lee, J. R.; De Vlaminck, I. Urinary Cell-Free DNA Is a Versatile Analyte for Monitoring Infections of the Urinary Tract. *Nat. Commun.* **2018**, *9*, 2412.

(55) Bierkens, M.; Hesselink, A. T.; Meijer, C. J. L. M.; Heideman, D. A. M.; Wisman, G. B. A.; van der Zee, A. G. J.; Snijders, P. J. F.; Steenbergen, R. D. M. CADM1 and MAL Promoter Methylation Levels in HrHPV-Positive Cervical Scrapes Increase Proportional to Degree and Duration of Underlying Cervical Disease. *Int. J. Cancer* **2013**, *133*, 1293–1299.

(56) Overmeer, R. M.; Louwers, J. A.; Meijer, C. J. L. M.; van Kemenade, F. J.; Hesselink, A. T.; Daalmeijer, N. F.; Wilting, S. M.; Heideman, D. A. M.; Verheijen, R. H. M.; Zaal, A.; Marchien van Baal, W.; Berkhof, J.; Snijders, P. J. F.; Steenbergen, R. D. M. Combined CADM1 and MAL Promoter Methylation Analysis to Detect (Pre-)Malignant Cervical Lesions in High-Risk HPV-Positive Women. *Int. J. Cancer* **2011**, *129*, 2218–2225.

(57) Schmittgen, T. D.; Livak, K. J. Analyzing Real-Time PCR Data by the Comparative CT Method. *Nat. Protoc.* **2008**, *3*, 1101–1108.

(58) Quackenbush, J. Microarray Data Normalization and Transformation. *Nat. Genet.* **2002**, *32*, 496–501.

(59) Bach, S.; Wever, B. M. M.; Van de Wiel, M. A.; Veltman, J. D.; Hashemi, S. M. S.; Kazemier, G.; Bahce, I.; Steenbergen, R. D. M. Dynamics of Methylated Cell-Free DNA in the Urine of Non-Small Cell Lung Cancer Patients. *Epigenetics* **2021**, 1–13.

(60) Steenbergen, R. D. M.; Kramer, D.; Braakhuis, B. J. M.; Stern, P. L.; Verheijen, R. H. M.; Meijer, C. J. L. M.; Snijders, P. J. F. TSLC1 Gene Silencing in Cervical Cancer Cell Lines and Cervical Neoplasia. *JNCI J. Natl. Cancer Inst.* **2004**, *96*, 294–305.

(61) Bosschieter, J.; Bach, S.; Bijnsdorp, I. V.; Segerink, L. I.; Rurup, W. F.; Van Splunter, A. P.; Bahce, I.; Novianti, P. W.; Kazemier, G.; van Moorselaar, R. J. A.; Steenbergen, R. D. M.; Nieuwenhuijzen, J. A. A Protocol for Urine Collection and Storage Prior to DNA Methylation Analysis. *PLoS One* **2018**, *13*, e0200906.

Chapter 7

Summary and outlook

7.1 Summary

Cancer detection at an early stage is essential to decrease cancer mortality and improve the chances of successful treatment. In The Netherlands early detection of cervical cancer, breast cancer and colon cancer are currently facilitated by screening the population without cancer symptoms. Other cancer types are typically detected after the onset of cancer symptoms. The detection of cancer-specific biomarkers in liquid biopsy samples is a promising approach to improve cancer diagnostics. Of upcoming interest is hypermethylated DNA (hmDNA)-based cancer detection in urine. Specific hmDNA genes can be a cancer biomarker for, among others, cervical cancer,[1] bladder cancer,[2] and lung cancer.[3] Urine is advantageous to use as urine can be collected non-invasively and repeatedly in a simple manner without the need of healthcare personnel. The detection of cancer-specific hmDNA in urine requires a preselection step where hmDNA is separated from non-methylated DNA. The preselection by methyl binding domain 2 (MBD2)-based enrichment is beneficial due to short assay times as only a binding and an elution step are involved. However, the current enrichment methods of hmDNA are limited due to co-enrichment of non-methylated DNA. The research in this thesis aims to develop a selective hmDNA enrichment method by implementing the principles of superselectivity and multivalent binding.

In **Chapter 2** a new method for the selective enrichment of hmDNA was proposed, involving the development of a multivalent binding platform. In this perspective, the proteins MeCp2, MBD1 and MBD2 from the MBD protein family were identified to have the highest intrinsic selectivities and found suitable to be used as bioreceptor for hmDNA enrichment. Current hmDNA enrichment systems suffer from low selectivities, especially at low hmDNA input concentrations. The theory of multivalency and superselectivity predicts a high dependence of the sensitivity and selectivity of hmDNA binding on the surface receptor density. As a result, the proposed design of the multivalent binding platform is based on optimization of the applied MeCp2, MBD1 or MBD2 protein surface receptor density.

Chapter 3 has discussed the development of a selective hmDNA enrichment platform. The platform employs control over the MBD2 surface receptor density by using a thiol-based self-assembled monolayer (SAM) on a gold surface. The SAM consists of hydroxyl

and azide-functionalized thiols, used to create an anti-fouling surface and to immobilize indirectly the MBD2 protein to the surface, respectively. To the azide-functionalized thiols a linker molecule with a dibenzocyclooctyne (DBCO) and a nickel(II)-complexed nitrilotriacetic acid (NiNTA) moiety was bound. The NiNTA interacts with the histidine-10-tagged MBD2 protein which enabled MBD2 immobilization. The stoichiometric ratio between the two types of thiols appeared to control the MBD2 surface receptor density. DNA with higher methylation levels bound to the MBD2 surface at lower receptor densities, resulted in higher DNA surface coverages and showed a higher degree of superselectivity.

The developed hmDNA enrichment platform was further evaluated by hmDNA enrichment of DNA mixtures with a content of 1% hmDNA and 99% non-methylated DNA, as shown in **Chapter 4.** DNA bound to the MBD2 surface was eluted from the surface successfully by the use of a high-pH buffer. The enriched DNA mixtures were treated with methyl-sensitive restriction enzymes to digest non-methylated DNA followed by quantitative polymerase chain reaction (qPCR) analysis to determine the hmDNA level. Enrichment of the DNA mixtures with hmDNA increased the hmDNA level to 7% and, by optimization of the MBD2 surface receptor density, further to approximately 30% hmDNA.

Chapter 5 has presented the use of a micropillar-structured electrode for DNA sensing. Micropillared electrodes were produced with varying surface areas by altering the pitch. Single-strand DNA was detected electrochemically using a sandwich assay with an electrochemically active reporter probe. The sensitivity for electrochemical DNA detection was increased upon reduction of the pitch.

The developed micropillar-structured substrate was integrated into a microfluidic chip and coated with an MBD2 layer, as was reported in **Chapter 6**. The hmDNA enrichment chip was used to enrich hmDNA from DNA isolated from cervical cancer and healthy control cells. The hmDNA enrichment of DNA samples was evaluated by detection of the cervical cancer-specific hmDNA gene *MAL* with qPCR. All *MAL* was removed selectively from the cervical cancer cell DNA upon hmDNA enrichment and detected in the enriched DNA sample. Also, upon hmDNA enrichment of DNA isolated from urine samples, *MAL* was only detected in the hmDNA-enriched DNA from the urine of a cervical cancer patient and not in the control sample, thereby providing proof-of-principle for hmDNA-based cervical cancer detection in urine using the hmDNA enrichment device.

7.2 Outlook

Integration of the steps presented in Chapters 2 - 5 resulted in the successful development of the hmDNA enrichment chip in Chapter 6. The chip was used to enrich hmDNA isolated from urine samples, which enabled cervical cancer detection. However, further optimization of the hmDNA enrichment chip and the method will likely result in further increase in the hmDNA enrichment performance. Several recommendations are presented in this section.

7.2.1 Improving the hmDNA enrichment selectivity

Optimization of the applied MBD2 surface receptor density upon hmDNA enrichment of DNA mixtures has resulted in a significant reduction of the co-isolation of non-methylated DNA (Chapters 3 and 4). Nevertheless, this development did not result in full prevention of the binding of non-methylated DNA. At the same time, results presented in Chapter 6 have shown that hmDNA is bound by the chip completely even in the presence of copious amounts of healthy DNA, indicating that the affinity for hmDNA is sufficient. A further improvement in the hmDNA enrichment selectivity can likely be made by reduction of the chip surface area. The surface area should be optimized, meaning that it should be large enough that all hmDNA can bind to the MBD2-modified surface but leaves little room for other DNA to bind. In case non-methylated DNA then binds to the surface, it is likely to be exchanged by hmDNA due to the avidity differences for the MBD2-modified surface. Nevertheless, if the chip exceeds the maximum required surface area for hmDNA, the binding of non-methylated DNA will likely occur. By systematically reducing the chip surface area the gain in the hmDNA enrichment selectivity of DNA mixtures can be evaluated.

Non-methylated DNA bound to an MBD2 surface is eluted preferentially separately from bound hmDNA to minimize the non-methylated DNA level in hmDNA enriched DNA samples. In Chapters 4 and 6 of this thesis an elution step with ammonium hydroxide solution has been applied to elute all surface-bound DNA, independent of the DNA methylation status. A gentler elution method can potentially be applied before, to elute non-methylated DNA first, since non-methylated DNA binds less strongly to MBD2-coated surfaces in comparison to hmDNA. For example, increasing the NaCl concentration in the buffer used to wash an MBD2 surface after the DNA binding step may be a possible method to achieve this.

7.2.2 Standardization of the hmDNA enrichment procedure

The developed hmDNA enrichment chip in this thesis requires to be more standardized and simplified in the future to enable easy implementation in the clinic. Limitations of

the current chip design are the cleaning of the chip, connecting tubing to the chip and the occurrence of chip leakage, therefore, requiring well trained lab personnel. Furthermore, the time needed to build up the hmDNA capture coating in the microfluidic chip is approximately 3 h. For each different analyte that is used, the tubing needs to be placed in a different vial. Currently, hmDNA enrichment of two DNA samples can be performed at the same chip in a total time of 1.5 h. Parallelization of multiple hmDNA enrichment experiments is not feasible with the current set-up due to the required sample handling approach.

To make the use of the hmDNA enrichment device in the clinic as easy as possible, ideally unprocessed urine is enriched for hmDNA to minimize sample handling. Therefore, it should be investigated whether the current properties of the hmDNA enrichment device remain upon enrichment of unprocessed urine. So far, DNA was first isolated from the urine followed by hmDNA enrichment of 150 ng isolated DNA and detection of the cervical cancer-specific hmDNA gene *MAL* with qPCR (Chapter 6). When considering that the DNA concentration in urine supernatant varies between 17 - 93 ng/mL,[4] at least 1.5 mL urine is required to enrich 150 ng DNA in hmDNA. However, this requires already a hmDNA enrichment time of 3 h upon use of a high flow rate of 10 µL/min. Preferably less than 150 ng DNA can be processed to reduce the assay time, however, it should be investigated whether the selectivity of hmDNA enrichment is affected by lower DNA input amounts.

An approach for standardization of the use of the hmDNA enrichment chip is to utilize programmable syringe pumps. After mounting the chip in the chip holder, the syringes need to be filled with reagents and samples needed for the experiment. Then the tubing needs to be connected to the chip holder and syringes. The syringe pump must be programmed such that after a specific time a different reagent/sample is flushed through the chip automatically to form the hmDNA capture layer and to enable hmDNA enrichment. The use of programmable syringe pumps also opens the possibility to perform hmDNA enrichment outside office hours. hmDNA enrichment can also be facilitated with a higher throughput when connecting multiple different chips to the syringes using microfluidic splitters. Another approach for standardization is the development of standardized operating procedures for hmDNA enrichment using the chip. This development enables the use of the chip by unpracticed users easily without the need of training and/or supervision by an expert. In this way knowledge transfer is made easily without the need to reproduce work based on complex described methods.

Producing ready-to-use microfluidic hmDNA enrichment chips is another step for standardization. Ideally, those chips are already pre-functionalized with MBD2 proteins at a central location by specialists. Subsequently, the chips can be sent to the clinic where the hmDNA enrichment of DNA samples will be performed. This is advantageous

for the clinic as the quality of the MBD2-based chips can be guaranteed. Furthermore, the total hmDNA enrichment assay time in the clinic is then only limited to the DNA binding and elution step. To enable use of ready-to-use hmDNA enrichment chips it needs to be investigated whether MBD2 proteins at a specific MBD2 surface receptor density can be stored stably in a dry or wet state for specific times and whether (long-term) storage affects the hmDNA enrichment selectivity.

7.2.3 Integrated hmDNA enrichment and detection on a chip

Ideally the enrichment of DNA samples in hmDNA is combined on the same chip with the detection of cancer-specific hmDNA. In this way sample handling is minimized, thereby making the technique suitable for use in the clinic and enabling point-of-care diagnostics. The required detection sensitivity of a specific hmDNA target is dependent on the concentration of cancer-specific hmDNA in a urine sample and, thus, also on the hmDNA enrichment efficiency. In general, the hmDNA concentration in urine is higher as the disease progresses due to increased excretion by tumor cells. To enable early-stage cancer detection, the used detection method requires to have a limit of detection of a few DNA copies per mL urine. On the other hand, if the detection of hmDNA will be used to monitor the cancer progression or treatment response, less sensitive detection methods can be used due to the higher hmDNA concentration.

A second requirement for an integrated hmDNA detection device is the ease of use as a point-of-care device. For that reason, the gold standard method used for DNA detection with qPCR is not applicable due to the need of a thermocycler and costs per assay. Two alternative and promising approaches that are likely suitable to fulfill these requirements for hmDNA detection are electrochemical[5,6] and CRISPR-based[7] sensing. Both methods enable the integration in a microfluidic device and possess a wide sensitivity range. Future work should therefore involve the combination of hmDNA enrichment and one of these detection methods in an integrated fashion on a single microfluidic chip.

7.2.4 Clinical validation

As a proof of principle, the developed hmDNA enrichment chip has been used to enrich hmDNA from a DNA sample from urine of a cervical cancer patient followed by detection of the cervical cancer-specific hmDNA *MAL* gene using qPCR (Chapter 6). Nevertheless, the chip requires to be further evaluated prior to use in the clinic. For example, to assess the selectivity and specificity of the chip in more detail, the hmDNA from urine samples of different cervical cancer patients and healthy controls should be enriched followed by detection of a specific hmDNA cancer gene. Additionally, the

ability of the hmDNA enrichment chip to enrich DNA from urine of persons with varying types of cancer should be evaluated. For instance, different cancer-specific hmDNA genes might vary in the degree of methylation and the number of CpGs, which affects, consequently, the avidity for the MBD2-coated surfaces. This also opens the possibility to determine the effect of varying DNA methylation levels between different cancer patients and healthy volunteers. Also, the impact of the cancer stage on the hmDNA enrichment selectivity should be assessed. Earlier cancer stages may result in lower concentrations of cancer-specific hmDNA in urine, therefore, making hmDNA enrichment more complicated.

Also, from the detection point-of-view, optimization can be made. In Chapter 6, after hmDNA enrichment of DNA isolated from the urine of a cervical cancer patient only an individual cervical cancer-specific hmDNA gene was detected with qPCR to confirm the disease. However, multiple cervical cancer-specific hmDNA genes are actually found in urine.[4] Detection of several cervical cancer-specific hmDNA biomarkers in the same enriched sample is likely to improve the selectivity of hmDNA-based cervical cancer detection as it reduces the effect of co-enriched non-methylated DNA.

Prior to clinical use, the hmDNA enrichment system coupled to a detection method should also be evaluated in a large study with hundreds of participants. Both cancer patients and healthy volunteers should participate. Critical here is to determine the numbers of false-positives and false-negatives, and the accuracy of cancer detection of the system in comparison to existing diagnostic methods.

7.3 References

(1) Van den Helder, R.; Steenbergen, R. D. M.; Van Splunter, A. P.; Mom, C. H.; Tjiong, M. Y.; Martin, I.; Rosier-van Dunné, F. M. F.; Van der Avoort, I. A. M.; Bleeker, M. C. G.; Van Trommel, N. E. HPV and DNA Methylation Testing in Urine for Cervical Intraepithelial Neoplasia and Cervical Cancer Detection. *Clin. Cancer Res.* **2022**, *28*, 2061–2068.

(2) Kandimalla, R.; Van Tilborg, A. A.; Zwarthoff, E. C. DNA Methylation-Based Biomarkers in Bladder Cancer. *Nat. Rev. Urol.* **2013**, *10*, 327–335.

(3) Liu, B.; Ricarte Filho, J.; Mallisetty, A.; Villani, C.; Kottorou, A.; Rodgers, K.; Chen, C.; Ito, T.; Holmes, K.; Gastala, N.; Valyi-Nagy, K.; David, O.; Gaba, R. C.; Ascoli, C.; Pasquinelli, M.; Feldman, L. E.; Massad, M. G.; Wang, T.-H.; Jusue-Torres, I.; Benedetti, E.; Winn, R. A.; Brock, M. V.; Herman, J. G.; Hulbert, A. Detection of Promoter DNA Methylation in Urine and Plasma Aids the Detection of Non–Small Cell Lung Cancer. *Clin. Cancer Res.* **2020**, *26*, 4339–4348.

(4) Van den Helder, R.; Van Trommel, N. E.; Van Splunter, A. P.; Lissenberg-Witte, B. I.; Bleeker, M. C. G.; Steenbergen, R. D. M. Methylation Analysis in Urine Fractions for Optimal CIN3 and Cervical Cancer Detection. *Papillomavirus Res.* **2020**, *9*, 100193.

(5) Wongkaew, N.; Simsek, M.; Griesche, C.; Baeumner, A. J. Functional Nanomaterials and Nanostructures Enhancing Electrochemical Biosensors and Lab-on-a-Chip Performances: Recent Progress, Applications, and Future Perspective. *Chem. Rev.* **2019**, *119*, 120–194.

(6) Thapa, K.; Liu, W.; Wang, R. Nucleic Acid-Based Electrochemical Biosensor: Recent Advances in Probe Immobilization and Signal Amplification Strategies. *Wiley Interdiscip. Rev. Nanomed. Nanobiotechnol.* **2022**, *14*, e1765.

(7) Kaminski, M. M.; Abudayyeh, O. O.; Gootenberg, J. S.; Zhang, F.; Collins, J. J. CRISPR-Based Diagnostics. *Nat. Biomed. Eng.* **2021**, *5*, 643–656.

Cartoon by Luvane.

Samenvatting

Vroegtijdige kankerdetectie is essentieel om kankersterfte terug te dringen en de kans op een succesvolle behandeling te vergroten. In Nederland wordt vroege diagnostiek van baarmoederhalskanker, borstkanker en darmkanker gefaciliteerd door bevolkingsonderzoeken. Andere kankersoorten worden meestal ontdekt nadat symptomen zijn ontstaan. Het detecteren van de specifieke biomarker hypergemethyleerd DNA (hmDNA) in urine is een veelbelovende methode om kankerdiagnostiek te verbeteren. De detectie van een specifieke hmDNA-sequentie in urine maakt diagnostiek mogelijk voor onder andere baarmoederhalskanker,[1] blaaskanker[2] en longkanker.[3] Kankerdetectie in urine heeft als voordeel dat urine kan worden opgevangen zonder dat daarvoor medisch personeel nodig is. De detectie van specifiek hmDNA in urine vereist een scheidingsstap waarbij hmDNA wordt gescheiden van het overige DNA. De scheiding van hmDNA door middel van een verrijkingsmethode met methyl binding domain 2 (MBD2)-eiwitten is snel uit te voeren omdat deze methode alleen een bindings- en een elutiestap bevat. De huidige verrijkingsmethoden van hmDNA zijn gelimiteerd omdat niet-gemethyleerd DNA niet selectief gescheiden kan worden van het hmDNA. Het onderzoek in dit proefschrift beschrijft de ontwikkeling van een selectieve hmDNA-verrijkingsmethode door de principes van multivalentie en superselectiviteit toe te passen.

Hoofdstuk 2 beschrijft een nieuwe methode voor de selectieve verrijking van hmDNA door middel van een multivalent bindingsplatform. De eiwitten MeCp2, MBD1 en MBD2 uit de MBD-eiwitfamilie hebben de hoogste selectiviteit en zijn daarom geschikt als biologische receptor tijdens hmDNA-verrijking op dit platform. Huidige hmDNA-verrijkingsmethodes zijn gelimiteerd door de lage selectiviteit van verrijking, met name tijdens het gebruik van kleine hoeveelheden hmDNA. De principes van multivalentie en superselectiviteit voorspellen een hoge afhankelijkheid van de gevoeligheid en selectiviteit van verrijking van de oppervlakte-receptordichtheid. Daarom is het ontwerp van het multivalente bindingsplatform gebaseerd op optimalisatie van de toegepaste MeCp2, MBD1 of MBD2 oppervlakte-receptordichtheid.

Hoofdstuk 3 beschrijft de ontwikkeling van een selectief hmDNA verrijkingsplatform. Het gebruik van een thiol-gebaseerde zelf-assemblerende monolaag (SAM) op een goudoppervlak maakte het mogelijk om de MBD2-dichtheid op dit platform te sturen. De monolaag bestaat uit hydroxyl- en azide-gefunctionaliseerde thiolen die gebruikt zijn om een beschermlaag te creëren die niet-specifieke binding voorkomt en om oppervlakte-immobilisatie van MBD2-eiwitten mogelijk te maken. Aan de azide-gefunctionaliseerde thiolen is een linker-molecuul met een dibenzocyclooctyne (DBCO) en een nickel(II)-gecomplexeerde nitrilotriacetic acid (NiNTA) functionele

groep gebonden. De NiNTA-groep bindt aan de histidine-10-gelabelde MBD2-eiwitten om zo deze MBD2-eiwitten op het oppervlak te binden. De verhouding tussen de twee soorten thiolen in de monolaag bepaalt de MBD2-oppervlakte-receptordichtheid. DNA met een toenemende methylatiegraad bond aan het MBD2-gefunctionaliseerde oppervlak bij lagere receptordichtheden, resulteerde in meer oppervlaktebinding van het DNA en vertoonde een hogere mate van superselectiviteit.

Het ontwikkelde hmDNA-verrijkingsplatform werd verder onderzocht in **hoofdstuk 4** door hmDNA-verrijking van DNA-mengsels met 1% hmDNA en 99% niet-gemethyleerd DNA. Het DNA gebonden op het MBD2-oppervlak werd succesvol van het oppervlak afgehaald door elutie met een buffer met een hoge pH. De hmDNA-verrijkte DNA-mengsels werden vervolgens gemengd met methylgevoelige restrictie-enzymen om niet-gemethyleerd DNA te knippen, gevolgd door kwantitatieve polymerase chain reaction (qPCR)-analyse om de hoeveelheid hmDNA te bepalen. Verrijking van de DNA-mengsels met hmDNA verhoogde de hoeveelheid van hmDNA tot 7% en door optimalisatie van de MBD2-oppervlakte-receptordichtheid verder tot ongeveer 30% hmDNA.

Hoofdstuk 5 laat het gebruik van met micropilaren gestructureerde elektrodes voor DNA-detectie zien. De micropilaar-elektrodes werden geproduceerd met variërende oppervlaktes door de afstand tussen de micropilaren te veranderen. Enkelstrengs DNA werd elektrochemisch gedetecteerd met behulp van een sandwich assay en een elektrochemisch reportermolecuul. De gevoeligheid van de elektrochemische DNA-detectie werd beter bij een kleinere afstand tussen de micropilaren.

Hoofdstuk 6 laat het gebruik van het ontwikkelde micropilaar-substraat zien in een microfluïdische chip. De chip werd gefunctionaliseerd met MBD2-eiwitten en gebruikt om hmDNA te verrijken in DNA geïsoleerd uit baarmoederhalskankercellen en gezonde cellen. Het hmDNA-verrijkte DNA werd vervolgens geanalyseerd met qPCR waarbij de aanwezigheid van het baarmoederhalskanker-specifieke hmDNA-gen *MAL* werd aangetoond. Al het *MAL* werd door de hmDNA-verrijking selectief uit het DNA van de baarmoederhalskankercellen gehaald en gedetecteerd in het verrijkte DNA. Ook werd DNA geïsoleerd uit urine en verrijkt met hmDNA. Hierin werd *MAL* gedetecteerd in het met hmDNA verrijkte DNA uit de urine van een baarmoederhalskankerpatiënt en niet in urine van een gezonde controle-persoon. De ontwikkeling van de microfluïdische chip voor hmDNA-verrijking heeft dus geresulteerd in een proof-of-concept voor hmDNA-gebaseerde detectie van baarmoederhalskanker in urine.

Hoofdstuk 7 geeft een samenvatting en kritische reflecties op mogelijke vervolgstappen.

Referenties

(1) Van den Helder, R.; Steenbergen, R. D. M.; Van Splunter, A. P.; Mom, C. H.; Tjiong, M. Y.; Martin, I.; Rosier-van Dunné, F. M. F.; Van der Avoort, I. A. M.; Bleeker, M. C. G.; Van Trommel, N. E. HPV and DNA Methylation Testing in Urine for Cervical Intraepithelial Neoplasia and Cervical Cancer Detection. *Clin. Cancer Res.* **2022**, *28*, 2061–2068.

(2) Kandimalla, R.; Van Tilborg, A. A.; Zwarthoff, E. C. DNA Methylation-Based Biomarkers in Bladder Cancer. *Nat. Rev. Urol.* **2013**, *10*, 327–335.

(3) Liu, B.; Ricarte Filho, J.; Mallisetty, A.; Villani, C.; Kottorou, A.; Rodgers, K.; Chen, C.; Ito, T.; Holmes, K.; Gastala, N.; Valyi-Nagy, K.; David, O.; Gaba, R. C.; Ascoli, C.; Pasquinelli, M.; Feldman, L. E.; Massad, M. G.; Wang, T.-H.; Jusue-Torres, I.; Benedetti, E.; Winn, R. A.; Brock, M. V.; Herman, J. G.; Hulbert, A. Detection of Promoter DNA Methylation in Urine and Plasma Aids the Detection of Non–Small Cell Lung Cancer. *Clin. Cancer Res.* **2020**, *26*, 4339–4348.

Scientific output

Publications

J. Movilli*, **R.W. Kolkman***, A. Rozzi, R. Corradini, L.I. Segerink, J. Huskens, Increasing the sensitivity of electrochemical DNA detection by a micropillar-structured biosensing surface. *Langmuir*, **2020**, *36*, 4272–4279.

J. Komen, E.Y. Westerbeek, **R.W. Kolkman**, J. Roesthuis, A. van den Berg, A D. van der Meer. Controlled pharmacokinetic anti-cancer drug concentration profiles lead to growth inhibition of colorectal cancer cells in a microfluidic device. *Lab Chip*, **2020**, *20*, 3167-3178.

R.W. Kolkman, L.I. Segerink, J. Huskens, Selective Enrichment of Hypermethylated DNA by a Multivalent Binding Platform. *Adv. Mater. Interfaces*, accepted.

R.W. Kolkman, S. Michel-Souzy, D. Wasserberg, L.I. Segerink, J. Huskens, Density control over MBD2 receptor-coated surfaces provides superselective binding of hypermethylated DNA. *ACS Appl. Mater. Interfaces*, **2022**, *14*, 40579-40589.

R.W. Kolkman, L.I. Segerink, J. Huskens. Enrichment of hypermethylated DNA from DNA mixtures. *Manuscript in preparation*.

R.W. Kolkman, B.M.M. Wever, A.P. van Splunter, J.G. Bomer, R.D.M. Steenbergen, L.I. Segerink, J. Huskens. Enrichment of DNA from cells and urine with hypermethylated DNA on chip to detect cervical cancer in urine. *Manuscript in preparation*.

* = authors contributed equally.

Patent

R.W. Kolkman, L.I. Segerink, J. Huskens. Method for separating high-methylated DNA and low-methylated DNA. Patent application number: P35615NL00/MJO.

Conference talks

Selective enrichment of the cancer biomarker hypermethylated DNA. *MESA+ meeting*, June 13, **2022**, Enschede, The Netherlands.

Selective enrichment of the cancer biomarker hypermethylated DNA by MBD2 surface receptor density control. *ACS Spring meeting*, March 20-24, **2022**, San Diego, California, USA.

Prizes

Poster prize winner and Business Impact prize winner. *MESA+ meeting*, June 13, **2022**, Enschede, The Netherlands.

Poster presentations

R.W. Kolkman, B.M.M. Wever, A.P. Van Splunter, J.G. Bomer, R.D.M. Steenbergen, L.I. Segerink, J. Huskens. Hypermethylated DNA enrichment enables cervical cancer detection in urine. NanoBioTech 2022, Montreux, Switzerland.

R.W. Kolkman, B.M.M. Wever, A.P. Van Splunter, J.G. Bomer, R.D.M. Steenbergen, L.I. Segerink, J. Huskens. Hypermethylated DNA enrichment to detect cancer in urine. Chains 2022, Veldhoven, The Netherlands.

J.E. van Dongen*, **R.W. Kolkman***, S. Michel-Souzy, J.T.W. Berendsen, D. Wasserberg, J.C.T. Eijkel, J. Huskens, L.I. Segerink. Cancer biomarker detection on chip in urine samples. MESA+ meeting 2022, Enschede, The Netherlands.

R.W. Kolkman, S. Michel-Souzy, D. Wasserberg, L.I. Segerink, J. Huskens. Hypermethylated DNA isolation for cancer diagnostics. Chains 2021, Veldhoven, The Netherlands.

R.W. Kolkman, J. Movilli, L.I. Segerink, J. Huskens. Increasing the sensitivity for the electrochemical detection of DNA by a micropillar-structured biosensing electrode. World Congress on Biosensors 2021, online.

J.E. van Dongen, **R.W. Kolkman**, D. Wasserberg, L.V. Knippenborg, J.C.T. Eijkel, L.I. Segerink. Localized surface plasmon resonance based gold nanoparticle-hairpin assay for optical detection of single DNA molecules. World Congress on Biosensors 2021, online.

R.W. Kolkman. Accelerating cancer detection in urine. Create tomorrow 2020, Enschede, the Netherlands.

R.W. Kolkman, D. Wasserberg, S. Michel-Souzy, J.E. van Dongen, E. Diepenbroek, H. de Vries, L.I. Segerink, J. Huskens. Specific surface immobilization of biorecognition elements to enable biosensing. Chains 2019, Veldhoven, the Netherlands.

J.E. van Dongen, H. Le The, **R.W. Kolkman**, D. Wasserberg, J. Huskens, J.C.T. Eijkel, L.I. Segerink. Gold nanoparticle assays: a new golden standard for optical DNA detection. CHAINS 2019, Veldhoven, the Netherlands.

M.J. Goodwin, **R.W. Kolkman**, T. Moazzenzade, J. Movilli, Fl. Falke, G.A.J. Besselink, J.J.L.M. Cornelissen, A Rozzi, R. Corradini, S.G. Lemay, L.I. Segerink, J. Huskens. Enabling biosensing with Poly-L-lysine. MESA+ meeting 2019, Enschede, the Netherlands.

* = authors contributed equally.

Dankwoord

Mijn proefschrift is af! Wat een ervaring was het en wat heeft mij dit veel gebracht. Ik heb met fantastische mensen mogen samenwerken en zonder jullie was het voltooien van mijn proefschrift niet gelukt, veel dank!

Als eerste wil ik Jurriaan bedanken. Voor mijn master afstudeeropdracht wou ik iets met “biologie en scheikunde” doen. Jij gaf mij de mogelijkheid om aan een DNA-detectie methode te werken. Daarna begon ik als PhD student bij jou en Loes, en dit was een goede keuze! Jij bent een fantastische mentor en ik heb ontzettend veel van je kunnen leren. Je deur stond altijd voor me open, zelfs als ik na 18:00 bij je langs kwam met een korte vraag/veelbelovende resultaten. Gewoonlijk bleven we dan nog lang discussiëren. Ook heel veel dank voor de gegeven feedback op alle manuscripten. Ik durf te zeggen dat jij mij hebt opgeleid tot een zelfstandige onderzoeker met veel zelfvertrouwen, ik blijf hier altijd dankbaar voor!

Loes, wat heb jij een enthousiasme en energie. Onze meetings waren altijd gezellig en vol met humor. Geregeld kwam de vraag van jou wanneer ik nu toch met chips zou gaan werken. Maar ja, de “scheikunde” bleek toch allemaal niet zo eenvoudig te zijn. De alles kan mentaliteit van jou vind ik fantastisch. Dit heeft mij enorm veel vrijheid voor het onderzoek gegeven, ik waardeer dit enorm. Jij hebt een oog voor detail en bent creatief. Hiermee heb jij mij altijd scherp kunnen houden. Daarnaast heb je ook altijd veel interesse getoond in mij buiten het “werk” om, dit waardeer ik zeer. Als laatste, dank voor het bewaken van de werk privé balans in je groep.

I would like to thank my PhD committee members: prof. dr. Serge Lemay, prof. dr. David Fernandez Rivas, prof. dr. Kevin Plaxco, prof. dr. ir. Luc Brunsveld, and prof. dr. Renske Steenbergen for their provided feedback on my thesis. I am looking forward to discuss my thesis in more detail during my defense.

Albert, bedankt dat ik onderdeel van de BIOS groep kon zijn. De sfeer in de groep is fantastisch, iets om trots op te zijn. Ik heb genoten van de sociale activiteiten waarbij we gingen mountainbiken, eten, en wandelen. Dank voor de gegeven feedback en het meedenken over carrière mogelijkheden na mijn PhD.

Nienke, we zijn bijna tegelijk met onze PhD begonnen op hetzelfde project. We hebben ontzettend veel samengewerkt, gebrainstormd, problemen verholpen, en gelachen. Ook zijn we veel op reis geweest voor conferenties en scholing. Uiteraard altijd met een afsluitend etentje: van een restaurant in een mooi pittoresk straatje in Bologna tot een fastfood restaurant. Het kon allemaal, dank! Met name het bezoek van Italië voor een zomerschool was een unieke ervaring. Jou kritische blik, enthousiasme en

motivatie hebben me enorm geholpen. Ik ben daarom ook blij dat jij als paranimf naast mij staat om mijn leven als PhD student af te sluiten.

Alessandro, thank you for being part of the Weijerhorst project. I really appreciate your help with my PCR experiments and our lab work discussions. Also, I always enjoyed your presence and enthusiasm about Italy and Football. All the best for the future!

Dodo, bij de start van mijn PhD heb jij mij geïntroduceerd in het Weijerhorst project. Ook heb jij mij enorm veel technieken in het lab geleerd die ik tot het einde van mijn PhD gebruikt heb. Ik kon mij op het lab geen betere introductie voorstellen! Zowel onze vakinhoudelijke discussies en kopjes koffie heb ik als zeer prettig ervaren.

Sandra, we started working together after I gave a talk for the group. You spend a lot of your time and effort in order to improve the MBD2 production. This was one of the key parts of my PhD work. We also spend a lot of time together to make fun and talk, thank you so much for everything!

Jacopo, we continued working together after my start as a PhD student. That was a good idea as it resulted in a shared publication. You inspired me with your hardworking mentality and knowledge about surface chemistry. I wish you all the best in the future.

My officemates Anke, Hugo, Edo, Heleen, and Pelin. Thank you for each goeiemorgen, coffee, games, chats, dining, and ability to show and discuss results. We shared so much with each other, thank you for that! Heleen, bedankt voor alle goeie gesprekken en je kritische blik. Edo, wij hebben samen veel tijd met elkaar doorgebracht tijdens lunchwandelingen en onze vrije tijd. Niet voor niets ben jij dan ook mijn paranimf. Dank voor de fijne tijd en we blijven elkaar zien!

Lisette, bedankt voor je hulp in het lab bij mijn PCR experimenten. Ook de pipetteer lessen die we voor lab-on-a-chip hebben gegeven samen met Paul waren erg gezellig.

Johan, dank voor het meedenken over het design en maken van de pillaren chip. Ik waardeer je vakbekwaamheid en de snelheid waarmee jij je werk gedaan krijgt enorm.

All the Weijerhorst people are gratefully acknowledged for their useful discussions and provided feedback. I really enjoyed each meeting every two weeks with you. Also the Weijerhorst meetings with our colleagues from Amsterdam were very joyful. I really liked to learn about the cancer-related research performed by all of you. Renske, ik wens jou en je collega's veel succes in de toekomt met het fantastische onderzoek dat jullie uitvoeren.

Ik heb verschillende studenten mogen begeleiden tijdens mijn PhD project; Huub, Esli, Adam, Laura, Sander, Daniel en Ike. Dank voor jullie bijdragen aan het project en jullie enthousiasme. Hopelijk hebben jullie er net zoveel van geleerd als ik. Huub, ik wil jou specifiek bedanken. Jij hebt door een foutje in een experiment een cruciale bijdrage

geleverd aan het maken van de MBD2 eiwitten. Dank voor het noteren hiervan in je labjournaal! Hierdoor kon ik de “fout” van toen later gebruiken. Dit geeft aan hoe belangrijk een labjournaal is, een les die ik sindsdien meegeef aan al mijn studenten.

Annina en Birgit, ik ben jullie enorm dankbaar voor onze samenwerking. Jullie hebben veel tijd in mij geïnvesteerd om de samenwerking concreet te maken. Birgit, bedankt voor het beantwoorden van mijn vele vragen over de interpretatie van de data. Niet voor niets heeft dit geleid tot een mooi hoofdstuk in mijn thesis. Veel dank!

Ik had het geluk om onderdeel te zijn van zowel de BIOS vakgroep als de MNF vakgroep. Dit gaf mij de mogelijkheid om samen te werken met mensen vanuit totaal verschillende disciplines. En ja, ook meer taartjes, feestjes en lunches. Ik bedank iedereen die eraan bijgedragen heeft om deze fantastisch werkomgevingen te creëren.

Marcel, hoe vaak heb ik jou niet om hulp gevraagd. Je stond altijd klaar wanneer iets moest gebeuren. In combinatie met jou vriendelijke karakter ben jij onmisbaar voor de groep.

Tijdens het begin van mijn PhD avontuur woonde ik in ons studentenhuis aan de Dennenweg. Bouwe, Jelte en Pascal bedankt voor de fantastische avonden, etentjes, en biertjes. Ik kijk hier met enorm veel plezier op terug. Pascal, wij brengen nu nog steeds veel tijd met elkaar door, en ik waardeer onze vriendschap enorm!

Bente, Jan-Willem, Jurjen, en Janine. Wij leerden elkaar kennen tijdens de eerste dag van onze pre-master op de UT. Sindsdien zijn wij nauw verbonden met elkaar en hebben we allemaal succesvol onze master afgerond. Samen hebben we veel lange (maar leuke!) dagen gemaakt. Onze vele eet en borrel afspraakjes zijn en waren fantastisch. Laten we dit nog lang blijven doen.

De familie Siebert, ik heb jullie mogen leren kennen nadat ik Leonie heb ontmoet. Wat een plezier heeft mij dit gebracht. De afgelopen jaren was ik regelmatig in de weekenden bij jullie te vinden. Er is altijd ruimte voor een goed gesprek, drankje, en eten. Ik ben blij dat ik ook in Zwolle mij heb kunnen ontspannen in de weekenden.

Ard en Martijn, jullie zijn een aantal jaren ouder dan mij en daarom altijd een goed voorbeeld geweest hoe situaties aan te pakken. Samen met Mirjam, Andreaa en de kids Lynn, Noud, en Milan gaan we een mooie toekomst tegemoet.

Papa en mama, ik vraag me nog steeds af hoe jullie onze opvoeding hebben gedaan. Een perfect combinatie van niets moeten, vrijheid en eigen verantwoordelijkheid. We zijn allemaal goed terechtgekomen en daar ben ik jullie enorm dankbaar voor. De liefde die jullie mij tot op de dag vandaag geven vind ik geweldig, ik ben blij met jullie!

Lieve Leonie, wat ben ik blij dat wij elkaar tegen zijn gekomen. Mijn leven is enorm verrijkt door jou. Dank voor al je steun en leuke uitjes tijdens stressvolle momenten. Ik ben je dankbaar voor je eerlijkheid, gezelligheid, en enthousiasme. Ik kijk met veel plezier uit op onze toekomst samen. ♥